

Coated Metal Hydrides for Stationary Energy Storage Applications

Priyen C. Mistry, MSc, BSc

Thesis submitted to the University of Nottingham

for the degree of Doctor of Philosophy

June 2016



The University of
Nottingham

UNITED KINGDOM · CHINA · MALAYSIA

Contents

| | |
|---|-----------|
| List of Figures | 5 |
| Abstract | 10 |
| Acknowledgements | 13 |
| 1 Introduction | 14 |
| 1.1 Path to a sustainable energy future | 14 |
| 1.2 Energy storage systems | 16 |
| 1.2.1 Electrical application | 16 |
| 1.2.2 Thermal application | 18 |
| 1.3 Hydrogen as an energy vector | 21 |
| 1.3.1 Forms of hydrogen storage | 21 |
| 1.4 Forms of Hydrides | 30 |
| 1.4.1 Complex Hydrides | 31 |
| 1.4.2 Binary Hydrides | 32 |
| 1.4.3 Intermetallic/Alloy Hydrides | 33 |
| 1.5 Aims & Objectives | 34 |

| | | |
|----------|--|-----------|
| 2 | Literature Review | 37 |
| 2.1 | Introduction | 37 |
| 2.2 | Intermetallic Hydrides | 37 |
| 2.2.1 | AB ₅ Intermetallics | 37 |
| 2.2.2 | A ₂ B Intermetallics | 38 |
| 2.2.3 | Solid Solution Alloys | 39 |
| 2.2.4 | AB Intermetallics | 40 |
| 2.2.5 | AB ₂ Intermetallics | 47 |
| 2.3 | Magnesium Hydride | 55 |
| 2.3.1 | Improving reaction kinetics | 60 |
| 2.3.2 | Cycling | 66 |
| 2.4 | Alternative Processing Technology | 69 |
| 2.5 | Coating Technologies | 73 |
| 2.6 | Summary | 75 |
| 3 | Experimental Methods | 78 |
| 3.1 | Introduction | 78 |
| 3.2 | Sample Preparation | 79 |
| 3.2.1 | Production & Sourcing | 79 |
| 3.2.2 | Particle Sizing | 82 |
| 3.2.3 | Magnetron Sputtering Conditions | 83 |
| 3.3 | Sample Characterisation Techniques | 86 |

| | | |
|----------|---|------------|
| 3.3.1 | X-Ray Diffraction | 86 |
| 3.3.2 | X-ray Photoelectron Spectroscopy | 89 |
| 3.3.3 | Electron Microscopy | 91 |
| 3.4 | Hydrogen Storage Measurements | 94 |
| 3.4.1 | Volumetric Sorption Methods | 95 |
| 3.4.2 | Differential Scanning Calorimetry | 100 |
| 3.4.3 | Thermogravimetric Analysis | 101 |
| 4 | Moderate temperature thermal storage | 103 |
| 4.1 | Introduction | 103 |
| 4.2 | Results | 104 |
| 4.2.1 | Hydrogen Storage Characteristics | 104 |
| 4.2.2 | Structural Analysis | 120 |
| 4.3 | Discussion | 124 |
| 5 | Domestic thermal and hydrogen stores | 133 |
| 5.1 | Introduction | 133 |
| 5.2 | TiFe Alloy Results | 134 |
| 5.2.1 | Hydrogen Storage Characteristics | 134 |
| 5.2.2 | Structural Analysis | 142 |
| 5.3 | TiFe Alloy Discussion | 159 |
| 5.3.1 | Properties of TiFe | 159 |
| 5.3.2 | Effect of Minor Ni Substitution | 161 |

| | | |
|----------|---|------------|
| 5.3.3 | Improving Ease of Activation | 163 |
| 5.4 | AB ₂ Alloy Results | 170 |
| 5.4.1 | Hydrogen Storage Characteristics | 170 |
| 5.4.2 | Structural Analysis | 177 |
| 5.5 | AB ₂ Alloys Discussion | 180 |
| 5.5.1 | Properties of Alloys | 180 |
| 5.5.2 | Kinetic Reaction Mechanisms | 182 |
| 5.5.3 | Summary of AB ₂ alloy comparison | 188 |
| 6 | Conclusions | 190 |
| 7 | Future Work | 194 |
| | Bibliography | 197 |

List of Figures

| | | |
|-----|---|----|
| 1.1 | Volumetric energy density of hydrogen compared with petrol | 23 |
| 1.2 | Differences between physisorption and chemisorption processes | 24 |
| 1.3 | A typical PCI, phase diagram and Van't Hoff plot of a metal hydride | 26 |
| 1.4 | Comparison between maximum and reversible storage capacity | 27 |
| 1.5 | Van't Hoff lines for binary hydrides | 32 |
| 2.1 | Volumetric and gravimetric hydrogen density of selected hydrides . . . | 41 |
| 2.2 | (a) The C14 Laves and (b) C15 Laves crystal structure | 48 |
| 2.3 | Correlation between cell volume V_{C14} and $-\Delta H$ | 49 |
| 2.4 | Mn-Ti phase diagram | 51 |
| 2.5 | Crystal structure of β -MgH ₂ | 56 |
| 2.6 | SEM/BSE micrographs of partially dehydrogenated MgH ₂ powder . . . | 59 |
| 2.7 | MgH ₂ particle size effect on onset temperature of H ₂ desorption | 61 |
| 2.8 | Potential energy diagram during metal hydride formation | 63 |
| 2.9 | Schematic of a basic magnetron sputtering set-up | 74 |
| 3.1 | (a) PSI HERMIGA 75 atomiser (b) hopper unit | 80 |

| | | |
|-----|--|-----|
| 3.2 | (a) Laser light scattering schematic (b) Optical bench within Malvern Mastersizer 2000 | 82 |
| 3.3 | ‘Tilted cup’ magnetron sputtering schematic | 84 |
| 3.4 | Instrument broadening from LaB ₆ reference sample with 2 nd order polynomial fit | 88 |
| 3.5 | Representation of incident electrons interacting with the sample | 91 |
| 3.6 | Schematic of double-manifold Sievert’s apparatus | 96 |
| 3.7 | Volume calibration data with fitted linear regression lines for the double-manifold Sievert’s apparatus used | 98 |
| 4.1 | (a) Hydrogen storage capacity and (b) Normalized capacity for activated & cycled Mg30 and V_Mg30 during the 10 th cycle at 400 °C | 105 |
| 4.2 | Normalized uptake for each sample during the activation process at 400 °C | 106 |
| 4.3 | Normalized uptake after 3 and 30 min against cycle number for coated and uncoated Mg samples when cycled at 400 °C with/without undergoing a prior activation process | 108 |
| 4.4 | Normalized uptake after 3 and 30 min for each ‘activated & cycled’ sample at (a) 400 °C during the 50 th hydrogenation cycle and (b) 350 °C during the 90 th hydrogenation cycle | 109 |

| | | |
|------|--|-----|
| 4.5 | Normalized uptake for each ‘activated & cycled’ sample at 400 °C during an extended final hydrogenation cycle post 50 cycles. | 110 |
| 4.6 | Normalized uptake for each sample during the activation process at 350 °C | 110 |
| 4.7 | Normalized uptake during selected cycles for samples when cycled at 350 °C | 112 |
| 4.8 | Normalized uptake for each ‘activated & cycled’ sample at 350 °C during an extended final hydrogenation cycle post 90 cycles | 114 |
| 4.9 | TGA graphs showing dehydrogenation weight loss post extended final hydrogenation | 115 |
| 4.10 | DSC endotherms of samples post 90 cycles at 350 °C | 116 |
| 4.11 | Kissinger plots of samples post 90 cycles at 350 °C | 117 |
| 4.12 | PCI (de)hydrogenation of Cr_Mg26 post 90 cycles at 350 °C | 119 |
| 4.13 | Van’t Hoff plot for Cr_Mg26 post 90 cycles at 350 °C | 119 |
| 4.14 | Particle size distribution of as received Mg powders | 120 |
| 4.15 | XRD pattern of V_Mg30 dehydrogenated following cycling at 400 °C | 121 |
| 4.16 | SEM images of as received Mg powder and cross-sections of porous samples post 90 cycles at 350 °C | 123 |
| 4.17 | Schematic comparing the proposed mechanisms for (un)catalysed Mg samples | 130 |

| | | |
|------|---|-----|
| 5.1 | Initial hydrogenation of TiFe and and TiFe _{0.96} Ni _{0.04} with/without a Pd coating | 135 |
| 5.2 | Hydrogenation kinetics comparison of TiFe _{0.96} Ni _{0.04} with/without a Pd coating | 136 |
| 5.3 | PCI (de)hydrogenation of TiFe | 137 |
| 5.4 | PCI (de)hydrogenation of TiFe _{0.96} Ni _{0.04} | 138 |
| 5.5 | PCI (de)hydrogenation of Pd_TiFe _{0.96} Ni _{0.04} | 139 |
| 5.6 | Van't Hoff plots for TiFe, TiFe _{0.96} Ni _{0.04} and Pd_TiFe _{0.96} Ni _{0.04} | 140 |
| 5.7 | XRD patterns for TiFe _{1-x} Ni _x (x = 0, 0.04 and 0.08) alloys | 143 |
| 5.8 | Unit cell volume versus Ni content in TiFe _{1-x} Ni _x alloys | 143 |
| 5.9 | SEM images of TiFe as prepared & post cycling | 146 |
| 5.10 | SEM images of TiFe _{0.96} Ni _{0.04} as prepared & post cycling | 147 |
| 5.11 | SEM images of Pd_TiFe _{0.96} Ni _{0.04} as prepared & post cycling | 148 |
| 5.12 | TEM images of Pd catalyst present on the surface of Pd_TiFe _{0.96} Ni _{0.04} | 149 |
| 5.13 | XPS spectrum of TiFe as prepared | 152 |
| 5.14 | XPS spectrum of TiFe post cycling | 153 |
| 5.15 | XPS spectrum of Pd_TiFe _{0.96} Ni _{0.04} as prepared | 154 |
| 5.16 | XPS spectrum of Pd_TiFe _{0.96} Ni _{0.04} post cycling | 155 |
| 5.17 | XPS high resolution spectra of Ti 2p, Fe 2p and Pd 3d from Pd_TiFe _{0.96} Ni _{0.04} as prepared | 156 |
| 5.18 | XPS spectrum of Ti _{0.6} Zr _{0.4} MnCr as prepared | 157 |

| | |
|--|-----|
| 5.19 XPS high resolution spectra of Ti 2p, Zr 3d, Mn 2p and Cr 2p from Ti _{0.6} Zr _{0.4} MnCr as prepared | 158 |
| 5.20 Comparing enthalpies with differing Ni content in TiFe _{1-x} Ni _x | 162 |
| 5.21 Hydrogenation kinetics comparison for AB ₂ alloys during cycles 1-5 | 170 |
| 5.22 Hydrogenation kinetics comparison for AB ₂ alloys at different temper- atures | 172 |
| 5.23 PCI (de)hydrogenation of Hydralloy C5 | 173 |
| 5.24 PCI (de)hydrogenation of Ti _{0.9} Zr _{0.2} Mn _{1.5} V _{0.2} Cr _{0.3} | 174 |
| 5.25 Van't Hoff plots for Hydralloy C5 and Ti _{0.9} Zr _{0.2} Mn _{1.5} V _{0.2} Cr _{0.3} | 175 |
| 5.26 XRD patterns for Hydralloy C5 and Ti _{0.9} Zr _{0.2} Mn _{1.5} V _{0.2} Cr _{0.3} | 177 |
| 5.27 SEM images of Hydralloy C5 and Ti _{0.9} Zr _{0.2} Mn _{1.5} V _{0.2} Cr _{0.3} as prepared and post cycling | 179 |
| 5.28 Hydralloy C5 and Ti _{0.9} Zr _{0.2} Mn _{1.5} V _{0.2} Cr _{0.3} hydrogenation kinetics fit- ted to the Avrami-Erofeev rate equation | 183 |
| 5.29 Hydralloy C5 and Ti _{0.9} Zr _{0.2} Mn _{1.5} V _{0.2} Cr _{0.3} hydrogenation kinetics at different temperatures fitted to a first order model | 185 |
| 5.30 β phase Arrhenius plot for Hydralloy C5 and Ti _{0.9} Zr _{0.2} Mn _{1.5} V _{0.2} Cr _{0.3} | 187 |
| 5.31 Working capacities for Hydralloy C5 and Ti _{0.9} Zr _{0.2} Mn _{1.5} V _{0.2} Cr _{0.3} | 188 |

Abstract

This thesis explores suitable materials for energy stores for stationary applications, specifically a prototype hydrogen store, domestic thermal store operating between 25-100 °C and a moderate thermal store for a concentrated solar power (CSP) plant operating at 400 °C. The approach incorporated a unique coating technique to deliver prototype hydrogen and thermal storage media, where the coating could offer commercial advantages, for example, in the form of hydride activation and enhanced kinetics during successive cycling.

The highly reversible Mg-MgH₂ system is particularly promising for thermal storage, obtaining an enthalpy of reaction of 74.5 kJ.mol⁻¹ H₂ that translates to a thermal energy capacity of approximately 2800 kJ.kg⁻¹ of MgH₂. Nevertheless, magnesium is hindered by slow activation and poor kinetics of (de)hydrogenation, even when approaching temperatures ideal for concentrated solar power applications (in the region 400 °C). Elevated temperature cycling studies were performed on commercial atomised Mg powder with magnetron sputtered catalysts (chromium, iron, vanadium and stainless steel) applied to their surfaces; the aim of which was to fabricate hydrogen storage materials that possess (de)hydrogenation characteristics equal to or even bettering their nanocrystalline equivalents, yet in a potentially economic and scalable manner.

Following 50 cycles at 400 °C, the coatings were found to have little to no positive impact on the behaviour of the atomised Mg powders. In addition, for both uncoated

and coated samples the effects of an activation process at 400 °C are matched by cycling the material 5 times from the outset, after which identical behaviour is observed during subsequent cycles. At 350 °C, the benefits of catalyst coatings on the hydrogen storage properties of atomised Mg powders are evident during activation and successive cycling up to 90 times. The material undergoes different microstructural evolution during cycling when in the presence of a surface catalyst, causing an enhancement of the ‘nucleation and growth’ stage of (de)hydrogenation. This was attributed to particle reorientation dominating particle sintering, whereas the opposite occurs for the uncoated material.

For the domestic thermal and prototype hydrogen stores a selection of AB and AB₂ intermetallic hydrides enhanced through catalysis or thermodynamic modification were investigated. TiFe produced via powder atomisation obtained thermodynamic properties (dehydrogenation $\Delta H = 28.9 \pm 0.7 \text{ kJ.mol}^{-1} \text{ H}_2$ and $\Delta S = 105 \pm 2 \text{ J.K}^{-1}\text{mol}^{-1} \text{ H}_2$) in line with published results. The minor substitution of Ni into TiFe_{1-x}Ni_x resulted in different hydrogenation characteristics to TiFe, for example, TiFe_{0.96}Ni_{0.04} possessed a dehydrogenation of $\Delta H = 29.9 \pm 0.9 \text{ kJ.mol}^{-1} \text{ H}_2$ and $\Delta S = 107 \pm 5 \text{ J.K}^{-1}\text{mol}^{-1} \text{ H}_2$. Discrepancies between maximum achieved and theoretical capacities were observed for both atomised TiFe and TiFe_{0.96}Ni_{0.04} and a range of possible contributing factors are discussed. A minor addition of Pd (1.17 wt.%) magnetron sputtered to the surface of TiFe_{0.96}Ni_{0.04} enabled successful room temperature hydrogenation with no activation treatment required. Characterisation (SEM and TEM) confirmed it is not necessary to have complete Pd coverage

in the form of a uniform coating and XPS was utilised to derive a theory for the activation mechanism.

The AB₂ alloy comparison between the commercially available Hydralloy C5 and in house fabricated Ti_{0.9}Zr_{0.2}Mn_{1.5}V_{0.2}Cr_{0.3} showed that Hydralloy C5 was the most promising alloy for the hydrogen store application with the higher working capacity (ca. 0.96 wt.%) in the pressure range of 4-15 bar at 22 °C, despite Ti_{0.9}Zr_{0.2}Mn_{1.5}V_{0.2}Cr_{0.3} obtaining a higher maximum storage capacity (1.82 wt.%). The hydrogenation kinetics of both alloys were studied with corresponding activation energies and hydrogen diffusion coefficients determined. The kinetics of hydrogenation for both alloys is sufficiently fast that only the heat transfer of the storage system is the rate limiting parameter for hydrogen exchange for most technical applications.

Acknowledgements

I would like to thank my supervisors, Prof. David Grant and Prof. Gavin Walker for providing me with the opportunity and guidance to carry out the research presented in this study.

Thank you also to Rory Scream and Dr Nicholas Botterill for their assistance in alloy fabrication, as well as Dr Dmitriy Ievlev for producing the magnetron sputtered coatings investigated. In addition, many thanks to Dr Nigel Neate and Mr Martin Roe for their help with the X-ray diffraction, X-ray photoelectron spectroscopy and electron microscopy techniques used for sample characterisation.

To my colleagues in the hydrogen research group past and present, especially Dr Andrew Patman, Dr Marwa Abbas, Dr Xuanli Luo and Dr Kandavel Manickam, thank you for the helpful pointers inside and outside of the laboratories.

Finally, thank you to my family for their life-long support, continued encouragement and ability to brighten my mood when in need of a break.

Research performed over the course of this thesis was in conjunction with an Innovate UK (formerly Technology Strategy Board) backed project known as the H-Store involving several industrial partners; Eminate Ltd., E.ON, ITM Power, Sunamp and Teer-Miba Coating Group.

Chapter 1

Introduction

1.1 Path to a sustainable energy future

The inevitable depletion of fossil fuel resources, coupled with the environmental impacts accompanying their procurement and use, has resulted in the highlighting of three key topics of concern: the future energy mix, global energy trading patterns and the carbon emissions pathway. Significant improvements in the production and management of energy are critical and efforts such as the 21st United Nations climate conference (COP21) are essential to promote the transition away from conventional energy sources and carriers towards sustainable ones.

With the exclusion of nuclear power, non-renewable energy sources amassed to 86% of the global share of primary energy (IEA, 2014a) and by 2040 the International Energy Agency (IEA) anticipates global energy demand to rise by a further 37% (IEA, 2014b). No single fossil fuel is expected to dominate, with each contributing 26-28%

to meet global energy demand (BP, 2015), and the remaining quarter accounted for by low-carbon fuels. Unfortunately, fossil fuels will persist as the prevailing form of energy with an overall share of 81% in 2035.

A continued long-term global trend towards electrification means that by 2040 the contribution from the power sector is set to rise to about half of primary energy consumption. Consequently, some 7200 GW of capacity needs to be built in conjunction with the replacement of 40% of the current power plant fleet due for retirement (IEA, 2014a) and as a result this is predicted to pave the way for strong growth of renewables.

In spite of increasing penetration of low-carbon technologies it is unlikely to sufficiently stem the growth in CO₂ emissions, which may rise by a fifth by 2040 (DECC, 2015). Subsequently, the current trajectory will result in a long-term global average temperature rise of 3.6 °C (IEA, 2014a), far exceeding the 2 °C limit internationally agreed upon to prevent the most damaging repercussions of climate change. Urgent action is required to tackle the fossil-fuel pillar of global energy supply, although no single initiative or improvement will be the solution.

As well as technological efficiency advancements and a refocus away from the importance of energy intensive industries, power generation from renewables such as hydroelectricity, biofuels, solar, wind and geothermal energy offer potential solutions to create a sustainable energy system. Putting aside the technical aspects associated with improving efficiencies from renewable energy sources, there remains a host of questions that needs addressing. Unresolved intermittency issues, mismatches

between peak supply and demand, and the overall increase in power that electrical grids will need to handle underlines the necessity for wide-scale energy storage deployment.

A variety of techniques are utilised presently, in the form of physical storage (pumped hydroelectricity and compressed air), chemical potential (batteries and combustible fuels) and thermal storage (sensible and latent heat materials). Another proposal receiving mounting attention is an economy centred on hydrogen. While not a renewable source of energy itself, the vision is founded upon hydrogen as a versatile energy carrier facilitating energy storage and distribution.

1.2 Energy storage systems

1.2.1 Electrical application

In order to have a reliance on a hydrogen economy, production needs to react to demand. As of 2013, the refining and ammonia production industries were responsible for approximately 90% of global hydrogen consumption (254.5 billion cubic meters). This demand is anticipated to increase 3.5% annually, reaching over 300 billion cubic meters by 2018, driven by clean fuel regulations and rising per capita vehicle ownership rates especially in developing countries in Asia ([Freedonia, 2014](#)).

Hydrogen is the most abundant element in the universe; however its reactive nature means it is seldom found in its molecular form, H_2 . As a result, other naturally occurring resources like water, fossil fuels and biomass are used for the extraction of

hydrogen. Reformation of fossil fuels, especially natural gas, is the current leading form of hydrogen production at 96%, with the rest accounted for by nuclear and electrolysis (IPHE, 2011).

The superior specific energy of hydrogen (142 MJ.kg^{-1}), compared to petrol (46.5 MJ.kg^{-1}), greatly strengthens its appeal as the base of a renewables-based energy system (Wengenmayr and Bürke, 2013). In view of the current CO_2 emissions trend, described in Section 1.1, hydrogen also offers an incentive of only emitting water vapour when used as an input in a combustion engine or fuel cell to generate electricity. The prospect of avoiding CO_2 emissions is particularly attractive for the transport sector, which accounted for 28% of primary energy consumption (EIA, 2015) and 23% of CO_2 emissions (IEA, 2014c) globally in 2012.

Apart from its potential as a combustible fuel, hydrogen used in a fuel cell and electric motor system can reach efficiencies of 45% (Jaccard, 2005), thus exceeding the traditional petrol internal combustion engine (ca. 20%) (Beggs, 2009). Furthermore, a hydrogen efficiency of up to 90% is achievable if fuel cells are configured into a combined heat and power (CHP) system, in which captured waste heat is utilised (FCHEA, 2015). Over the past decade fuel cell system cost ($\$124 \text{ kW}^{-1}$ in 2006) has prevented the exploitation of automotive applications but the predicted $\$55 \text{ kW}^{-1}$, based on producing 500,000 systems per year (DOE, 2014), shows the gap to petrol internal combustion engine costs have significantly narrowed.

1.2.2 Thermal application

Of all renewable energy resources, solar energy is undoubtedly the most abundant and thus one can rationalise it should be given the highest priority (Abbott, 2010). A technology roadmap published by the IEA (IEA, 2014d) envisions about 27% of global electricity generation to be derived from solar energy by 2050, of which solar photovoltaic (PV) systems and concentrated solar power (CSP) systems are expected to contribute 60% and 40% respectively. To realise this target, economical electricity generation from solar energy is vital, together with the implementation of cost-effective energy storage technologies to resolve the issues mentioned in Section 1.1.

The cost of solar PV systems has sharply fallen in recent years and this trend is widely anticipated to continue (Reichelstein and Yorston, 2013), mostly owing to cheaper manufacturing costs. Nevertheless, the storage of electricity via battery technology or through electrolysis conversion to hydrogen is hindered by high costs and a low solar-to-hydrogen efficiency of about 14% on the laboratory scale (May et al., 2015). If the gap to potential solar-to-hydrogen (17.4%) can be minimized further it could become commercially feasible ($\$4 \text{ kg}^{-1}$) (Pinaud et al., 2013).

CSP systems are considered to have the capability to fill the rest of the generation target. The principle of electricity production in a CSP system and conventional power plants are the same, in which produced steam drives turbines. Yet, to reach comparable generation costs of $\$0.06 \text{ kWh}^{-1}$ (DOE, 2013a) CSP plants will need

financially viable thermal storage systems designed to store appropriate amounts of heat for sustained periods; hence enabling formerly daily and seasonal dependent CSP plants to become dispatchable.

Existing CSP plants are only cost-effective if constructed on a utility scale (≥ 50 MW) (Tian and Zhao, 2013). Although this enables established steam turbine generation and simple solar field technologies to be employed, it does lead to one major drawback: the transfer of electricity produced, into the existing power grid, will necessitate large collateral investment into transmission infrastructure upgrades. To evade this potential predicament it has been proposed that CSP plant size should be downscaled. This is attainable by increasing the quantity of heat stored through both higher energy storage temperatures, to improve overall solar-to-electricity efficiencies, and the use of higher energy density storage materials, thus lowering the volume of material needed (Harries et al., 2012). If achieved, CSP technology will be more accessible as a distributed generation option capable of stand-alone applications and providing supplements to existing grids.

The materials used for CSP energy storage can be classified into three categories: sensible heat storage, latent heat storage and thermochemical storage. Sensible heat storage is the simplest and most established technology used in conjunction with CSP plants (Kuravi et al., 2013). This particular system relies upon thermal energy being stored in a material, as a function of its specific heat capacity, by raising its temperature. Materials used typically take on the form of a solid (e.g. concrete) or a molten salt mixture (e.g. 60% NaNO_3 ; 40% KNO_3) because they are reasonably

| Type of thermal storage | Example material | Material heat storage capacity [kJ/kg] | Volumetric energy density [MJ/m ³] | Cost [£/kg] |
|-------------------------|---|--|--|-------------|
| Sensible heat | Molten salt mixtures | 153 | 290 | 0.7 |
| Latent heat/PCMs | LiNO ₃ | 360 | 860 | 53 |
| Thermochemical | Oxidation of Co ₃ O ₄ | 1055 | 6450 | >100 |
| Metal hydride | Mg + H ₂ ⇌ MgH ₂ | 2814 | 4080 | 2.7 |

Table 1.1: Types of thermal storage, adapted from [Harries et al. \(2012\)](#).

inexpensive and obtain decent thermal conductivities ([Tamme, 2003](#)). While a mature technology, the ultimate concern still lies with the sheer volume of molten salt storage required. For example, Solar Millenium’s 50 MW Andosol 1 plant needs 28,500 ton of molten salt for 7.5 h storage ([RWE Solar Millennium, 2009](#)).

Latent heat storage, via phase change materials (PCMs), are seen as the next advancement. Since these materials also utilise the heat of fusion or solidification during phase change they offer the advantage of higher energy densities and improved efficiency owing to the isothermal nature of the storage mechanism ([Ward et al., 2015](#); [Yan et al., 2015](#)). Nevertheless, concerns regarding the cycling durability and corrosive nature of many high temperature PCMs limit their current practicality.

Thermochemical storage offers the unique prospect of more compact storage given that energy densities can be an order of magnitude higher than those of the two storage techniques previously described ([Harries et al., 2012](#)). If integrated with a CSP plant, heat from the solar energy is used to initiate an endothermic chemical decomposition reaction, in what is a reversible closed loop system. The heat energy necessary to cause the dissociation is equivalent to the enthalpy of formation of the chemical. If the products are kept under ambient temperatures

there is little to no energy loss incurred, unless the reaction products initially need to be cooled (Abedin and Rosen, 2011). Upon demand, the products are recombined to synthesise the original chemical in an exothermic reaction. To date, materials utilising carbonation, oxidation and hydrogenation reactions have been explored. Of these reactions, hydrogenation of metal hydrides have the exclusive capability to absorb/desorb large amounts of hydrogen at a constant pressure (see Section 1.3.1), making them especially suited for thermochemical storage in CSP applications.

1.3 Hydrogen as an energy vector

1.3.1 Forms of hydrogen storage

The clean and versatile aspects of hydrogen, together with its high energy density, undoubtedly make it an attractive technology. Yet, the fruition of a hydrogen economy is unlikely unless a safe and cost efficient technique of storing hydrogen can be developed. Hydrogen is naturally gaseous and under standard atmospheric conditions (25 °C and 1.01325 bar) 1 kg of hydrogen has a volume of 11.126 m³. Even at 350 bar the volumetric density of hydrogen is only 0.77 kWh.l⁻¹, in comparison with petrol (8.76 kWh.l⁻¹), which means a larger tank size or a sacrifice of vehicle range is required (Stolten, 2010).

To provide a clearer guide for real end-user application, the DOE set out performance targets for on-board storage of hydrogen as presented in Table 1.2. It is important to recognise the on-board targets quoted here are representative of

| Storage Parameter | Revised 2010 goal | 2020 goal | Ultimate goal |
|--|-------------------|-----------|---------------|
| Gravimetric capacity [wt.%] | 4.5 | 5.5 | 7.5 |
| Volumetric energy density [kWh.l ⁻¹] | 0.9 | 1.3 | 2.3 |
| Operational cycle life | 1000 | 1500 | 1500 |
| Fill time [min, 5 kg H ₂ store] | 4.2 | 3.3 | 2.5 |
| Storage system cost [\$.gge ^{-1*}] | 2-4 | 2-4 | 2-4 |

Table 1.2: US DOE targets for on-board hydrogen storage systems for light-duty vehicles (DOE, 2009). * gallon gasoline equivalent

the whole system, not only of the storage material, and total system densities are generally half those of the working material (Yang et al., 2010).

Presently there are three common methods to store hydrogen: as a compressed gas, as a cryogenic liquid, or in a solid form. Compression of hydrogen to 700 bar increases volumetric density (1.35 kWh.l⁻¹) but the non-ideal gas behaviour of hydrogen means the marginal gains in energy content are not justified by the increasing demands on tank wall thickness (Züttel, 2003). Also, there are concerns about the safety of high pressurised cylinders, as well as the cost of compression which is estimated at 10-15 % of the lower heating value of hydrogen (Hordeski, 2009).

Liquefaction of hydrogen to store cryogenically at -252 °C leads to a volumetric density of 2.4 kWh.l⁻¹. Nevertheless, this value reduces further after taking into consideration the well-insulated storage tanks necessary to prevent the evaporation losses from hydrogen boil-off, ranging between 0.3-3 % per day (Hirscher, 2010). Another concern is the energy penalty associated with the liquefying process which is equivalent to about 40% of the hydrogen energy content (Hordeski, 2009).

As a consequence of the shortcomings of compression and liquefaction of hydrogen,

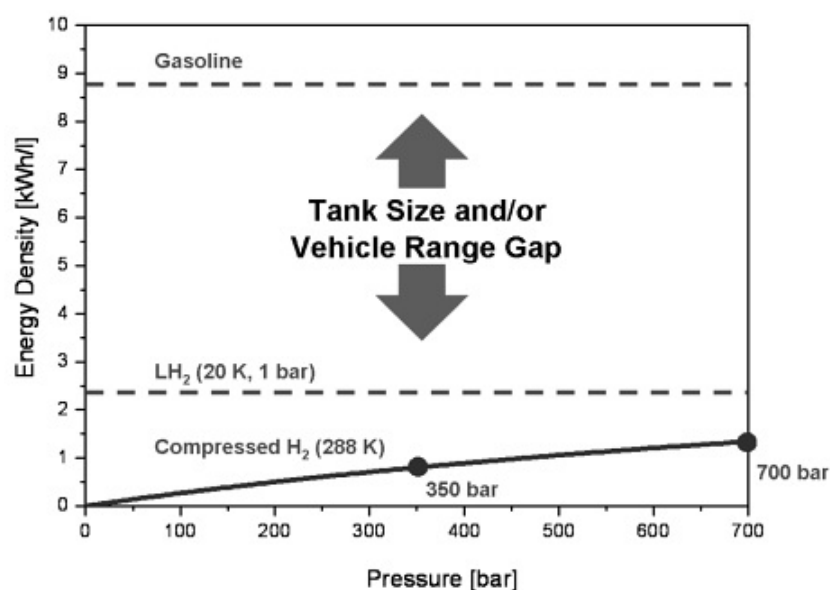


Figure 1.1: Volumetric energy density of hydrogen compared with petrol, taken from (Stolten, 2010).

solid-state storage is now at the forefront of hydrogen storage research. Solid-state storage can be divided into two categories: physisorption - whereby hydrogen is physically bound onto a surface, or chemisorption - through which hydrogen is chemically bound to other elements.

Physisorption

The van der Waals interaction between molecular hydrogen and a substrate surface form the basis of physisorption. These interactions possess a low enthalpy of adsorption ranging between 4 and 10 $\text{kJ}\cdot\text{mol}^{-1}$, so low temperatures (ca. $-196\text{ }^\circ\text{C}$) are a necessity before a notable amount of hydrogen adsorption can occur (Walker, 2008). While this results in inevitable energy costs associated with cryogenic storage vessels required; the weak nature of the bond is advantageous in that the kinetics of reaction

are inherently fast (Neto et al., 2012).

Material surface area (Züttel et al., 2004) and pore geometry (bulk density) (Nijkamp et al., 2001) have been demonstrated as key characteristics in influencing hydrogen storage properties. In an attempt to optimise these parameters, extensive studies of adsorbents have been conducted including activated carbons (Yang et al., 2012), carbon nano-tubes (CNTs) (Oriňáková and Oriňák, 2011), zeolites (Broom, 2011) and metal-organic frameworks (MOFs) (Thomas, 2009). At 80 bar MOF-210 obtains a total uptake of 15 wt.% H_2 but only at $-196\text{ }^\circ\text{C}$ (Furukawa et al., 2010).

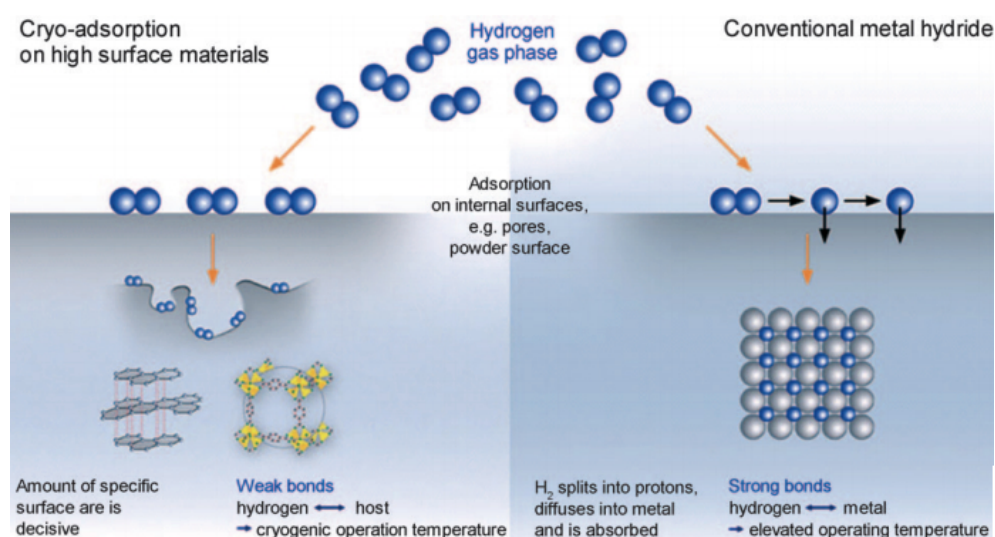


Figure 1.2: Illustrating the differences between the physisorption and chemisorption processes, taken from Eberle et al. (2009).

Chemisorption

Combining the innately safe behaviour of chemically bound hydrogen with relatively moderate operating conditions and high volumetric capacities, it is understandable why these materials are prime candidates for solid state storage of hydrogen. The

process for chemisorption involves several stages: dissociation of molecular hydrogen adsorbed onto the metal surface, interaction between atomic hydrogen (H) and the metal (M) forming a strong valence bond and lastly diffusion of hydrogen, mainly into the bulk of the material. The generic expression for reversible hydride formation is as follows:



where MH is the metal hydride, x is the ratio of hydrogen to metal and Q is the heat of reaction.

While the hydrogen concentration remains fairly low in the M - H solid solution generated, this state is commonly recognised as the α -phase. As H -atoms saturate the crystal lattice, the hydrogen concentration increases rapidly at an almost constant pressure, known as the $\alpha+\beta$ transition or plateau pressure. The dissolution of hydrogen atoms typically leads to expansion of the metal lattice by approximately 2-3 Å per hydrogen atom (Dornheim, 2011). Following the significant rise in hydrogen concentration, the material completely enters the stable hydride state, called the β -phase, in which further hydrogenation occurs but with a rise in pressure. Dependent on the specific system (see Section 2), transition to the β -phase is accompanied by just simple expansion or a morphology change causing new crystal structure formation.

A pressure-composition-isotherm (PCI) (see Figure 1.3) links the hydrogen capacity of a metal hydride to pressure at a given temperature. If the temperature of the

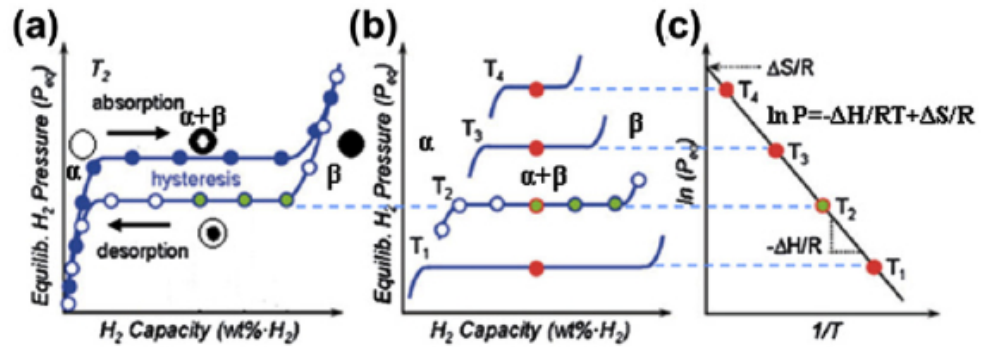


Figure 1.3: (a) A typical PCI plot, (b) phase diagram and (c) corresponding Van't Hoff plot of a metal hydride, taken from Suib (2013).

metal hydride is kept constant, an increase in applied hydrogen pressure will result in hydrogenation until saturation. The process can be reversed by decreasing the applied hydrogen pressure to below the equilibrium pressure, leading to the release of hydrogen from the hydride material until depletion. Likewise, for a given pressure, raising the temperature will cause hydrogen to be released until the new equilibrium pressure is reached. Thus, conversely if the temperature is reduced, the hydride will hydrogenate until saturation.

While PCI plots with flat plateaus are attainable, the majority of metal hydrides possess a sloping plateau to some extent, defined as $d\ln P_d/d\ln(H/M)$. This is possibly due to different equilibrium pressure lattice expansions and relaxation of residual forces to relieve the stress in the metal matrix (Reilly et al., 1980). Another feature commonly observed is hysteresis, $\ln(P_a/P_d)$, in which the desorption isotherm has a lower equilibrium pressure than the absorption isotherm. This is thought to be caused by surface inhomogeneities and localized defects as Flanagan and Clewley (1982) demonstrated using a quantitative model.

The general approach taken to describe the hydrogen storage capability of a material is to reference the volumetric capacity, and this defined as the amount of hydrogen stored per unit volume, or the H/M ratio, which is the number of hydrogen atoms (H) absorbed per metal unit (M). In reality there are often operating constraints for practical applications prompting the citation of other definitions such as working storage capacity.

Working storage capacity is recognised as the amount of hydrogen stored and released between the lower and upper operating pressures of the hydrogen store (Broom, 2011; Manickam et al., 2015). Notable discrepancies between working and maximum storage capacities may arise if a material takes up a relatively large amount of hydrogen at pressures outside that defined by the store design limits. As shown

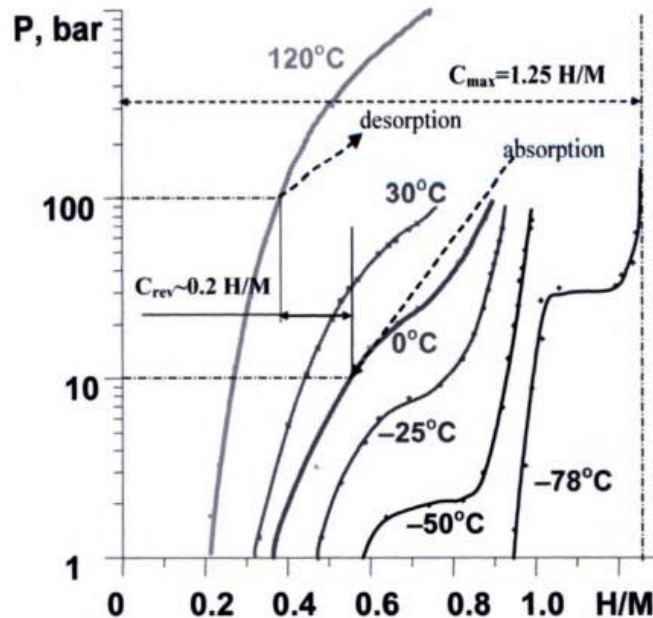


Figure 1.4: Comparison between the maximum (C_{max}) and reversible (C_{rev}) storage capacities for the TiCr_{2-x} system, taken from Johnson (1980).

in Figure 1.4, the TiCr_{2-x} system obtains a maximum capacity of 2.43 wt.% but less than 20% of this is attainable reversibly between temperatures of 0-120 °C and pressures of 10-100 bar (Johnson, 1980). In addition, irreversible hydrogen trapping occurs in some systems causing future cycles to have a lower reversible capacity than observed in the first cycle (Callear et al., 2014).

Knowledge about the thermodynamic properties of hydrides is fundamental when establishing how to promote the (de)hydrogenation processes. The direction of a reaction is relatable to the pressure and temperature of a hydride system by observing the change in standard Gibbs free energy, ΔG^0 , a determinant for whether a reaction will occur or not. The standard Gibbs free energy is linked to the enthalpy of the reaction ΔH^0 (equation 1.2) and the equilibrium constant K_p (equation 1.3) (Andreasen, 2004):

$$\Delta G^0 = \Delta H^0 - T\Delta S^0 \quad (1.2)$$

$$\Delta G^0 = -RT \ln K_p \quad (1.3)$$

where ΔS^0 is the standard entropy of the reaction and R is the gas constant.

Given that K_p for a solid hydride decomposing is:

$$K_p = \frac{P_{H_2}}{P^0} \quad (1.4)$$

where P_{H_2} is the actual hydrogen pressure and P^0 is the thermodynamic reference pressure (1 bar).

By equating 1.2 with 1.3 and substituting in 1.4 the resultant equation can be

re-arranged to:

$$\ln \frac{P_{H_2}}{P^0} = \frac{\Delta H^0}{RT} - \frac{\Delta S^0}{R} \quad (1.5)$$

This is known as the Van't Hoff equation (Bérubé et al., 2007). If the changes in the standard enthalpy, ΔH^0 , and entropy, ΔS^0 , are both known the equilibrium conditions for a specific pressure or temperature can be derived. Alternatively, in reverse, PCI data can be used to calculate the changes in enthalpy and entropy of a metal hydride. By plotting the natural logarithm of the equilibrium pressure, $\ln P_{H_2}$, (plateau pressures from several PCI measurements) against the reciprocal of the corresponding temperature, $1/T$, a linear relationship between the data points should be obtained (see Figure 1.3). The slope of the Van't Hoff plot equates to $\Delta H^0/R$ and the larger the value the higher the hydride stability. The intercept represents $\Delta S^0/R$ and all metal hydrides have almost the same entropy change (ca. $130 \text{ J.K}^{-1}\text{mol}^{-1}$), as it signifies the transition from atomic hydrogen into molecular hydrogen upon dehydrogenation or the reverse process for hydrogenation (Suib, 2013).

A value often cited is T_{1bar} which is the temperature at which the reaction ensues spontaneously under atmospheric pressure. In this case the left side of equation 1.5 will be zero, thus giving:

$$T_{1bar} = \frac{\Delta H^0}{\Delta S^0} \quad (1.6)$$

While a material's thermodynamics signify a vital characteristic upon deciding a potential hydrogen storage application; there are other properties that are

arguably as important for instance reaction kinetics, poisoning susceptibility, decrepitation and cycling stability. Thermodynamics will govern the pressures required for (de)hydrogenation but kinetics determine the rate of reaction, varying profoundly with different materials and the experimental conditions utilised, such as temperature and driving pressure. The evolution of a materials kinetics and reversible capacity, resulting from structural degradation and grain growth during extensive cycling studies, are equally crucial in the fabrication of a commercially successful hydride material. This is because the hydride must be able to achieve the proposed targets set for the desired application until the end of service life (typically 1,500 cycles for on-board and $> 10,000$ cycles for CSP thermal storage). In addition, the purity of hydrogen utilised in laboratory studies must be representative of those in commercial application because a discrepancy whereby a lower purity grade used in real life scenarios may result in hydrogen cycling capacities not being met, as a result of poisoning from impurities in the gas supply.

1.4 Forms of Hydrides

Considerable effort has been spent investigating the properties of many existing hydride materials, leading to the compilation of an extensive database listing possible materials for application in hydrogen storage by the US DOE (DOE, 2013b). In general, chemically bound hydrogen can be split into three main classifications: complex hydrides, binary hydrides and intermetallic/alloy hydrides. Each has been

reviewed in detail to explore their unique advantages and disadvantages (Sandrock, 1999; Sakintuna et al., 2007; Jain et al., 2010).

1.4.1 Complex Hydrides

Complex hydrides are generally expressed as $M(M'H_n)$, where M is a metal cation from Group IA or IIA (e.g. Na^+ , Li^+) and $M'H_n$ represents a hydrogen-containing 'complex' anion for example alanates $(\text{AlH}_4)^-$, borohydrides $(\text{BH}_4)^-$ and amides $(\text{NH}_2)^-$. Recognised as potential candidates for on-board application, due to their light weight and high hydrogen content (up to 20.8 wt.% for $\text{Be}(\text{BH}_4)_2$ (Hirscher, 2010)), a great deal of attention has been focussed towards resolving high operating temperatures, poor kinetics and limited reversibility with minimal energy penalty. The complex hydride BaReH_9 has been stated to decompose at less than 100 °C but a low hydrogen content of 2.7 wt.% leaves it largely unsuitable as a storage material (Yvon, 1998). Following key research in which NaAlH_4 was demonstrated to reversibly store up to 4.2 wt.% through catalyst enhanced Ti-doping (Bogdanovic and Schwickardi, 1997), research into multicomponent systems has yielded lower dehydrogenation temperatures and/or improved reversibility compared to conventional systems. However, this is often at the expense of storage capacity (Orimo et al., 2007; Schüth et al., 2004).

1.4.2 Binary Hydrides

The majority of metals in the periodic table can form binary hydrides; however most remain outside the realm of practical application. Binary hydride formation is accompanied by essential changes in the mutual locations of the metal atoms occurring as the crystal lattice expands. The lattice either remains invariant or as in most cases rearranges itself, a process requiring a considerable energy contribution. This means high pressures and temperatures are necessary or else storage capacities remain inadequate as to render the hydrides ineffective.

As shown in Figure 1.5, vanadium has been identified as the only element whose hydride can be attained within reasonable conditions (0-100 °C and 1-10 bar range for PEM fuel cell application (Sandrock, 1997)); yet its difficult activation necessitating

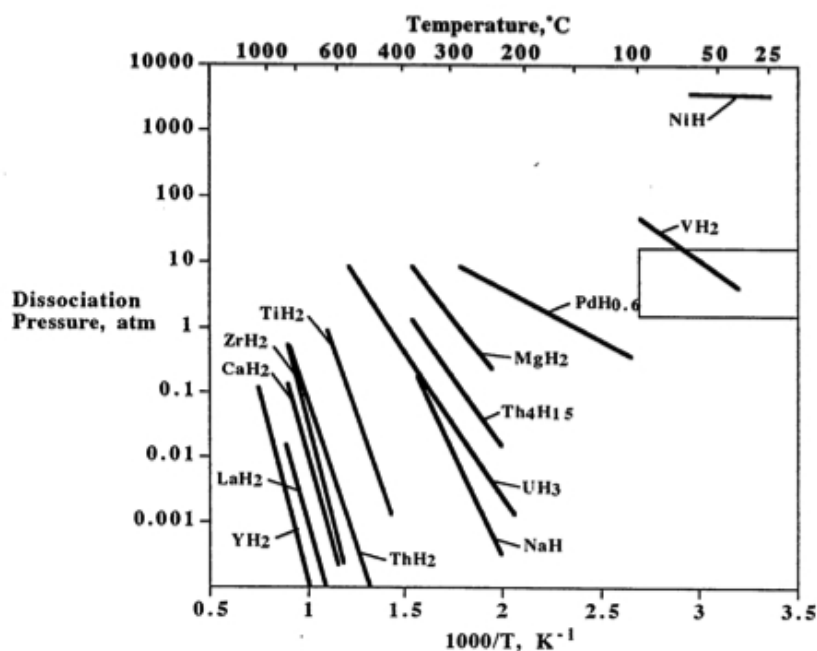


Figure 1.5: Van't Hoff lines (dehydrogenation) for binary hydrides, taken from Sandrock (1997).

cycling under hydrogen at 350-450 °C (Reilly and Wiswall, 1970) and high cost (ca. \$25 kg⁻¹ between 2011 and 2014 (Infomine, 2015a)) has eliminated it as a feasible storage material. Another hydride of particular interest is aluminium hydride (alane, AlH₃), which stores ca. 10 wt.% H₂ but obtains a large hydrogen fugacity, prohibiting thermodynamic stability at room temperature (Ahluwalia et al., 2009). Conversely, magnesium hydride, MgH₂, is a highly reversible stable hydride with dehydrogenation enthalpy of ca. -74.5 kJ.mol⁻¹H₂ (Stampfer et al., 1960) which translates to a T_{1bar} value of 279 °C. Although this high thermodynamic stability hampers its potential for on-board application, the equivalent thermal energy capacity of approximately 2800 kJ.kg⁻¹ of MgH₂ has a potential exploitation for thermal energy storage purposes. Coupled with the low cost of magnesium (ca. \$3 kg⁻¹ between 2011 and 2014 (Infomine, 2015b)) and a respectable storage capacity (7.66 wt.%), these properties make magnesium especially appealing as a hydrogen storage material.

1.4.3 Intermetallic/Alloy Hydrides

The discovery of intermetallic or alloy hydrides in the mid-twentieth century (Libowitz et al., 1958) propelled the concept of hydrogen storage into a realistic possibility, following the classical and quite limited elementary hydrides. Since the hydrogen binding energy varies greatly among the different elements, intermetallic hydrides were developed with the aim to ‘tune’ thermodynamic properties more favourably. The general theory for these alloys was that a combination of elements with opposing thermodynamic stabilities would result in the generation of an intermetallic with

intermediate hydride properties. A well-known example is CaNi_5 whose dehydrogenation enthalpy is $-31.9 \text{ kJ}\cdot\text{mol}^{-1}\text{H}_2$ (Sandrock et al., 1982) which lies between that of CaH_2 ($-181.5 \text{ kJ}\cdot\text{mol}^{-1}\text{H}_2$ (Grochala and Edwards, 2004)) and NiH ($-8.8 \text{ kJ}\cdot\text{mol}^{-1}\text{H}_2$ (Sandrock, 1999)).

Intermetallic alloys can be branched into several hydride families (AB_5 , AB_2 , AB , A_2B and solid solution alloys) where A typically represents a strong hydride forming lanthanide element, calcium or mischmetal, and B is weak hydriding transition element (Sandrock, 1999). Usually characterised by reversible capacities of less than 2 wt.% at near ambient temperatures, intermetallic hydrides are better suited to stationary storage applications where system mass is not imperative and their good volumetric hydrogen densities can be utilised, such as $117 \text{ kg}\cdot\text{m}^{-3}$ for $\text{TiFeH}_{1.7}$ (see Figure 2.1).

1.5 Aims & Objectives

The principal aim of this work was to explore unique materials for stationary applications, specifically a prototype hydrogen store, domestic thermal store operating between 25-100 °C and a moderate thermal store for a CSP plant operating at 400 °C. The approach incorporated a unique coating technique to deliver prototype hydrogen and thermal stores, where the coating may offer commercial advantages, for example, in the form of hydride activation and enhanced kinetics during successive cycling. The main objectives of this research can be categorised into several sections:

1) Objectives for moderate temperature thermal storage materials

Magnesium hydride was chosen as the focal point for the moderate thermal store to exploit the high thermal energy capacity available (ca. 2800 kJ.kg^{-1} of MgH_2). The importance of an activation process prior to the cycling of atomised magnesium powder with/without catalytic coatings was investigated. In parallel, the effects of temperature and pressure on these samples were studied. Lastly, the potential fabrication of porous magnesium structures through successive cycling was explored.

2) Objectives for domestic thermal and hydrogen storage materials

A selection of intermetallics were considered for the prototype hydrogen store and domestic thermal store, given that their respectable volumetric hydrogen densities and thermodynamic properties align well with near ambient temperature applications. A Pd coating was applied to a TiFe-based alloy to explore the challenges and advantages of a coating to aid hydrogen dissociation during activation, prevent oxidation and enhance sorption kinetics via catalytic behaviour. The effect of Ni substitution was also investigated with the purpose to tune the thermodynamic properties of the TiFe-based alloy for the domestic thermal store. Lastly, an optimised AB_2 alloy was designed to operate within the 4-15 bar and ca. $25 \text{ }^\circ\text{C}$ limits set by the prototype hydrogen store and this was compared against a similar commercially available AB_2 alloy.

The basis and motivation behind these objectives are explored in Chapter 2,

which provides a critical review of the published literature surrounding intermetallic hydrides (in particular TiFe-based alloys and TiMn₂-based alloys), magnesium hydride and the coating technologies currently in practice. Chapter 3 describes the experimental processes and conditions used to produce and characterise the range of hydride materials studied. The following two chapters presents results and discussions, with Chapter 4 addressing the effectiveness of candidate catalyst coatings on atomised magnesium powder under a variety of conditions and Chapter 5 focussing on intermetallic hydrides for meeting the conditions of a domestic thermal store and prototype hydrogen store. Chapter 6 will summarise the main concluding findings from this research and Chapter 7 will provide an outlook suggesting possible ideas for future related research.

Chapter 2

Literature Review

2.1 Introduction

This chapter provides a critical review of the published literature surrounding intermetallic hydrides (in particular TiFe-based alloys and TiMn₂-based alloys), magnesium hydride and the coating technologies currently in practice.

2.2 Intermetallic Hydrides

2.2.1 AB₅ Intermetallics

The capacity to facilitate the substitution of many different elemental species, or at least partially, into the A and B sites of their lattice structure makes AB₅ alloys one of the most versatile intermetallic hydrides. A-elements commonly comprise of one or more of the lanthanides (at. no. 57-71), Ca, Zr or Y and the B-elements tend to

be Ni which can be substituted to various extents by many elements such as Al, Co, Mn, Fe, Ti, etc.

This permutation of elements results in high thermodynamic tunability and enables a 25 °C plateau pressure ranging between at least three orders of magnitude depending on the composition (Sandrock, 1999). Generally AB₅ alloys have low hysteresis, with the exception of some mischmetal combinations (Liu and Huston, 1983), and flat plateaus can be attained following annealing of as-cast alloys. Reversible gravimetric capacities are restricted to approximately 1.3 wt.% and high raw material costs compared to other intermetallic systems limit their on-board application practicality.

However, AB₅ alloys do possess a good resistance to small quantities of O₂ and H₂O impurities, and the absence of a protective oxide layer means they are easy to activate (Sandrock and Goodell, 1984). Combined with the near-ambient PCT properties of many AB₅ alloys, they are suitable for stationary and metal hydride battery applications. A well-known example is LaNi₅, which has been utilized commercially in Ni-MH battery technology for over two decades (Sakai et al., 1990).

2.2.2 A₂B Intermetallics

Another class of intermetallic hydrides is in the form of A₂B compounds. Here the A-element often corresponds to a Group IVA element, like Ti, Zr, Hf or Mg and the B-element refers to a transition metal, usually Ni. Unfortunately, the majority of A₂B compounds are too stable, resulting in their PCT properties lying outside the

practical (PEM fuel cell) application range of 0-100 °C and 1-10 bar.

An A_2B alloy that has been researched comprehensively is Mg_2Ni , which unlike other intermetallic compounds, converts into a transition metal complex upon hydrogenation. This reaction involves the two Mg atoms donating their valence electrons to stabilize the high-H transition metal complex, $[NiH_4]^{-4}$ (Sandrock, 1999).

Possessing a high reversible storage capacity of 3.6 wt.%, substantially greater than any other intermetallic system, it is unsurprising why Mg_2Ni is considered an attractive storage material. However, from a thermodynamics perspective the outlook is not as promising. Apart from a high hydride stability ($\Delta H = -64.5 \text{ kJ.mol}^{-1} \text{ H}_2$ and $T_{1bar} = 255 \text{ °C}$ (Reilly and Wiswall, 1968)) limiting transition to practical application, efforts to destabilize the system by elemental substitution have so far proven futile.

2.2.3 Solid Solution Alloys

From a metallurgic viewpoint, a solid solution alloy consists of one or more minor elements (solutes) being dissolved into a primary element (solvent). Notably, a stoichiometric relationship is not necessary between solute and solvent, thus distinguishing them from standard intermetallic compounds, and the solute is present in a disordered interstitial distribution within the crystal structure. Seeing as they are non-stoichiometric compounds, thermodynamic modification can be achieved more readily through substitution, eliminating the need for additional alloy components, and hence simplifying the synthesis process.

A selection of solid solution alloys whose primary element are based on Pd, Ti, Zr or V are known to form reversible hydrides; many of which have been researched from a thermodynamic perspective (Fukai, 2005). With Pd-based solid solution alloys being prohibitively expensive and Ti- and Zr-based alloys forming too stable hydrides (see Figure 1.5), only V-based alloys are left as a realistic hydrogen storage material.

As mentioned in Section 1.4.2, the properties of vanadium dihydride are well-suited to hydrogen storage at near ambient temperature and the concept of substituting in cheaper alternative elements, such as ferrovandium, is an appealing prospect (Sandrock, 1999). All V-based alloys possess a body-centered-cubic (A2) crystal structure in the α -phase and following hydrogenation to the γ -phase typically transform to a face-centered-cubic (C1) structure (Maeland, 1964). A number of systems have been investigated together with Laves phase-related BCC solid solution alloys for example Ti-V-Cr, Ti-V-Mn and Ti-V-Cr-Mn compounds (Akiba and Okada, 2002). The high metal concentration typically limits the gravimetric capacity to 3 wt.% and although Ti-V-Cr-Mn has been reported to store nearly 4 wt.%, this is at the expense of high operating temperatures (ca. 300 °C) (Yu et al., 2004). These materials have many promising properties and research is on-going.

2.2.4 AB Intermetallics

Reversible intermetallic hydride formation was first validated with the AB compound ZrNi (Libowitz et al., 1958). Unfortunately, ZrNiH₃ obtains a $T_{1bar} \approx 300$ °C, thus

making it unviable for practical application. High decomposition temperature is a common feature among many of the AB hydrides such as ZrCo, $T_{1bar} \approx 430$ °C (Nemirovskaya et al., 1991), TiNi, $T_{1bar} \approx 200$ °C (Yamanaka et al., 1975) and HfCo, $T_{1bar} \approx 270$ °C (Van-Essen and Buschow, 1979). In addition, potential RE-B intermetallics, such as CeAg and GdCu, are inclined to disproportionate upon hydrogenation (Beck and Mueller, 1962). It was only with the discovery of TiFe, $T_{1bar} \approx -8$ °C (Hoffman et al., 1969; Reilly and Wiswall, 1974), that practical room temperature AB hydrides were proven to exist.

During the 1980s, TiFe was viewed as one of the most promising hydrogen storage materials due to its low cost and abundance of raw materials; however it

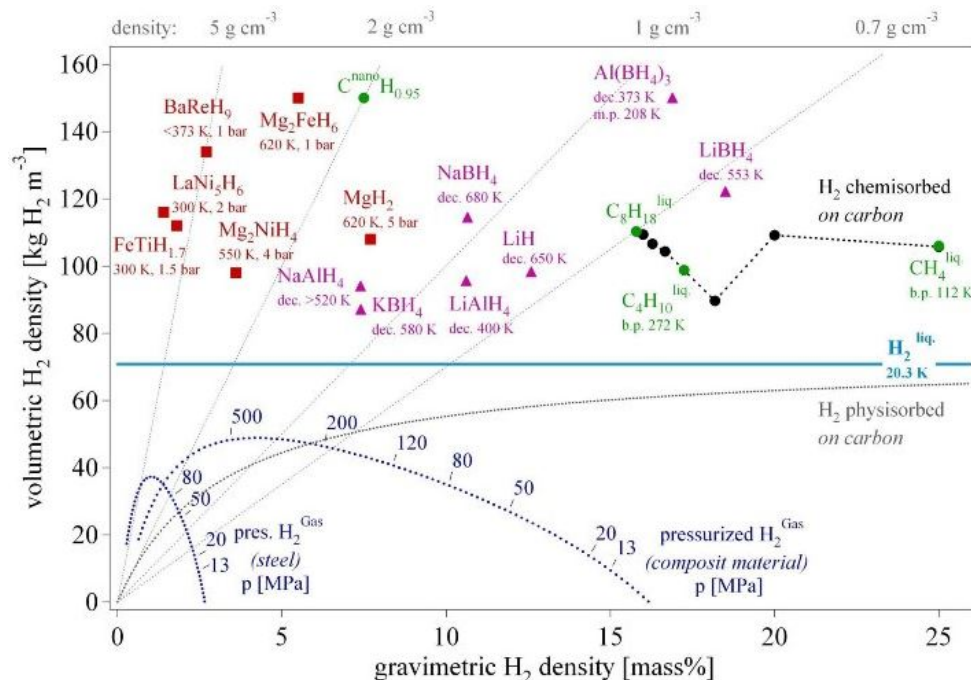


Figure 2.1: Volumetric and gravimetric hydrogen density of some selected hydrides, taken from Züttel et al. (2010).

was soon overlooked in favour for complex hydrides as research began to focus on mobile application. Nevertheless, in more recent years there has been a growing emphasis towards thermal storage and stationary applications causing volumetric hydrogen density to become more decisive than gravimetric hydrogen density. Figure 2.1 illustrates the volumetric hydrogen densities of intermetallics, such as TiFe and LaNi₅, are competitive against binary and complex hydrides and this has led to a resurgence of interest in these systems. TiFe is particularly attractive for stationary and near-ambient thermal storage systems because it has a moderate enthalpy of formation ($\Delta H = 28.1 \text{ kJ}\cdot\text{mol}^{-1} \text{ H}_2$), storage capacity of 1.9 wt.% and flat dehydrogenation plateau pressure of 4.1 bar at 25 °C (Reilly, 1979).

Like most AB intermetallics, TiFe has a simple B2 (CsCl-type) crystal structure thus belonging to the space group Pm3m and obtains a lattice parameter of 2.9789 Å (Thompson et al., 1979). With hydrogenation two notable hydride phases tend to form, an orthorhombic monohydride β_1 phase (TiFeH_{~1}) and a monoclinic dihydride γ phase (TiFeH_{~2}) (Thompson et al., 1989). Schober (1979) later reported that a secondary orthorhombic β_2 phase (TiFeH_{~1.4}) may be visible, yet the absence of another corresponding plateau region in PCI plots raises skepticism.

Confirmation of crystal structure by neutron diffraction investigation of TiFeD_{1.94} identified octahedral sites of Ti₄Fe₂ and Ti₂Fe₄ available for deuterium. Initially, deuterium occupies the sites among Ti₄Fe₂, resulting in structural distortion from simple cubic to orthorhombic β phase with TiFeD. Further deuteration but now among Ti₂Fe₄ sites cause the formation of the monoclinic γ phase, leaving the Ti₄Fe₂

and Ti_2Fe_4 sites 100% and 91% occupied by deuterium respectively (Fischer et al., 1987).

TiFe does not readily form a hydride and an activation process is essential. In general the activation of TiFe comprises of two steps: initially heat treatment removes the film of surface oxide covering the bulk material and secondly the generation of new clean surfaces by cracking of the alloy during (de)hydrogenation cycling. Reilly and Wiswall (1974) demonstrated that TiFe could be activated by heating to 400-450 °C under vacuum, applying a 7 bar H_2 pressure for half an hour and then cooling back to room temperature under vacuum before hydrogenating under high pressure H_2 (> 50 bar) over several days. Furthermore this process often needs to be repeated several times to obtain reproducible PCI plots. The alloy is not pulverized upon hydrogenation, although the γ phase is very brittle and highly strained, thus causing extensive micro-cracking (Reilly, 1979).

While the requirements for achieving TiFe activation are widely acknowledged, the exact mechanisms behind this phenomenon have been subject to much debate. Following XPS and Auger electron spectroscopy, Schlapbach et al. (1980) suggested Ti diffuses to the surface forming TiO_2 , thus leaving an excess of subsurface iron clusters in the metallic state, possibly acting as sites for H_2 chemisorption.

Through SEM observations Pande et al. (1980) reported a different concept whereby the oxide layer is physically detached from the underlying TiFe layer, which is free to absorb hydrogen. Building upon this, Matsumoto and Amano (1981) observed the formation of a $\text{Fe}_5\text{Ti}_7\text{O}_2$ phase on the alloy surface, which they suggested

initially absorbs hydrogen along with TiFe phases, and that crack formation, a result of varying phase expansion coefficients during heat treatment, results in an increased rate of absorption. [Schober \(1979\)](#) found Fe_2Ti , TiO_2 and FeTiO_x (suboxide) on the surface via TEM and thought hydrogen chemisorption occurred on the suboxide, however no sub-surface compositional analysis was undertaken to check for metallic iron clusters.

In addition to discovering that excess titanium in the alloy Ti_xFe ($1 \leq x \leq 2$) drastically promotes activation, [Mizuno and Morozumi \(1982\)](#) found evidence of iron clusters forming and disappearing during heat treatment. Combining this with similar findings made by [Kim and Lee \(1985\)](#) and [Sevlam et al. \(1987\)](#) where heat treatment created iron clusters, but their existence suffered continuously from oxygen contamination, implies that Schlapbach's segregation model for TiFe may be the most credible.

In an attempt to overcome the difficult and time consuming activation of TiFe the effects of various severe plastic deformation (SPD) techniques to create nanostructured TiFe have been investigated. Ball-milled nanocrystalline TiFe was found to activate after a single annealing at 400 °C for 0.5 h under vacuum, although careful synthesis is required because TiFe formation during mechanical alloying is severely impacted by small amounts of oxygen ([Zaluski et al., 1993, 1994](#)). More recent studies demonstrated TiFe samples can remain activated even after several months exposure to air when processed by high-pressure torsion (HPT) or groove rolling (GR). However, the sample quantity is very limited (< 1 g) for the HPT process and GR samples

require several cycles before full activation is achieved (Edalati et al., 2014).

There has also been research into the ball milling of TiFe with additives of proven hydrogen dissociation catalysts, Pd (Zaluski et al., 1995) and Ni (Bououdina et al., 1999). Zaluski et al. (1995) results were especially promising showing less than 1 wt.% Pd enables TiFe to readily absorb hydrogen at room temperature with no activation applied. No alloying zone was detected between the TiFe powder and Pd during TEM analysis and the catalysis mechanism was attributed to the “spillover effect” (Kramer and Andre, 1979; Prins, 2012). Here, the catalyst is thought to aid hydrogen dissociation and the adsorbed hydrogen atoms can then spill over onto the substrate surface and subsequently diffuse into the material bulk. While hydrogen spillover has been demonstrated in several solid state reactions such as Pd/MnO₂ (Xu et al., 1997), Pt/CeO₂ (Lykhach et al., 2012) and Pd-Ti³⁺/TiO₂ (Gorodetskii and Matveev, 2001), the precise effect has not been investigated for catalyst coated TiFe thus far. Another viewpoint is that the Pd provides an alternate hydrogen diffusion pathway, therefore reducing the activation barrier (discussed in more detail in Section 2.3.1). The latter mechanism is most likely given that palladium can form a hydride under ambient conditions (PdH_{0.6} at 0.02 bar and 25 °C) (Schlapbach and Züttel, 2001), enabling atomic hydrogen to then diffuse directly into the substrate bulk. Regardless of the exact mechanism, this work implies complete encapsulation of TiFe powder with a Pd layer may be avoided and suggests small clusters or particles of well dispersed Pd is sufficient.

Physical vapour deposition (PVD) studies revealed that a 20 nm Pd coating on

a 100-200 nm thick TiFe film (deposited on Si substrate) instigates hydrogenation without prior activation and the rate of hydrogen uptake can be increased by annealing the Pd-capped TiFe in air up to 250 °C (Heller et al., 2006). The formation of oxygen-containing phases ($\text{Ti}_4\text{Fe}_2\text{O}_{1-x}$), which have been demonstrated to readily absorb hydrogen at room temperature, have been proposed for the reason behind this improvement (Hiebl et al., 1979; Amano et al., 1983; Rupp, 1984).

Besides PVD, a variety of other metal coating techniques have been used to deposit Pd on TiFe, including wet chemical autocatalytic deposition (Williams et al., 2011) and chemical vapour deposition of metal organic substances (MOCVD) (Davids et al., 2011). While both methods again result in hydrogenation of TiFe without activation, wet chemical vapour deposition is a fairly inefficient use of the expensive Pd precursor and the hydrogenation performance of surface modified TiFe was found to be quite sensitive to MOCVD conditions.

Partial substitution of a third element for Fe in TiFe has frequently been used to modify thermodynamic properties, enhance resistance to impurities and promote activation during the initial hydriding process. Kim and Lee (1985) demonstrated if TiFe is combined with transition metals, which obtain lower oxide stability than that of Fe no activation is achievable irrespective of heat treatment. On the other hand, elements with higher oxide stability will stimulate activation of TiFe. The formation of $\text{TiFe}_{1-x}\text{M}_x$ alloys where M is the transition element Mn, Zr, Cr or Ni represents the most effective way to improve the activation characteristics of the alloy.

The $\text{TiFe}_{1-x}\text{Ni}_x$ system has been investigated by a good number of researchers.

Substitution of Ni ($x \geq 0.1$) has been found to enable room temperature activation of $\text{TiFe}_{1-x}\text{Ni}_x$ alloys and while increasing Ni content appears to accelerate the process it can still take about one day to reach saturation when $x = 0.2$ (Lee and Perng, 1999). Ni substitution of $x = 0.2$ almost eliminates unfavourable hysteresis ($\ln(P_a/P_d) = 0.05$) (Huston and Sandrock, 1980) compared to TiFe (0.64) (Mintz et al., 1981) and also yields flatter plateau regions compared to other third element substitutions. This appears to be due to suppression of γ -phase formation and consequently a reduction in storage capacity. For $\text{TiFe}_{0.8}\text{Ni}_{0.2}$, a high cycling stability was reported by Bershinsky et al. (1991) in which the capacity reduced by only 16% after 65,000 (de)hydrogenation cycles.

From a thermodynamics viewpoint, Mintz et al. (1981) observed that as Ni content increase from $x = 0.1$ to 0.5 in $\text{TiFe}_{1-x}\text{Ni}_x$, the plateau pressure decreased below 1 bar at room temperature, leading to a rise in formation enthalpy ($\Delta H = 35\text{--}45 \text{ kJ}\cdot\text{mol}^{-1} \text{ H}_2$) and hydride stability relative to TiFe. Lastly, partial substitution of Ni for Fe in TiFe results in improved hydriding kinetics and unlike TiFe the characteristic feature of nucleation and growth mechanism is not observed (Chung and Lee, 1986). In spite of all prior investigations, there is little information available regarding the impact of minor Ni substitution ($x < 0.1$) for Fe in TiFe.

2.2.5 AB_2 Intermetallics

The family of AB_2 alloys are similar to AB_5 intermetallics in that they embody a versatile group of hydriding compounds with tunable PCI properties applicable to

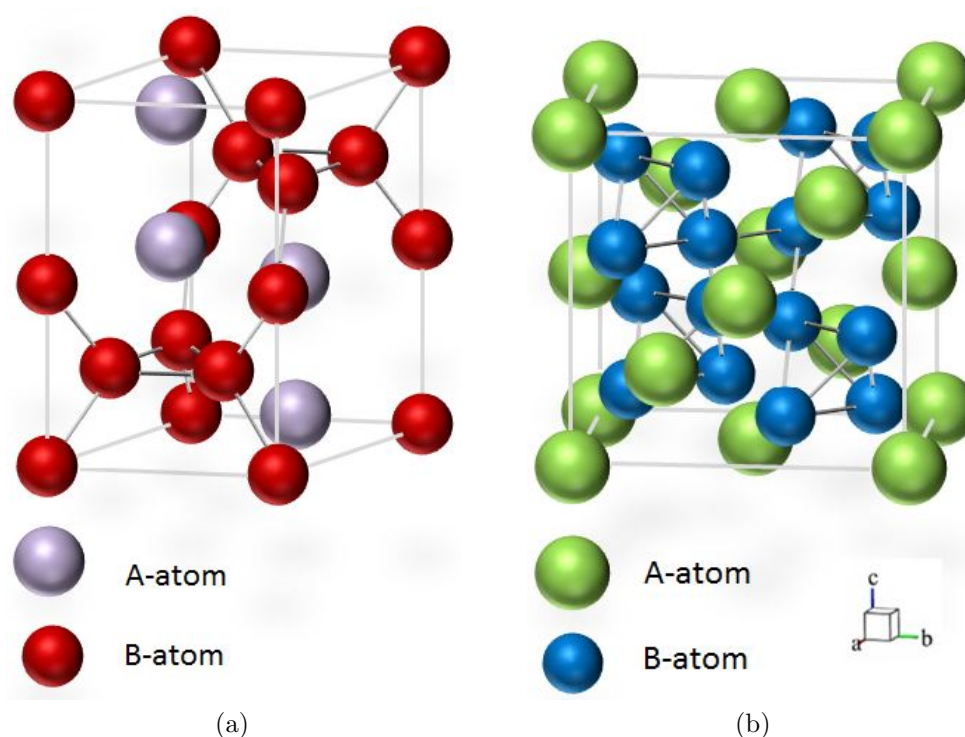


Figure 2.2: (a) The C14 Laves and (b) C15 Laves crystal structures, reproduced using balls and sticks from [Barrett \(1973\)](#) and [Wernick \(1967\)](#) respectively.

ambient temperature applications. The A-elements are typically from Group IVA (Ti, Zr, Hf) and/or the lanthanides (at. no. 57-71). The B-elements can be a selection of transition or non-transition metals, although there seems to be preferentiality towards V, Cr, Mn and Fe ([Sandrock, 1999](#)).

Nearly all AB_2 intermetallics are accounted by either one of two related Laves phase crystal structures: C14 hexagonal, $MgZn_2$ structure, space group $P6_3/mmc$ and C15 cubic, $MgCu_2$ structure, space group $Fd-3m$ (see Figure 2.2). These two crystal structures are linked by an identical basic unit layer but are differentiated by their unit layer stacking sequences.

The discovery of the first AB_2 intermetallic hydride, ZrM_2 where $M = V, Cr, Fe$,

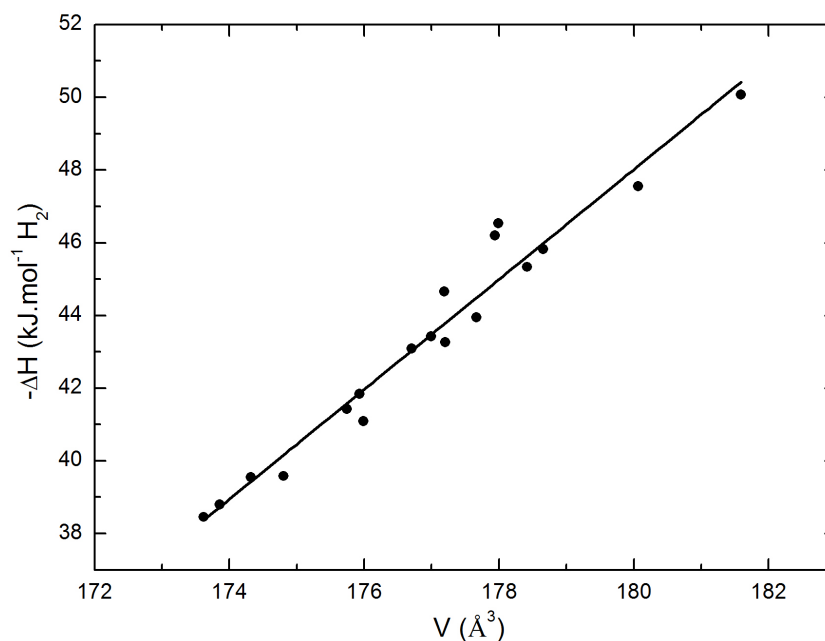


Figure 2.3: Correlation between cell volume V_{C14} and $-\Delta H$, replotted from Nakano et al. (1997).

Co, Ni, Cu, Mo, Nb and Sn (Pebler and Gulbransen, 1967) led to numerous research groups identifying a multitude of practical AB_2 hydrides. Among such research, a strong correlation between unit cell volume and plateau pressure and thus enthalpy value was demonstrated experimentally by Nakano et al. (1997), as shown in Figure 2.3.

Generally, the maximum storage capacities of AB_2 alloys are greater than their AB_5 counterparts but these capacities become more comparable if considering reversible capacity. AB_2 alloys characteristically obtain a narrower (less prominent) plateau region and a residual capacity upon dehydrogenation due to trapping unless the material is heated (Sandrock, 1999).

The ease with which AB_2 intermetallics are activated typically lies between AB

and AB₅ alloys, although the necessity for heating can usually be eliminated with a higher Zr or Mn content compared to Ti or Cr (Young et al., 2008, 2009). Furthermore, the presence of secondary phases tends to promote activation as well hydrogenation kinetics (Bououdina et al., 1998). Upon hydrogen cycling, AB₂ alloys are known to decrepitate and those with higher Zr or Mn contents are highly pyrophoric which raises concerns with the packing and handling of powder in vessels (Bernauer and Halene, 1987). Once active, AB₂ alloys are quite susceptible to impurities such as O₂ but capacity is often recoverable since the impurity acts more like a poison rather than a reactant.

In terms of cost, AB₂'s are more affordable than AB₅ alloys especially if Ti and Mn account for most of the A-element and B-element respectively. Several Ti-Mn Laves phase intermetallics are commercially produced. In fact one based on a (Ti-Zr)₁(Mn-V-Cr-Fe)₂ alloy was used as the metal hydride material onboard the first hydrogen powered canal boat (Bevan et al., 2011) and Type 212 U-boat submarines operated by German and Italian navies for several decades (Eberle et al., 2009; Angstrom, 2015). It is also important to recognize the implications on the usage of V in AB₂ alloys. Two AB₂ alloys that obtain relatable compositions (including V content) are TiMn_{1.4}V_{0.62} and the GfE commercial alloy Ti_{0.98}Zr_{0.02}Mn_{1.5}V_{0.43}Fe_{0.09}Cr_{0.05}. The capacity and enthalpy for both are similar but the raw material cost of the latter is approximately six times less because ferrovandium is used rather than pure vanadium (Sandrock, 1999). On the other hand, increased ferrovandium content has been shown to increase plateau slope in both AB₂ (Xu et al., 2001) and solid solution

alloys (Ulmer et al., 2015) due to compositional inhomogeneities. This highlights the potential implications and difficulties when attempting to produce a commercial alloy tailored to a specific application.

TiMn₂ alloys

Besides their relatively low cost, as mentioned above, Ti-Mn Laves phase alloys are regarded as a particularly promising category of AB₂ hydrides due to their easy activation and good (de)hydriding kinetics. According to Gamo et al. (1985) they

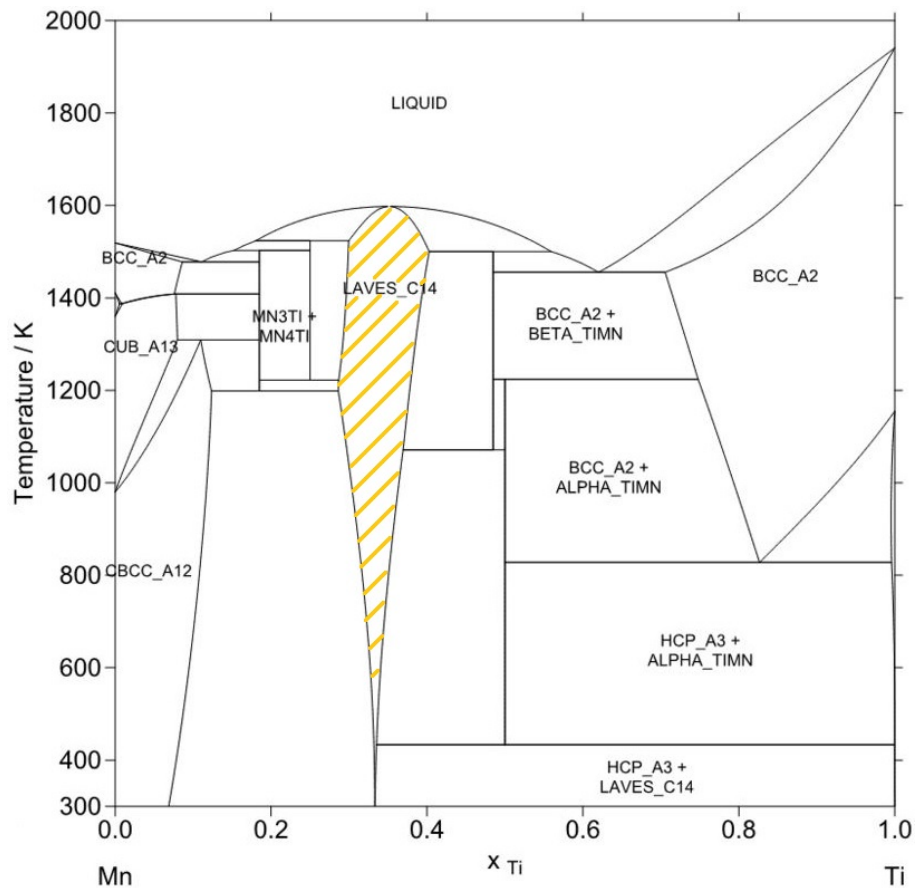


Figure 2.4: Mn-Ti phase diagram with the TiMn₂ phase highlighted, taken from Murray (1981).

also possess a respectable storage capacity reported to be 1.5-1.8 wt.%. However, there are two critical concerns inhibiting their application as a hydrogen source for fuel cells. One is a too high equilibrium plateau pressure at room temperature and the other is a serious hysteresis effect. For instance, even after annealing TiMn_2 was reported to have a hysteresis as large as 200 bar between hydrogenation and dehydrogenation pressures at 20 °C (Klyamkin et al., 1994), meanwhile TiCr_2 has almost no hysteresis even at -76 °C (Reilly, 1978). The Mn-Ti binary phase diagram indicated that Laves phase TiMn_2 compound is formed over a wide composition range (64-70 at.% Mn) (Mitrokhin et al., 2002), suggesting its hydrogen storage properties could be strongly influenced by elemental substitution while maintaining the same phase constitution.

The substitution of Zr for Ti has been a common method to improve hydrogenation capacity and decrease the plateau pressure (Oesterreicher and Bittner, 1978; Li et al., 2005). Yet increasing Zr content has also been shown to produce a distinctly steep plateau, which is partly due to compositional inhomogeneity and requires annealing to be removed (Liu et al., 1996). Partial substitutions of the B-elements to form multicomponent systems have proven effective in favourably altering plateau pressure, plateau slope and hysteresis.

Bobet et al. (2000a) examined the single substitution effect of transition metals (M = Al, V, Cr, Co and Ni) in $\text{Ti}_{0.95}\text{Zr}_{0.05}\text{Mn}_{1.45}\text{M}_{0.5}$. Ni substitution led to an increase of the plateau pressure which could be correlated to the decrease of cell volume; meanwhile Co substitution barely affected the hydride properties despite

a change in the lattice parameters. Al substitution was suitable to reduce plateau pressure but also led to a large decrease of storage capacity (1.5 wt.%). This capacity loss is attributed to a reduction in the available interstitial sites for hydrogen since Ti_2Al_2 and TiAl_3 sites do not contain hydrogen, an observation previously reported for AB_5 phase (Bobet et al., 1998). Cr substitution led to a slight reduction in plateau pressure and an improvement of hysteresis characteristics by lowering of the absorption plateau while leaving the desorption plateau unchanged. This outcome is linked to the opposing hysteresis nature of TiMn_2 and TiCr_2 described earlier. V substitution was effective at lowering the plateau pressure and improving the hydrogen capacity (2.1 wt.%). This result is in agreement with the increase in lattice parameters reported but should also be credited to the larger affinity of V with H compared with that of Mn. Overall, substitution of Mn for Cr and V produced alloys with the best absorption properties, a result also reported by Hong et al. (1994) who explored similar transition metal substitutions in $\text{Ti}_{0.8}\text{Zr}_{0.2}\text{Mn}_{1.5}\text{M}_{0.5}$.

$(\text{TiZr})_1(\text{MnVCr})_2$ alloys

The simultaneous substitution of Cr and V for Mn in TiMn-based alloys has yielded some promising results. Liu et al. (1996) studied the impact of non-stoichiometry and Ti:Zr ratio in $\text{Ti}_{0.75-1.05}\text{Zr}_{0.1-0.2}\text{MnCr}_{0.9}\text{V}_{0.1}$ alloys. No definitive trend was found for the hysteresis effect but flatter plateau regions were achieved with stoichiometric compositions, highlighting a constant compromise between preferred characteristics. The plateau pressure decreases with increasing Zr content due to increasing cell

volume, a trend also seen in the four component systems Ti-Zr-Mn-Cr (Guo and Wu, 2008) and Ti-Zr-Mn-V (Villeroy et al., 2006). The substitution effects of Cr and V were also similar to that found by (Bobet et al., 1998).

The majority of TiMn_2 alloys activate fairly easily however, Yu et al. (2007) investigated the influence of V on activation performance, by comparing $\text{TiMn}_{1.25}\text{Cr}_{0.25}$ against $\text{TiMn}_{0.95}\text{Cr}_{0.25}\text{V}_{0.3}$. Both alloys (crushed pieces $< 400 \mu\text{m}$) activated under 10 bar H_2 at 25 °C in less than 20 min and were fully activated after 2 cycles. When exposed to air for 30 days, $\text{TiMn}_{0.95}\text{Cr}_{0.25}\text{V}_{0.3}$ activated after a 40 min incubation period and fully after 5 cycles but no measurable hydrogen absorption occurred for $\text{TiMn}_{1.25}\text{Cr}_{0.25}$ even after 10 activation cycles. Auger electron spectroscopy revealed after exposure to air for 30 days, unidentified surface oxide layers of approximately 2 nm and 7 nm were formed on the top surface of $\text{TiMn}_{0.95}\text{Cr}_{0.25}\text{V}_{0.3}$ and $\text{TiMn}_{1.25}\text{Cr}_{0.25}$ respectively. It also highlighted a significant disparity in the Mn/Ti ratio on the top surface with $\text{TiMn}_{1.25}\text{Cr}_{0.25}$ at 11:1, while $\text{TiMn}_{0.95}\text{Cr}_{0.25}\text{V}_{0.3}$ remained closer to its bulk components. This suggested V substitution for partial Mn could assist activation via the prevention of oxide layer formation and changes to the surface chemistry of the alloy, although the dominant factor was not determined. SEM images showed the average particle size of the air exposed $\text{TiMn}_{0.95}\text{Cr}_{0.25}\text{V}_{0.3}$ was reduced to 30 μm after 10 activation cycles; however $\text{TiMn}_{1.25}\text{Cr}_{0.25}$ did not undergo any change. The addition of V also caused an increase in cell volume, thus inducing particle fragmentation upon cycling.

Xu et al. (2001) gathered thermodynamic and capacity data for a range of Ti-Zr-

Mn-(V, VFe)-(Cr, Ni) alloys. Reversible storage capacities of up to 1.9 wt.% were obtained although this was slightly lower when VFe replaced V. Substitutions of V, Cr and Ni produced similar outcomes to those already discussed during single element substitution for Mn.

2.3 Magnesium Hydride

Magnesium hydride has long been recognized as a leading candidate for solid state hydrogen storage due to the abundance of magnesium, its low cost and possession of one of the highest energy densities (9 MJ.kg^{-1}) among all reversible hydrides. Furthermore, with increased research efforts to utilize MgH_2 in CSP thermal energy stores, opposed to onboard applications, the issue regarding high decomposition temperature ($> 300 \text{ }^\circ\text{C}$) can largely be circumvented. Nevertheless, there are still several factors presently hindering the transition of MgH_2 from laboratory prototypes to wide-scale commercial application that requires discussion.

Synthesis of MgH_2 was first reported by Jolibois (1912) via the pyrolysis of ethyl magnesium halides. Subsequent to this a number of techniques were established including the formation of magnesium hydride in the solid state directly from elemental magnesium and hydrogen, in a slow reaction demanding high temperature and high hydrogen pressure (Stampfer et al., 1960).

The hydrogenation reaction of $\text{Mg} + \text{H}_2 \rightleftharpoons \text{MgH}_2$ ensues when hydrogen atoms, dissociated at sites on the magnesium surface, diffuse into the hexagonally-close

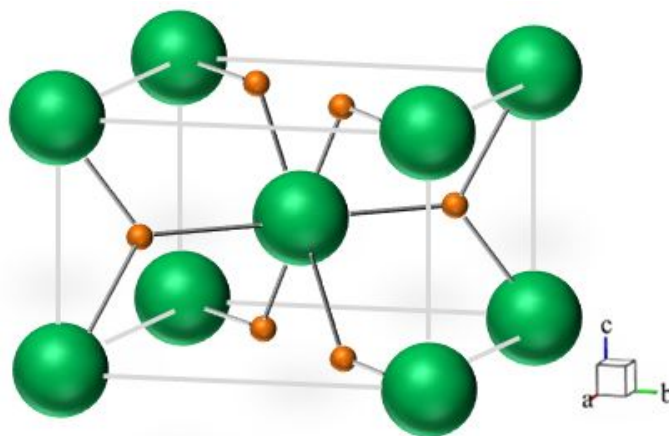


Figure 2.5: Crystal structure of β -MgH₂ reproduced using balls and sticks from [San-Martin and Manchester \(1987\)](#).

packed (HCP) magnesium lattice. A solid solution (α phase) is formed as the hydrogen atoms initially occupy tetrahedral interstitial sites, for H concentrations up to a maximum of ca. 9 at.% near the melting point of ca. 650 °C ([San-Martin and Manchester, 1987](#)). Upon further exposure to hydrogen, the rutile, body-centred cubic magnesium hydride phase is formed with space group P4₂/mnm and lattice parameters $a = 0.452$ nm and $c = 0.302$ nm ([Noritake et al., 2002](#)). Each Mg atom is octahedrally coordinated to six H atoms, while each H atom is coordinated to three Mg atoms in a planar coordination, as illustrated in [Figure 2.5](#).

Over the past 60 years, a spread of thermodynamic data has been reported for the decomposition of magnesium hydride (see [Table 2.1](#)). Most frequently quoted is the dehydrogenation enthalpy of $\Delta H = 74.5$ kJ.mol⁻¹ H₂ obtained by [Stampfer et al. \(1960\)](#) using a series of PCI measurements. This value remains within error of a recent Round Robin study performed by 14 laboratories, in which they report a dehydrogenation enthalpy of $\Delta H = 76.3$ kJ.mol⁻¹ H₂ with a relative standard

| Source | ΔH [kJ.mol ⁻¹ H ₂] | ΔS [J.K ⁻¹ mol ⁻¹ H ₂] |
|--------------------------------|---|--|
| Stampfer et al. (1960) | 74.5 ± 0.3 | 135.1 ± 1.9 |
| Reilly and Wiswall (1968) | 77.4 ± 4.2 | 138.3 ± 2.9 |
| Pedersen et al. (1983) | 70 | 126 |
| Friedlmeier and Bolcich (1988) | 74.3 ± 0.5 | 136 ± 1 |
| Klose and Stuke (1995) | 81.86 | 146.1 |
| Shao et al. (2004) | 75.0 | 135.6 |

Table 2.1: Summary of published thermodynamic data for the decomposition of magnesium hydride.

deviation of 8.5% (Moretto et al., 2013). Bogdanovic et al. (1999) previously attributed these differences to be a result of the magnesium particle size, stating an increase of ca. 2 kJ.mol⁻¹ H₂ in the enthalpy value as particle size increased from 25-40 μm to 70-100 μm. The discrepancies between values are more likely to be caused by the poor dehydrogenation kinetics of MgH₂ (discussed later) not being adequately accounted for in some studies; although a dependence of thermodynamic properties on particle size has been observed for magnesium nanoparticles (ca. 3-25 nm) (Paskevicius et al., 2010; Liu and Kondo-Francois, 2014a; Liu et al., 2014b; Zlota et al., 2015).

Substitution of the Stampfer et al. (1960) values into equation 1.6 corresponds to the release of 1 bar of hydrogen at 279 °C; yet in practical usage temperatures in the region of 350-400 °C are necessary to (de)hydrogenate magnesium (Mushnikov et al., 2006). While such temperatures align well with CSP applications and the high heat of formation translates to a thermal energy capacity of approximately 2800 kJ.kg⁻¹ of MgH₂, a major drawback persists in that kinetics are very slow, taking several hours to hydrogenate (Zaluska et al., 1999).

Like all metal hydrides, overall sorption kinetics are controlled by the slowest step in the reaction chain. For magnesium there are numerous aspects that can hamper the rate of hydrogenation. Firstly, exposure to air results in surface oxidation. The creation of a MgO barrier inhibits hydrogen molecules penetrating the magnesium. To instigate hydrogen absorption the oxide layer must be broken down by an activation process, which typically consists of several cycles at high temperature (400 °C) under vacuum or hydrogen atmosphere (Chen et al., 1993).

In the 1980s, Vigeholm et al. (1983) investigated how particle structure of starting material impacts the activation of magnesium. The effects of variation in temperature at constant pressure and variation in pressure at constant temperature were observed during (de)hydrogenation thermogravimetric analysis on three different nearly spherical Mg powder particles (purity approximately 99.9 %). The samples varied in terms of preparation technique and average particle size: the first was atomised ($12.5 \pm 7.5 \mu\text{m}$), the second was mechanically comminuted ($<50 \mu\text{m}$), and the third was mechanically manufactured ($50 \pm 26 \mu\text{m}$). Both surface morphology and particle size were demonstrated to play significant roles during hydrogen activation. As anticipated, the atomised sample underwent a slow initial reaction due to its smooth surface, while in contrast the cracked, irregular surface of the mechanically produced samples led to immediate hydrogen absorption. Cycling experiments revealed no apparent changes in storage capacity for all three samples, however this was only over the course of 10-30 cycles.

Poor dissociation of hydrogen molecules on the magnesium surface is another

common cause for sluggish hydrogenation (Montone et al., 2010). Even after activation, a clean surface of pure magnesium requires a very high energy for dissociation (Norskov et al., 1981). At 327 °C the absorption mechanism of the hydride phase was found to form at the Mg grain surface (along the Mg-MgH₂ interface) and its rate of formation was controlled by the density of nucleation sites (Belkbir et al., 1981). The nucleation rate is dependent on the hydrogen pressure, thus by increasing the pressure, the thermodynamic driving force for reaction increases. However, if the hydrogen pressure is too high, such as 48 bar at 400 °C (ca. 28 bar above the plateau pressure), initial hydrogenation is sufficiently fast and results in the formation of a MgH₂ shell (Vigeholm et al., 1987). This abruptly blocks hydrogen diffusion into the Mg lattice because diffusion through MgH₂ is approximately three orders of magnitude slower than through pure Mg (Sholl, 2007). Once the hydride

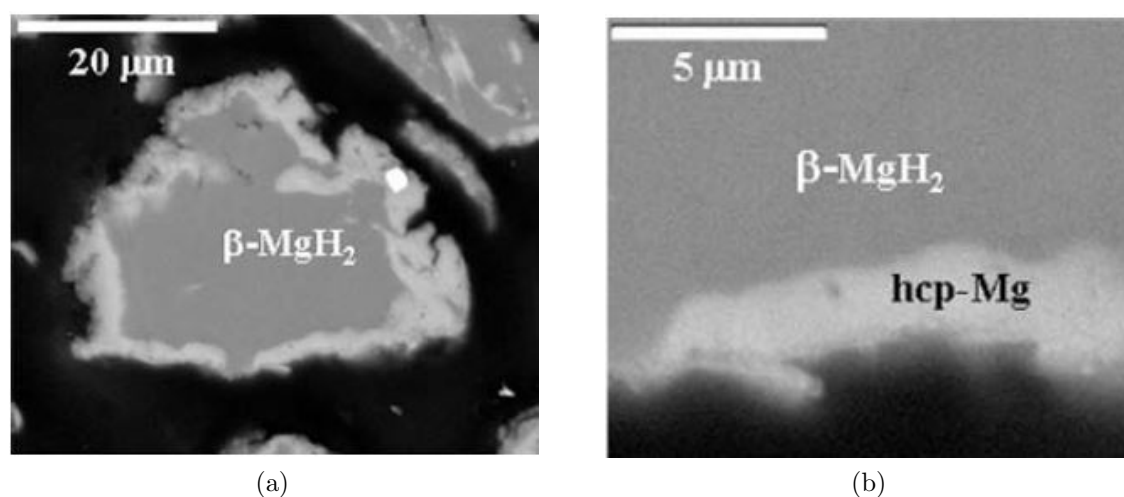


Figure 2.6: SEM/BSE micrographs of partially dehydrogenated MgH₂ powder (a) lower magnification showing the release of hydrogen around the particle with β-MgH₂ inside the particle and (b) higher magnification showing the extension of the hcp-Mg phase to the surface of the particle, taken from (Tanniru et al., 2010).

layer thickness exceeds 30-50 μm fast diffusion of hydrogen to the core of the particle is prevented, effectively ceasing further hydrogenation (Vigeholm et al., 1987).

Following isothermal DSC measurements, Bohmhammel et al. (1998) proposed a decomposition model for magnesium hydride consisting of three stages. The dehydrogenation process incorporates the initial formation of $\alpha\text{-Mg}$ at the surface of the particle, followed by the formation and growth of Mg nuclei, which is consistent with observations by Tanniru et al. (2010). Lastly, the Mg phase is formed along with volume contraction of the particle causing crack formation, thus creating more diffusion options.

2.3.1 Improving reaction kinetics

Improving the sorption behaviour of magnesium hydride i.e. accelerating the reaction rate and reducing the activation energy, E_a , has been the focus of many research groups. A number of approaches have been adopted to overcome the kinetic limitations of MgH_2 such as the production of nanocrystalline structures and catalysis.

Nanocrystalline structures

The fabrication of nanocrystalline structures via SPD techniques, most commonly ball milling, have proven successful at speeding up both the dissociation and diffusion kinetics of Mg. Various studies have proven a relationship exists between the particle- and grain size of magnesium hydride and the sorption kinetics. Zaluska et al. (2001)

reported the hydrogenation rate of micron-sized Mg powder at 300°C can be increased from less than 0.25 wt.% to over 6 wt.% in ca. 2 h, purely through the application of milling to generate Mg powder with an approximate grain size of 30 nm. [Huot et al. \(1999\)](#) observed a similar trend for the dehydrogenation of MgH₂ milled for up to 20 h. These improvements were explained by increased surface area from 1 to 10 m².g⁻¹ and the introduction of defects which increased nucleation sites and shortened the diffusion path length for hydrogen leaving the hydride.

Further investigation into the properties of ball milled MgH₂ have validated the effect of particle size on the desorption time of H₂ as well as the decomposition temperature. [Varin et al. \(2006\)](#) studied MgH₂ milled for time periods between 0.25 and 100 h in a planetary-style mill, finding a near linear reduction of the decomposition onset temperature from ca. 380°C to 340°C by reducing particle sizes

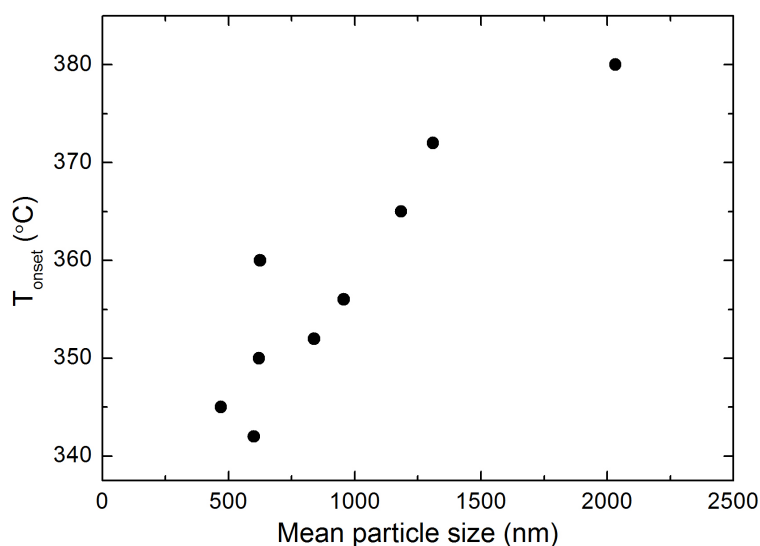


Figure 2.7: MgH₂ particle size effect on onset temperature of H₂ desorption, plotted from data in [Varin et al. \(2006\)](#).

from 2000 to 500 nm (see Figure 2.7).

More recently, [Dornheim et al. \(2006\)](#) attempted to clarify whether a certain grain size is necessary to obtain fast sorption behaviour. Their results suggested the influence of grain size on sorption kinetics is most obvious when particle size is larger than 700 nm but the additional benefit from grain sizes less than 80 nm on kinetics become less substantial.

While the exact mechanism of H₂ desorption from MgH₂ remains ambiguous (rate limiting step proposed to be either diffusion of H₂ through Mg forming at particle surface or recombination of H₂ molecules on the particle surface), these results suggest the optimum nanocrystalline structure should combine in the right proportion: a high surface-to-volume ratio enabling hydrogen access, with a large number of grain boundaries and structural defects promoting hydrogen diffusion ([Bérubé et al., 2007](#)).

Catalysis

The role of a catalyst is to modify the reaction pathway as to accelerate reaction kinetics without being consumed or changing the products of a chemical process. Additives combined with MgH₂ have been demonstrated to favourably encourage sorption kinetics, often in conjunction with particle- and grain refinement achieved during the milling process. Surface catalysts like palladium ([Zaluski et al., 1995](#)) present on the bulk metal surface can significantly improve the kinetics by stimulating hydrogen dissociation and this was often associated with the “spillover effect” ([Zaluski](#)

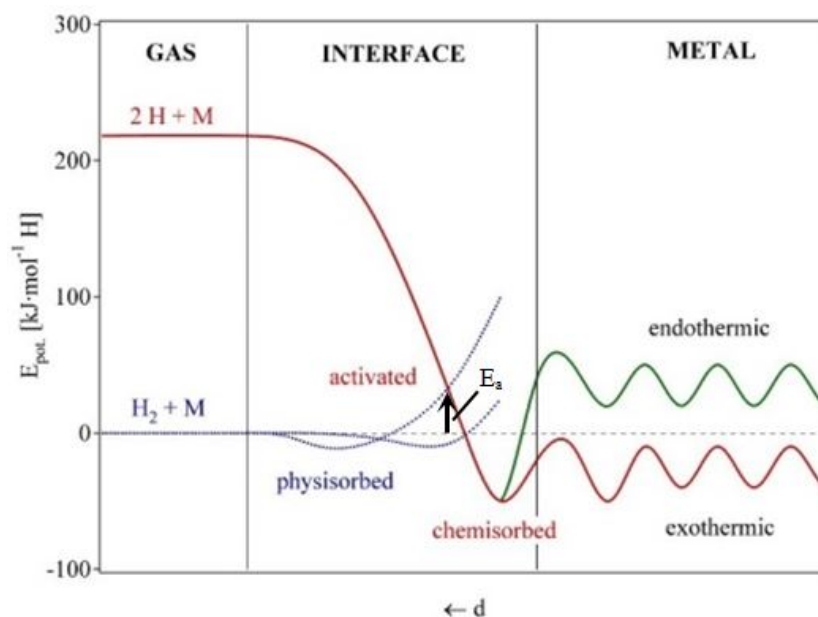


Figure 2.8: Potential energy diagram for the interactions of hydrogen with a metal surface during metal hydride formation/decomposition, adapted from Züttel (2003).

et al., 1995; Mitchell et al., 2003). A simpler rationale is that the catalyst enables an alternative pathway for the formation of the hydrogen metal bond by reducing the height of the activation barrier for hydrogen molecule dissociation ca. $436 \text{ kJ.mol}^{-1}\text{H}_2$ (Arboleda et al., 2004; Züttel, 2003)(see Figure 2.8). Subsequently, the chemisorbed hydrogen atom can migrate into the subsurface layer and finally diffuse into the bulk of the host metal. Another benefit of a surface catalyst is their capacity to nullify a passivating oxide layer that forms on the metal surface (Zaluski et al., 1997). This improved resistance to contaminants and air exposure can remove the need for activation.

The precise mechanisms through which catalysts enhance rates of reaction are not well understood (Bérubé et al., 2007). However, what is acknowledged is the

importance of an even catalyst distribution throughout the magnesium matrix in order to have the maximum influence (Zaluska et al., 2001; He et al., 2010). Freidrichs et al. (2006) explored the role of nano-sizing the additive on MgH_2 sorption kinetics. They demonstrated by using a Nb_2O_5 nanoparticulate additive (15 nm) the required milling time could be shortened by 200 times to produce the same effect as its micrometric counterpart, emphasizing nanocatalysts offer a larger area of contact with the storage medium. Nonetheless, milling was still necessary for adequate dispersion of the additive throughout the MgH_2 . Another important aspect is to keep the catalyst concentration to a minimum given that it does not usually store any hydrogen at the operating conditions and they are often heavy transition metal elements, which decreases the overall storage capacity.

The effects on the sorption kinetics of magnesium hydride have been explored with a wide range of catalysts, including combining magnesium with transition metals such as Co (Bobet et al., 2000b), Cr (Bystrzycki et al., 2005), Cu (Hanada et al., 2005), Fe (Amirkhiz et al., 2011), Mn (Liang et al., 1999a), Nb (Huot et al., 2003), Ni (Bobet et al., 2002), Pd (Zaluska et al., 1999), Ti (Pitt et al., 2012) and V (Oelerich et al., 2001a). There has also been substantial research into the catalysis with intermetallics such as TiFe (Vijay et al., 2004), TiVCr (Laversenne et al., 2013) and ZrNi (Pighin et al., 2012) to form nanocomposites when milled with magnesium hydride.

Similar or even better hydrogen sorption kinetics have been reported when magnesium hydride has been milled together with transition metal oxides compared

to transition metals (Oelerich et al., 2001b; Barkhordarian et al., 2003; Croston et al., 2010). Oelerich et al. (2001b) also suggested the kinetic effect observed was dependent on the valence of the transition metal in the oxide compound. Oxides that have metals that are multivalent enhance the kinetics, while those that possess only a single oxidation state have no effect. In addition, metal oxide additives have a positive influence on particle refinement during the milling process due to their brittle nature (Güvendiren et al., 2004; Panzas et al., 2006).

Evidently, a collection of Mg-based hydrides of different elemental and relative composition have been prepared from a variety of techniques. Seeing as the range of experimental conditions used to test the hydrogen sorption kinetics of these materials are equally as broad, including temperatures from room temperature to approximately 400 °C and pressures from vacuum up to 200 bar, a fair comparison is very difficult as shown by (Sakintuna et al., 2007; Jain et al., 2010). They assembled comprehensive tables comparing the hydrogen storage kinetics, capacity and cycling stability of a range of materials that had been measured by numerous research groups under different conditions. To simplify and emphasize the improvements that various catalyzed magnesium systems can exert over as-received magnesium hydride, a comparison of their respective activation energy for the dehydrogenation reactions has been compiled in Table 2.2.

| Composition | Activation Energy [kJ.mol ⁻¹ H ₂] | Reference |
|---|--|----------------------|
| 70 μm MgH ₂ as-received | 206 | Patah et al. (2009) |
| 20 μm MgH ₂ as-received | 156 | Huot et al. (1999) |
| 20 μm MgH ₂ milled | 120 | Huot et al. (1999) |
| MgH ₂ +5 at.% Ni | 88.1 | Liang et al. (1999a) |
| MgH ₂ +5 at.% Fe | 67.6 | Liang et al. (1999a) |
| MgH ₂ +5 at.% V | 62.3 | Liang et al. (1999b) |

Table 2.2: A collection of reported activation energies for as-received magnesium hydride, milled magnesium hydride and several milled transition metal catalysed magnesium hydride samples.

2.3.2 Cycling

Another property critical in determining the feasibility of any hydrogen storage system is the cycling stability. Ideally, the material must cope with repeated cycles of hydrogen absorption and desorption without suffering a detrimental impact on storage capacity or sorption kinetics. To date, numerous studies into the cycling behaviour of MgH₂ on different scales have been completed.

Verga et al. (2009) performed hydrogen cycling on a 500 g milled MgH₂ sample under hydrogenation and dehydrogenation temperatures of 260 °C and 335 °C respectively. A severe degradation in the specimen's properties was reported, culminating in an approximate 60% reduction in kinetics and a halving of storage capacity by only the 20th cycle. The reasoning was two-fold, a compaction of the powder with successive expansion and contraction of the particles, thus inhibiting hydrogen flow into the bed, as well as sintering of the compacted particles leading to increased diffusion path length for hydrogen. Garrier et al. (2011) observed a similar trend when an intermediate scale tank (1.8 kg) of milled MgH₂ compacted with 5 wt.% expanded natural graphite (ENG) was cycled over 100 times at 320 °C. During the

initial 20 cycles the capacity decreased by about 1 wt.%, in conjunction with a slight decline in sorption kinetics, after which the capacity stabilized at around 5 wt.% for the remaining cycles. [Delhomme et al. \(2012\)](#) studied a large scale tank (10 kg) of milled MgH_2 compacted with 10 wt.% ENG. An improvement in sorption kinetics was observed during the first ten cycles owing to the material thermal conductivity modifications. However, a decline in kinetics and capacity were observed in subsequent cycles due to substantial grain recrystallization. This differs from other metal hydrides such as LaNi_5 , the behaviour of which has been demonstrated to be unaffected up to 40,000 cycles due to powder decrepitation preventing grain growth ([Friedlmeier et al., 1995](#)).

[Dehouche et al. \(2000, 2002\)](#) have also explored the addition of catalysts on the cycling behaviour of MgH_2 . Additives of both Cr_2O_3 and V led to improved cycling stability, with a storage capacity increase of ca. 0.5 wt.% reported for MgH_2 - 0.2 mol Cr_2O_3 cycled 1000 times, while a less pronounced capacity increase of 0.2 wt.% was noted for MgH_2 - 5 at.% V cycled 2000 times. In both cases the absorption rates remained unchanged during cycling, although slightly decreased desorption rates were observed and attributed to crystallite growth of the MgH_2 phase.

The impact of various hydrogen cycling conditions on the microstructural evolution of Mg nanocomposites have also been explored. [Pasquini et al. \(2011\)](#) demonstrated the formation of hollow structures associated with the metal-hydride transition in Mg/MgO core/shell nanoparticles. The mechanism is attributed to successive cycles at sufficiently high temperature (≥ 370 °C) causing core Mg to progressively

diffuse outward and evaporate, leaving a hollow shell with the original shape and thickness. It is proposed this phenomenon might be a general approach to the design of materials with controlled porosity.

A further investigation, [Montone et al. \(2013\)](#) examined whether the described morphological changes were a result of a cycling effect or a heating one. For this a ball milled Fe-doped MgH_2 sample that had been cycled 20 times at $350\text{ }^\circ\text{C}$ was compared against two identical samples that were thermally treated at $350\text{ }^\circ\text{C}$ under 0.2 bar or 10 bar of H_2 pressure for the same time required as the 20 isothermal cycles. Both thermally treated samples showed a sharper morphology than the cycled sample and an evident lack of hollow worm-like structures, thus confirming the necessity for cycling and the negligible effect of the isothermic and isobaric treatments.

Parallel experiments were carried out to observe how cycling temperature and the nature of the catalyst affect the morphological modifications and reaction kinetics. SEM observations of Fe-doped MgH_2 cycled 20 times at $300\text{ }^\circ\text{C}$, $350\text{ }^\circ\text{C}$ and $380\text{ }^\circ\text{C}$ confirmed cycling temperature could be correlated to eventual microstructural changes, with higher temperatures causing a greater density of worm-like structures. As anticipated, the presence of a catalyst in the ball milled MgH_2 improved sorption kinetics and helped to prevent degradation following cycling. However, the type of catalyst such as Fe (ductile) or Nb_2O_5 (fragile ceramic) was determined to have a negligible effect on the main phenomenon occurring during the cycling process.

2.4 Alternative Processing Technology

The technique of amalgamating hydrogen into nanocrystalline thin film structures presents the opportunity to create metal hydrides that obtain considerably different properties to their bulk counterparts. Besides the clear advantage of supplying a large surface area, protective transition metal coatings can also be applied to thin films to lessen surface oxidation effects and enhance kinetics (Jain et al., 1988). The hydrogen storage properties of Mg thin film structures have been extensively investigated in terms of pure Mg thin films (Léon et al., 2002; Akyildiz et al., 2006; Ingason and Olafsson, 2006; Qu et al., 2010), catalyst capped Mg films (Higuchi et al., 2002; Ouyang et al., 2007; Tan et al., 2009) and multilayered Mg films (Kalisvaart et al., 2011; Baldi et al., 2009; Ferrer et al., 2007).

Some promising results have been demonstrated for ball milled and thin film multilayer structures but there is considerable uncertainty surrounding the scalability of these technologies. Both techniques are effective means of fabricating gram quantities of hydrogen storage materials over several hours however, in the event of the emergence of a hydrogen economy relying heavily on solid-state storage, economical production of large quantities of metal hydride materials becomes a critical factor (Eigen et al., 2007). Thus, alternate processing techniques must be pursued.

Horizontal attrition mills enable more rapid saturation of crystallite refinement at lower power consumption than traditional planetary ball mills (Krozer and Kasemo,

1989). Yet, they remain unfavourable being another batch-manufacturing process with relatively high investment costs. Tube vibration milling offers a continuous processing solution and is capable of handling tonnage loads. This is a proven method, used for comminution and activation of minerals, with milling kinematics already optimized for low energy consumption and efficient mixing of milled material (Gock and Kurrer, 1999). There have also been comprehensive studies into how efficient crystallite refinement is impacted by key parameters such as milling time, ball to powder ratio and shape of grinding bodies (Kurrer and Gock, 1986; Dornheim et al., 2006).

Dornheim et al. (2006) showed if milled for 20 h with the same oxide catalyst content, there is little discrepancy in the total hydrogen storage capacity, kinetics and crystallite size (ca. 11 nm) of MgH_2 powder processed in a planetary ball mill and a tube vibration mill despite milling loads being 40 g and 2 kg respectively. Since 20 h of milling is too time consuming for an industrial process, a 2 kg batch of the same sample was milled for only 2 h, resulting in comparable storage capacity and charging time (<5 min). Discharging time approximately doubled but remained under 20 min, which should be sufficient for most applications. In spite of this, the use of fine powders, potentially on the nano-scale, exacerbates concerns associated with safe handling of hydrogen storage materials due to the size of the powder and potentially pyrophoric and explosive nature of Mg-based hydrides.

Nanocrystalline hydrogen storage materials can be generated via several other SPD processes including high pressure torsion (HPT), equal channel angular pressing

(ECAP) and cold rolling. The storage capabilities of magnesium-based hydrides have been improved through each of these processes (Huot, 2012; Kusadome et al., 2007; Skripnyuk et al., 2007) but the majority of literature on alternative synthesis routes focuses on cold rolling being a mass production option.

Lang et al. (2011) demonstrated the efficacy of cold rolling by assessing the performance of MgH_2 powder that was processed using vertical cold rolling apparatus against as-received MgH_2 and ball milled MgH_2 . Further enhancement of reaction kinetics is possible through the addition of metal- and metal oxide catalysts to MgH_2 and cold rolling the mixture 5 times, resulting in performance only slightly bettered by ball milling performed under argon for 30 min (Bellemare and Huot, 2012; Vincent et al., 2012). Poor dispersion of the catalyst material among the magnesium matrix was determined as the main suppressing factor, given the pre-established importance of even catalyst distribution in Section 2.3.1. The researchers propose better sorption kinetics may be attained with an increased number of rolls under an inert atmosphere, thus increasing grain refinement and limiting oxidation effects.

The cold rolling process typically consolidates starting powder into sheet-like material after a single rolling pass. Substitution of starting powder for sheet metal can also create layered structures by repetitive cold rolling and folding of stacked layers in a process known as accumulative roll-bonding (ARB), which may be advantageous from a manufacturing perspective. ARB has been utilized to fabricate a variety of Mg-based nanocomposites with high levels of strain induced grain refinement (Danaie et al., 2011; Gupta et al., 2015), in turn typically leading to faster activation and

enhanced hydrogen storage properties. Although, limited hydrogen capacity has been reported in several cases and an additional filing process was deemed necessary to overcome the very low specific surface area of the rolled materials (Lang et al., 2011; Asselli et al., 2014).

Gas powder atomisation is another proven method of powder fabrication on the industrial scale. This technique overcomes the low efficiencies and complicated procedures encountered with other rapid solidification options such as melt spinning. Details on the mechanisms involved in the process and the preceding vacuum induction melting are described in Section 3.2.1. Gas atomisation is tailored to generate consistently spherical powders with particle sizes typically ranging from 10-500 μm , of which the 10-60 μm range accounts for approximately 50% of total yield (Anderson and Terpstra, 2002).

Since being used to initially investigate the formation and decomposition of magnesium hydride in the 1980s (Vigeholm et al., 1983), there has been no published research into the direct feasibility of atomised Mg powder as a hydrogen storage material. This is mainly due to the hydrogen storage benefits observed with nanocrystalline structures (Zaluski et al., 1997). Nevertheless, utilization of atomised Mg powder may have multiple practical advantages, firstly spherical powders flow more freely than coarse, irregular powders thus simplifying the filling of a hydride vessel, and secondly micron-scale powders help to minimize safety concerns associated with nano-particulates. In addition, the use of Mg opposed to MgH_2 as a starting material and the elimination of any secondary processing technique such as milling underlines

potential reductions in fabrication costs.

In an attempt to overcome the unfavourable smooth surfaces and low surface area to volume ratios inherent to atomised powders, which hinder the activation and sorption kinetics of Mg respectively, the application of a suitable coating technology has been selected. As a result, these coated atomised powders may act as a suitable alternative to the processed magnesium-based hydrides conventionally used.

2.5 Coating Technologies

In the past, a technique known as electroless plating was employed to encapsulate intermetallic hydride powder in transition metals such as Cu or Ni (Hajdu et al., 1990). Unlike classical electroplating, this process did not require the application of an electric current through the solution. Instead, it comprises of intermetallic powder activation in an acidic solution, after which it is submerged into a solution containing a chemical reducing agent causing deposition of the coating on the powder. Given the complexity of the technique and high loss of active materials, (Park, 1992) developed a simpler displacement plating process that worked best with AB₅ intermetallics but could not be applied to AB intermetallics. Later, Law et al. (1996) designed a closed-loop process minimizing waste during electroless plating, by using the hydrogen already present in the metal hydride as the reducing agent. Whilst this method was self-limiting because as the coating thickness increased, the diffusion of hydrogen reduced, it also meant that the overall coating process was time consuming.

Two other noteworthy coating technologies are gas-phase deposition and laser surface alloying. The former differs from previously discussed coating processes in that it does not rely on wet chemical surface treatments, with the advantage of causing very little environmental damage, although it does demand high capital costs. Laser surface alloying can generate metastable solid solutions on metal surfaces where the cooling rate can reach 10^{10} K.s^{-1} , thus enabling complex geometries to be treated, however considerable control of the processing technique is necessary (Gray and Luan, 2002).

Another common coating technique is magnetron-assisted physical vapour deposition, also known magnetron sputtering. This process involves the bombardment of a target (cathode) plate by energetic ions generated inside a discharge plasma, situated near the target. This results in the release, or sputtering, of target atoms, which may then condense onto a substrate (Rossnagel, 1995). The ion bombardment onto the target also instigates the emittance of secondary electrons which is critical

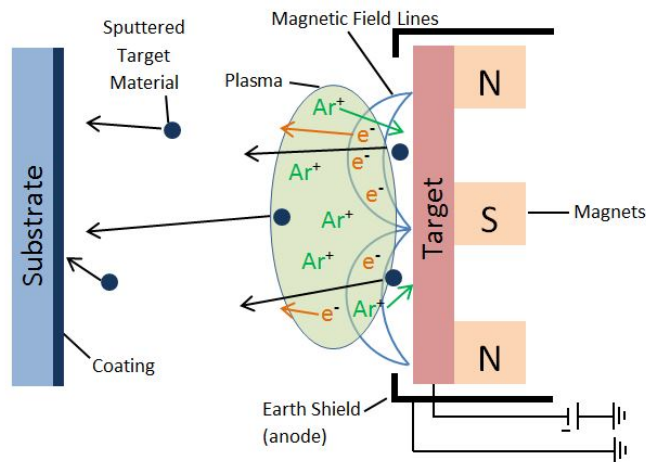


Figure 2.9: Schematic of a basic magnetron sputtering set-up.

in maintaining the plasma (Kelly and Arnell, 2000).

In this research, magnetron sputtering has been chosen as the coating technique because it has the capability of coating different morphologies including micron-scale powders if they can be successfully tumbled. To date, several devices have been employed for coating granulates or powders by sputtering, such as the rotating wing drum (Ensinger and Muller, 2003), single tilted cup (Wang et al., 1997) and barrel coater design (Fernandes et al., 2003). More recently Schmid et al. (2010) explored the potential of a double rotating tilted cup design, which was also optimised with an internal cup geometry that enabled complete uniform films to be deposited on hollow glass microspheres (2-80 μm diameter) which can be used for hydrogen storage. The addition of an optimised internal cup geometry may not be necessary for the substrate materials in this project as they are not as fragile as the glass microspheres and the literature suggests complete uniform catalyst films are not required to have their desired effect. This technique is also highly flexible, in that only replacement of the target material is required for producing different coatings, which is an appealing aspect given the variety of coatings to be tested. As a result, this may prove a useful and commercially viable method for coating potential metal hydrides.

2.6 Summary

Extensive research into hydrogen storage materials has revealed a selection of metal hydride systems ideal for stationary energy storage applications. Improvements in

the hydrogen storage properties of these materials have been achieved through thermodynamic modification, system specific catalysis and fabrication of nanocrystalline structures. Nonetheless, the critical concept of feasible scalability must be addressed in order for the realization of a future hydrogen economy. As a result, there is scope for research into economical, large-scale production of metal hydrides with properties matching or bettering their nanocrystalline counterparts.

It has been established the slow and challenging activation of TiFe can be circumvented by several means. The application of a well distributed Pd catalyst via SPD techniques and PVD on to TiFe thin films have been demonstrated to be particularly effective, enabling initial hydriding at ambient temperature and eliminating the necessity for prior heat treatments. Another approach, as of yet untested and appealing due to its potential scalability, is the magnetron sputtering of Pd nanoparticles onto atomised TiFe (ca. 100 μm). It has also been established the partial substitution of a third element (M) with higher oxide stability than Fe into $\text{TiFe}_{1-x}\text{M}_x$ can stimulate activation. Although the effect of Ni substitution has also been studied from thermodynamics and impurity perspectives, there is little published data regarding the impact of minor Ni substitution ($x < 0.1$). From the available information on TiMn_2 -based alloys, another metal hydride system identified as a potential prototype hydrogen store or domestic thermal store is the $(\text{TiZr})_1(\text{MnVCr})_2$ intermetallic, as they tend to activate easily, possess respectable reversible storage capacities (1.6-2.0 wt.% H_2) and reasonable plateau pressures at ambient temperature. To evaluate a novel $(\text{TiZr})_1(\text{MnVCr})_2$ intermetallic a comparison will be conducted

against a commercially available AB₂ alloy.

The fabrication of nanocrystalline structures using SPD techniques, especially milling, is a well validated approach for improving the typically slow activation and cycling kinetics of MgH₂. The optimum nanocrystalline structure should combine a high surface-to-volume ratio to encourage hydrogen dissociation at the surface, alongside a large number of grain boundaries to increase diffusion pathways into the bulk material. Catalysts in the form of transition metal or metal oxides dispersed evenly within a Mg matrix represent another means of accelerating sorption kinetics; however it is unknown whether any long-term benefit will be observed when, as proposed, magnetron sputtered catalysts are applied to the surface of atomised Mg powder. The reason for this is two-fold: the smooth and spherical nature of atomised Mg powder contradicts the high surface area prerequisite for fast kinetics and secondly the sintering of compacted Mg particles through successive cycling has been shown to degrade hydrogen storage properties. Lastly, the development of porous structures, a phenomenon shown to be reliant on successive cycling opposed to isothermic and isobaric treatments (Montone et al., 2013), has not yet been conducted on atomised Mg powder.

Chapter 3

Experimental Methods

3.1 Introduction

AB and AB₂ alloys developed for use in a prototype hydrogen store and a domestic thermal store were synthesised in-house through vacuum induction melting and selected samples also underwent powder atomisation. Atomised magnesium powders tested for a moderate temperature thermal store were sourced from two external suppliers.

This chapter details the experimental procedures used during sample preparation (Section 3.2), in addition to the material characterisation techniques employed to examine hydrogen storage capabilities and microstructural evolution (Section 3.3 & 3.4).

3.2 Sample Preparation

3.2.1 Production & Sourcing

The majority of AB and AB₂ alloys reported in the literature have been fabricated through arc melting on a water-cooled copper hearth in an argon atmosphere (Mintz et al., 1981; Nagai et al., 1987). Seeing as a project target was the potential scale up of alloy production to mid-scale quantities (ca. 1-2 kg), and laboratory arc-melting furnaces being limited typically to less than 200 g, an alternative technique known as vacuum induction melting was employed.

A vacuum induction furnace uses the principle of induction heating to melt and mix several metals, in turn producing alloys. The sample material to be melted is placed within a copper crucible, which is surrounded by a water-cooled induction coil. By passing a high frequency alternating current through the coil, a rapid alternating magnetic field is initiated and penetrates the sample charge. This results in circular electric currents, eddy currents, being induced within the sample charge and the opposing electrical resistance faced leads to intense heat by Joule heating. Once melted, the eddy currents also have a beneficial stirring effect, assuring improved homogeneity, reducing the necessity for remelting steps usually performed during arc-melting (Kabiri et al., 2012).

Gas powder atomisation following successful induction melting of the charge offers the opportunity to manufacture high quality spherical powders. Powder atomisation is achieved by forcing the molten sample through an orifice situated

under the induction furnace at reasonable pressures (20-90 bar) (Chang and Zhao, 2013). Argon gas jets are intermixed with the melt as it exits the orifice resulting in turbulent flow, which is further incited by filling the collection volume with the inert gas. Undergoing rapid solidification, with cooling rates in the region of 10^3 - 10^6 °C.s⁻¹, spherical powders are fabricated as they gradually descend and aggregate at the bottom of the atomiser unit.

A PSI HERMIGA 75 atomiser fitted with a hopper unit, as illustrated in Figure 3.1, was used during these studies. Prior to each melt, the melt chamber was vacuum pumped down to a pressure of ca. 4×10^{-1} mbar, and purged with Argon three times leading to an O₂ level in the range of 50 ± 20 ppm. The power was varied by altering the voltage (400-480 V) to the induction coil depending on the sample charge. Each sample was remelted two to three times and when required an atomisation pressure of ca. 70 bar was utilised.



Figure 3.1: (a) PSI HERMIGA 75 atomiser with (b) hopper unit located underneath.

TiFe_{1-x}Ni_x (x = 0, 0.04 and 0.08) alloys produced in bulk (ca. 900 g) were both

induction melted and atomised, with a sieved mesh size -100 to +140 (106-150 μm) selected for testing and coating. For a comparison study of two AB_2 alloys, a commercially available master alloy, Hydralloy C5 ($\text{Ti}_{0.95}\text{Zr}_{0.05}\text{Mn}_{1.5}\text{V}_{0.45}\text{Fe}_{0.1}\text{Cr}_{0.05}$), was purchased from GfE and compared to an in-house melted alloy (ca. 20 g) of composition ($\text{Ti}_{0.9}\text{Zr}_{0.2}\text{Mn}_{1.5}\text{V}_{0.2}\text{Cr}_{0.3}$). Hydralloy C5 was selected as a base because it was identified to have plateau pressures close to those desired for the prototype hydrogen store, meanwhile $\text{Ti}_{0.9}\text{Zr}_{0.2}\text{Mn}_{1.5}\text{V}_{0.2}\text{Cr}_{0.3}$ was fabricated with the aim to produce a more cost competitive alloy which also possessed better hydrogen storage properties compared to the base. Both alloys were melted, crushed under normal ambient conditions and a mesh size of -100 ($< 150 \mu\text{m}$) was selected for testing.

Commercial grade atomised magnesium powders were purchased from Advanced Powder Technologies (APT) and Société pour la Fabrication du Magnésium (SFM). The two magnesium powders were passivised prior to particle size and distribution analysis (Section 3.2.2) and being outsourced to Teer-Miba Coating Group for coating with candidate catalysts (Section 3.2.3).

| Material | Form | Purity [%] | Source |
|----------|-----------------|------------|--------------------------|
| Ti | 10 mm rod | >99.2 | Unicorn Metals |
| Fe | 2-10 mm chip | 99.98 | Sigma-Aldrich |
| Ni | 3-25 mm shot | >99.95 | Alfa Aesar |
| Zr | 3-6 mm lump | 99.8 | Alfa Aesar |
| Mn | 1-3 mm chip | 99.9 | Alfa Aesar |
| V | 1-3 mm granule | 99.7 | Alfa Aesar |
| Cr | 3-12 mm piece | 99.2 | Alfa Aesar |
| Mg | Atomised powder | >99 | University of Birmingham |
| Mg | Atomised powder | >99 | SFM, Switzerland |

Table 3.1: Raw materials, purity and suppliers.

3.2.2 Particle Sizing

While scanning electron microscopy can provide an initial estimation of particle size it is a fairly selective approach. More accurate verification of average particle size and distribution within a powder sample was achieved using a Malvern Mastersizer 2000. This apparatus utilises laser diffraction in order to measure particle size within a range of $0.02 \mu\text{m}$ up to 2 mm . Although the Mastersizer cannot analyse particle shape characteristics, like a CAMSIZER, this was not regarded as critical since the Mg powders investigated were all manufactured by gas atomisation, a technique well recognised for producing consistently spherical particles.

Laser diffraction determines particle size distributions by analysing the variation in intensity of scattered light as a laser beam passes through the dispersed sample. In principle, smaller particles cause the light to scatter at large angles relative to the laser beam, whilst larger particles result in light scattered at small angles. Using Mie theory of scattered light (Horvath, 2009) and assuming a volume equivalent sphere diameter, the post scattered angle intensity data can be evaluated to calculate size

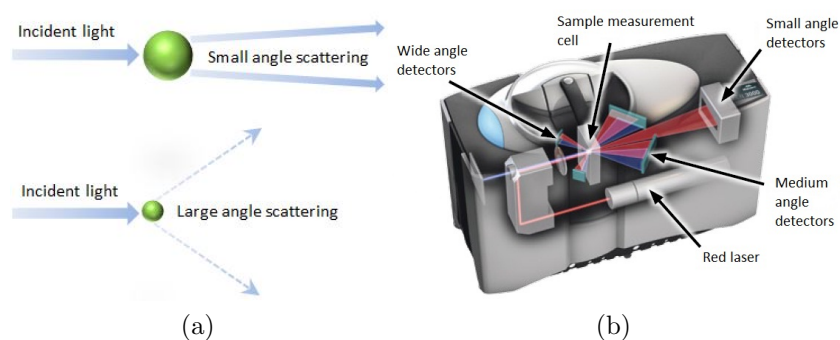


Figure 3.2: (a) Scattering of light from large and small particles (b) Optical bench within Malvern Mastersizer 2000.

of the particles. Mie theory is dependent on knowledge of the optical properties (refractive index and imaginary component) of both the dispersant and sample under investigation. During this testing, dry air and magnesium were the dispersant and sample respectively, both of which the relevant properties were readily accessible.

The Mastersizer 2000 system comprises of three main elements: a sample dispersion unit, an optical bench and instrument software. Prior to measurement, a sample dispersion unit is used to suspend the sample in a flowing dry air stream, thus ensuring the particles are delivered in the correct concentration and in a stable state of dispersion. Once dispersed, the sample enters the measurement area within the optical bench, where a laser beam illuminates the particles. The light scattered by particles within the sample are recorded by a series of detectors over a wide range of angles, as shown in Figure 3.2, and this information is interpreted by the instrument software to generate particle size distribution information.

The commercial grade atomised magnesium powders purchased from Advanced Powder Technologies (APT) and Société pour la Fabrication du Magnésium (SFM) were analysed using the Malvern Mastersizer 2000. The mean particle sizes (D_{50}) were determined to be $30\ \mu\text{m}$ and $26\ \mu\text{m}$ and from here forth will be referred to as Mg30 and Mg26 respectively.

3.2.3 Magnetron Sputtering Conditions

All coating work was performed in collaboration with Teer-Miba Coating Group due to their access to magnetron sputtering systems. Given that a thin film structure

typically forms the substrate during magnetron sputtering; to enable the deposition of coatings onto micron-scale powders, a Teer Coatings UDP450 closed field unbalanced magnetron sputter ion plating system, based on an argon plasma, was modified to a ‘tilted cup’ design.

The coating system, illustrated schematically in Figure 3.3, was customised by replacement of the traditional rotating jig with a tilted stainless-steel cup arrangement, which was attached to the motor drive in the bottom of the chamber. The cup was tilted at 45° from normal and could be rotated at speeds from approximately 10 to 100 $\text{rev}\cdot\text{min}^{-1}$. A secondary smaller cup containing the powder substrate, capable of handling batches of up to 50 g, was placed inside the first cup and rotation of the outer cup caused the inner cup to tumble. Consequently, the powder was agitated, constantly changing the substrate orientation. Instead of using the four large linear magnetrons (from the original UDP450 system) for the coating process an external

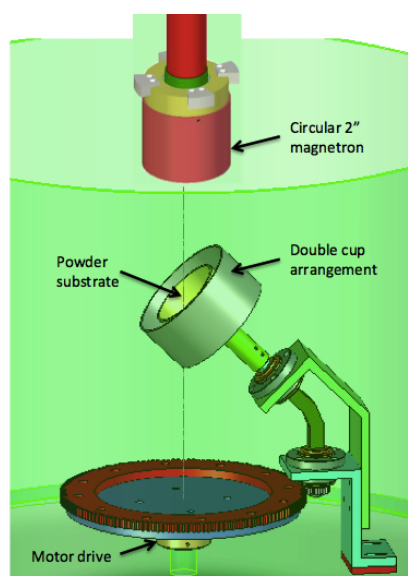


Figure 3.3: ‘Tilted cup’ magnetron sputtering schematic.

circular two-inch magnetron was fitted to the chamber from the top flange above the tilted cup.

A range of different target materials were used to produce the coatings, as shown in Table 3.2. The choice of catalyst materials was derived from the literature, with Pd proven to aid the activation of TiFe and transition metals such as vanadium, iron and chromium recognised for enhancing the sorption kinetics of MgH₂. Stainless steel (grade 321) was also chosen as a catalyst for MgH₂ due to an interest into multi-element catalytic effects (see Section 2.3.1), which could then be compared against its main components (68 wt.% Fe and 17-19 wt.% Cr).

Following the initial feasibility study, a selection of key parameters were kept fixed for every coating applied. This included reaching a chamber vacuum of at least 3×10^{-5} mbar prior to coating, an argon flow of 8.5 sccm, a magnetron-to-substrate distance of 13.5 ± 0.5 cm and a cup rotation speed of 52 rev.min^{-1} . To draw more ion current from the plasma to the powder substrate a -40 V substrate bias was applied to the cup, resulting in a current of 0.06 A being drawn to the cup. The powder load volume and mean particle size (D_{50}) also required consideration; higher powder volumes mean the exposure time of each particle to the target flux is reduced and more critically the finer the powder the higher the total surface area. Therefore, when possible the powder volume and mean particle size across samples were kept consistent.

| Sample code | Substrate | Target | Purity [%] (source) | Deposition conditions | Substrate mass [g] | EDX [wt.%] |
|--|---|--------------------------------|-------------------------|--------------------------------|-----------------------|-----------------|
| Pd_TiFe _{0.96} Ni _{0.04} | TiFe _{0.96} Ni _{0.04} (106 μm) | Palladium | 99.99 (PI-KEM Ltd) | 20 W x 2 h | 17 | 1.17 \pm 0.10 |
| SS_Mg30 | Mg (30 μm) | Stainless steel (grade 321) | (Unknown) | (100 W x 1 h + 150 W x 4 h) | 7 | 3.14 \pm 0.66 |
| V_Mg30 | Mg (30 μm) | Vanadium | 99.5 (Kurt J Lesker) | 150 W x 4.5 h | 7 | 0.93 \pm 0.12 |
| Fe_Mg30 | Mg (30 μm) | Iron | 99.9 (Kurt J Lesker) | 100 W x 2 h | 7 | 0.82 \pm 0.28 |
| Cr_Mg30 | Mg (30 μm) | Chromium | 99.95 (PI-KEM Ltd) | 150 W x 4.5 h | 7 | 2.32 \pm 0.40 |
| Cr_Mg26 | Mg (26 μm) | Chromium | 99.95 (PI-KEM Ltd) | 150 W x 3.33 h | 7 | 1.58 \pm 0.18 |

Table 3.2: Magnetron sputtering deposition conditions for the coated samples.

3.3 Sample Characterisation Techniques

3.3.1 X-Ray Diffraction

The microstructure of all samples as received and post hydrogen cycling were analysed using powder X-ray diffraction (XRD). This technique was used to reveal information about unit cell dimensions and structural phases present in a crystalline solid compound. The incident X-ray beam is produced by bombarding a metal target (e.g. Cu anode) with electrons that have been accelerated through a potential difference in the range of 10^3 - 10^6 V within a sealed vacuum tube. XRD depends on the interaction between the irradiated X-rays and crystallites critically altering the X-ray signal due to scattering.

Upon satisfying two conditions where the angle of the incident beam is equivalent to that of the scattered beam (θ), and the path length difference is equal to an integer number of wavelengths (λ), peaks of scattered intensity are obtained. This can be stated by Bragg's Law:

$$n\lambda = 2d\sin\theta \quad (3.1)$$

where n is the order of diffraction and d is the interplanar spacing.

For phase identification the raw data collected for each sample was compared against reference diffraction data on the JCPDS-ICDD Powder Diffraction File using Bruker EVA software.

Additionally, in cases where crystallites are sufficiently small (< 100 nm) it is possible to deduce the average crystallite size and level of internal strain from the substantial line broadening in an X-ray diffraction pattern (Suryanarayana and Grant-Norton, 2013). The Scherrer equation:

$$\tau = \frac{K\lambda}{\beta_{obs}\cos\theta} \quad (3.2)$$

relates the crystallite size τ to the diffraction angle θ , the shape factor K , the X-ray wavelength λ and the observed line broadening β_{obs} which is the full width of the diffracted X-ray peak at half maximum peak intensity (FWHM).

Observed line broadening β_{obs} can also arise from instrumental contributions such as diffractometer set-up and the potential presence of a K_{α_2} component from the X-ray source. To account for instrumental broadening effects β_{ins} a coarse grained LaB_6 reference sample is used to obtain a diffraction pattern where size- and strain-broadening is assumed negligible (see Figure 3.4). By subtracting β_{ins} from β_{obs} the modified β is determined.

Internal strain within the crystallites is another potential contribution to observed

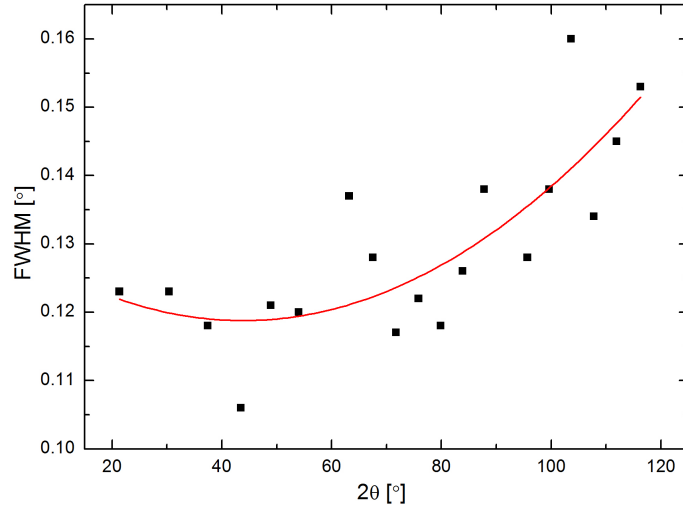


Figure 3.4: Instrument broadening from LaB_6 reference sample with 2^{nd} order polynomial fit.

broadening of diffraction peaks (Hall, 1949). A Williamson-Hall plot can generate approximations for the microstrain and crystallite size, however for the purposes of this thesis XRD is utilised for phase indexing only. Strain analysis was not conducted because accurate crystallite sizes could not be determined, as any line broadening which resulted from cycling under hydrogen was less than those from instrumental contributions and therefore were not observable.

Powder X-ray diffraction measurements were performed on a Bruker D8 Advance using a monochromatic Cu K_α source ($\lambda = 1.5418 \text{ \AA}$) at 40 kV and 35 mA, emitted through a 0.6 mm slit. Samples were scanned over a 2θ range of 10° - 80° , with a step size of 0.05° and a dwell time of 4 s using a Scintillation detector. Samples were loaded in milligram quantities onto single crystal Si wafers and covered with an amorphous polymer tape limit powder movement during XRD measurement since the samples were rotated to improve crystallite homogenisation. The tape causes

the resultant diffraction pattern to have an amorphous bump between 2θ values of 10° - 30° .

3.3.2 X-ray Photoelectron Spectroscopy

The as prepared and post cycled surfaces of TiFe and Pd-TiFe_{0.96}Ni_{0.04} were analysed by X-ray photoelectron spectroscopy (XPS). This technique, which has an average depth analysis of ca. 5 nm, was used to determine the concentration and chemical state of each component present on the surface of a sample. During the measurement, a monochromatic beam of X-rays is irradiated on to the sample surface, prompting the emission of electrons of binding energy (BE) specific to the local environment of the atoms from which they originate. The measured kinetic energy (KE) is directly related to the binding energy (BE) by the relationship (equation 3.3), where $h\nu$ is the energy of a photon and ϕ is the work function also known as the minimum energy required to move an electron from the highest occupied energy level in atom to the vacuum level.

$$BE = h\nu - KE - \phi \quad (3.3)$$

Measurements were conducted on a VG ESCALab Mark II XPS system with a monochromated Al K_α X-ray source ($h\nu = 1486.6$ eV) operated at 12 mA and 20 kV. Samples were prepared by mounting powders onto double-sided tape attached to a sample bar. Wide scans were collected for all samples across the kinetic energy range of 300-1500 eV using a step size of 1 eV and a pass energy of 60 eV. High

resolution scans were then run over the desired regions specific to each sample, using a step size of 0.25 eV and a pass energy of 20 eV.

Analysis of the XPS data was carried out using CasaXPS software. The C 1s peak at 285 eV was used for charge correction. For peak fitting, the background was corrected using a Shirley background type and Gaussian/Lorentzian contributions of 30/70 were utilised for the fitted components. Experimental peak positions were cross-referenced with the NIST X-ray Photoelectron Spectroscopy Database 20 (version 4.1) with the relevant reference peaks detailed in Table 3.3.

| Element | Component | Reference Binding Energy [eV] |
|---------|---------------------------------------|-------------------------------|
| O 1s | O 1s | 532.0 |
| | 2p TiO ₂ 3/2 | 458.6 |
| Ti 2p | 2p TiO ₂ 1/2 | 464.7 |
| | 2p Ti 3/2 | 454.0 |
| | 2p Ti 1/2 | 460.0 |
| Fe 2p | 2p Fe ₂ O ₃ 3/2 | 711.0 |
| | 2p Fe ₂ O ₃ 1/2 | 724.0 |
| Ni 2p | 2p NiO 3/2 | 854.4 |
| | 2p NiO 1/2 | 871.9 |
| Pd 3d | 3d PdO 5/2 | 337.0 |
| | 3d PdO 3/2 | 342.4 |
| | 3d Pd 5/2 | 335.2 |
| | 3d Pd 3/2 | 340.4 |
| Mn 2p | 2p Mn ₂ O ₃ 3/2 | 641.6 |
| | 2p Mn ₂ O ₃ 1/2 | 653.6 |
| | 2p MnO ₂ 3/2 | 642.5 |
| | 2p MnO ₂ 1/2 | 653.9 |
| Cr 2p | 2p Cr ₂ O ₃ 3/2 | 576.6 |
| | 2p Cr ₂ O ₃ 1/2 | 586.3 |
| Zr 3d | 3d ZrO ₂ 5/2 | 182.6 |
| | 3d ZrO ₂ 3/2 | 185.5 |

Table 3.3: Reference peak binding energies obtained from NIST Photoelectron Spectroscopy Database 20.

3.3.3 Electron Microscopy

Scanning Electron Microscopy

Scanning electron microscopy (SEM) facilitates the surface of a solid material to be examined to a high-resolution (ca. 3 nm). The interaction between the focussed electron beam and the sample leads to the emission of a variety of signals including secondary electrons, back scattered electrons and X-rays. The secondary electrons, a by-product of inelastic scattering, assist in the understanding of the surface topology of the sample; while the back scattered electrons, a by-product of elastic scattering, provide information about differences in atomic weight within the sample. Also, quantitative analysis of the elemental composition within the sample can be undertaken using an Energy Dispersive (EDX) detector to measure the number of emitted X-rays, another resultant of elastic scattering, against their energy.

SEM and EDX measurements were conducted on a Philips XL 30 ESEM-FEG

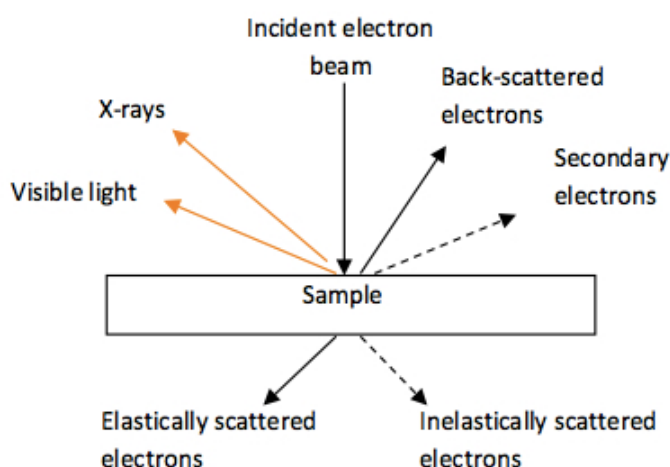


Figure 3.5: Representation of incident electrons interacting with the sample.

with an Oxford Instruments silicon drift EDX detector to study coating concentration and distribution, as well as post-cycling powder morphology. A 20 kV electron beam with a spot size 4 and a working distance of 10 mm was maintained throughout analysis. Elemental composition analysis of the AB and AB₂ alloys were prepared by embedding the sample in conductive (carbon) resin followed by a polishing process to establish a smooth surface. Catalyst coated samples were mounted on adhesive-coated carbon tabs for analysis of coating concentrations and distributions. Samples were also mounted on to adhesive-coated carbon tabs for post cycling morphology observations. Each porous Mg sample produced by cycling at 350 °C (which had taken on the cylindrical shape of the sample holder) was cut into half using a scalpel. One half of the remaining segments of material was mounted on to an Al stub using conductive carbon cement and carbon coated to improve conductivity during cross-sectional SEM analysis of the fractured surface at what was the midpoint of the sample.

Transmission Electron Microscopy

Transmission electron microscopy (TEM) enables visualisation and analysis up to a very high resolution of 0.1-0.5 nm by passing an electron beam through a sufficiently thin (< 100 nm) sample. Similar to SEM, an assortment of signals are emitted when the electron beam interacts with the specimen; although in this case the beam contribution that transmits through the specimen is used and focussed on to a fluorescent screen or a charged couple device (CCD) camera.

After passing through the TEM specimen, this portion of the beam comprises of three potential components, these include unscattered electrons, elastically scattered electrons and inelastically scattered electrons. Unscattered electrons are those which transmit directly through the sample without any interaction, while scattered electrons occur from interactions with the crystal structure of the sample.

Various types of images can be generated depending on whether directly transmitted electrons or scattered electrons are selected. Bright field images are the most commonly produced and arise when the objective aperture is used to select the unscattered electron beam, whilst filtering out the scattered electrons, thus enhancing the contrast in the image. On the other hand, if the unscattered electron beam is excluded as opposed to the scattered electrons, this results in a dark field image. Dark field imaging can be used to highlight crystal defects and produce selected area electron diffraction (SAED) patterns which reveal information about the crystal structure of the specimen.

By inserting a selective area aperture to delimit the region of interest this guarantees an area specific electron diffraction pattern. Depending whether the region under examination is crystalline or amorphous, the pattern will be represented around the electron beam focal point by a number of bright dots or set of diffuse rings respectively. Due to the geometry of the TEM set-up, Bragg's law can be manipulated to calculate the interplanar spacing corresponding to a specific diffraction ring in the SAED, see equation 3.4.

$$\lambda L = Rd \tag{3.4}$$

Both the camera length L , which is the distance between the sample and photographic film or CCD, and the incident electron wavelength λ are fixed, leading to a term known as camera constant. Once the camera constant has been determined by using a reference sample of known lattice parameters, the diffraction ring radius R can be used to obtain the corresponding interplanar spacing d .

This technique was performed on Pd.FeTiNi to confirm the presence of Pd on the alloy powder surface. Preparation entailed sandwiching a small amount of powder between two copper grids each with a fine carbon grid (mesh size 300) and imaging was carried out using a Joel 2000FXII microscope with a camera length of 1.00 m and an electron beam accelerated by a 200 kV potential. A ‘glancing angle’ approach was utilised which involved the imaging of particles’ edges and, due to their spherical nature, a change in the image contrast helped to identify the thickness of the catalyst on the alloy.

3.4 Hydrogen Storage Measurements

To accurately determine the hydrogen storage properties of the samples investigated a combination of volumetric and calorimetric analyses were undertaken. Manually operated and automated Sievert’s apparatus as well as differential scanning calorimetry (DSC) and thermogravimetric analysis (TGA) were used to obtain information

regarding hydrogen capacities, kinetics, thermodynamics and cycling behaviour.

3.4.1 Volumetric Sorption Methods

The volumetric sorption technique utilises the virial equation (equation 3.5) to convert changes in gas pressure within a reaction vessel into the equivalent amount of gas absorbed or released by the sample.

$$\frac{PV}{nRT} = 1 + B(T)\frac{n}{V} + C(T)\frac{n^2}{V^2} \quad (3.5)$$

This links the pressure P , gas constant R , volume V , moles n and temperature T to temperature dependent virial coefficients $B(T)$ and $C(T)$. The virial coefficients for He and H₂ gases at the desired temperature can be found from the Nist Standard Reference Database 134 (NIST, 2009). Multiplication of molar mass of the gas and the volume calculated from the virial equation enabled the density of gas in the system to be determined.

Under isothermal conditions, if a calibrated reference volume (manifold) filled to a known hydrogen pressure is then opened to a secondary volume containing the sample under vacuum (sample holder), the new equilibrium pressure resulting from expansion of the fixed quantity of hydrogen gas across the two volumes can be determined. If a further pressure drop is observed, the sample has absorbed a fraction of the hydrogen. Given the known sample mass, the hydrogen capacity of the sample can be obtained from this pressure drop. Similarly, in the reverse case in which a pressure rise ensues between the two volumes beyond the initial equilibrium

pressure, the sample has released hydrogen.

Shown in Figure 3.6 is a schematic of the manually operated double-manifold Sievert's apparatus. The system consisted of a stainless steel sample cell (A), which could be removed and handled inside the Ar glove box, connected to a manifold (volume represented by dashed box C) via stainless steel piping and a ball valve (V1). If additional manifold volume (D) was required the ball valve (V3) could be opened. The sample cell was fitted into a Watlow ring heater (B) capable of heating a sample to 760 °C with a temperature control of ± 1 °C. To account for heat transfer discrepancies between ring heater and sample, the heater was controlled by a thermocouple inserted into the base of the sample holder (ca. 1 cm from the sample).

A General Electric PTX 5000 pressure transducer (E) with an accuracy of $\pm 0.04\%$ of full scale reading and pressure range of 0-150 bar was fitted to the top of the

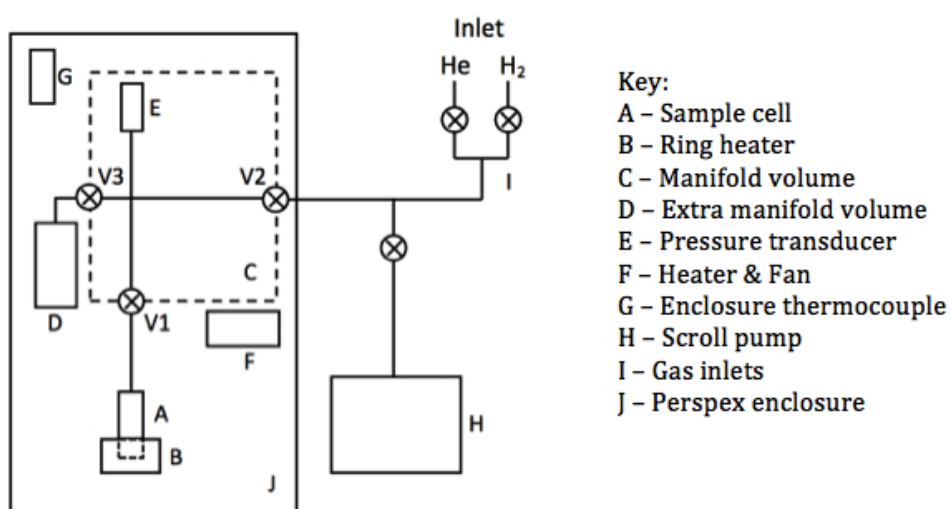


Figure 3.6: Schematic of double-manifold Sievert's apparatus.

manifold and using Labview software the pressure could be continuously tracked, thus enabling accurate kinetics measurements. The system was enclosed inside a Perspex box (J) fitted with a heater and fan (F) to maintain a fixed manifold temperature (20 °C), monitored by a thermocouple (G). Via ball valve (V2) the apparatus was also connected to an Edwards XDS-5 oil free dry scroll pump (H) and gas inlets (I) for He (purity 99.996 %, BOC) and Ultra Pure Plus H₂ (purity 99.99996 %, Air Products).

Prior to any measurements, volume calibration of the sample cell and manifold was undertaken using He gas. By adding different pre-determined volumes of stainless steel ball bearings V_B to the sample cell volume V_S , its volume decreased by known quantities. Since the mass of gas in the system remains constant, upon exposing the pressurised manifold volume V_M to the evacuated sample cell containing ball bearings ($V_S - xV_B$), it can be stated:

$$V_M\rho_M = (V_M + V_S - xV_B)\rho_{total} \quad (3.6)$$

where x is the number of ball bearings added to the sample cell, and ρ_M and ρ_{total} are the densities of the manifold gas and equilibrium gas across the two volumes respectively. These densities were calculated by converting the pressure values prior and post expansion into the sample cell using equation 3.5. Rearrangement of equation 3.6 gives:

$$\left(\frac{\rho_{total}}{\rho_M} - 1\right)V_M = V_S - xV_B \quad (3.7)$$

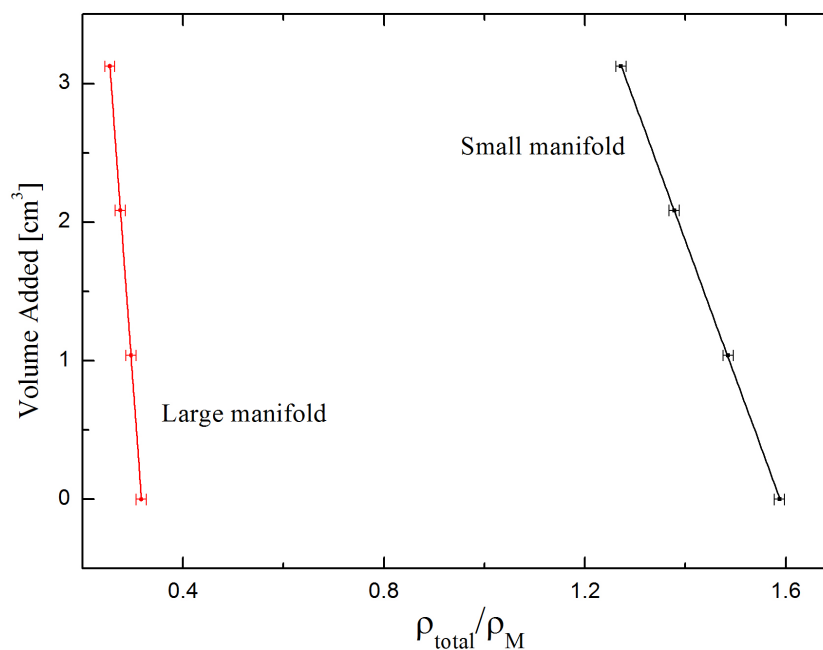


Figure 3.7: Volume calibration data with fitted linear regression lines for the double-manifold Sievert's apparatus used.

By plotting the density ratio (ρ_{total}/ρ_M) against the added volume (xV_B), the manifold V_M and sample cell V_S volumes were deduced from the slope and intercept of the linear fit obtained. The calibration curves illustrated in Figure 3.7 correspond to volumes of $9.9 \pm 0.1 \text{ cm}^3$ and $49.8 \pm 0.2 \text{ cm}^3$ for the small and large manifolds respectively. Using these manifold volumes and a known sample mass the effective sample cell volume was ascertainable at a given temperature and pressure via equation 3.5.

The availability of two manifold volumes permitted a greater accuracy in both pressure-composition isotherms and kinetics measurements. During PCI measurements in which a step-wise approach was taken, the smaller manifold volume was beneficial as a greater pressure change occurred upon exposure to the sample, in turn

making it easier to distinguish when an equilibrium pressure had been reached. In contrast, a larger manifold volume during kinetics measurements enabled an adequate over/under pressure to be maintained throughout hydrogenation or dehydrogenation because the pressure change was sufficiently small.

The manually operated Sievert's system was used to obtain activation, kinetic and PCI data for the AB and AB₂ alloys, the results of which are presented in Chapter 5. No explicit rule states where the plateau pressure at any given temperature should be measured although it should be close to the plateau mid-point. For this reason the plateau pressures of the TiFe based alloys and AB₂ alloys were measured at 0.5 wt.% and 0.85 wt.% respectively. It should be noted if different plateau pressure values are chosen this would impact the calculated enthalpy and entropy. The magnitude of this impact would be greater for metal hydrides that possess increasingly sloped plateaus and significant capacity reductions when exposed to only minor temperature increases.

A commercial, fully automated Setaram PCTpro 2000 Sieverts system was used for extended hydrogen cycling experiments. The instrument offered greater flexibility than the manually operated Sieverts system, allowing the user to select from five possible manifold volumes ranging from 6 ml up to 1000 ml and was able to conduct hydrogen cycling and PCI measurements. Throughout all experiments the manifold temperature was fixed at 30 ± 1 °C, although a sinusoidal temperature deviation of ± 0.4 °C within the instrument was recorded. The system used an identical sample heating control mechanism to the manual Sieverts apparatus but under the test

conditions of 350-400 °C it was less stable and had an accuracy of ± 3 °C. The pressure measured by a capacitance manometer had an accuracy of 1% of reading. The PCTpro 2000 was used to collect activation, kinetic, cycling stability and PCI data for the atomised magnesium powders with/without catalytic coatings, the results of which are presented in Chapter 4.

3.4.2 Differential Scanning Calorimetry

Differential scanning calorimetry (DSC) is a technique that can reveal the exothermic and/or endothermic behaviour of a chemical reaction, through analysis of the heat flux in and out of a sample. Weighed samples (typically < 10 mg) are placed into an alumina crucible, which in turn is sealed within an aluminium pan and lid arrangement to minimise sample oxidation during transfer between the argon glovebox and instrument. Prior to loading the sample into the DSC the aluminium lid was pierced with a needle to enable gas flow into the sample during the experiment. By placing a reference sample, which consisted of an empty alumina crucible sealed within an aluminium pan and lid, alongside the test sample, both could be simultaneously heated at a controlled rate under a chosen atmosphere. Since both the sample and reference undergo identical experimental conditions any differences in the heat flow rates between the two represent a transition within the sample.

While the enthalpy of transition can be estimated through integration of the area within a curve, the activation energy of a reaction can also be calculated using DSC. The Arrhenius equation, given below, links temperature dependence to reaction rates

(Blaine and Kissinger, 2012):

$$\frac{E_a \beta}{RT_p^2} = A e^{\frac{-E_a}{RT_p}} \quad (3.8)$$

can be rearranged to:

$$\ln\left(\frac{\beta}{T_p^2}\right) = \ln\left(\frac{AR}{E_a}\right) - \frac{E_a}{RT_p} \quad (3.9)$$

This relates the activation energy E_a to the heating rate β (dT/dt), gas constant R , pre-exponential factor also known as the frequency factor A and temperature of the dehydrogenation maximum T_p . Using different heating rates a Kissinger plot can be constructed, where $\ln(\beta/T_p^2)$ is plotted against $1/T_p$, and the activation energy E_a can be derived from the slope of the linear fit.

A Netzsch 204 HP Phoenix was utilized to study the atomised magnesium powders with/without catalytic coatings following cycling on the PCTpro 2000. The hydrided samples were heated from room temperature up to 550 °C under ramps of 3, 5, 10 and 20 °C.min⁻¹ with 1 bar of flowing Ar at a rate of 100 ml.min⁻¹. The results obtained were used to construct Kissinger plots to determine the activation energy of dehydrogenation for each sample.

3.4.3 Thermogravimetric Analysis

Gravimetric methods were used to verify the hydrogen storage capacity of the atomised magnesium powders with/without catalytic coatings obtained by volumetric methods following cycling on the PCTpro 2000. Thermogravimetric analysis (TGA)

of the hydride samples were performed on a Netzsch 209 F1 Iris with a similar sample preparation procedure to DSC samples. To account for buoyancy, a blank test consisting a reference sample (identical to that in DSC experiments) was run under conditions matching those employed for the hydride samples. Subtraction of the blank test from the sample test, meant the true mass loss of the sample due to dehydrogenation was determinable. Samples were held at 30 °C to allow system stabilisation and formation of a baseline under 1 bar of flowing Ar at a rate of 100 ml.min⁻¹, after which mass loss was measured during heating at 10 °C.min⁻¹ up to 550 °C.

Chapter 4

Moderate temperature thermal storage

4.1 Introduction

The highly reversible Mg-MgH₂ system is particularly promising for thermal storage, obtaining an enthalpy of reaction of 74.5 kJ.mol⁻¹ H₂ that translates to a thermal energy capacity of approximately 2800 kJ.kg⁻¹ of MgH₂. Nevertheless, magnesium is hindered by slow activation and poor kinetics of (de)hydrogenation, even when approaching temperatures ideal for concentrated solar power applications (in the region 400 °C) (Zaluska et al., 1999).

Elevated temperature cycling studies (350 & 400 °C) were performed on commercial atomised Mg powder with magnetron sputtered catalysts (chromium, iron, vanadium and stainless steel) applied to their surfaces; the aim of which was to

fabricate hydrogen storage materials that possess (de)hydrogenation characteristics equal to or even bettering their nanocrystalline equivalents (Hanada et al., 2005), yet in a potentially economic and scalable manner. The reasoning for conducting studies at these temperatures was to replicate conditions of a CSP plant in which the typical temperature of the heat transfer fluid as it exits the solar field is ca. 400 °C and as steam exits the generator, flowing back to the metal hydride store, it is at ca. 350 °C.

The hydrogen storage cycling behaviour of the samples were investigated using the Setaram PCTpro 2000, thermogravimetric analysis and differential scanning calorimetry, which are reported in Section 4.2.1. Structural analysis of the as received and cycled powders includes particle size analysis, XRD and SEM which is detailed in Section 4.2.2. Discussion of findings and the proposal of a mechanism explaining the differing results between uncoated and coated Mg powders is explained in Section 4.3.

4.2 Results

4.2.1 Hydrogen Storage Characteristics

Cycling behaviour

The hydrogen storage capacity results (example shown in Figure 4.1(a)) have been converted into normalized capacity ranging from ca. 20-80% depending on cycling

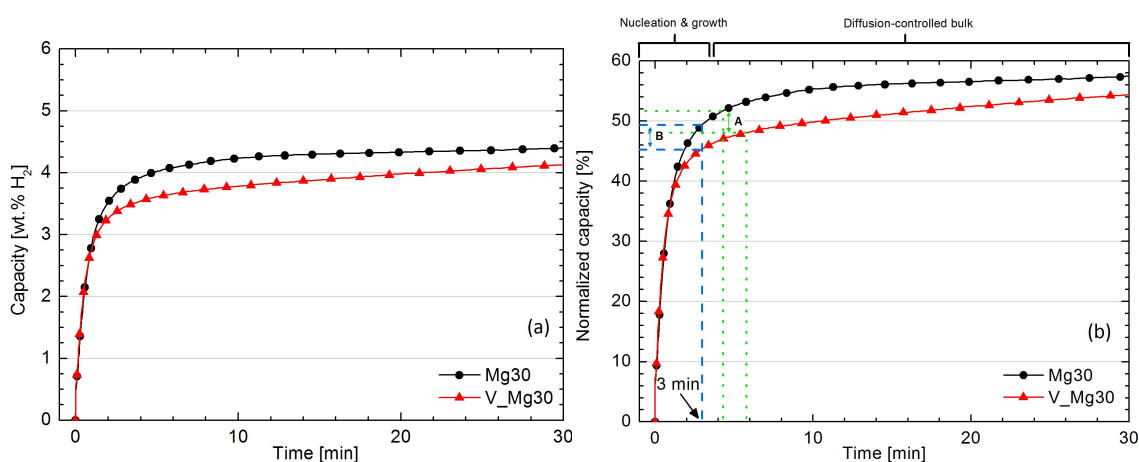


Figure 4.1: (a) Hydrogen storage capacity and (b) Normalized capacity versus time for activated & cycled Mg30 and V_Mg30 during the 10th hydrogenation cycle at 400 °C. Data points have been used in the plots so each sample is distinguishable. Data was actually collected asymptotically reaching a maximum of 20 s between measurements. There is a 1% error in all of the normalized capacities measured.

variables such as temperature and catalyst material and concentration. Normalized values were determined by deducting the catalyst concentrations from the theoretical capacity of MgH₂ and rescaling the measured hydrogen storage capacities against these new theoretical maximums. The theoretical capacities of all of the catalyst coated Mg powders were lower than pure MgH₂ (7.66 wt.%) since all of the catalyst materials (chromium (Pan, 1991), vanadium (Reilly and Wiswall, 1970) and iron (Antonov et al., 1998)) require pressures far exceeding 10,000 bar to form their elemental hydrides in the region of 300-400 °C.

The kinetics of reaction is typically defined by the time to achieve 90% of the available reaction value Verga et al. (2009); Sabitu and Goudy (2012). Figure 4.1(b) illustrates the typical hydrogenation kinetics for both the uncoated Mg30 and coated V_Mg30 during the 10th cycle at 400 °C where normalized capacity is displayed on the

y-axis. The 3 min marker helps to highlight the distinct change in the hydrogenation kinetics in both samples, characteristic of the transition in reaction mechanism between magnesium and hydrogen from the initial ‘nucleation and growth’ region to the ‘diffusion-controlled bulk’ process [Vigeholm et al. \(1987\)](#) (see Figure 4.1(b)). Although only a small uptake disparity exists between 90% of the available reactions (marked A) and the 3 min capacities of both samples (marked B), the bearing on time is more significant. This is because for these atomised powders 90% of the available reaction appears to be well into the slower ‘diffusion-controlled bulk’ stage of hydrogenation. Based on these results, it was judged more appropriate to define

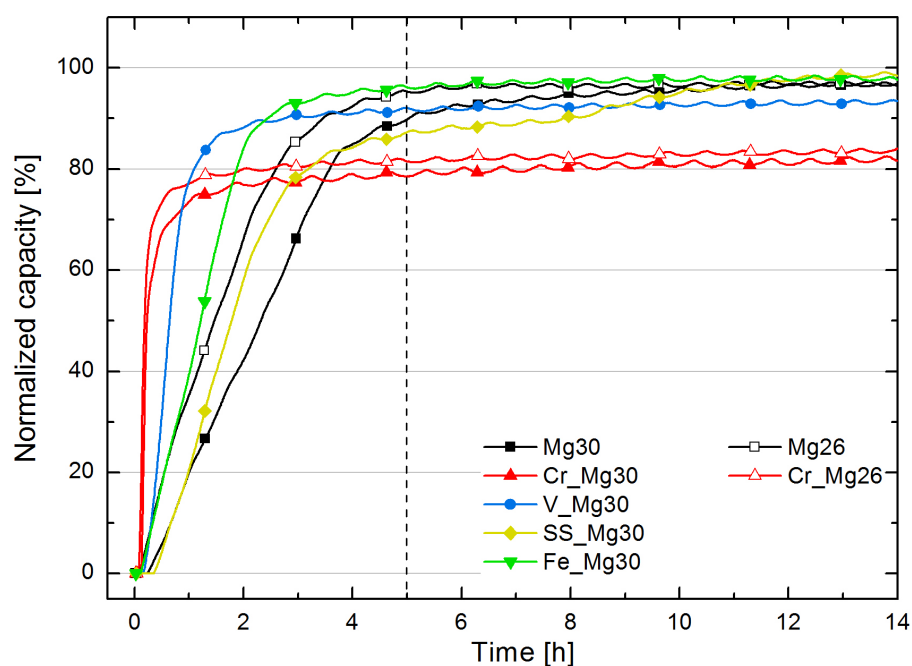


Figure 4.2: Normalized capacity versus time for each sample during the activation process at 400 °C and a starting pressure 40 bar. Data points have been used in the plots so each sample is distinguishable. Data was actually collected asymptotically reaching a maximum of 20 s between measurements and the slight fluctuations represent temperature variations within the system. There is a 1% error in all of the normalized capacities measured.

the hydrogenation kinetics after 3 min and capacities during cycling after 30 minutes.

Figure 4.2 displays the initial hydrogenation of samples at 400 °C during activation. Uptake of hydrogen can be seen to occur within the first 30 minutes and saturation is either completed or being approached by all samples within the first 5 h of measurement. All of the coated samples obtain faster kinetics than their uncoated counterparts, for example Cr_Mg26 obtained the highest initial rate of hydrogenation ($2.1 \text{ \%}\cdot\text{min}^{-1}$ during the initial 90% of uptake) compared to Mg26 ($0.47 \text{ \%}\cdot\text{min}^{-1}$ during the initial 90% of uptake).

Figure 4.3 demonstrates the impact of the activation process prior to cycling at 400 °C by examining hydrogenation kinetics and total capacity as a function of cycle number. By the 5th cycle, both the hydrogenation kinetics and total capacity of the cycled Mg30 match those of the activated & cycled Mg30, after which they are observed to follow the same trend with increasing cycle number. Almost identical behaviour can be seen for the catalyst coated Mg samples (Figure 4.3 b,c,d and f).

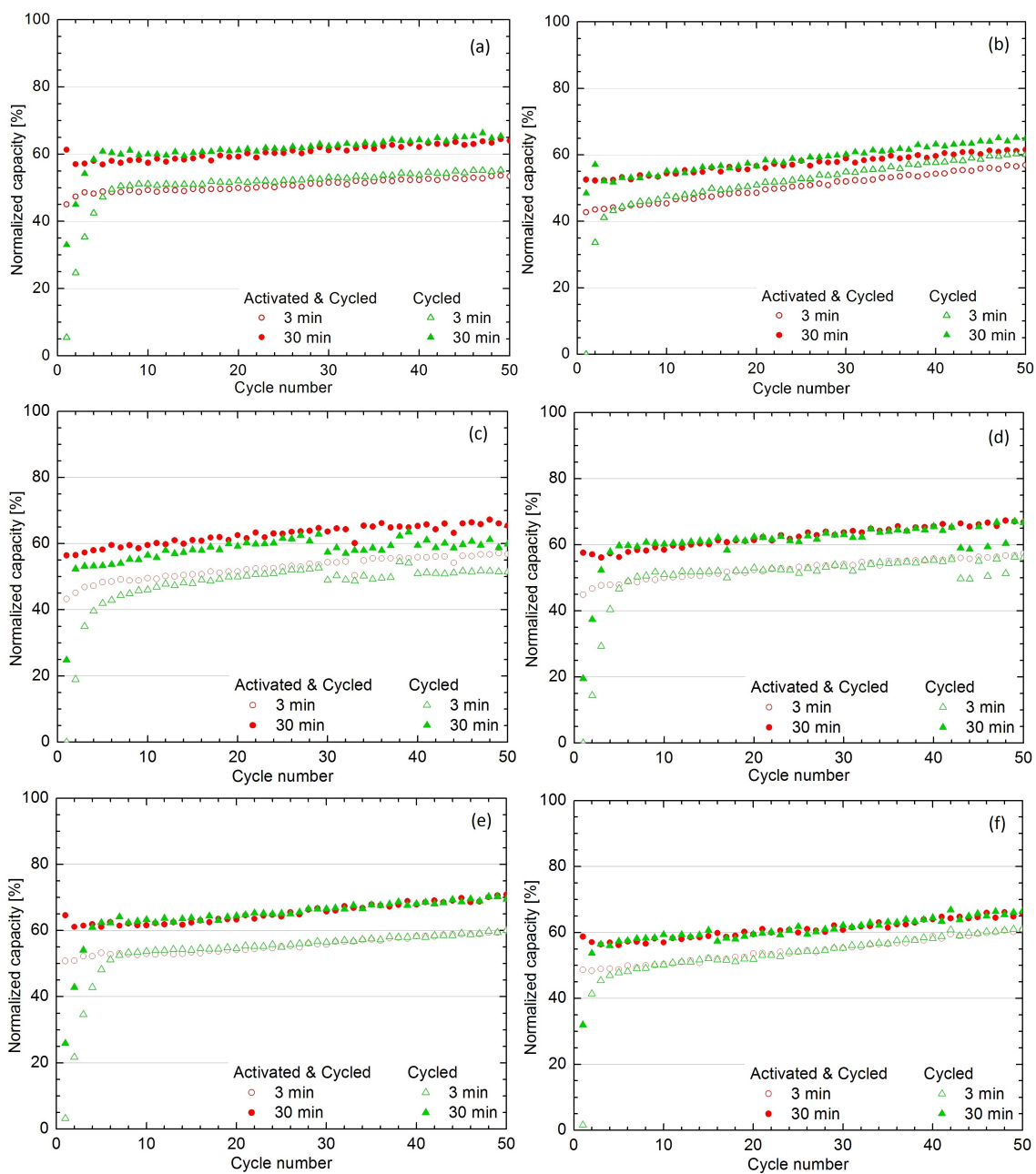


Figure 4.3: Comparing the normalized hydrogen capacity after 3 and 30 min against cycle number for (a) Mg30, (b) V_Mg30, (c) SS_Mg30, (d) Fe_Mg30, (e) Mg26 and (f) Cr_Mg26 when cycled at 400 °C with/without undergoing a prior activation process. There is a 1% error in all of the normalized capacities measured.

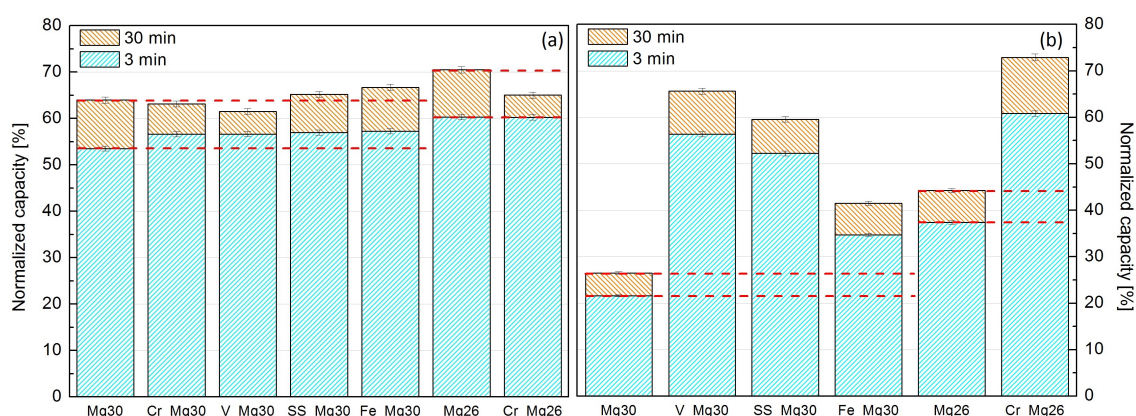


Figure 4.4: Normalized capacity after 3 and 30 min for each ‘activated & cycled’ sample at (a) 400 °C during the 50th hydrogenation cycle and (b) 350 °C during the 90th hydrogenation cycle.

The hydrogenation characteristics of the activated & cycled samples during their 50th cycle at 400 °C have been compared in Figure 4.4(a). As anticipated, cycling of the finer Mg26 led to an improvement in both kinetics and capacity by approximately 6.5 ± 0.1 % when compared to Mg30. The kinetics of the coated samples were found to improve by only 3-4% and in the case of Cr_Mg26 no kinetic improvement was exhibited with respect to Mg26. No clear trend is evident between the capacities of the uncoated and coated Mg samples after 30 minutes, with SS_Mg30 and Fe_Mg30 exceeding the capacity of Mg30 but the opposite occurred for Cr_Mg30 and V_Mg30.

The effect of the coatings on total capacity can be seen more clearly in Figure 4.5, in which uptake was monitored over a 14 h period following the 50 cycles. All of the catalyst concentrations, with the exception of Fe, were found to have a detrimental impact by up to 6.5% on the final capacity of the Mg powders. Overall, the uncoated Mg26 continued to display the best hydrogenation characteristics achieving a final capacity of 82.5 ± 0.8 % after 14 h.

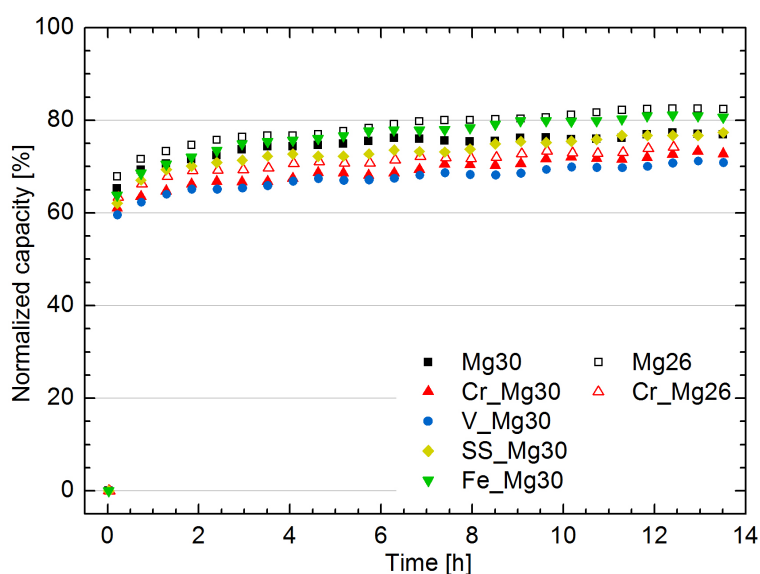


Figure 4.5: Normalized capacity versus time for each ‘activated & cycled’ sample at 400 °C during an extended final hydrogenation cycle post 50 cycles. Data was actually collected asymptotically reaching a maximum of 20 s between measurements. There is a 1% error in all of the normalized capacities measured.

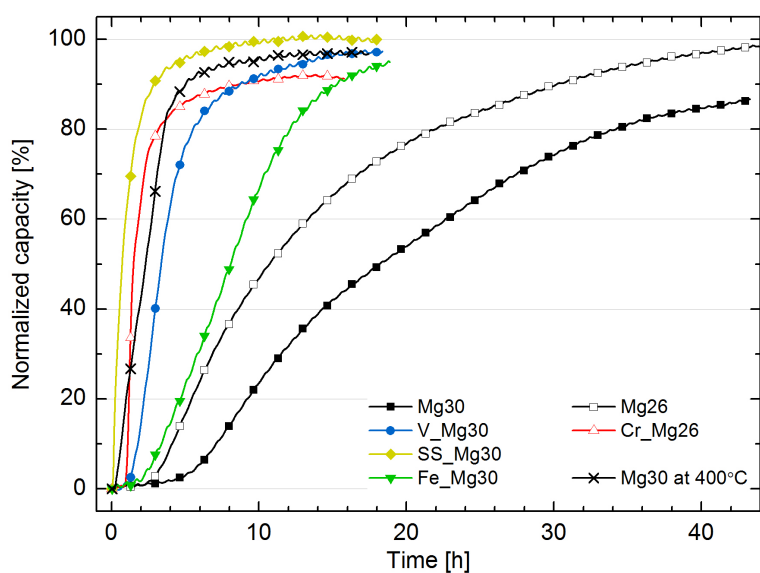


Figure 4.6: Normalized capacity versus time for each sample during the activation process at 350 °C and a starting pressure 40 bar. The activation curve of Mg30 at 400 °C has been included as a reference. Data was actually collected asymptotically reaching a maximum of 20 s between measurements and the slight fluctuations represent temperature variations within the system. There is a 1% error in all of the normalized capacities measured.

Figure 4.6 displays the initial hydrogenation of samples at 350 °C versus Mg30 at 400 °C also undergoing the activation process. Prior to hydrogenation both Mg26 and Mg30 at 350 °C undergo an incubation period lasting a minimum of 2.5 h. Subsequent to this, Mg26 approaches complete saturation after 44 h, however Mg30 is yet to reach 90% of normalized capacity in the same duration. In contrast, an increase in temperature to 400 °C enabled hydrogenation of Mg30 from the outset and resulted in the time to achieve saturation being approximately quartered. The influence of catalytic coatings to promote activation is unmistakable with a significant reduction in the incubation periods and all coated samples requiring, at most, half as long to complete hydrogenation compared to Mg30 at 350 °C. In fact, the incubation period appears to be completely eliminated for SS_Mg30, in turn causing it to obtain the highest initial rate of hydrogenation ($0.52 \text{ \%}\cdot\text{min}^{-1}$ during the initial 90% of uptake) and accomplish saturation more rapidly than even Mg30 at 400 °C ($0.30 \text{ \%}\cdot\text{min}^{-1}$ during the initial 90% of uptake).

Figure 4.7 shows the 1st, 2nd, 10th, 30th, 45th and final 90th cycle as a function of time for all samples cycled at 350 °C. Mg_30 (a) and V_Mg30 (b) were chosen for the particular focus of the following analysis. In the 1st cycle, while both samples exhibit a crossover in hydrogenation mechanism during the initial 3-5 minutes, the total capacity of V_Mg30 exceeded Mg30 by approximately $18.5 \pm 0.4 \text{ \%}$. Contrasting trends are observed in successive cycles demonstrating the fundamentally different hydrogenation behaviour experienced by the two samples. In the case of Mg30, the capacity rose marginally in the 2nd cycle before eventually dropping to slightly below

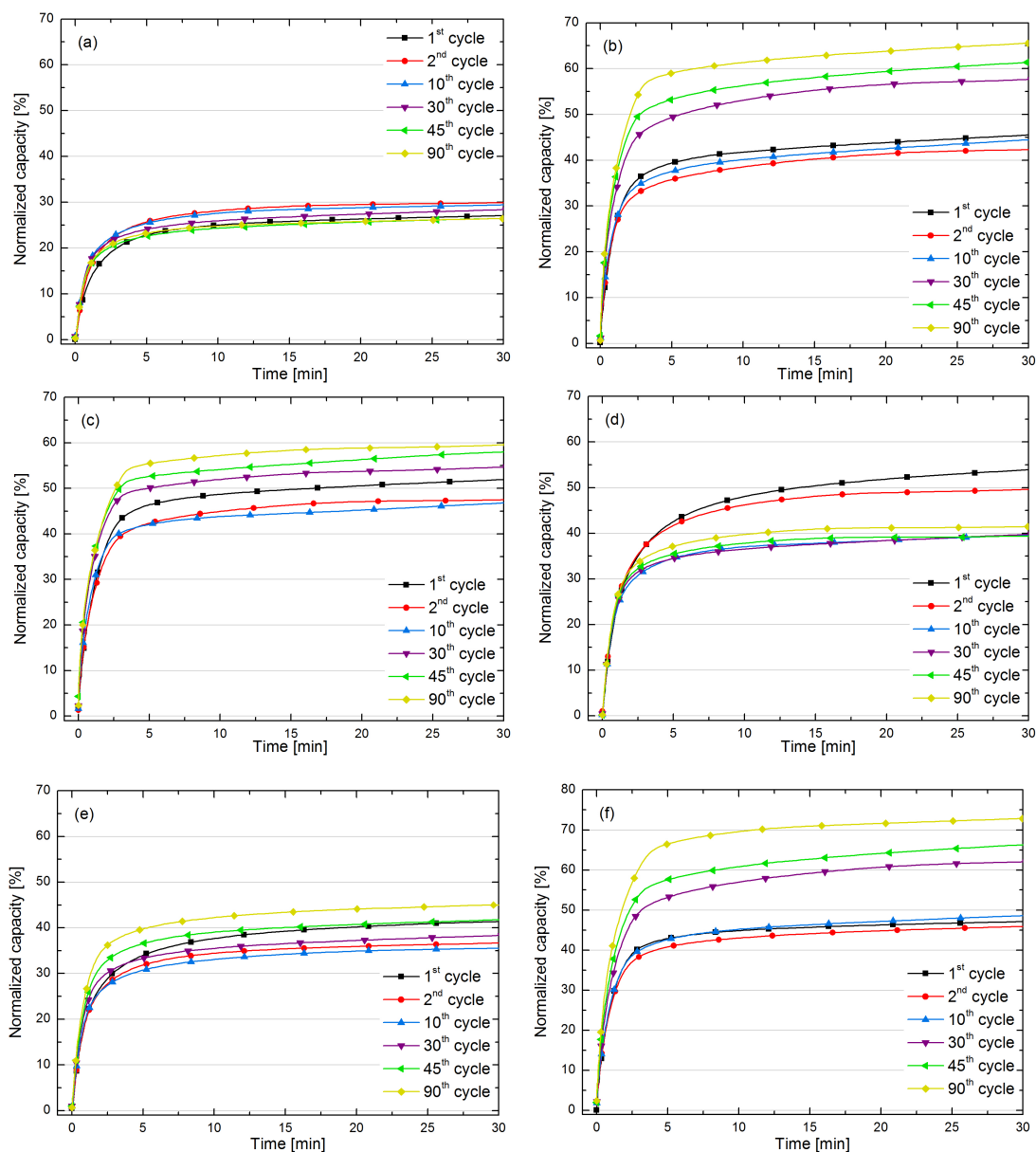


Figure 4.7: Comparing the normalized capacity versus time during selected cycles for (a) Mg30, (b) V_Mg30, (c) SS_Mg30, (d) Fe_Mg30, (e) Mg26 and (f) Cr_Mg26 when cycled at 350 °C.

that measured during the 1st cycle. A much more drastic change is seen for V_Mg30, with the normalized capacity reducing from $45.5 \pm 0.5 \%$ to $42.5 \pm 0.4 \%$ in the 2nd cycle after which uptake continued to markedly improve, approaching $65.5 \pm 0.7 \%$ by the 90th cycle. Unlike Mg30, with continued cycling not only does the duration of the fast nucleation and growth region of V_Mg30 continue to higher capacity, the rate itself improves from $16.02 \%. \text{min}^{-1}$ in cycle 1 to $18.23 \%. \text{min}^{-1}$ in cycle 90, as indicated by the increase in the slope of the initial part of the curve.

Given the large quantity of data, the hydrogenation characteristics were selected for samples during their 90th cycle at 350 °C, as illustrated in Figure 4.4(b). As observed in Figure 4.4(a), cycling of the finer Mg26 led to faster kinetics and a higher capacity relative to Mg30 but at 350 °C the variation between these samples appeared to be more profound with a $17.0 \pm 0.3 \%$ higher normalized capacity, opposed to an increase of $6.5 \pm 0.1 \%$ at 400 °C. Unlike in Figure 4.4(a), a definite trend is visible with all coated samples drastically outperforming their uncoated versions despite undergoing 40 more cycles than the samples tested at 400 °C. Interestingly, V_Mg30 and Cr_Mg26 exhibit higher total capacities than when they were cycled at 400 °C reaching $65.5 \pm 0.7 \%$ and $73 \pm 0.7 \%$ respectively. Furthermore, the capacity of Cr_Mg26 was found to even exceed the best sample at 400 °C, Mg26, despite being cycled at 50 °C lower.

Figure 4.8 provides further confirmation the total capacity all of the coated samples exceed that of their uncoated versions when cycled at 350 °C and after 14 h Cr_Mg26 continues to obtain the highest capacity at approximately $84.6 \pm 0.8 \%$.

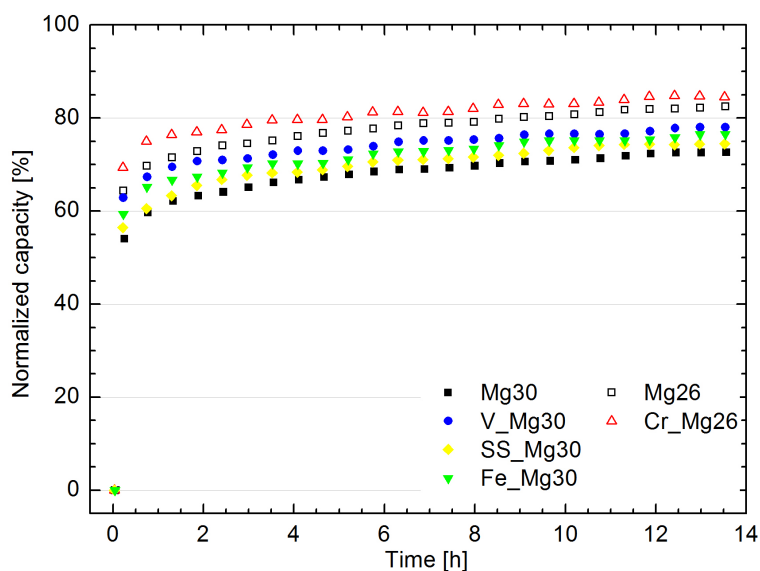


Figure 4.8: Normalized capacity versus time for each ‘activated & cycled’ sample at 350 °C during an extended final hydrogenation cycle post 90 cycles. Data was actually collected asymptotically reaching a maximum of 20 s between measurements. There is a 1% error in all of the normalized capacities measured.

Thermogravimetric analysis

The final storage capacities obtained during the extended hydrogenation post 90 cycles were validated by gravimetric measurements during heating of the samples to 550 °C in the TGA, as shown in Figure 4.9(a-f). A comparison of the results from Figure 4.8 and Figure 4.9(a-f) have been summarised in Table 4.1.

| Sample name | PCTpro capacity at 350 °C | | TGA capacity | |
|-------------|-------------------------------|----------------|-------------------------------|----------------|
| | Actual [wt.% H ₂] | Normalized [%] | Actual [wt.% H ₂] | Normalized [%] |
| Mg30 | 5.6 ± 0.1 | 72.9 ± 0.7 | 5.5 ± 0.1 | 72.2 ± 1.3 |
| V_Mg30 | 5.9 ± 0.1 | 77.9 ± 0.8 | 5.6 ± 0.1 | 73.9 ± 1.3 |
| SS_Mg30 | 5.6 ± 0.1 | 74.7 ± 0.7 | 5.4 ± 0.1 | 73.1 ± 1.3 |
| Fe_Mg30 | 5.8 ± 0.1 | 76.3 ± 0.8 | 5.8 ± 0.1 | 76.0 ± 1.3 |
| Mg26 | 6.4 ± 0.1 | 83.0 ± 0.8 | 6.3 ± 0.1 | 81.7 ± 1.3 |
| Cr_Mg26 | 6.4 ± 0.1 | 84.6 ± 0.8 | 6.2 ± 0.1 | 82.6 ± 1.3 |

Table 4.1: Table comparing the materials’ capacities measured by volumetric (PCT-pro) and gravimetric (TGA) methods.

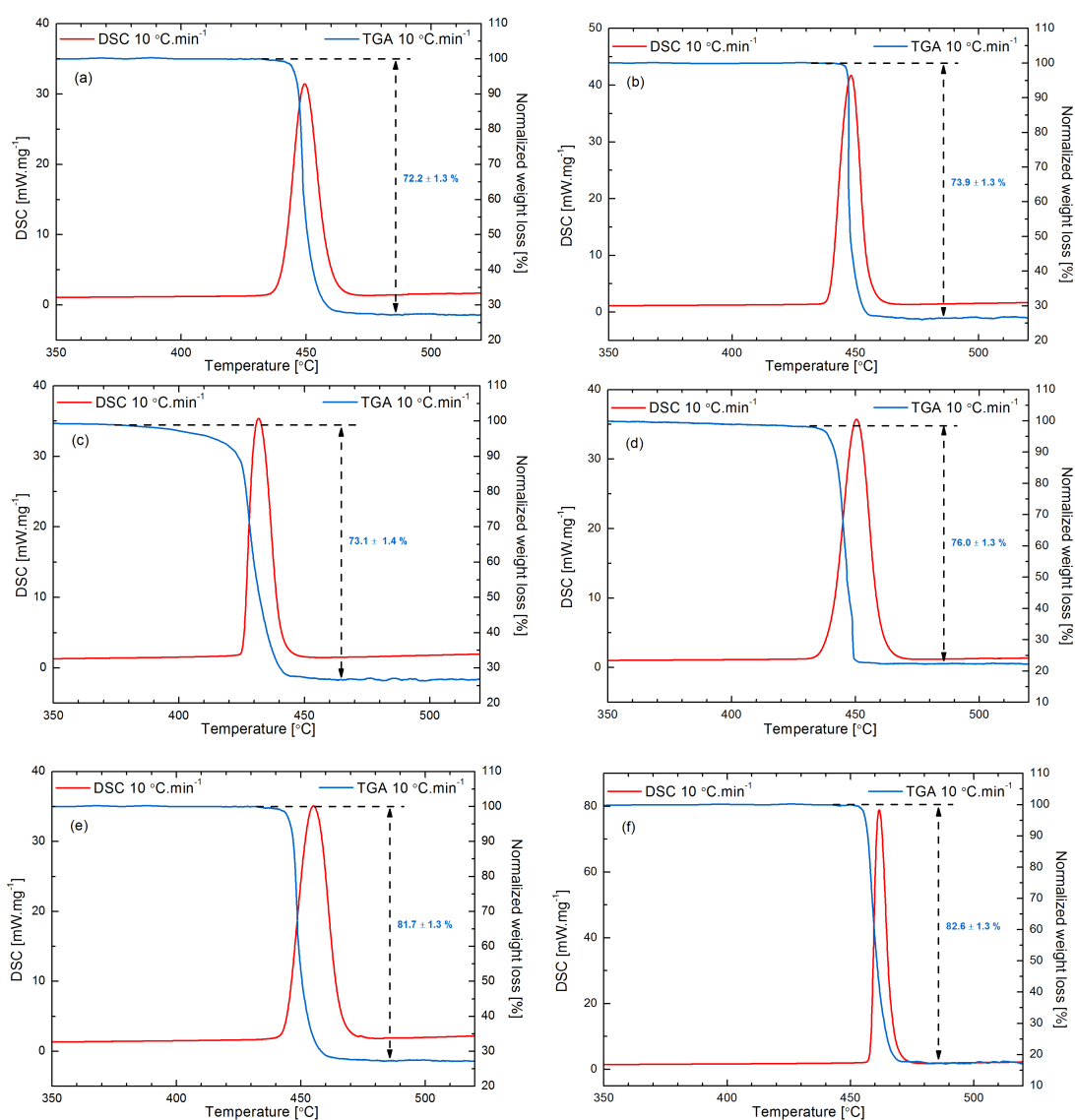


Figure 4.9: Graphs illustrating the weight loss due to dehydrogenation post extended final hydrogenation, upon heating at 10 °C.min⁻¹ for (a) Mg30, (b) V_Mg30, (c) SS_Mg30, (d) Fe_Mg30, (e) Mg26 and (f) Cr_Mg26. Overlaid are DSC traces at the same heating rates for each sample.

Differential scanning calorimetry

Kissinger plots (Figure 4.11) were constructed with the peak temperatures from the DSC endotherms of the 350 °C hydride samples post 90 cycles (Figure 4.10). The resulting activation energy of dehydrogenation for each sample is shown in Table 4.2.

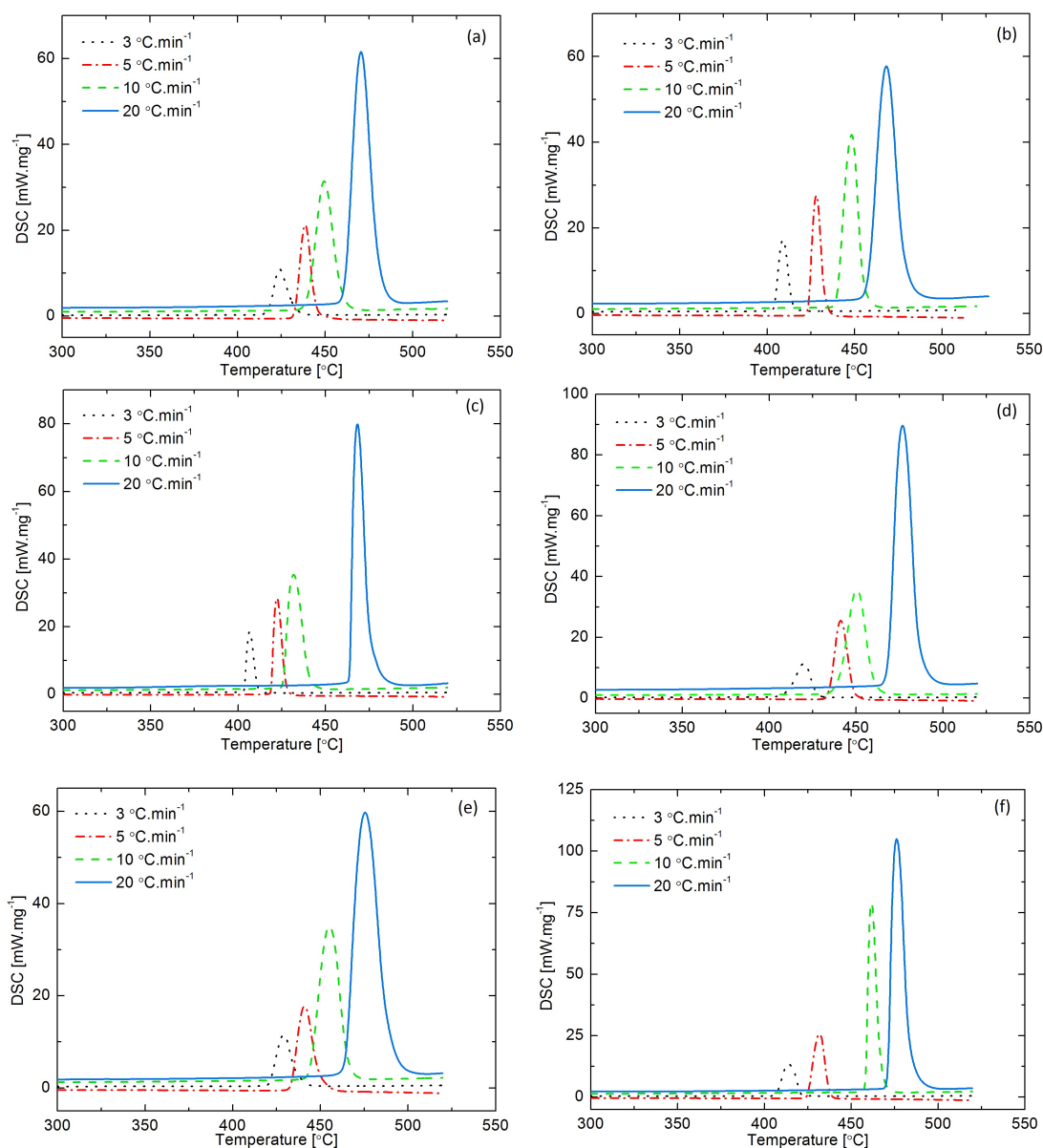


Figure 4.10: DSC endotherms produced under 1 bar of flowing Ar at a rate of 100 ml.min⁻¹, using heating rates of 3, 5, 10 and 20 °C.min⁻¹ for (a) Mg₃₀, (b) V-Mg₃₀, (c) SS-Mg₃₀, (d) Fe-Mg₃₀, (e) Mg₂₆ and (f) Cr-Mg₂₆.

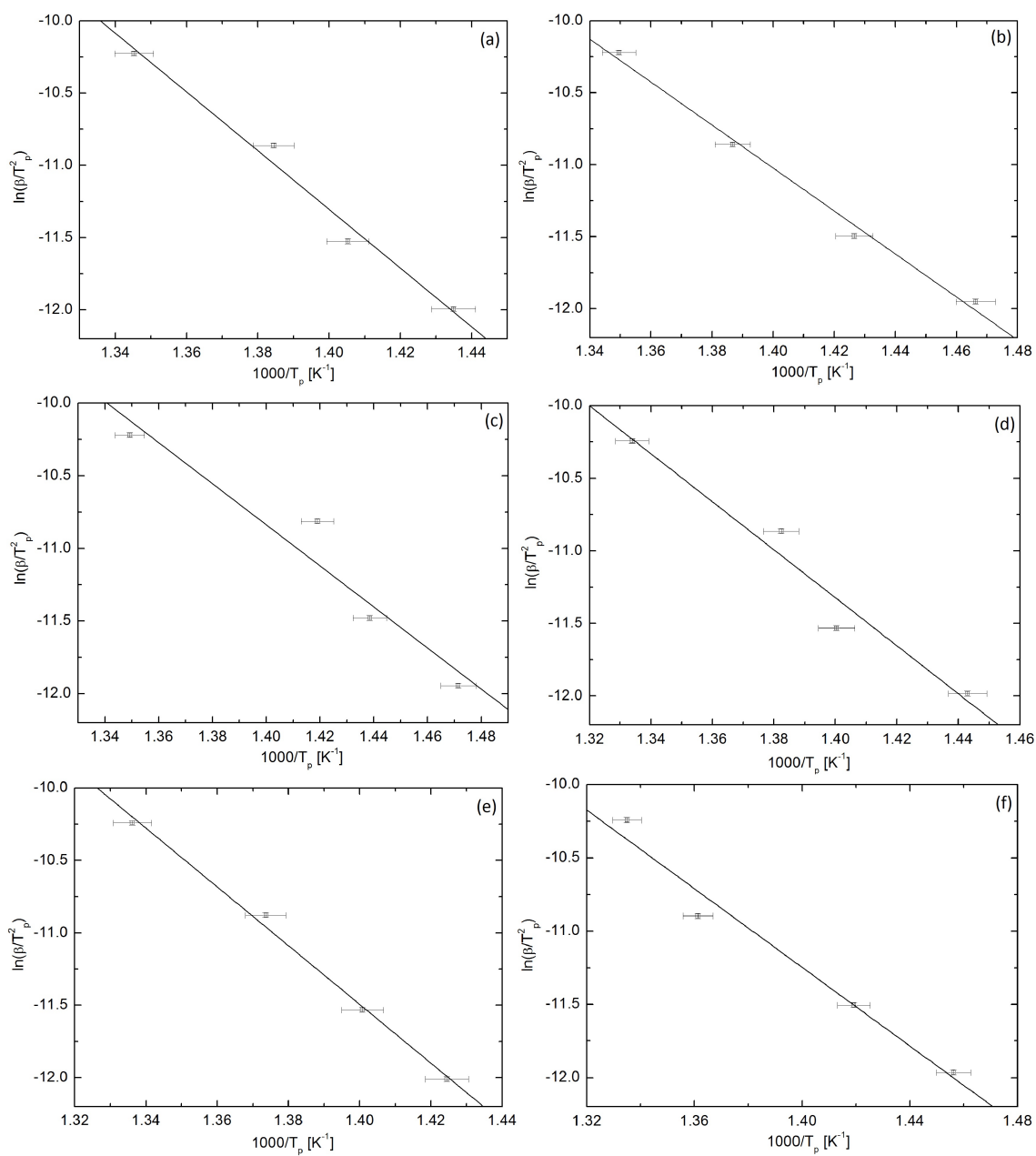


Figure 4.11: Kissinger plots produced via DSC endotherms of the samples post 90 cycles at 350 °C where (a) Mg30, (b) V_Mg30, (c) SS_Mg30, (d) Fe_Mg30, (e) Mg26 and (f) Cr_Mg26.

| Sample name | E_a [kJ.mol ⁻¹] |
|-------------|-------------------------------|
| Mg30 | 169 ± 16 |
| V_Mg30 | 124 ± 8 |
| SS_Mg30 | 118 ± 22 |
| Fe_Mg30 | 137 ± 20 |
| Mg26 | 169 ± 9 |
| Cr_Mg26 | 112 ± 13 |

Table 4.2: Table showing the activation energies of the samples' dehydrogenation reaction derived from Kissinger plots.

Thermodynamics

The hydrogenation and dehydrogenation pressure-composition-isotherms of Cr_Mg26 following 90 cycles at 350 °C is shown in Figure 4.12. Hydrogenation plateau pressures of 8.0, 13.9 and 23.5 bar were obtained at temperatures of at 350, 375 and 400 °C. For the dehydrogenation process at same temperatures the corresponding plateau pressures were 6.5, 11.5 and 19.5 bar. A van't Hoff plot was produced as shown in Figure 4.13 with the slope and intercept of the linear regression line used to determine the enthalpies and entropies for the (de)hydrogenation processes. For the hydrogenation process an enthalpy ΔH of -75.6 ± 0.9 kJ.mol⁻¹ H₂ and entropy ΔS of -138 ± 2 J.K⁻¹mol⁻¹ H₂ were calculated. For the dehydrogenation process an enthalpy ΔH of 77.0 ± 0.9 kJ.mol⁻¹ H₂ and entropy ΔS of 139 ± 2 J.K⁻¹mol⁻¹ H₂ were calculated.

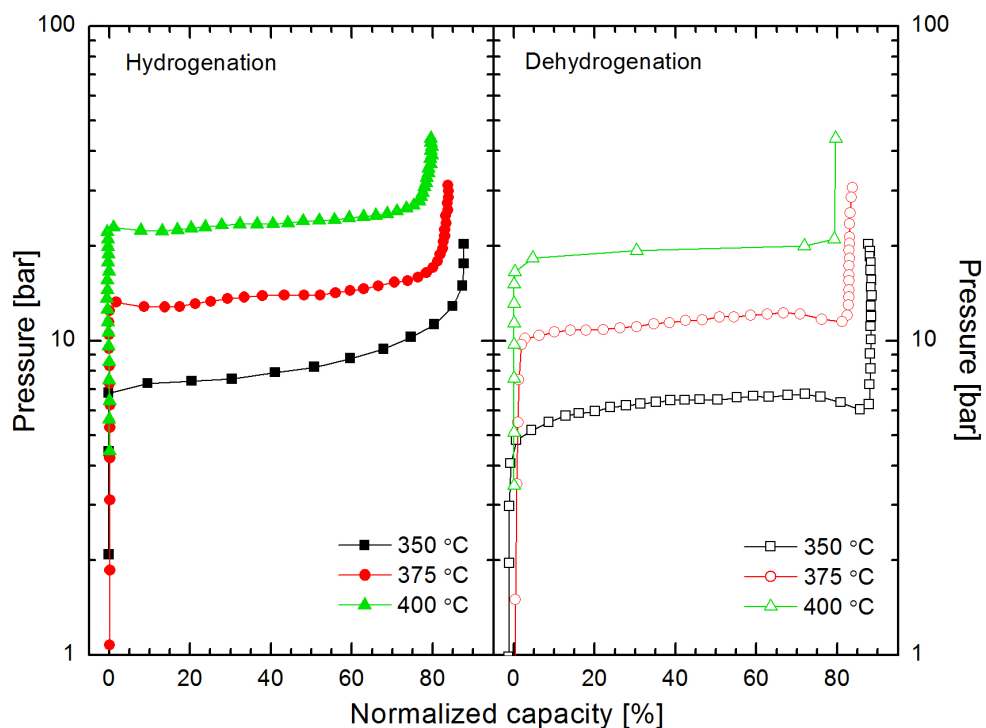


Figure 4.12: Pressure-composition hydrogenation and dehydrogenation isotherms of Cr.Mg₂₆ post 90 cycles at 350 °C in the temperature range 350-400 °C.

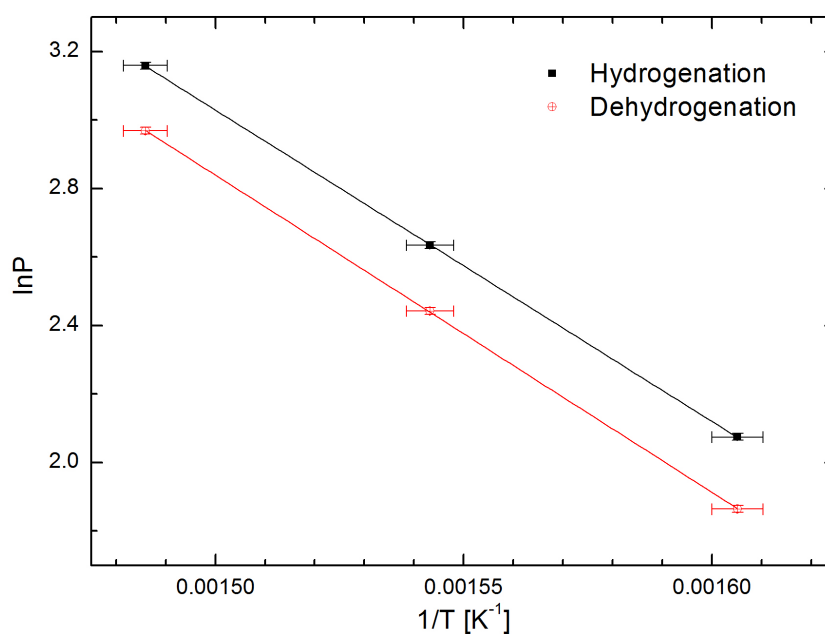


Figure 4.13: van't Hoff plot of $\ln P$ versus $1/T$ for the hydrogenation and dehydrogenation process of Cr.Mg₂₆ post 90 cycles at 350 °C.

4.2.2 Structural Analysis

Particle size analysis

The particle size distributions of the as received uncoated powders are shown in Figure 4.14. In laser diffraction a common value stated to express distribution width is the span and this is defined as $D_{0.9}-D_{0.1}/D_{0.5}$. The span of Mg26 was 1.73 and for Mg30 it was 1.97. More detailed analysis of the overall powder compositions shows Mg26 has 11% more within a range of 8 μm to 36 μm , while Mg30 has 10% more within a range of 36 μm to 120 μm , as shown by the red and black striped regions respectively. Mg26 also possessed a lower D_{90} value of 55 μm compared to 68 μm for Mg30.

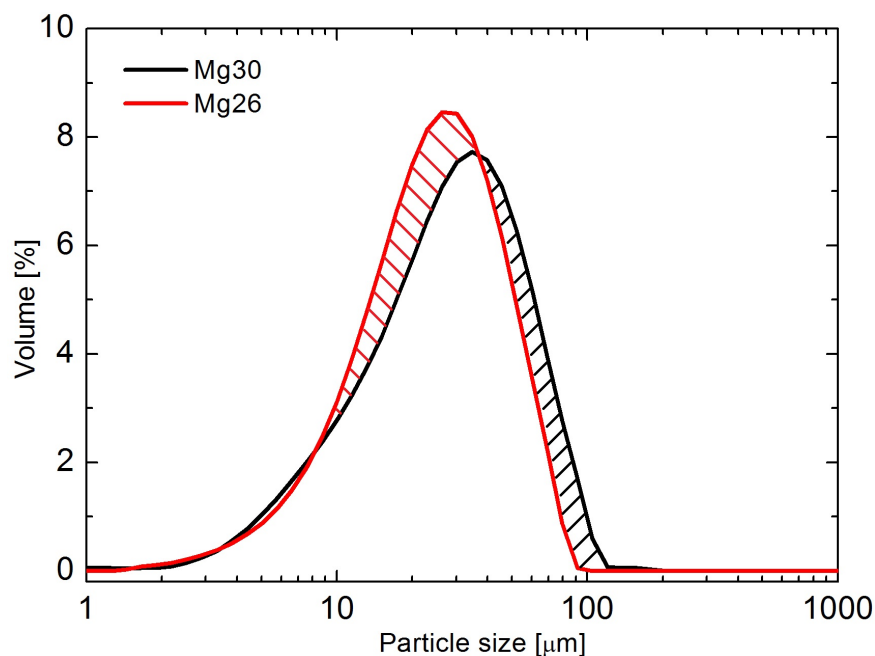


Figure 4.14: Particle size distributions of the two as received magnesium powders.

X-ray diffraction

Figure 4.15 shows the X-ray diffraction pattern of V_Mg30 in its dehydrogenated state following cycling at 400 °C. The identified peaks correspond only to Mg, with no presence of V, although there are possibly traces of MgO.

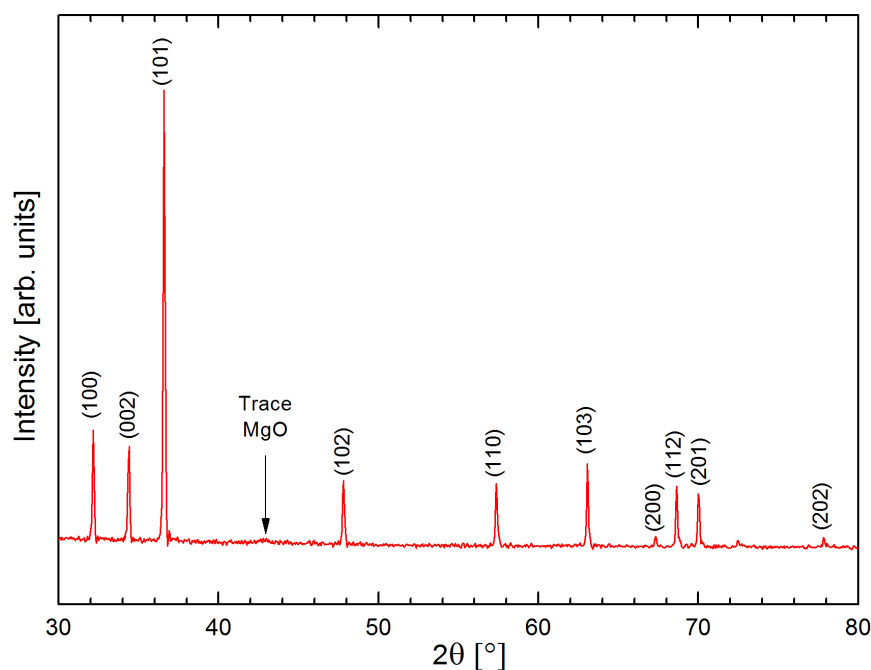


Figure 4.15: Powder X-ray diffraction pattern of V_Mg30 dehydrogenated following cycling at 400 °C. Peaks correspond only to Mg although there may be a trace presence of MgO.

Scanning electron microscopy

Images (a) and (b) in Figure 4.16 display SEM micrographs of the as received uncoated powders Mg30 and Mg26, validating the high density of spherical particulates present with sizes that agree with the particle size analysis in Figure 4.14. As expected, after cycling at 350 °C (images (c) and (d) in Figure 4.16) both powders underwent

almost identical microstructural evolution, with the original spherical particulates still discernible among the sintered clusters that have formed. The surface topology of these surrounding clusters is highly irregular compared to the smooth particulates in images (a) and (b) and is associated with the conjoining of numerous smaller particles during cycling.

Porous structures were also fabricated during the cycling of the coated samples at 350 °C, however substantial morphological differences are evident as presented by the cross-sectional images (e) to (h) in Figure 4.16. Both V_Mg30 and SS_Mg30 shown in images (e) and (f) respectively, exhibit significant microstructural changes with no noticeable retention of the starting spherical particulates and instead resemble a series of spheroid globules (ca. 5 μm) sintered together. Image (d) reveals Fe_Mg30 displays distinct similarities to the cycled uncoated powders as some starting spherical particulates remain distinguishable, although there is also more pronounced surface evolution in line with V_Mg30 and SS_Mg30. Cr_Mg26 shown in image (h) experienced the most extensive transformation with the creation of elongated particulates (ca. 10 μm) that are entwined into larger agglomerations.

Lastly, it is clear that following cycling the uncoated samples possess considerable voids (ca. 50 μm) between the sintered clusters, where as the agglomerations formed among the coated samples are more evenly distributed throughout the overall structures, with the possible exclusion of Fe_Mg30.

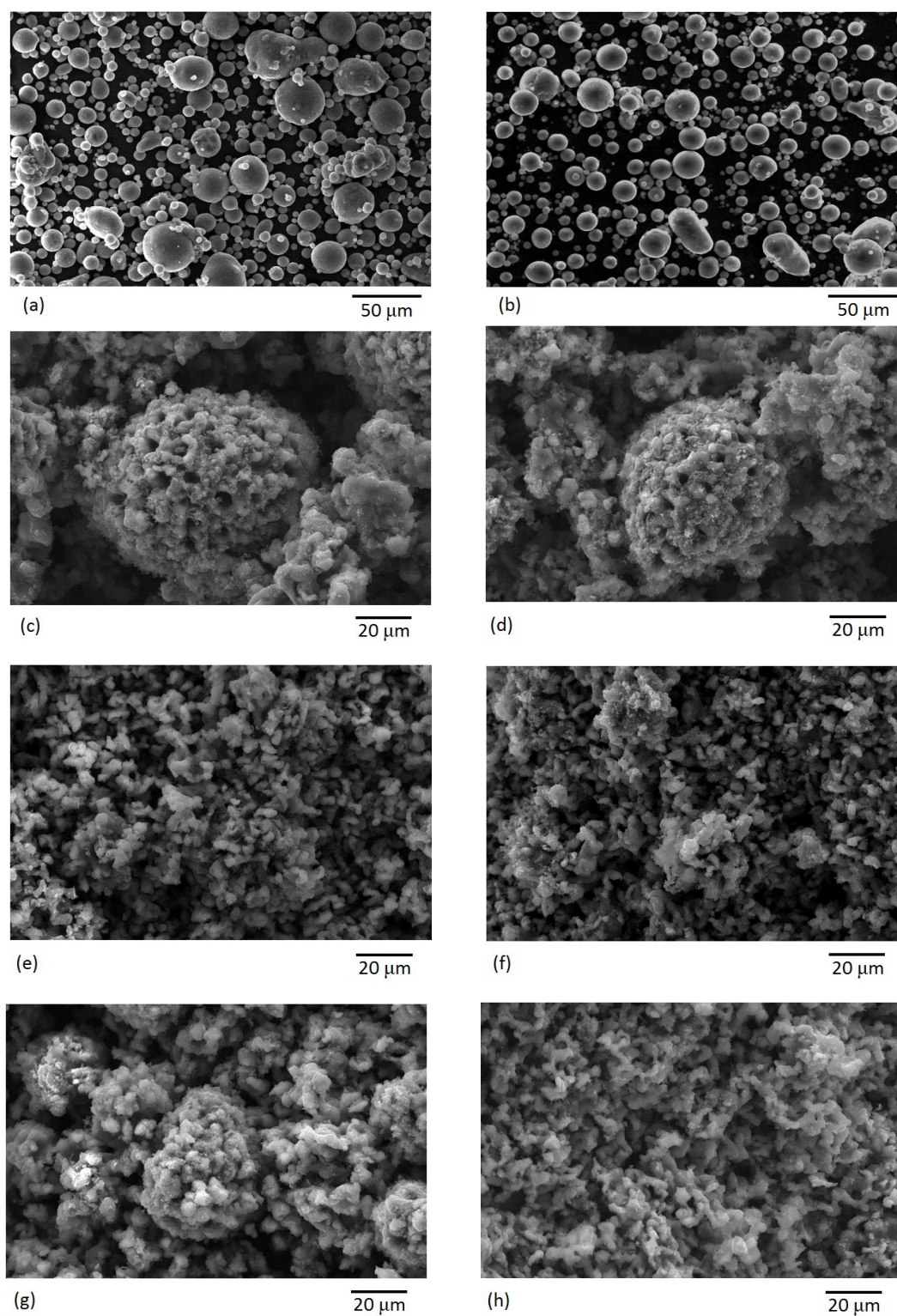


Figure 4.16: SEM images of the as received powders (a) Mg30 (AR) and (b) Mg26 (AR). Cross-sectional fracture surface SEM images at the midpoints of the porous samples produced following 90 cycles at 350 °C where (c) Mg30; (d) Mg26; (e) V_Mg30; (f) SS_Mg30; (g) Fe_Mg30 and (h) Cr_Mg26.

4.3 Discussion

Cycling at 400 °C

Besides minor improvements in the hydrogenation kinetics of the samples, it may be argued the coatings have an overall detrimental impact on the final capacity, as highlighted in Figure 4.5. These findings are in agreement with [Huhn et al. \(2005\)](#) who reported a drastic reduction in kinetics and capacity of ball milled MgH_2 with 0.5 mol% Nb_2O_5 at 300 °C when annealed for 5 h at temperatures greater than 370 °C. This suggests regardless of the processing technique, type of additive and experimental conditions utilised, if catalyst-doped magnesium is exposed to temperatures exceeding 370 °C for extended periods (>5 h) there is a significant deterioration in sorption properties, even below that of uncatalysed material.

[Huhn et al. \(2005\)](#) proposed since MgO is more stable than Nb_2O_5 , at these temperatures Mg reduces Nb_2O_5 forming MgO which impedes hydrogen transport. MgO is also more stable than the metal oxide states of the catalysts used here, although no distinct MgO peak was distinguishable in the post cycling XRD analysis of the coated samples such as V_Mg30 (Figure 4.15). This was not unexpected given the low catalyst concentrations used in these experiments and suggests poisoning of Mg causing the capacity reduction may be a smaller secondary effect. Instead the primary cause may relate to the lack of multivalency of the catalysts, brought about by this reduction action leading to the catalysts being in their metallic states. Research has indicated transition metal oxides act as better catalysts than their

metal counterparts [Barkhordarian et al. \(2003\)](#); [Croston et al. \(2010\)](#); [Oelerich et al. \(2001b\)](#), yet metal catalysts have still been reported to enhance sorption kinetics of MgH_2 [Bystrzycki et al. \(2005\)](#); [Bobet et al. \(2000b\)](#). Therefore, even if the catalysts were reduced completely to their metallic states, improved sorption properties compared to Mg26 and Mg30 would still be anticipated. However, as this was not the case, this lends support to the idea that the kinetic benefits is dependent on the multivalency of the transition metal in the oxide compound [Oelerich et al. \(2001b\)](#).

At 400 °C, the activation process can be circumvented by cycling the sample up to 5 times, which in total lasted 5 h (Figure 4.3). This was approximately equivalent to the time needed for activated & cycled samples to reach saturation during the activation stage (Figure 4.2). Therefore, this implies the expansion/contraction process that the Mg lattice underwent during successive cycling is as effective at breaking down the initial surface oxide layer, as a single extended hydrogenation in which all of the material reached the hydride state. Nevertheless, if the best performing sample (Mg26) was selected for a practical large scale storage system operating at 400 °C it may be more suitable to activate the sample prior to cycling because it would ensure respectable hydrogenation characteristics from the 1st cycle, as well as consume a smaller quantity of hydrogen.

Cycling at 350 °C

The disparity between the capacities of the uncoated powders at different temperatures, in which Mg26 betters Mg30 by 17% at 350 °C (Figure 4.4(a)) but only by 6.5% at 400 °C (Figure 4.4(b)), has been associated with variations in the particle sizes (Figure 4.14). The span of Mg30 exceeded Mg26 by 14% demonstrating that the latter had a narrower powder distribution width. In addition, Mg30 possessed 10% more powder within the range of 36-200 μm . Combining these factors may have led to the powder sample selected to represent Mg30 in the 350 °C experiment to consist of an average powder size larger than its determined D_{50} value. This would cause the diffusion distance for hydrogen into the bulk Mg to increase, thus potentially leading to the 10.5% greater capacity disparity between Mg30 and Mg26, compared to the same samples cycled at 400 °C.

The behaviour of Mg30 with successive cycling at 350 °C (Figure 4.7(a)) is validated by [Garrier et al. \(2011\)](#) who observed a similar trend when an intermediate scale tank (1.8 kg) of milled MgH_2 compacted with 5 wt.% expanded natural graphite was cycled over 100 times at 320 °C. Following a slight decline in sorption kinetics and capacity during the initial 20 cycles, the capacity then stabilised for the remaining cycles, much like Mg30. Contrastingly, [Pedersen et al. \(1984\)](#) reported a consistent drop in capacity, totalling approximately 1 wt.%, after the first 100 cycles at 390 °C. This difference has been attributed to the lower cycling temperature of Mg30 restricting the degree of excess sintering in the sample and thus also grain

recrystallisation.

The behaviour of V_Mg30 with successive cycling at 350 °C (Figure 4.7(b)) agrees with literature in that catalysts prevented the degeneration of the materials, but to significantly opposing extents. [Dehouche et al. \(2000, 2002\)](#) reported catalyst dependent rises in capacity of 0.2-0.5 wt.% and little change in the microstructure and specific surface area of the milled materials were detectable even after 2000 cycles. On the other hand, following only 90 cycles the microstructure of V_Mg30 (Figure 4.16 (e)) drastically diverges from its as received state (Figure 4.16 (a)) and is speculated to have caused the much larger increase in capacity of 20% (ca. 1.5 wt.%).

By lowering the temperature to 350 °C the advantages of catalyst coatings on atomised magnesium are clear, not only in terms of initial activation (Figure 4.6) but also the kinetic and capacity improvements with respect to uncoated samples during successive cycling up to 90 times (Figure 4.4(b)). Comparison of Mg30 and V_Mg30 at 350 °C, in Figure 4.7, highlights how the presence of a catalyst promotes faster reaction kinetics and increased capacity until approaching stabilisation by the 90th cycle. In the 1st cycle V_Mg30 demonstrates a rate of reaction of 19.87 %·min⁻¹ during the initial 30% of uptake that is indeed faster than the diffusion limited, latter section of the curve (0.21 %·min⁻¹ from 10 min onwards). By the 90th cycle the rate of reaction reached 24.15 %·min⁻¹ during the initial 50% of uptake and the transition between hydrogenation mechanisms is more pronounced, suggesting that nucleation and growth is becoming dominant for the majority of uptake. Excluding Fe_Mg30 (Figure 4.7(d)), similar results are observed for the remaining coated samples (Figure

4.7(c & f)).

As anticipated, the activation energies (Table 4.2) determined for uncoated Mg30 and Mg26 were found to lie between that of published values for as received 70 μm MgH₂ (206 kJ.mol⁻¹ (Patah et al., 2009)) and 20 μm MgH₂ (156 kJ.mol⁻¹ (Huot et al., 1999)). The addition of coating catalysts prompted reductions in activation energy and while they remain greater than similar thin film structures, such as Mg+3.3 wt.% Cr (65.7 \pm 2.5 kJ.mol⁻¹ (Fry et al., 2014)) and Mg+5.2 wt.% V (67.6 \pm 1.2 kJ.mol⁻¹ (Fry et al., 2014)), it must be noted the catalyst concentrations used in these experiments were between 20-50% less than those in the reported thin film materials. Furthermore, Amirkhiz et al. (2011) demonstrated that the reduced activation energies of catalysed as-milled Mg returns back to its initial unmilled value upon annealing treatment and successive cycling. For example, they reported the activation energy of milled Mg+10at.% Fe to increase from 92 kJ.mol⁻¹ to 119 kJ.mol⁻¹ following 75 cycles at 250 °C. This latter activation energy is consistent with the values reported for these samples which had undergone 15 more cycles at a 100 °C higher.

The evolution of the coated spherical magnesium particulates into sintered elongated structures congregated in twisting branches (Figure 4.16 (e), (f) & (h)) appears to generate new nucleation sites and maintains a good catalyst distribution throughout the material, as illustrated by the evolution of kinetics (Figure 4.4(b)) and the determined activation energies in Table 4.2. This higher density of nucleation sites means more hydrogen can avoid having to diffuse through layers of hydride to

reach new Mg. For example, at around 400 °C the diffusion coefficient of hydrogen within the hydride phase ($2.78 \times 10^{-7} \text{ cm}^2.\text{s}^{-1}$ (Cemak and Kral, 2008)) is three orders of magnitude lower compared to the unhydrided phase ($3 \times 10^{-4} \text{ cm}^2.\text{s}^{-1}$ (Renner and Grabke, 1978; Ramzan et al., 2009)), thus the reaction rate during initial stages was substantially improved. Furthermore, the lack of large voids ($<50 \mu\text{m}$) in cycled coated samples may help to prevent the hydride layer thickness exceeding 30-50 μm , a known cause for ceasing further hydrogenation Vigeholm et al. (1987) but this may not be applicable for the cycled uncoated samples with their larger voids (Figure 4.16 (c) & (d)).

The cause of the different microstructural evolution between the coated and uncoated samples during cycling at 350 °C is speculated to be an extension of a complex process in which particle sintering competes with particle reorientation (see Figure 4.17). A degree of structure in the sample can be created by restriction of particle reorientation during successive cycling under hydrogen. Given the reasonable self-diffusion coefficient of Mg atoms at 350 °C ($9.26 \times 10^{-16} \text{ m}^2 \text{ s}^{-1}$ Kalkarni et al. (2014)), this may occur through the prior formation of sintered bridges at points of contact between particles, which remain in the metallic state for longer, due to slower hydrogenation kinetics as shown. Reinforcement of the bridges occurs upon the onset of dehydrogenation when the surface of the particles transform to the metallic state, yet their cores are still hydrogenated and thus have not undergone particle contraction. Successive cycling causes the process to renew.

For the cycled coated samples at 350 °C, we postulate particle reorientation may

dominate the evolution process. Due to their faster kinetics, the formation and growth of the hydride state during hydrogenation may occur too rapidly to enable the generation of sintered bridges at contact points. In addition, sintered bridge formation was not possible at contact points where the catalysts were present given their immiscibility with magnesium at these temperatures and significantly higher melting points. Upon dehydrogenation, complete transition to the metallic state is too fast preventing sintering and instead particle contraction and reorientation ensues. In conjunction, decrepitation of the particles to $5 \mu\text{m}$ spheroid globules enables the catalysts, formerly on the outer surfaces of particles, to diffuse into freshly exposed Mg surface which is likely to have given rise to the progressive hydrogenation improvements observed with cycling. Furthermore, the specimens produced following cycling would be expected to obtain smaller voids, which was confirmed by Figure

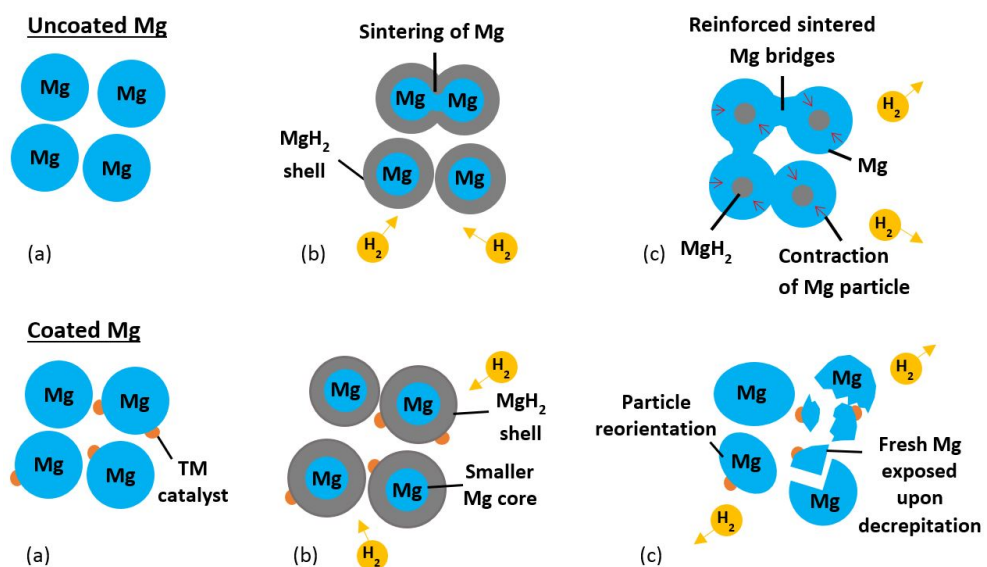


Figure 4.17: Schematic illustrating the different suggested mechanisms for the evolution of Mg and catalysed Mg samples through cycling (a) prior to cycling (b) the onset of hydrogenation and (c) during dehydrogenation.

4.16 (e), (f) & (h).

The results of Fe_Mg30 help to validate this concept acting as a midpoint between the uncoated and coated samples given its low catalyst concentration. During the activation process at 350 °C (Figure 4.6) it was clearly the slowest of the coated samples to reach saturation and it also underwent an incubation period like Mg26 and Mg30. While some benefits of the Fe catalyst were seen during cycling (Figure 4.4(b)), the evolution of kinetics follows a similar trend to Mg30 in that nucleation and growth does not become more prominent upon cycling (Figure 4.7(d)), with an activation energy and microstructural traits (Figure 4.16 (g)) that lie midway between that of the uncoated and coated samples. Therefore, for Fe_Mg30 a steady state point may have been reached between particle sintering and particle reorientation.

Thermodynamics

A range of pressure-composition-isotherms at temperatures between 350 and 400 °C were measured for Cr_Mg26 post 90 cycles at 350 °C, which were used to derive the thermodynamic properties of the material. The PCI curves presented in Figure 4.12 show flat (de)hydrogenation plateaus, characteristic of magnesium hydride. The corresponding van't Hoff plot (Figure 4.13) demonstrates a very good fit of the linear regression lines that were utilized to determine the enthalpies and entropies of the (de)hydrogenation reactions.

At $\Delta H = 77.0 \pm 0.9 \text{ kJ.mol}^{-1} \text{ H}_2$, the enthalpy of the dehydrogenation reaction is very close to a recently published value for magnesium hydride of $\Delta H = 76.3 \text{ kJ.mol}^{-1} \text{ H}_2$

(Moretto et al., 2013), as well as other literature values stated in Table 2.1. This confirms the pathway of reaction is that of $\text{Mg} + \text{H}_2 \rightleftharpoons \text{MgH}_2$, which was expected given the catalyst and magnesium are immiscible at these temperatures. Similarly, the dehydrogenation entropy $\Delta S = 139 \pm 2 \text{ J.K}^{-1}\text{mol}^{-1} \text{ H}_2$ is close to published values for magnesium hydride such as $138.3 \pm 2.9 \text{ J.K}^{-1}\text{mol}^{-1} \text{ H}_2$ (Reilly and Wiswall, 1968) and $135.1 \pm 1.9 \text{ J.K}^{-1}\text{mol}^{-1} \text{ H}_2$ (Stampfer et al., 1960). Using equation 1.6, the temperature at which Cr-Mg26 releases 1 bar of hydrogen was calculated to be $281.0 \pm 5.2 \text{ }^\circ\text{C}$, which is in strong agreement with the literature value of $279 \text{ }^\circ\text{C}$ (Stampfer et al., 1960). Combining these findings confirm the pathway reaction is that of $\text{Mg} + \text{H}_2 \rightleftharpoons \text{MgH}_2$, which was expected given the catalyst and magnesium are immiscible at these temperatures.

Chapter 5

Domestic thermal and hydrogen stores

5.1 Introduction

Intermetallic hydrides offer respectable volumetric hydrogen densities and thermodynamic properties that align well with near ambient temperature stationary storage applications. In Section 5.2.1 the effects of catalyst coatings and minor Ni substitution on the activation, kinetics and thermodynamic behaviour of TiFe-based alloys were explored. Structural analysis was performed in the form of XRD, SEM, TEM and XPS, as presented in Section 5.2.2. The properties of the TiFe-based alloys, effect of minor Ni substitution and improvement of activation ease is discussed in Section 5.3.

The hydrogen storage properties of two AB₂ alloys were explored for their potential

use in a hydrogen store. In Section 5.4.1 the kinetics and thermodynamics of the commercially available Hydralloy C5 was compared to an in house fabricated alloy of composition $\text{Ti}_{0.9}\text{Zr}_{0.2}\text{Mn}_{1.5}\text{V}_{0.2}\text{Cr}_{0.3}$. Characterisation of both alloys is detailed in Section 5.4.2. Thermodynamic properties and kinetic reaction mechanisms are discussed in Section 5.5.

5.2 TiFe Alloy Results

5.2.1 Hydrogen Storage Characteristics

Hydrogenation kinetics (activation & cycling)

Figure 5.1 showed successful room temperature activation of TiFe only occurred once it had been exposed to 40 bar H_2 at 500 °C for 95 h. Prior activation attempts by exposing the same TiFe sample to 40 bar H_2 for similar extended durations at 100, 200, 300 and 400 °C had all failed and even after successful activation post soaking at 500 °C an incubation period of 30 h was observed. On the same sample, a second exposure to 40 bar H_2 at 500 °C, but for 1 h, led to this incubation period being eradicated, although the sample still took about 75 h to approach saturation. Subsequent to a third soak at 500 °C, again for 1 h, the kinetics of the TiFe sample improved substantially approaching saturation in less than 1 h.

The activation behaviour of $\text{TiFe}_{0.96}\text{Ni}_{0.04}$ varies considerably with the presence of 1.17 wt.% Pd surface catalyst. $\text{Pd-TiFe}_{0.96}\text{Ni}_{0.04}$ began to hydrogenate at room

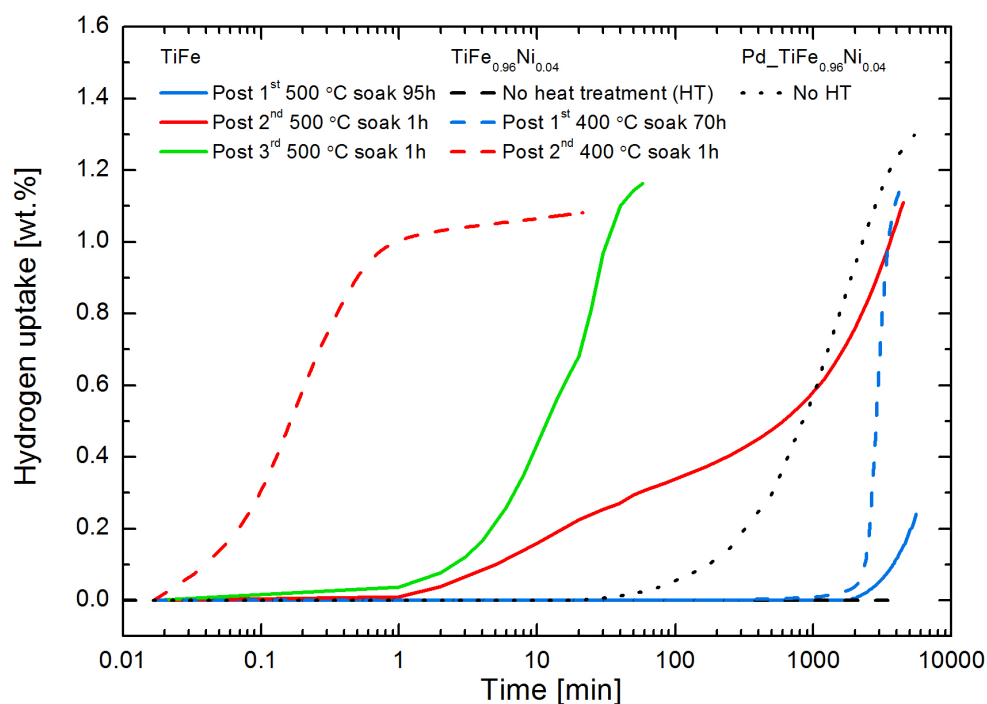


Figure 5.1: Amount of hydrogenation during the initial hydriding process versus time at room temperature for TiFe and $\text{TiFe}_{0.96}\text{Ni}_{0.04}$ with/without a Pd coating.

temperature after 20 min before reaching 1.3 wt.% after 90 h, which was taken to be complete activation. Meanwhile, under identical conditions uncoated $\text{TiFe}_{0.96}\text{Ni}_{0.04}$ failed to hydrogenate even after 72 h. Only following exposure to 40 bar H_2 at 400 °C for 70 h did $\text{TiFe}_{0.96}\text{Ni}_{0.04}$ hydrogenate, although an incubation period lasting 5 h was still observed. After a second exposure to 40 bar H_2 at 400 °C but for 1 h, the incubation period for hydrogenation at room temperature was completely eliminated.

Upon completion of the initial hydriding process, the hydrogenation kinetics of $\text{TiFe}_{0.96}\text{Ni}_{0.04}$ with and without a Pd coating are observed to possess almost identical uptake behaviour, although the final capacity of $\text{TiFe}_{0.96}\text{Ni}_{0.04}$ did exceed $\text{Pd-TiFe}_{0.96}\text{Ni}_{0.04}$ by approximately 0.05 wt.% (Figure 5.2). No significant changes

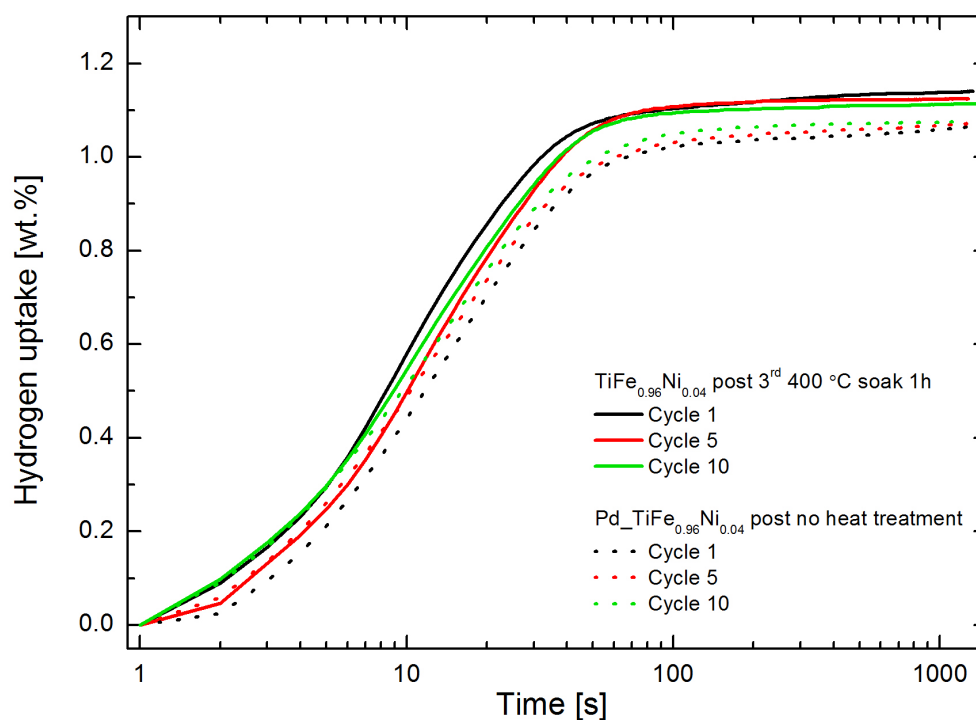


Figure 5.2: Hydrogen uptake versus time at room temperature during the 1st, 5th and 10th cycles following the initial hydriding process for $\text{TiFe}_{0.96}\text{Ni}_{0.04}$ with/without a Pd coating.

were seen in the uptake behaviour of either sample over 10 successive cycles. For both samples, over 90% of total hydrogen uptake occurred within the first 40 s, leading to hydrogenation rates between $(1.44\text{-}1.50 \text{ wt.\% H}_2\cdot\text{min}^{-1})$. The remainder of hydrogenation ensued much slower $(2.4\text{-}3.0 \times 10^{-3} \text{ wt.\% H}_2\cdot\text{min}^{-1})$, as indicated by the decrease in the gradient of the curve after approximately 60 s. To verify the kinetic similarities of both samples, a second sample of $\text{Pd}_x\text{TiFe}_{0.96}\text{Ni}_{0.04}$ was activated at a higher temperature of 200 °C. It displayed almost identical kinetics to the $\text{Pd}_x\text{TiFe}_{0.96}\text{Ni}_{0.04}$ sample activated at room temperature, for instance in the 5th cycle it obtained a final capacity of about 1.13 wt.% and reached 90% of total hydrogen uptake within 37 s.

PCI characteristics

The hydrogenation and dehydrogenation pressure-composition-isotherms of TiFe, TiFe_{0.96}Ni_{0.04} and Pd-TiFe_{0.96}Ni_{0.04} are shown in Figures 5.3, 5.4 and 5.6 respectively. The PCIs for TiFe_{0.96}Ni_{0.04} and Pd-TiFe_{0.96}Ni_{0.04} show the existence of three different regions, the α , $\alpha+\beta$ and β phase. The additional γ phase is evident in the PCI of TiFe at 45 °C between hydrogen concentrations 0.8-1.4 wt.%. The plateau pressure (P_{plat}) of these alloys were measured at 0.5 wt.%. From these PCIs, it was found that the dehydrogenation plateau pressure at 45 °C decreased from 5.6 bar to 4.5 bar as the Ni content increased from 0 to 0.04. In addition, the maximum hydrogen storage capacity was observed to be approximately 1.39 wt.% at 50 bar and 45 °C for TiFe

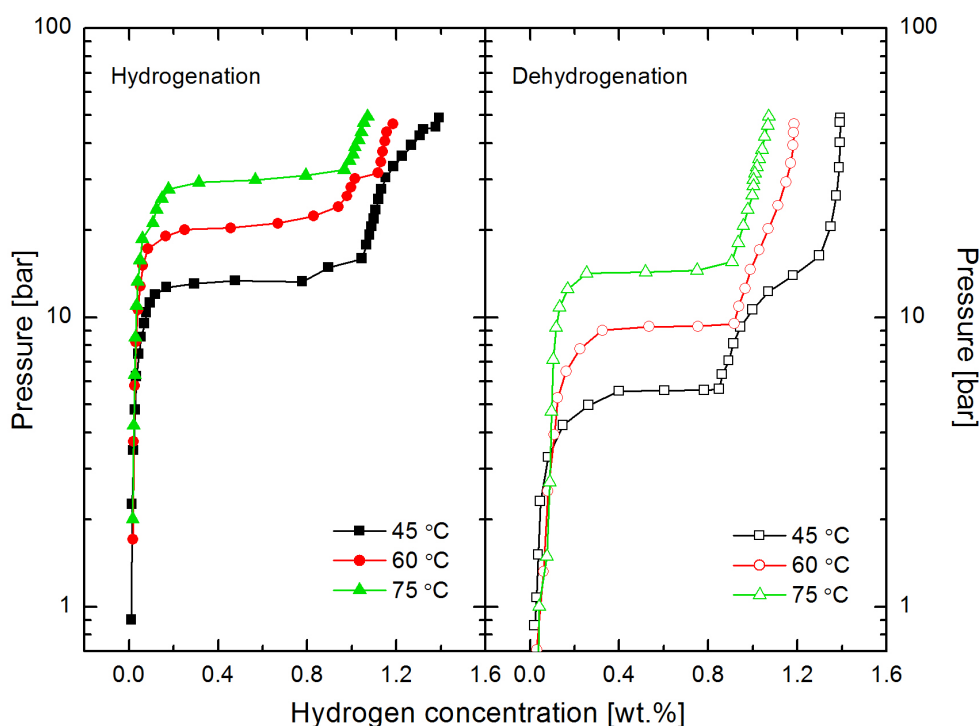


Figure 5.3: Pressure-composition hydrogenation and dehydrogenation isotherms of TiFe in the temperature range 45-75 °C.

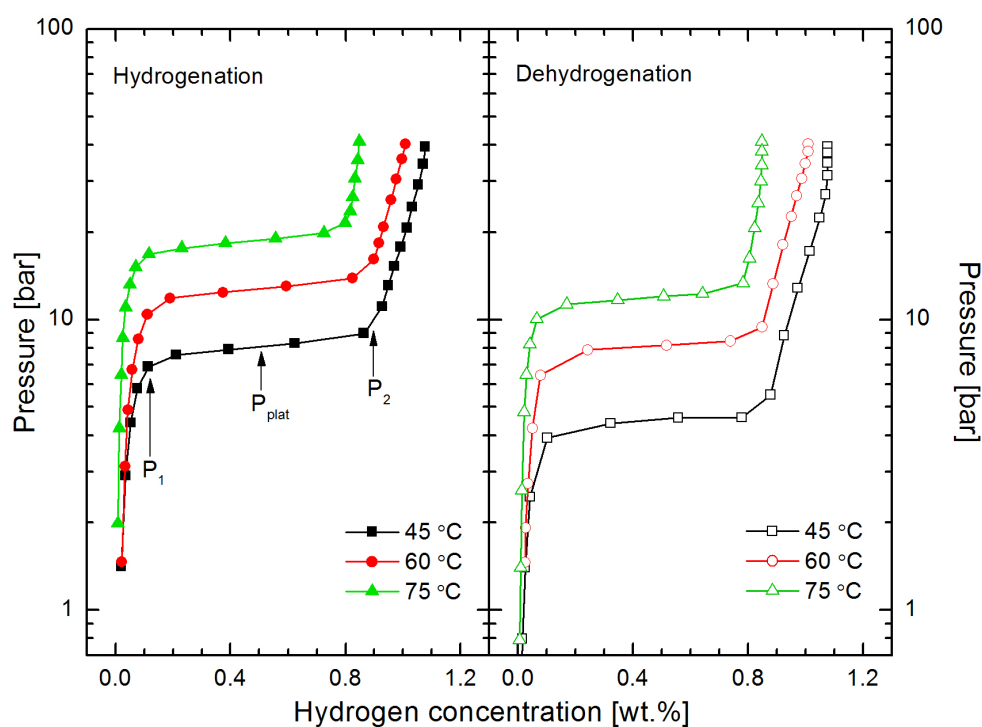


Figure 5.4: Pressure-composition hydrogenation and dehydrogenation isotherms of $\text{TiFe}_{0.96}\text{Ni}_{0.04}$ in the temperature range 45-75 °C.

but this fell to 1.08 wt.% with a Ni presence of 0.04 for Fe. $\text{TiFe}_{0.96}\text{Ni}_{0.04}$ possessed the best hydrogenation kinetics, with the alloy achieving 95% of maximum capacity approximately 15 times faster than TiFe (Table 5.1).

In an attempt to maximise the storage capacity of the fabricated TiFe, a 2 g batch of atomised powder was sealed under vacuum inside a quartz ampule and annealed at 950 °C for 120 h. Despite following the same activation procedure as for the unannealed TiFe sample (repeated exposure to 40 bar H_2 at 500 °C for 95 h) the annealed TiFe did not take up any hydrogen within 40 h at room temperature.

The values of (de)hydrogenation plateau pressure at 45 °C, 60 °C and 75 °C, activation temperature, maximum hydrogen storage capacity and charge time both

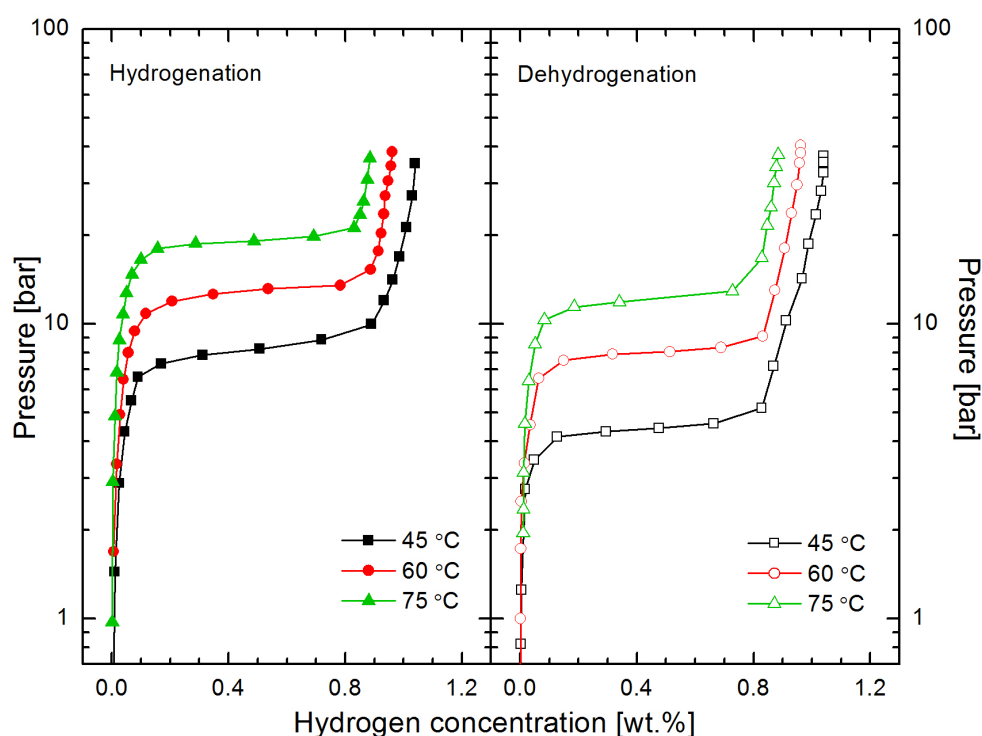


Figure 5.5: Pressure-composition hydrogenation and dehydrogenation isotherms of Pd.TiFe_{0.96}Ni_{0.04} in the temperature range 45-75 °C.

at 45 °C for the three alloys investigated are listed in Table 5.1. The hydrogenation and dehydrogenation isotherms of these alloys display the presence of hysteresis which decreased as the Ni content increased from 0 to 0.04. The plateau slope factors were calculated using $\ln(P_2/P_1)$ where P_1 is $\alpha \rightleftharpoons \alpha+\beta$ phase transition pressure and pressure P_2 is $\alpha+\beta \rightleftharpoons \beta$ phase transition pressure, as shown in Figure 5.4. The increase in Ni content from 0 to 0.04 resulted in the plateau slope factor increasing by 0.09 for hydrogenation at 45 °C, while the corresponding variation plateau slope factors for dehydrogenation were minor (Table 5.2).

The thermodynamic properties of dissolved hydrogen in these hydrides have been determined using the van't Hoff equation (see equation 1.5). The ΔH and ΔS for

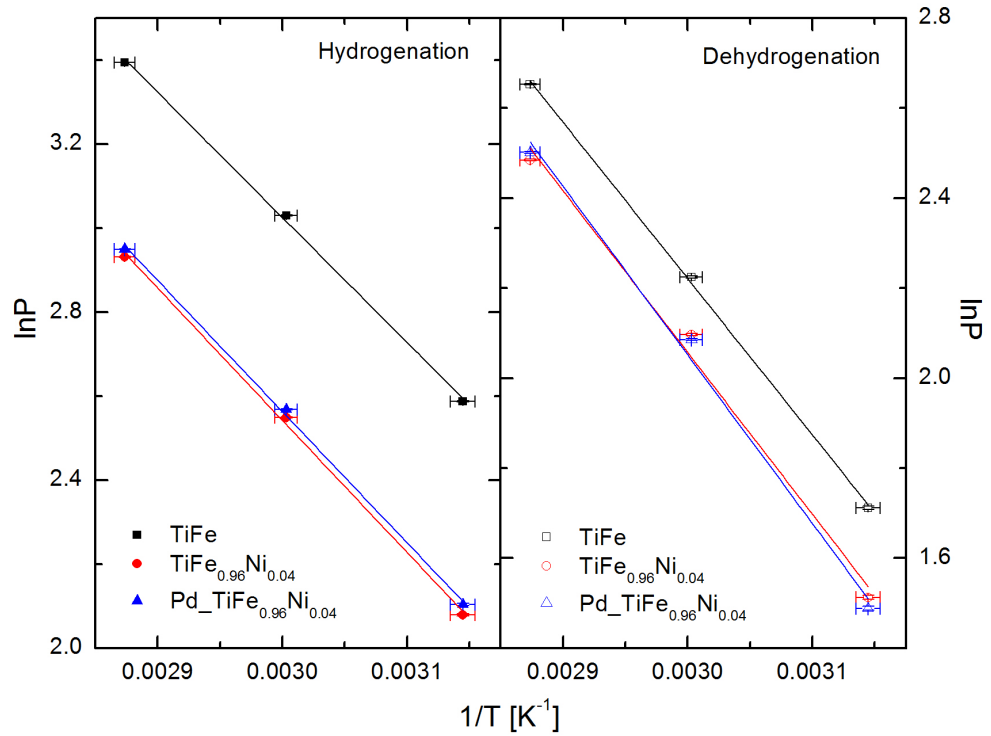


Figure 5.6: van't Hoff plot of $\ln P$ versus $1/T$ for hydrogenation and dehydrogenation process for TiFe , $\text{TiFe}_{0.96}\text{Ni}_{0.04}$ and $\text{Pd-TiFe}_{0.96}\text{Ni}_{0.04}$. Errors in $\ln P$ contained in symbols.

the de(hydrogenation) processes of these alloys have been calculated from the slope and intercept of the van't Hoff plot respectively (Figure 5.6). The values of ΔH and ΔS in $\text{TiFe}_{1-x}\text{Ni}_x$ ($x = 0$ and 0.04) are -24.8 and $-26.2 \text{ kJ}\cdot\text{mol}^{-1} \text{ H}_2$, and -99 and $-100 \text{ J}\cdot\text{K}^{-1}\text{mol}^{-1} \text{ H}_2$ for the hydrogenation process. For the dehydrogenation process ΔH is 28.9 and $29.9 \text{ kJ}\cdot\text{mol}^{-1} \text{ H}_2$ and ΔS is 105 and $107 \text{ J}\cdot\text{K}^{-1}\text{mol}^{-1} \text{ H}_2$, as detailed in Table 5.2. $\text{Pd-TiFe}_{0.96}\text{Ni}_{0.04}$ was observed to have similar hydrogen storage and thermodynamic characteristics to its uncoated counterpart ($\text{TiFe}_{0.96}\text{Ni}_{0.04}$), the only difference being the temperature required for activation, as described earlier.

| Alloy | Plateau Pressure [bar] | | | Activation temperature [°C] | Max. storage capacity [wt.%] at ~ 50 bar | Charge time: 95% [min] |
|--|--------------------------|--------------------------|---------------------------|-----------------------------|--|------------------------|
| | 45 °C | 60 °C | 75 °C | | | |
| TiFe | 13.3 5.5 ^d | 20.7 9.3 ^d | 29.8 14.2 ^d | 500 | 1.39 | 13 |
| TiFe _{0.96} Ni _{0.04} | 8.0 4.5 ^d | 12.8 8.1 ^d | 18.8 12.0 ^d | 400 | 1.08 | 0.83 |
| Pd-TiFe _{0.96} Ni _{0.04} | 8.2 4.4 ^d | 13.1 8.0 ^d | 19.1 12.2 ^d | 30 | 1.04 | 1 |

d - dehydrogenation plateau pressure

Table 5.1: The values of plateau pressure at 45 °C, 60 °C and 75 °C for (de)hydrogenation, activation temperature, maximum storage capacity and charge time both at 45 °C for TiFe, TiFe_{0.96}Ni_{0.04} and Pd-TiFe_{0.96}Ni_{0.04}.

| Alloy | Plateau slope factor $\ln(P_2/P_1)$ | | Hysteresis $\ln(P_a/P_d)$ at 45 °C | ΔH [kJ.mol ⁻¹ H ₂] | | ΔS [J.K ⁻¹ mol ⁻¹ H ₂] | |
|--|--|-------|--|---|------------|--|---------|
| | Hyd | Dehyd | | Hyd | Dehyd | Hyd | Dehyd |
| | | | | | | | |
| TiFe | 0.34 | 0.34 | 0.86 | -24.8 ± 0.7 | 28.9 ± 0.7 | -99 ± 2 | 105 ± 2 |
| TiFe _{0.96} Ni _{0.04} | 0.43 | 0.32 | 0.58 | -26.2 ± 0.9 | 29.9 ± 0.9 | -100 ± 3 | 107 ± 5 |
| Pd-TiFe _{0.96} Ni _{0.04} | 0.44 | 0.32 | 0.62 | -26.0 ± 0.8 | 31.1 ± 0.9 | -99 ± 2 | 110 ± 7 |

P_1 is $\alpha \rightleftharpoons \alpha+\beta$ phase transition pressure and pressure P_2 is $\alpha+\beta \rightleftharpoons \beta$ phase transition pressure, respectively Figure 5.4.

Table 5.2: The values of plateau slope factor and hysteresis at 45 °C, molar enthalpy (ΔH) and molar entropy (ΔS) for the (de)hydrogenation processes obtained from PCI measurements for TiFe, TiFe_{0.96}Ni_{0.04} and Pd-TiFe_{0.96}Ni_{0.04}.

5.2.2 Structural Analysis

X-ray diffraction

X-ray diffraction patterns of $\text{TiFe}_{1-x}\text{Ni}_x$ ($x = 0, 0.04$ and 0.08) reveal the single phase formation of these alloys (Figure 5.7), which crystallizes in the simple B2 cubic structure with the space group of Pm3m. The X-ray diffraction patterns show the diffraction peaks shift towards a lower angle as the Ni content x increases from 0 to 0.08. The lattice parameters of these alloys were calculated from the X-ray diffraction peak positions. The lattice parameter (a) for TiFe was determined to be $2.9759(2) \text{ \AA}$ and found to increase to $2.981(1) \text{ \AA}$ with increasing Ni content up to $x = 0.08$. The unit cell volume, calculated from the lattice parameters, for TiFe was found to be $26.355(9) \text{ \AA}^3$, and increases linearly to $26.49(2) \text{ \AA}^3$ with the amount of Ni at the B site (Figure 5.8).

| Alloy | Lattice parameter (a) [\AA] | Unit cell volume (V) [\AA^3] | Composition (EDX) |
|--------------------------------------|--|---|---|
| TiFe | 2.9759(2) | 26.355(9) | $\text{Ti}_{1.04}\text{Fe}_{0.96}$ |
| $\text{TiFe}_{0.96}\text{Ni}_{0.04}$ | 2.979(1) | 26.44(2) | $\text{TiFe}_{0.95}\text{Ni}_{0.04}\text{C}_{0.01}$ |
| $\text{TiFe}_{0.92}\text{Ni}_{0.08}$ | 2.981(1) | 26.49(2) | $\text{Ti}_{1.02}\text{Fe}_{0.89}\text{Ni}_{0.08}\text{C}_{0.01}$ |

Table 5.3: The unit cell parameter, unit cell volume and elemental composition of TiFe, $\text{TiFe}_{0.96}\text{Ni}_{0.04}$ and $\text{TiFe}_{0.92}\text{Ni}_{0.08}$.

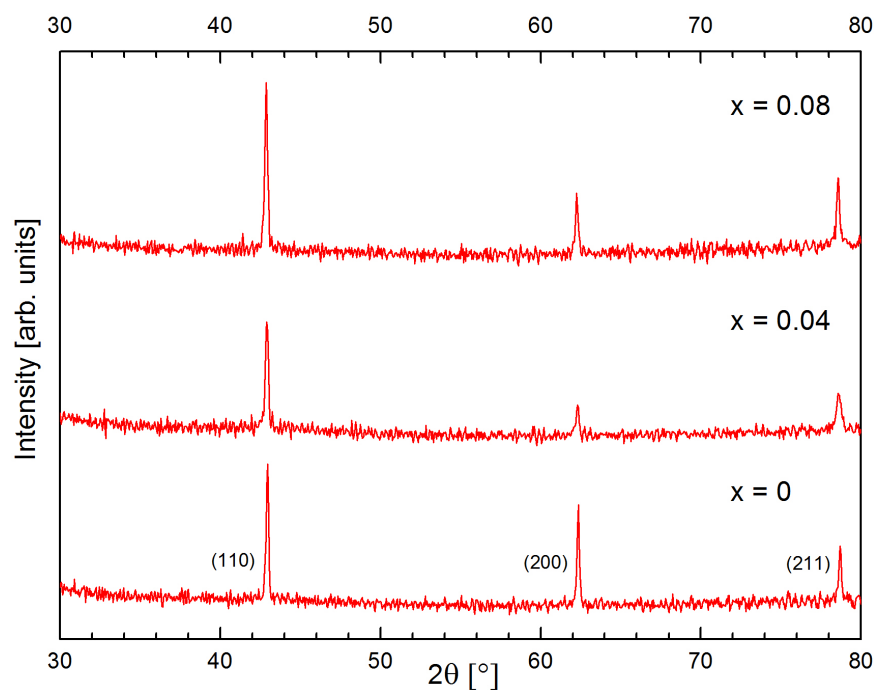


Figure 5.7: Powder X-ray diffraction patterns for TiFe_{1-x}Ni_x (x = 0, 0.04 and 0.08) alloys using Cu K_α radiation ($\lambda = 1.5418 \text{ \AA}$).

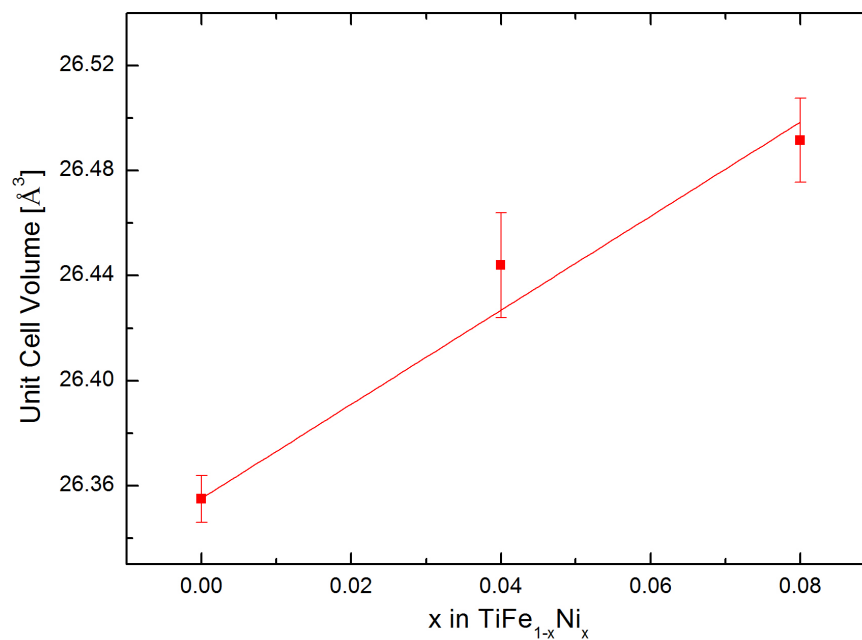


Figure 5.8: Variation of unit cell volume with the amount of x in TiFe_{1-x}Ni_x (x = 0, 0.04 and 0.08) alloys.

Scanning electron microscopy

As anticipated, atomised TiFe possessed consistently spherical and smooth surfaced particles, although there was a small addition of irregular flaky particulates, as seen in Figure 5.9(a & b). This is a common feature among all of the as prepared samples (Figure 5.10(a) & 5.11(b)). Post cycling, no change in the overall microstructural evolution could be detected (Figure 5.9(d)) but micro cracks did appear along the particle surface as evident in Figure 5.9(e). Back scattered cross sectional analysis verified no internal change in the microstructure occurred during activation or successive cycling with the powder maintaining a TiFe single phase. In addition, the majority of micro cracks were found to penetrate approximately 20 μm in to the particulate bulk, however several longer micro cracks (ca. 60 μm) were also visible.

The surfaces of the as prepared and cycled $\text{TiFe}_{0.96}\text{Ni}_{0.04}$ were much like TiFe in that a number of micro cracks were created due to activation and cycling (Figure 5.10(e)). A noticeable difference in the internal microstructure compared to TiFe was the presence of Ti rich spots, as highlighted by the arrows in Figure 5.10(c). These Ti rich regions remained a feature following activation and cycling (Figure 5.10(f)).

The arrows in Figure 5.11(c) indicate the presence of Pd sputtered on to the surface of $\text{Pd-TiFe}_{0.96}\text{Ni}_{0.04}$. The Pd appeared to be reasonably well distributed across the alloy surface, with particles in clusters (<1 μm diameter) and a radial separation distance typically of 10-20 μm . Due to Pd being present in clusters as opposed to complete encompassing layers on $\text{TiFe}_{0.96}\text{Ni}_{0.04}$, the concentration

throughout the sample was determined by averaging the Pd content measured during area scans (ca. $600\ \mu\text{m} \times 500\ \mu\text{m}$) across 10 sites, leading to a value of 1.17 wt.%. Post cycling, micro cracks are again visible along the particle surface (Figure 5.11(f)), as well as the maintained presence of Pd spots (Figure 5.11(g)). The cross-sectional images (Figure 5.11(d) & (h)) revealed the Ti rich spots also observed in that of the uncoated $\text{TiFe}_{0.96}\text{Ni}_{0.04}$.

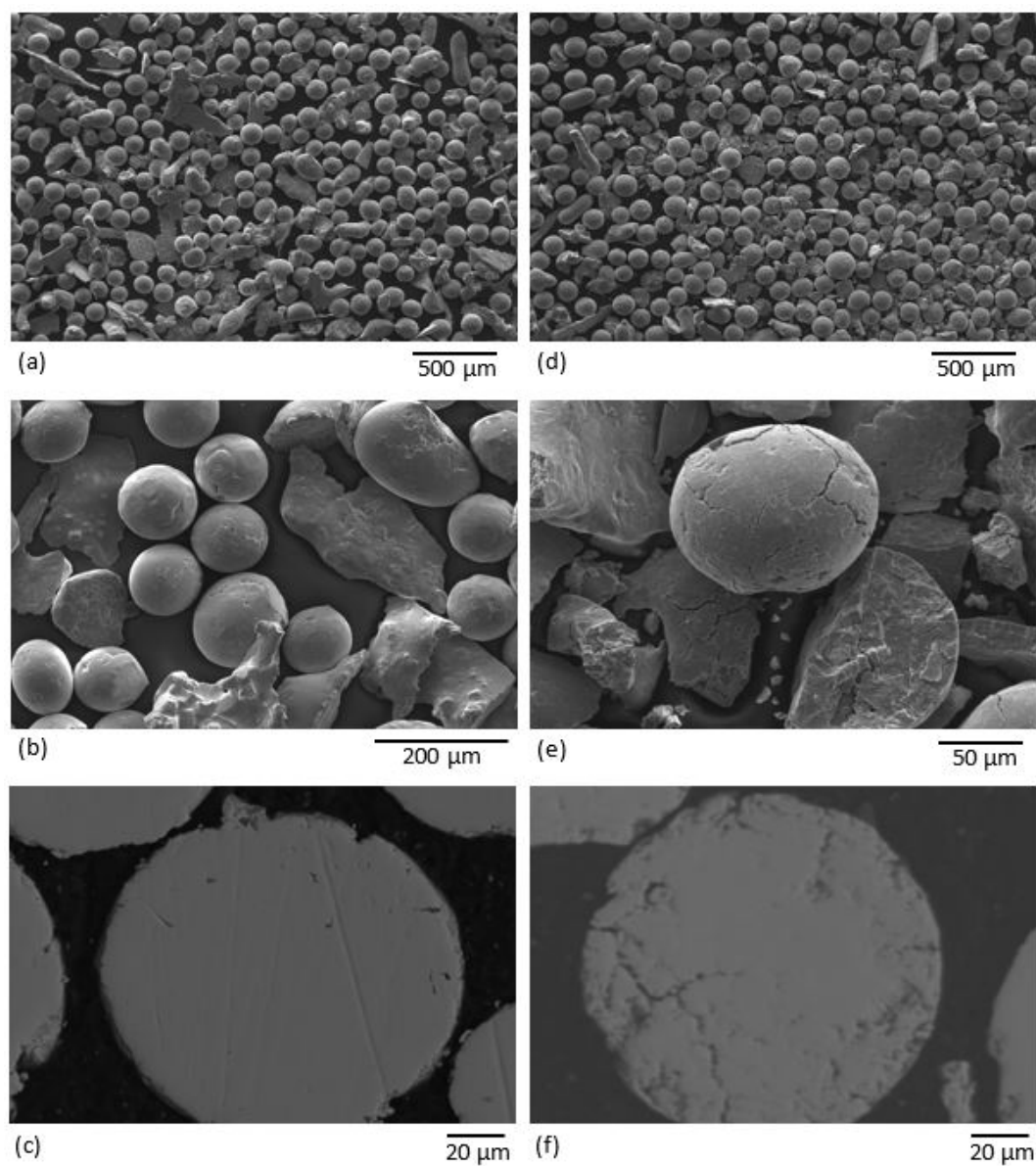


Figure 5.9: Scanning electron images of TiFe as prepared (a & b) and following cycling (d & e). Back scattered cross-sectional images of TiFe as prepared and following cycling are shown in (c) and (f) respectively.

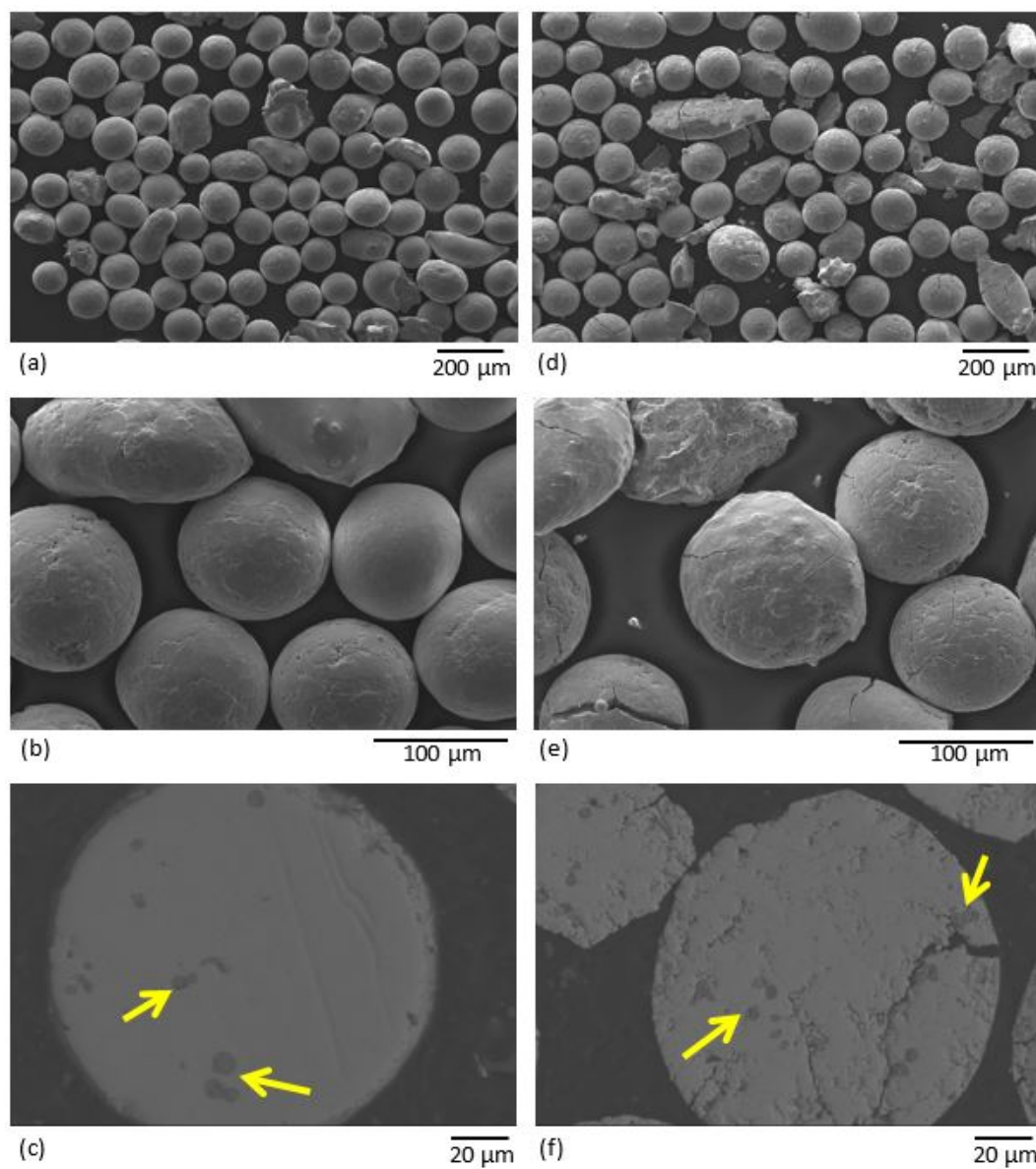


Figure 5.10: Scanning electron images of $\text{TiFe}_{0.96}\text{Ni}_{0.04}$ as prepared (a & b) and following cycling (d & e). Back scattered cross-sectional images of $\text{TiFe}_{0.96}\text{Ni}_{0.04}$ as prepared and following cycling are shown in (c) and (f) respectively.

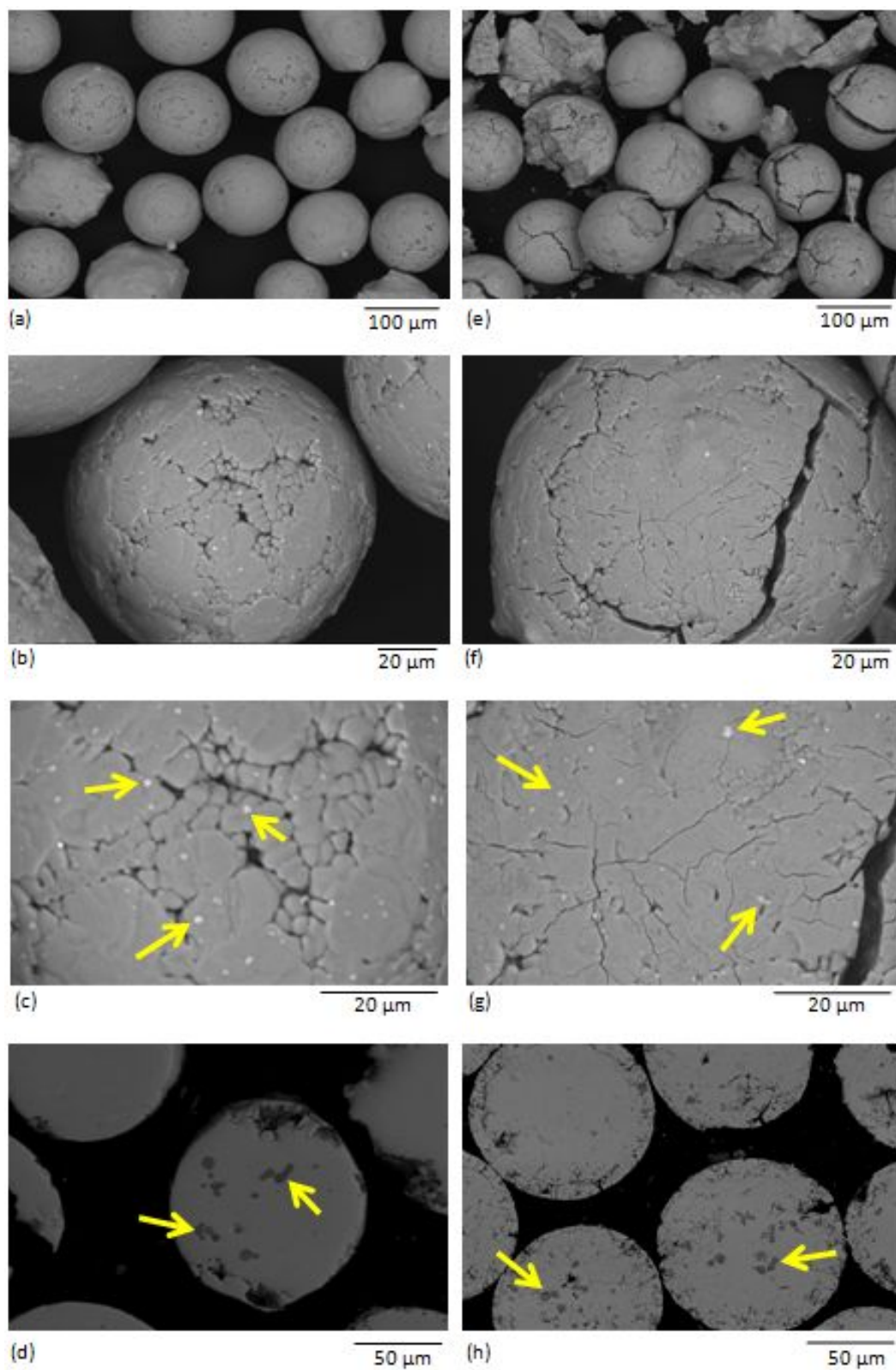


Figure 5.11: Back scattered images of Pd-TiFe_{0.96}Ni_{0.04} as prepared (a, b & c) and following cycling (e, f & g). Back scattered cross-sectional images of Pd-TiFe_{0.96}Ni_{0.04} as prepared and following cycling are shown in (d) and (h) respectively.

Transmission electron microscopy

The ‘glancing angle’ approach (see Section 3.3.3) utilised during TEM analysis of Pd-TiFe_{0.96}Ni_{0.04} enabled the detection of the catalyst thickness and distribution on the surface of the TiFe_{0.96}Ni_{0.04} powder. As seen in Figure 5.12(a), a translucent layer ranging between 20-30 nm in thickness is visible on the surface of the alloy (black region). This layer was confirmed to be a combination of Pd and PdO via determination of the d-spacing values (Table 5.4) obtained from the SAED pattern shown in Figure 5.12(b). Figure 5.12(c) illustrates the Pd coating present on a different Pd-TiFe_{0.96}Ni_{0.04} particle. In contrast to Figure 5.12(a), this Pd layer was only ca. 10 nm thick and regions of the alloy appear free of Pd, thus leaving these surfaces exposed to atmosphere.

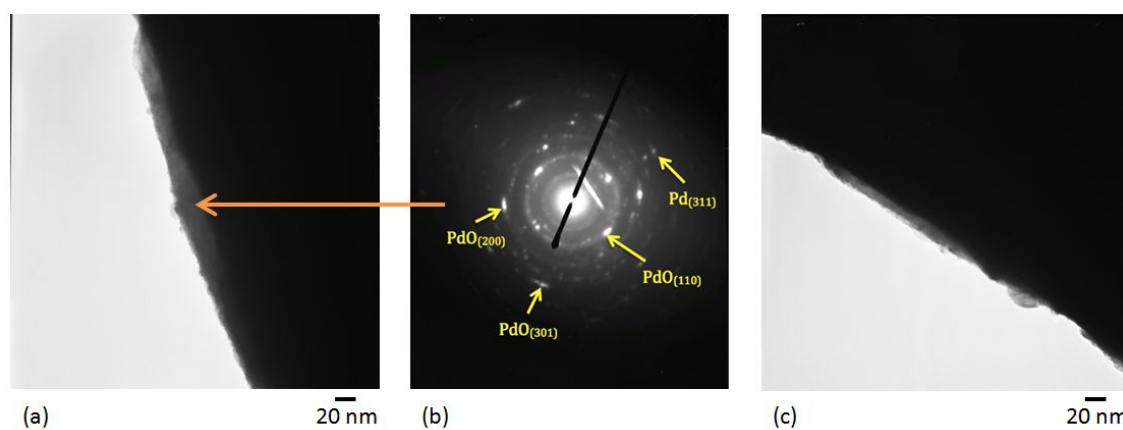


Figure 5.12: TEM images (a) and (c) reveal the Pd catalyst present on the surface of Pd-TiFe_{0.96}Ni_{0.04} on two different particles using a ‘glancing angle’ approach. Image (b) is a SAED pattern taken from the coating seen in image (a) to verify its composition.

| Miller Index | Reference d-spacing [\AA] | Calculated d-spacing [\AA] |
|--------------|--------------------------------------|---------------------------------------|
| PdO (110) | 2.152 | 2.2052 |
| PdO (200) | 1.5215 | 1.5186 |
| Pd (311) | 1.1702 | 1.1627 |
| PdO (301) | 0.9965 | 0.9892 |

Table 5.4: Comparison of the d-spacing values determined from the SAED pattern shown in Figure 5.12(b).

X-ray photoelectron spectroscopy

For as prepared TiFe (Figure 5.13), the Ti and Fe surface contributions were alike at 9.4 at.% and 9.7 at.% respectively. Fitting of the high resolution scans for each element (examples shown in Figure 5.17) led to identification of the contributions from the metallic and oxide states, of which the reference binding energy peak positions were given in Table 3.3. From the Ti 2p high resolution scan, TiO₂ was seen to dominate contributing to ca. 84% of the total and in the Fe 2p high resolution scan no metallic Fe was detected.

Following activation and cycling of TiFe (Figure 5.14), the surface contribution of Ti more than doubled to 22 at.%, meanwhile surface Fe decreased by about 40%. Examining the components of the Ti high resolution scan revealed the TiO₂ contribution was largely unaffected at ca. 82% and in the Fe 2p high resolution scan no metallic Fe was detected again.

For as prepared Pd-TiFe_{0.96}Ni_{0.04} (Figure 5.15), again the initial Ti and Fe surface contributions were similar at 2.7 at.% and 2.3 at.% respectively and the Pd contribution was found to be 20.3 at.%. As anticipated, the ratio of metallic to oxide

state contributions of the Ti and Fe matched the as prepared TiFe. Peak fitting of Pd 3d (see Figure 5.17) revealed the ratio of components Pd:PdO was 54:46.

Following activation and cycling of Pd-TiFe_{0.96}Ni_{0.04} (Figure 5.16), both Ti and Fe surface concentrations were observed to increase but to significantly differing proportions, resulting in the Ti:Fe ratio altering from 1:0.85 to 1:2.36. From the Ti 2p high resolution scan, the TiO₂ contribution was seen to increase by 8% following activation and cycling, while again no metallic Fe was detected in the high resolution scan of Fe 2p. The overall presence of surface Pd was found to reduce by ca. 60% post activation and cycling, and through component fitting of the high resolution Pd 3d scan it was indicated that only metallic Pd was present and PdO was no longer measurable.

Investigations into other potential magnetron sputtered catalysts on TiFe were also undertaken. To assist the decision of what catalysts to explore, the XPS spectra of an AB₂ alloy (Ti_{0.6}Zr_{0.4}MnCr), shown in Figure 5.18, was analysed to better understand the surface behaviour, seeing as the alloy readily absorbed hydrogen at room temperature. Table 5.9 revealed the highly oxidised as prepared surface was dominated by Mn at 17.6 at.% and this was at least double that of any other metal present in the alloy.

For this reason, four TiFe samples with various concentrations of Mn applied to the surface ranging from 0.96 to 3.56 wt.% were tested for room temperature activation. Unfortunately, even the highest Mn catalyst concentration of 3.56 wt.% failed to activate TiFe and this was also in spite of exposing the sample to 40 bar H₂

at 350 °C for 20 h prior to attempting initial hydrogenation at room temperature.

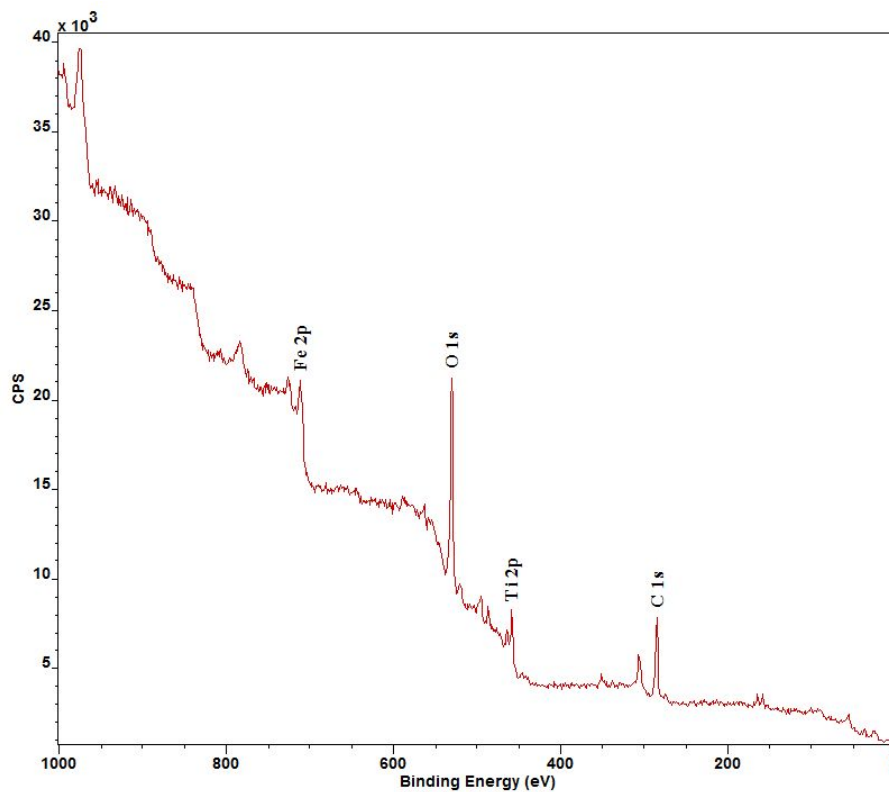


Figure 5.13: XPS wide spectrum scan of TiFe as prepared.

| Element | Component | FWHM [eV] | Area [%] | Component relative concentration [at.%] | Element relative concentration [at.%] |
|---------|---------------------------------------|-----------|----------|---|---------------------------------------|
| O 1s | O 1s | 3.41 | 100 | 80.9 | 80.9 |
| | 2p TiO ₂ 3/2 | 2.26 | 66 | 5.3 | |
| Ti 2p | 2p TiO ₂ 1/2 | 3.06 | 33 | 2.6 | 9.4 |
| | 2p Ti 3/2 | 2.52 | 66 | 1.0 | |
| | 2p Ti 1/2 | 1.98 | 33 | 0.5 | |
| Fe 2p | 2p Fe ₂ O ₃ 3/2 | 4.56 | 66 | 6.4 | 9.7 |
| | 2p Fe ₂ O ₃ 1/2 | 6.49 | 33 | 3.3 | |

Table 5.5: Summary of FWHM, areas and relative component and elemental concentrations measured from high resolution scans of TiFe as prepared.

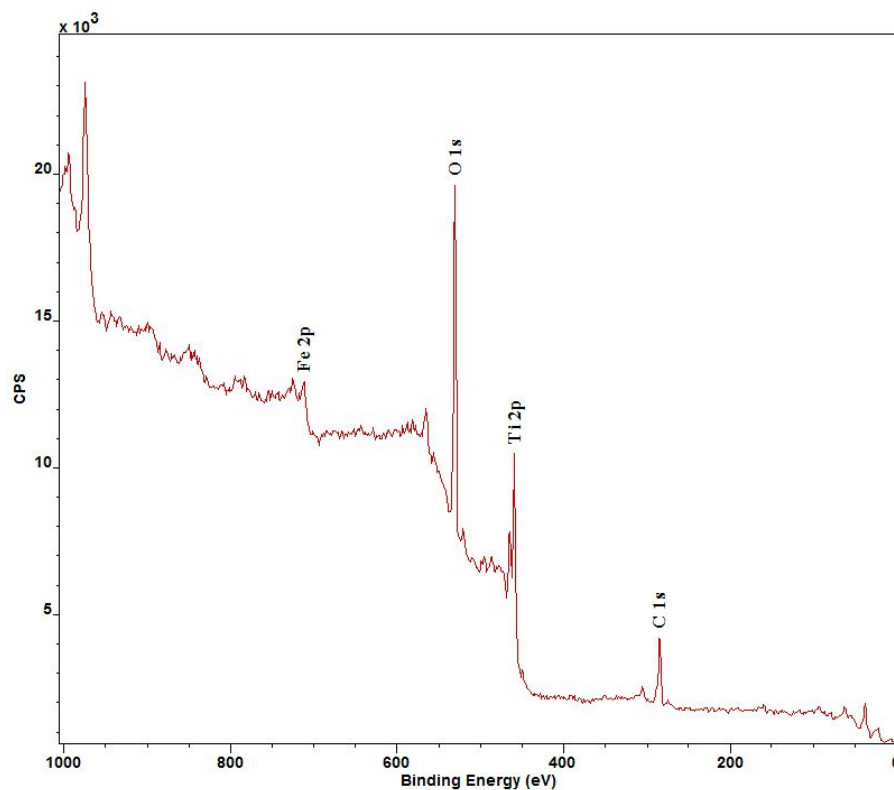
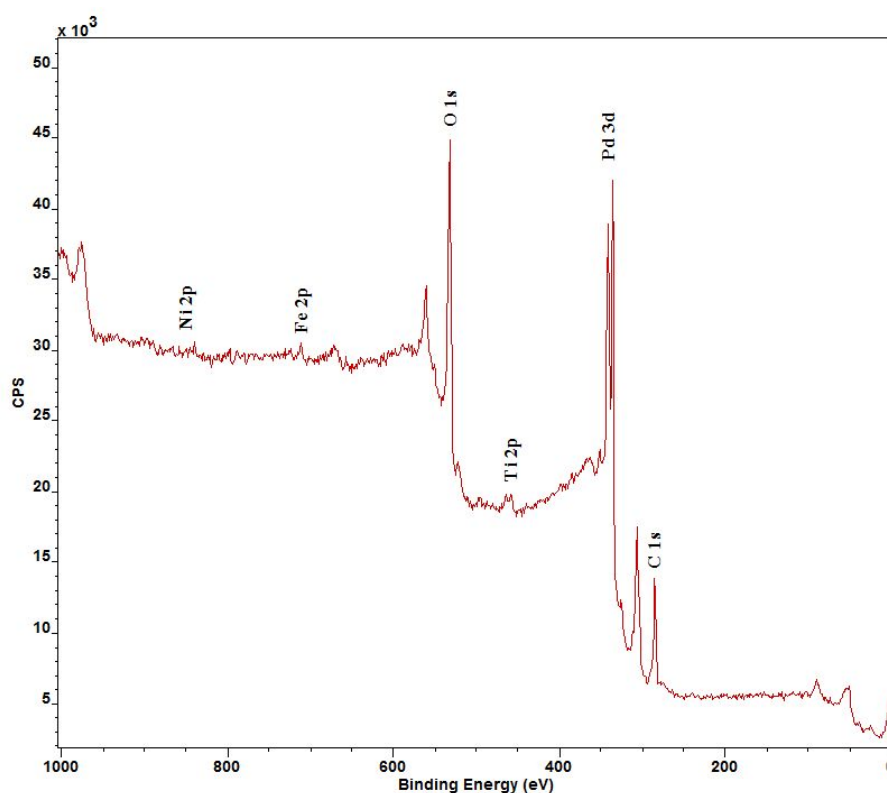


Figure 5.14: XPS wide spectrum scan of TiFe following activation and cycling under hydrogen.

| Element | Component | FWHM [eV] | Area [%] | Component relative concentration [at.%] | Element relative concentration [at.%] |
|---------|---------------------------------------|-----------|----------|---|---------------------------------------|
| O 1s | O 1s | 2.30 | 100 | 72.3 | 72.3 |
| | 2p TiO ₂ 3/2 | 1.86 | 66 | 12.0 | |
| Ti 2p | 2p TiO ₂ 1/2 | 2.66 | 33 | 6.0 | 22 |
| | 2p Ti 3/2 | 3.93 | 66 | 2.7 | |
| | 2p Ti 1/2 | 2.62 | 33 | 1.3 | |
| Fe 2p | 2p Fe ₂ O ₃ 3/2 | 4.90 | 66 | 3.8 | 5.7 |
| | 2p Fe ₂ O ₃ 1/2 | 6.60 | 33 | 1.9 | |

Table 5.6: Summary of FWHM, areas and relative component and elemental concentrations measured from high resolution scans of TiFe following activation and cycling under hydrogen.

Figure 5.15: XPS wide spectrum scan of Pd-TiFe_{0.96}Ni_{0.04} as prepared.

| Element | Component | FWHM [eV] | Area [%] | Component relative concentration [at.%] | Element relative concentration [at.%] |
|---------|---------------------------------------|-----------|----------|---|---------------------------------------|
| O 1s | O 1s | 3.65 | 100 | 73.5 | 73.5 |
| | 2p TiO ₂ 3/2 | 2.86 | 66 | 1.5 | |
| Ti 2p | 2p TiO ₂ 1/2 | 3.16 | 33 | 0.8 | 2.7 |
| | 2p Ti 3/2 | 2.39 | 66 | 0.3 | |
| | 2p Ti 1/2 | 2.12 | 33 | 0.1 | |
| Fe 2p | 2p Fe ₂ O ₃ 3/2 | 8.06 | 66 | 1.5 | 2.3 |
| | 2p Fe ₂ O ₃ 1/2 | 7.59 | 33 | 0.8 | |
| Ni 2p | 2p NiO 3/2 | 16.89 | 66 | 0.8 | 1.2 |
| | 2p NiO 1/2 | 9.49 | 33 | 0.4 | |
| Pd 3d | 3d PdO 5/2 | 2.91 | 60 | 5.6 | 20.3 |
| | 3d PdO 3/2 | 2.72 | 40 | 3.7 | |
| | 3d Pd 5/2 | 1.58 | 60 | 6.6 | |
| | 3d Pd 3/2 | 1.64 | 40 | 4.4 | |

Table 5.7: Summary of FWHM, areas and relative component and elemental concentrations measured from high resolution scans of Pd-TiFe_{0.96}Ni_{0.04} as prepared.

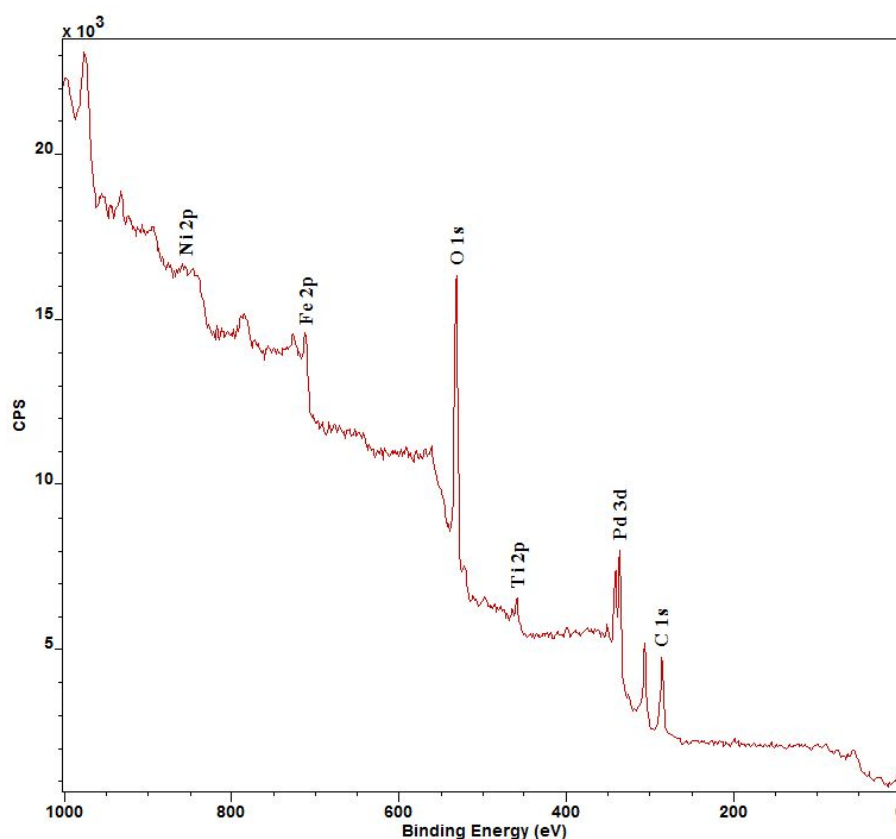


Figure 5.16: XPS wide spectrum scan of Pd_TiFe_{0.96}Ni_{0.04} following activation and cycling under hydrogen.

| Element | Component | FWHM [eV] | Area [%] | Component relative concentration [at.%] | Element relative concentration [at.%] |
|---------|---------------------------------------|-----------|----------|---|---------------------------------------|
| O 1s | O 1s | 4.18 | 100 | 78.9 | 78.9 |
| | 2p TiO ₂ 3/2 | 3.06 | 66 | 2.2 | |
| Ti 2p | 2p TiO ₂ 1/2 | 3.50 | 33 | 1.1 | 3.6 |
| | 2p Ti 3/2 | 1.61 | 66 | 0.2 | |
| | 2p Ti 1/2 | 0.97 | 33 | 0.1 | |
| Fe 2p | 2p Fe ₂ O ₃ 3/2 | 6.21 | 66 | 5.6 | 8.5 |
| | 2p Fe ₂ O ₃ 1/2 | 9.16 | 33 | 2.9 | |
| Ni 2p | 2p NiO 3/2 | 6.62 | 66 | 0.5 | 0.8 |
| | 2p NiO 1/2 | 3.74 | 33 | 0.3 | |
| Pd 3d | 3d Pd 5/2 | 9.02 | 60 | 4.9 | 8.2 |
| | 3d Pd 3/2 | 6.48 | 40 | 3.3 | |

Table 5.8: Summary of FWHM, areas and relative component and elemental concentrations measured from high resolution scans of Pd_TiFe_{0.96}Ni_{0.04} following activation and cycling under hydrogen.

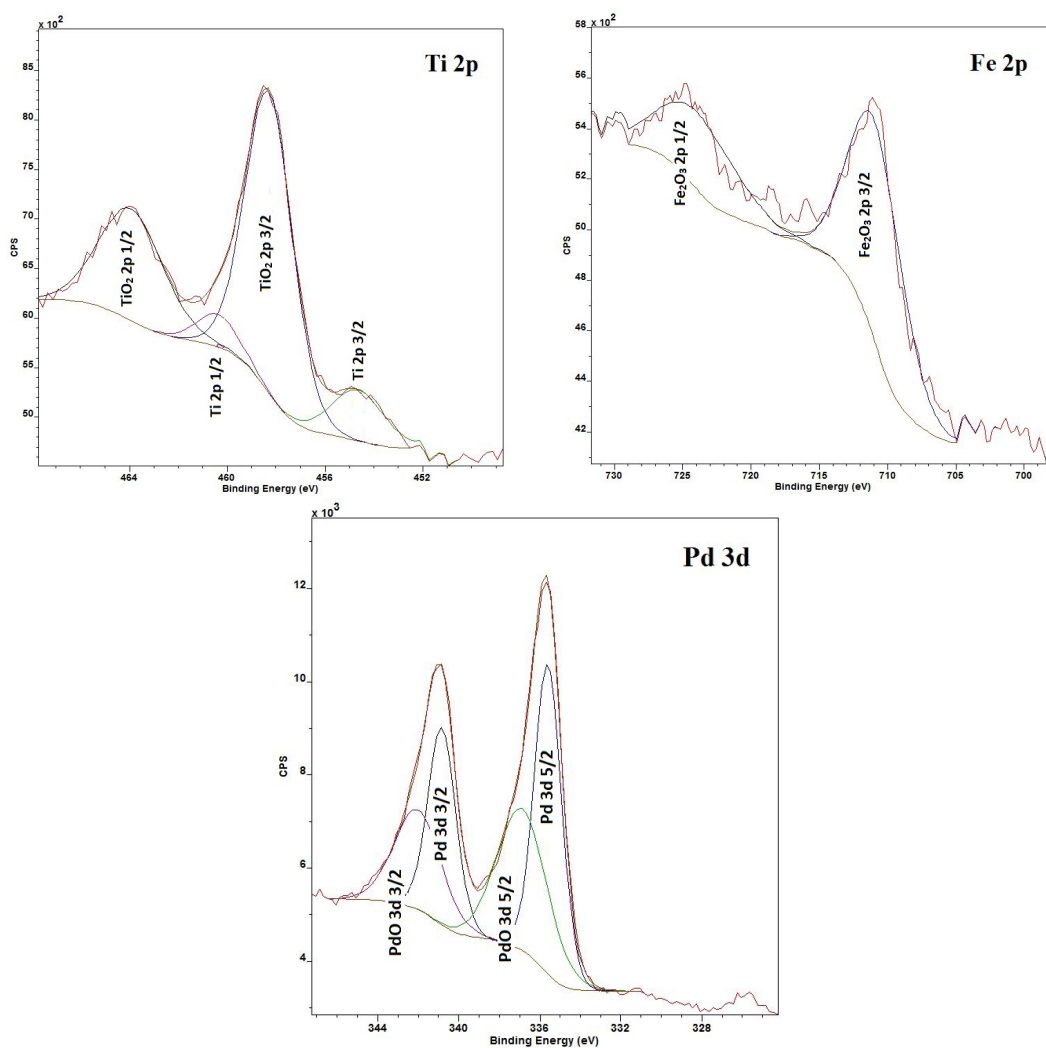
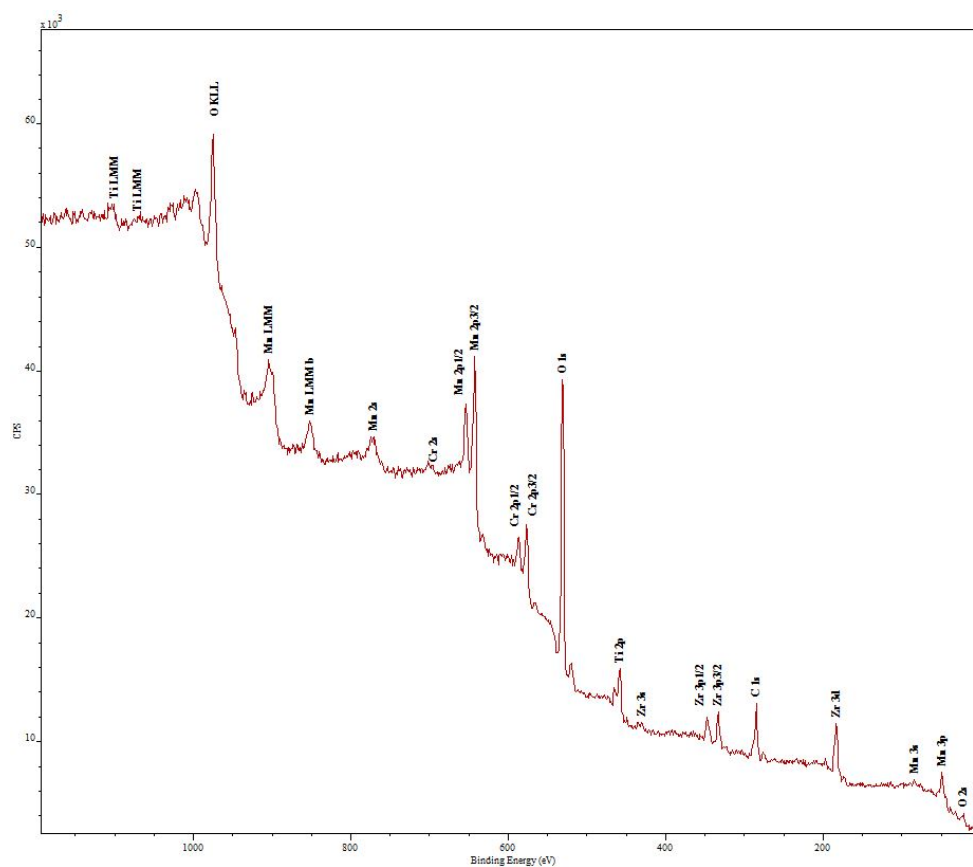


Figure 5.17: XPS high resolution spectra of Ti 2p, Fe 2p and Pd 3d from Pd.TiFe_{0.96}Ni_{0.04} as prepared, with fittings applied to determine metallic and oxide state contributions.

Figure 5.18: XPS wide spectrum scan of $\text{Ti}_{0.6}\text{Zr}_{0.4}\text{MnCr}$ as prepared.

| Element | Component | FWHM [eV] | Area [%] | Component relative concentration [at.%] | Element relative concentration [at.%] |
|---------|--------------------------------|-----------|----------|---|---------------------------------------|
| O 1s | O 1s | 3.01 | 100 | 63.0 | 63.0 |
| | 2p Mn_2O_3 3/2 | 3.26 | 66 | 7.6 | |
| Mn 2p | 2p Mn_2O_3 1/2 | 6.24 | 33 | 3.8 | 17.6 |
| | 2p MnO_2 3/2 | 5.71 | 66 | 4.1 | |
| | 2p MnO_2 1/2 | 2.80 | 33 | 2.1 | |
| Cr 2p | 2p Cr_2O_3 3/2 | 4.11 | 66 | 5.3 | 8.0 |
| | 2p Cr_2O_3 1/2 | 4.48 | 33 | 2.7 | |
| | 2p TiO_2 3/2 | 2.72 | 66 | 3.1 | |
| Ti 2p | 2p TiO_2 1/2 | 3.40 | 33 | 1.5 | 5.8 |
| | 2p Ti 3/2 | 2.92 | 66 | 0.6 | |
| | 2p Ti 1/2 | 2.38 | 33 | 0.6 | |
| Zr 3d | 3d ZrO_2 5/2 | 2.40 | 60 | 3.4 | 5.6 |
| | 3d ZrO_2 3/2 | 2.22 | 40 | 2.2 | |

Table 5.9: Summary of FWHM, areas and relative component and elemental concentrations measured from high resolution scans of $\text{Ti}_{0.6}\text{Zr}_{0.4}\text{MnCr}$ as prepared.

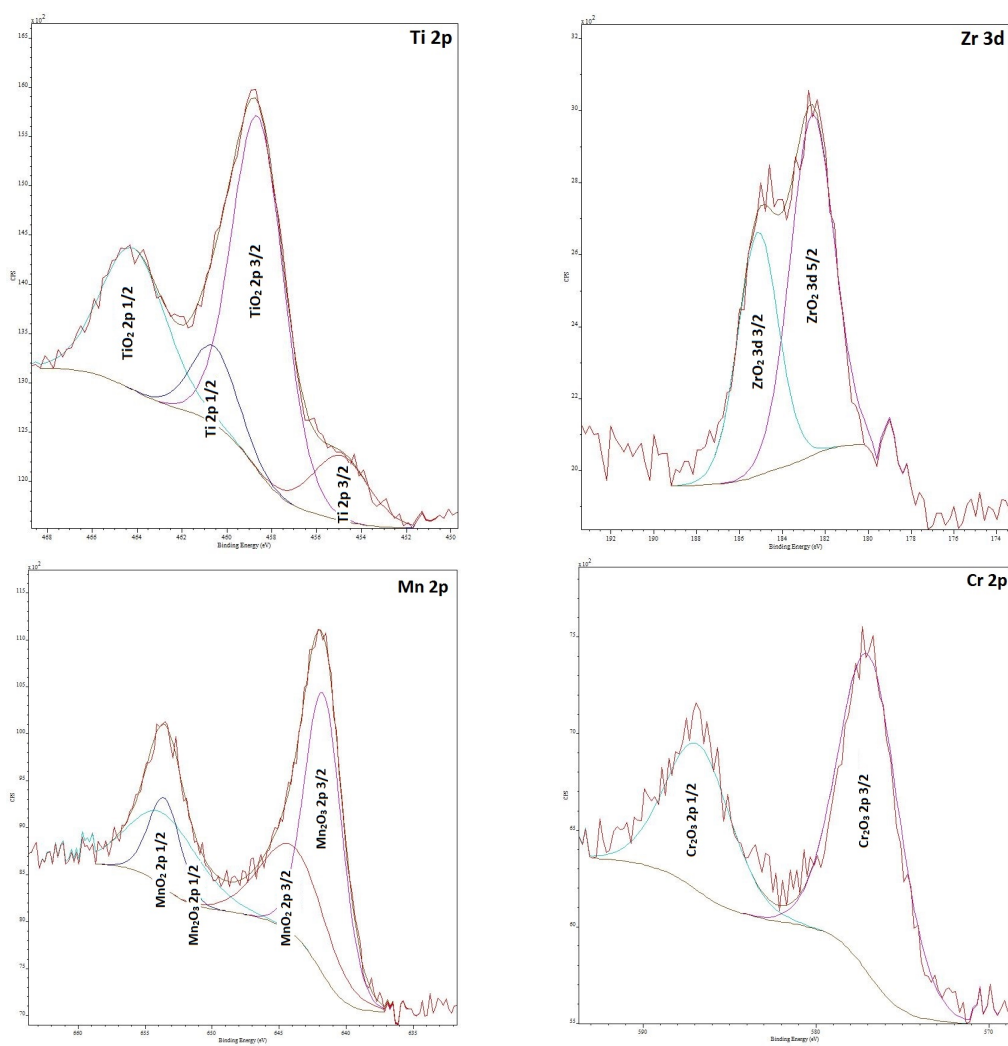


Figure 5.19: XPS high resolution spectra of Ti 2p, Zr 3d, Mn 2p and Cr 2p from $\text{Ti}_{0.6}\text{Zr}_{0.4}\text{MnCr}$ as prepared, with fittings applied to determine metallic and oxide state contributions.

5.3 TiFe Alloy Discussion

5.3.1 Properties of TiFe

X-ray diffraction analysis (Figure 5.7) revealed the TiFe sample studied here obtained the well known B2 cubic structure. The lattice parameter calculated (a) = 2.9759 (2) Å was in very good agreement with the literature value of 2.980 (2) Å (Thompson et al., 1979). In turn, the determined unit cell volume $V = 26.355$ (9) Å³ agreed well with the literature value of 26.365(3) Å³ (Reilly et al., 1980). From a thermodynamics perspective, the plateau pressures obtained for TiFe in the temperature range of 45-75 °C revealed the resultant dehydrogenation enthalpy $\Delta H = 28.9 \pm 0.7$ kJ.mol⁻¹ H₂ and entropy $\Delta S = 105 \pm 2$ J.K⁻¹mol⁻¹ H₂ are close to published values of $\Delta H = 28.1$ kJ.mol⁻¹ H₂ and $\Delta S = 106$ J.K⁻¹mol⁻¹ H₂ (Reilly, 1979).

This being said, there was a clear problem achieving total theoretical capacity. Reilly (1979) showed the capacity of TiFe between 40-55 °C is about 1.8-1.85 wt.%, however the maximum capacity measured for our sample was 1.39 wt.%. There was also a reduction in the size of the $\alpha+\beta$ phase (monohydride) which only extended to 0.8 wt.% at 45 °C. Cross sectional compositional (EDX) analysis of the as prepared TiFe revealed no carbon impurities, as pure raw materials (not a base Fe alloy) was used for fabrication, but the capacity loss may be attributed to the actual sample composition, Ti_{1.04}Fe_{0.96} (Table 5.3). Reilly and Wiswall (1972) demonstrated once TiFe becomes Ti rich the alloy departs from a single-phase region to a mixture of

TiFe and an unhydriding phase TiFe_2 , thus reducing storage capacity. Nevertheless, only trace amounts of TiFe_2 could be present in the alloy, given that it was not detected during XRD or cross sectional analysis (Figure 5.7 & 5.9(c)), and so this does not completely explain the large capacity reduction of ca. 0.4 wt.%.

The capacity disparity may also be linked to the alloy fabrication method. A difference in our powder atomisation route compared to conventional preparation during arc melting was the exclusion of a heat treatment stage, where the re-melted TiFe ingots are exposed to annealing at ca. 1000 °C for >12 h (Reilly et al., 1980). This implies that while re-melting an ingot several times prior to atomisation produces a single phase alloy, an annealing stage is still necessary. This idea corroborated with the higher than typical plateau slope factor of 0.34 and hysteresis of 0.86 measured for our TiFe sample compared to literature values of 0 and 0.64 respectively (Huston and Sandrock, 1980).

For this reason a TiFe sample was sealed under vacuum inside a quartz ampule and annealed at 950 °C for 120 h. Unfortunately the annealed sample did not take up any hydrogen even when undergoing the same activation process as the unannealed TiFe (repeated exposure to 40 bar H_2 at 500 °C for 95 h). Interestingly, this suggests the annealing process actually had a negative impact on ease of activation, as well as failing to remove internal stresses in the TiFe structure which would have potentially improved the storage properties of the atomised TiFe.

5.3.2 Effect of Minor Ni Substitution

Although all of the $\text{TiFe}_{1-x}\text{Ni}_x$ ($x = 0.04$ and 0.08) alloys studied here formed complete solid solutions with the same lattice as TiFe (Figure 5.7), their pressure-composition isotherms illustrate quite different hydrogenation characteristics. The plateau pressures of $\text{TiFe}_{0.96}\text{Ni}_{0.04}$ were considerably lower than those of TiFe in the range of 45-75 °C (Table 5.1). As described in Section 2.2.4, TiFe has a CsCl-type structure with 12 tetrahedral and 6 octahedral sites per unit cell. Hydrogen atoms primarily occupy the octahedral sites which are surrounded by four titanium atoms and two iron atoms (Fischer et al., 1987). As a result, the stabilities of $\text{TiFe}_{1-x}\text{Ni}_x$ alloys are closely linked to the size of the octahedral sites and compositions of the alloys.

Ni obtains a slightly larger atomic radius (0.1246 nm) compared to Fe (0.1241 nm). As more Ni atoms are substituted in for Fe atoms an increase in unit cell volume is observed (Figure 5.8), which is thought to increase the size of the interstitial sites. Larger interstitial sites results in a lower energy requirement to accommodate hydrogen atoms in these interstitial sites, thus leading to a reduction in the plateau pressure. As expected, this led to a rise in the formation enthalpy (ΔH) calculated from the PCI measurements compared to TiFe , as shown in Table 5.2, and demonstrate the increased hydride stability of the Ni substituted alloys. The calculated hydrogenation $\Delta H = -26.2 \pm 0.9 \text{ kJ.mol}^{-1} \text{ H}_2$ and dehydrogenation $\Delta H = 29.9 \pm 0.9 \text{ kJ.mol}^{-1} \text{ H}_2$ were also found to follow the same linear enthalpy trends as those in $\text{TiFe}_{1-x}\text{Ni}_x$

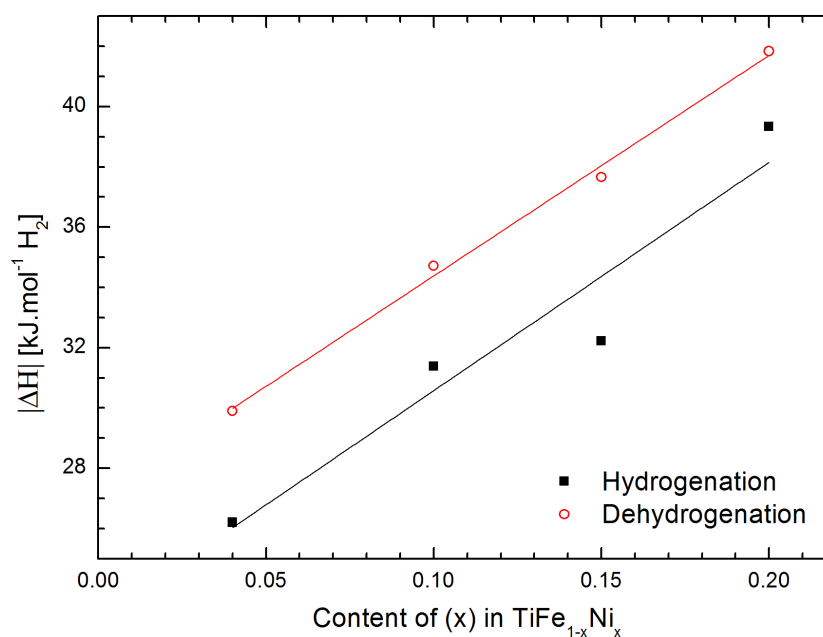


Figure 5.20: Comparing the hydrogenation and dehydrogenation enthalpies of $\text{TiFe}_{0.96}\text{Ni}_{0.04}$ to those of $\text{TiFe}_{1-x}\text{Ni}_x$ where $x = 0.1, 0.15$ and 0.2 as published by Mintz et al. (1981).

alloys with greater Ni content ($x = 0.1, 0.15$ & 0.2) (Mintz et al., 1981), as illustrated in Figure 5.20.

The measured hysteresis of 0.58 lies closer to that of TiFe (0.64) compared to $\text{TiFe}_{0.8}\text{Ni}_{0.2}$ (0.05) (Huston and Sandrock, 1980) given only the minor addition of Ni. The slight increase of 0.09 in the hydrogenation plateau slope compared to TiFe is due to the introduction of a ternary element creating a more complex multicomponent alloy possessing various interstitial sites with various different radii. The measured dehydrogenation slope factor 0.32 was surprisingly high, almost equal to the 0.36 found for $\text{TiFe}_{0.8}\text{Ni}_{0.2}$. As with the TiFe sample, this again may be associated with the lack of an annealing stage to improve homogeneity because Ti rich spots were visible during cross sectional analysis of the atomised $\text{TiFe}_{0.96}\text{Ni}_{0.04}$ (Figure 5.10(c) &

f)).

TiFe_{0.96}Ni_{0.04} was also observed to suffer from a severe capacity reduction. Literature has shown the capacities of TiFe_{0.9}Ni_{0.1} to be ca. 1.6 wt.% (Reilly and Wiswall, 1972) and TiFe_{0.8}Ni_{0.2} to be ca. 1.2-1.3 wt.% (Huston and Sandrock, 1980; Oguro et al., 1983), meanwhile we found TiFe_{0.96}Ni_{0.04} was limited to ca. 1.08 wt.% at 45 °C. This capacity loss could derive from the 0.5 at.% carbon contamination found in the alloy during compositional analysis (Table 5.3). Lee and Perng (2000) demonstrated even a carbon presence of 0.05 at.% in TiFe was sufficient to reduce the capacity by ca. 0.5 wt.%. The introduction of carbon into the TiFe_{1-x}Ni_x alloys is likely to be a resultant of using a base Fe alloy with trace amounts of carbon and emphasises the importance of fabricating TiFe based alloys from pure elements. Without neutron diffraction data and Rietveld refinement to accurately determine the position of different atoms in the structure it is difficult to verify the locations of the carbon atoms; however given the large capacity loss it may be suggested that they primarily occupy Ti sites as Fischer et al. (1987) demonstrated Ti₄Fe₂ sites are initially occupied by hydrogen in TiFe.

5.3.3 Improving Ease of Activation

The activation of the TiFe sample investigated in this study demanded more extreme heat treatment conditions than those published in the literature. While Reilly and Wiswall (1974) demonstrated successful activation was possible via heating to 400-450 °C under vacuum and applying a 7 bar H₂ pressure for 0.5 h, in our case

the required heat treatment temperature was 100 °C higher over an exposure time lasting almost four days. This disparity is likely to be associated with the alternate alloy fabrication method utilised in this study. In previous reports, TiFe ingots were commonly prepared in an arc furnace, being re-melted several times to ensure homogeneity. In addition, ingots were typically annealed at ca. 1000 °C for >12 h prior to being crushed (ca. 2 mm) ready for testing (Reilly et al., 1980). In contrast, our TiFe sample comprised of 106 μm atomised powder that was not handled in an inert atmosphere following production. Given that the atomised powder would possess a thicker oxide layer compared to crushed ingot powder with fresh surfaces, the reported activation results are unsurprising.

The mechanism behind the initial stage of activation in TiFe was investigated by comparison of XPS surface spectra of the as prepared and cycled samples (Figure 5.13 & 5.14). Air exposed atomised 106 μm TiFe, which did not readily absorb hydrogen, was covered with an oxide layer consisting of Ti^{IV} and Fe^{III} . The as prepared sample obtained an initial Ti:Fe ratio of 1:1, which is agreement with Schober and Westlake (1981); Schlapbach and Riesterer (1983). The XPS results following activation and cycling of TiFe are in partial agreement with findings by Schlapbach and Riesterer (1983). Ti segregation at the surface was observed as the Ti:Fe ratio increased to approximately 4:1, which is between the 2:1 and 10:1 range at a probing depth of 2 nm stated by Schlapbach and Riesterer (1983). However, there was a lack of elemental Fe visible at the surface of the cycled TiFe sample, in agreement with Sevlam et al. (1987). This creates some doubts regarding Schlapbach's theory of excess metallic

iron clusters, formed via the redox reaction of Ti to TiO_2 , acting as sites for hydrogen dissociation on top of activated TiFe and diffusion as atomic hydrogen across TiO_2 , or migration along Fe/ TiO_2 grain boundaries before being dissolved into underlying TiFe. An alternative theory may involve hydrogen molecules penetrating the two phase surface layer and dissociating on TiFe or elemental Fe on the subsurface, yet depth profiling would be necessary to provide confirmation.

The ease of activation was not drastically improved with the substitution of 0.04 Ni for Fe in $\text{TiFe}_{1-x}\text{Ni}_x$, as the required heat treatment temperature reduced by only 100 °C to 400 °C. This was not a completely unexpected result given that [Lee and Perng \(1999\)](#) reported even with a Ni content of 0.2 in $\text{TiFe}_{1-x}\text{Ni}_x$ room temperature activation still took about one day to reach saturation. Therefore, it may be argued if the $\text{TiFe}_{0.96}\text{Ni}_{0.04}$ sample was exposed to 40 bar H_2 for greater than 72 h, unlike the case here, it may eventually begin to hydrogenate. Nevertheless, following this procedure when aiming to produce a commercial metal hydride remains highly impractical.

On the other hand, with only a minor addition of Pd (1.17 wt.%) magnetron sputtered to the surface of $\text{TiFe}_{0.96}\text{Ni}_{0.04}$ successful room temperature hydrogenation is achieved with no activation treatment required. Pd clusters of $<1 \mu\text{m}$ diameter, identified in the back scattered images (Figure 5.11(b & c)), were verified upon closer examination via the ‘glancing angle’ approach during TEM analysis. The reasonably large radial separation between Pd clusters (ca. 10-20 μm) and variation in cluster thickness (ca. 10-30 nm) demonstrate it is not necessary to have complete

Pd coverage in the form of a uniform coating. Many factors can affect the grain size and density of sputtered thin film structures (Harsha, 2006) and some are also likely to be applicable in controlling the size of sputtered particle clusters on atomized powders. For example, higher substrate temperature would increase the nucleation rate of sputtered particles, higher power would lead to increased ion bombardment and higher vacuum conditions cause larger particle clusters due to fewer sputtered particles colliding with the discharge plasma as they travel towards the substrate. This minimal Pd catalyst concentration of 1.17 wt.% is in agreement with Zaluski et al. (1995) who reported nanocrystalline and amorphous TiFe could readily absorb hydrogen at room temperature when ball milled with <1 wt.% Pd. Furthermore, it confirms Zaluski et al. (1995) findings that the effectiveness of the Pd does not rely upon it alloying with the TiFe powder, which is also seen in Figure 5.12(a & c).

The mechanism explaining how Pd enhances activation of TiFe has been commonly been attributed to the spillover effect, as described in Section 2.2.4, however to date no research into the characterisation of hydrogen spillover on to TiFe via a Pd catalyst has been published. As with the TiFe sample, the role of Pd was investigated by comparison of XPS surface spectra of the as prepared and cycled samples (Figure 5.15 & 5.16). XPS analysis revealed the Pd in the as prepared Pd-TiFe_{0.96}Ni_{0.04} composed of both Pd and PdO (Table 5.7) which is consistent with the findings from the SAED pattern taken of the Pd catalyst during TEM analysis (Figure 5.12(b)). Following activation and cycling, in contrast to TiFe, no Ti segregation at the surface was observed in Pd-TiFe_{0.96}Ni_{0.04}. This was anticipated given that the sample did

not undergo any activation heat treatment and confirms the initial hydrogenation path for the Pd-catalysed sample is different.

At 25 °C, PdO obtains a $\Delta G = -164.1 \text{ kJ.mol}^{-1}$, while the corresponding values for Fe_2O_3 , NiO and TiO_2 are $-492.9 \text{ kJ.mol}^{-1}$, $-419.9 \text{ kJ.mol}^{-1}$ and $-888.0 \text{ kJ.mol}^{-1}$ respectively. Given ΔG for PdO is a third of Fe_2O_3 and under a fifth of TiO_2 , PdO is the most easily reduced and changes to Pd. This corresponds with the XPS findings of Pd-TiFe_{0.96}Ni_{0.04} in which the PdO initially present was all converted to metallic Pd post activation and cycling, meanwhile there was little change in the metallic to oxide ratios in the other metals (Table 5.8). The Pd then adsorbs hydrogen molecules and dissociates it into atomic hydrogen, which may then spillover onto Fe_2O_3 , a phenomenon demonstrated by Xu et al. (1997) during temperature programmed reduction (TPR) of Pd/ Fe_2O_3 systems. Another simpler interpretation is for the atomic hydrogen to diffuse through the thin Pd layer and directly into the alloy, without spillover, because hydrogen diffusion through Pd is high at room temperature ($1.3\text{-}1.6 \times 10^{-7} \text{ cm}^2.\text{s}^{-1}$) (Stackelberg and Ludwig, 1964; Devanathan and Stachurski, 1962) especially compared to TiFe ($1.2 \times 10^{-12} \text{ cm}^2.\text{s}^{-1}$) (Bowman and Tadlock, 1979).

The superior kinetics possessed by Pd-TiFe_{0.96}Ni_{0.04} compared to TiFe_{0.96}Ni_{0.04} in initial hydrogenation may have been expected to continue during cycling, given the maintained presence of Pd on the surface of TiFe_{0.96}Ni_{0.04} particles after several cycles (Figure 5.11(g)), yet this was not observed. In fact, Pd-TiFe_{0.96}Ni_{0.04} and TiFe_{0.96}Ni_{0.04} obtained almost matching hydrogenation cycling kinetics, as shown in

Figure 5.2. Therefore, while the dissociation of hydrogen molecules at the surface was rate limiting during initial hydrogenation, the micro cracks evidently produced in both samples (Figure 5.10(e) and 5.11(e)) appear to overcome this barrier providing alternative pathways for hydrogen to possibly reach Fe sites in the subsurface at which diffusion into the particle bulk occurs and becomes rate determining.

Based on commodity prices, the addition of only 1.17 wt.% Pd to TiFe is estimated to increase the alloy cost by about 17 times per kilogram and so it was decided that alternative cheaper catalyst materials would be investigated. The activation of TiFe can be enhanced by the substitution of $x > 0.2$ Mn for Fe in $\text{TiFe}_{1-x}\text{Mn}_x$ alloys (Nagai et al., 1987). XPS analysis was also undertaken on an AB_2 alloy ($\text{Ti}_{0.6}\text{Zr}_{0.4}\text{MnCr}$) which was found to require no activation for hydrogenation. The surface was found to be dominated by 17.6 at.% Mn (see Table 5.9), a feature also seen in $\text{TiFe}_{0.9}\text{Mn}_{0.1}$ (Shenzhong et al., 1988). Based on this, it was judged testing magnetron sputtered Mn on TiFe would be a sensible approach.

Unfortunately, even the sample obtaining the highest Mn catalyst concentration of 3.56 wt.% failed to activate TiFe and this was despite exposing the sample to 40 bar H_2 at 350 °C for 20 h prior to attempting initial hydrogenation at room temperature. It remains unknown whether a critical concentration of magnetron sputtered Mn can enable successful room temperature hydrogenation of TiFe, or if the process demands alloying between Ti and Mn.

Furthermore, if this problem was solved, a solution would still need to be found to enable the TiFe and $\text{TiFe}_{1-x}\text{Ni}_x$ atomised powders to reach their theoretical ca-

capacities. Magnetron sputtering using the modified ‘tilted cup’ design was successfully demonstrated as a fairly rudimentary technique for applying catalysts to the surface of micron sized atomised powders; however given the time constraints of the project it was decided a pair of AB_2 alloys would be investigated as potential alternatives to the catalysed TiFe-based alloys for application in domestic thermal and hydrogen stores, and this is discussed in Section 5.4.

5.4 AB₂ Alloy Results

5.4.1 Hydrogen Storage Characteristics

Hydrogenation kinetics

Figure 5.21 shows Hydralloy C5 and $\text{Ti}_{0.9}\text{Zr}_{0.2}\text{Mn}_{1.5}\text{V}_{0.2}\text{Cr}_{0.3}$ hydrogenated at room temperature with no heat treatment prerequisite. During their first hydrogenations neither sample experienced an incubation period however $\text{Ti}_{0.9}\text{Zr}_{0.2}\text{Mn}_{1.5}\text{V}_{0.2}\text{Cr}_{0.3}$ did reach saturation within 30 min, approximately half that of Hydralloy C5. Furthermore, $\text{Ti}_{0.9}\text{Zr}_{0.2}\text{Mn}_{1.5}\text{V}_{0.2}\text{Cr}_{0.3}$ obtained a total capacity of 2.00 wt.%, exceeding

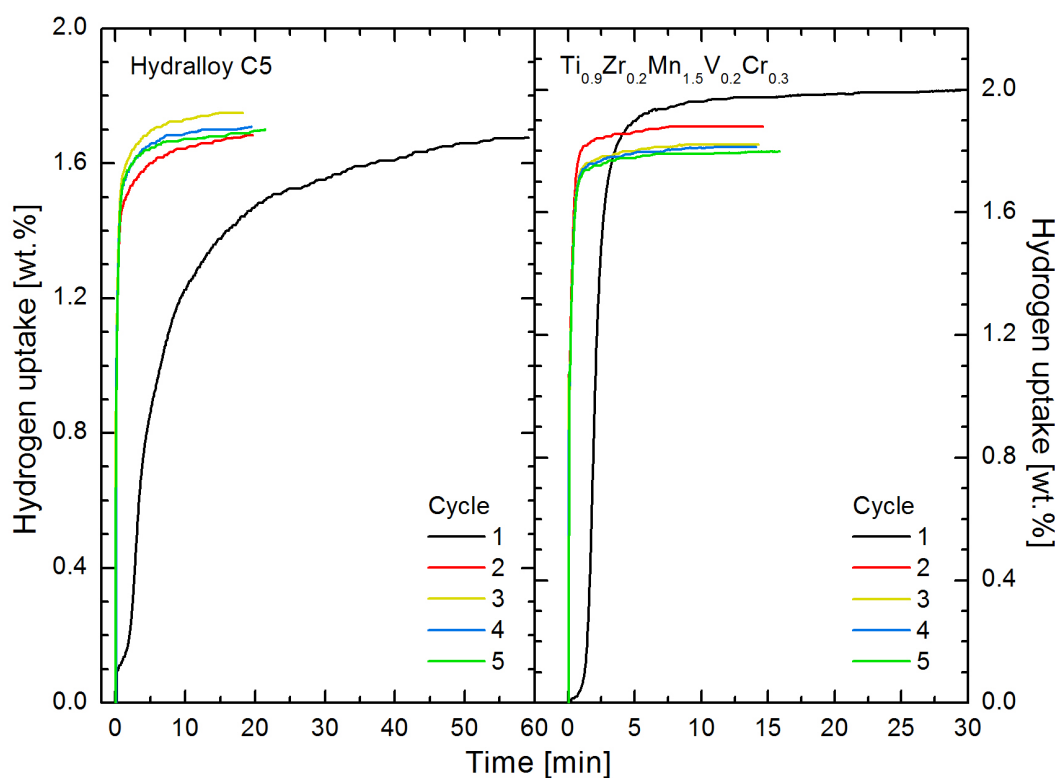


Figure 5.21: Hydrogenation kinetics during cycles 1-5 for Hydralloy C5 and $\text{Ti}_{0.9}\text{Zr}_{0.2}\text{Mn}_{1.5}\text{V}_{0.2}\text{Cr}_{0.3}$ at room temperature.

Hydralloy C5 by 0.32 wt.%.

Successive cycling resulted in the kinetics of both samples improving significantly and by the 5th cycle the hydrogenation rates during the initial 90% of uptake were 1.53 wt.%.min⁻¹ and 2.86 wt.%.min⁻¹ for Hydralloy C5 and Ti_{0.9}Zr_{0.2}Mn_{1.5}V_{0.2}Cr_{0.3} respectively. Although both alloys undergo similar kinetic improvements with cycling, different trends in total capacity are observed for each sample. The total capacity of Hydralloy C5 remained largely constant from the first cycle varying by a maximum of 0.06 wt.%, meanwhile for Ti_{0.9}Zr_{0.2}Mn_{1.5}V_{0.2}Cr_{0.3} the total capacity was observed to reduce by 0.2 wt.%, before stabilising at 1.80 wt.% in the 5th cycle.

The hydrogenation kinetics of Hydralloy C5 and Ti_{0.9}Zr_{0.2}Mn_{1.5}V_{0.2}Cr_{0.3} in the temperature range of 25-50 °C after 5 (de)hydrogenation cycles are shown Figure 5.22. The initial pressure was adjusted at each reaction temperature to help maintain a similar reaction driving pressure. For Hydralloy C5 the initial and equilibrium pressures (in bar) were 22.60 and 21.45 at 25 °C, 34.49 and 33.46 at 35 °C, and 46.98 and 45.98 at 50 °C. For Ti_{0.9}Zr_{0.2}Mn_{1.5}V_{0.2}Cr_{0.3} the initial and equilibrium pressures (in bar) were 23.26 and 21.94 at 25 °C, 27.56 and 26.33 at 35 °C, and 33.24 and 32.07 at 50 °C. As the temperature increases the saturation capacity is reached sooner, which is due to the increased kinetic energy of the hydrogen atoms at high temperature, which leads to the higher diffusion coefficient. Study into the hydrogenation reaction mechanisms of the two alloys are discussed in more detail in Section 5.5.2.

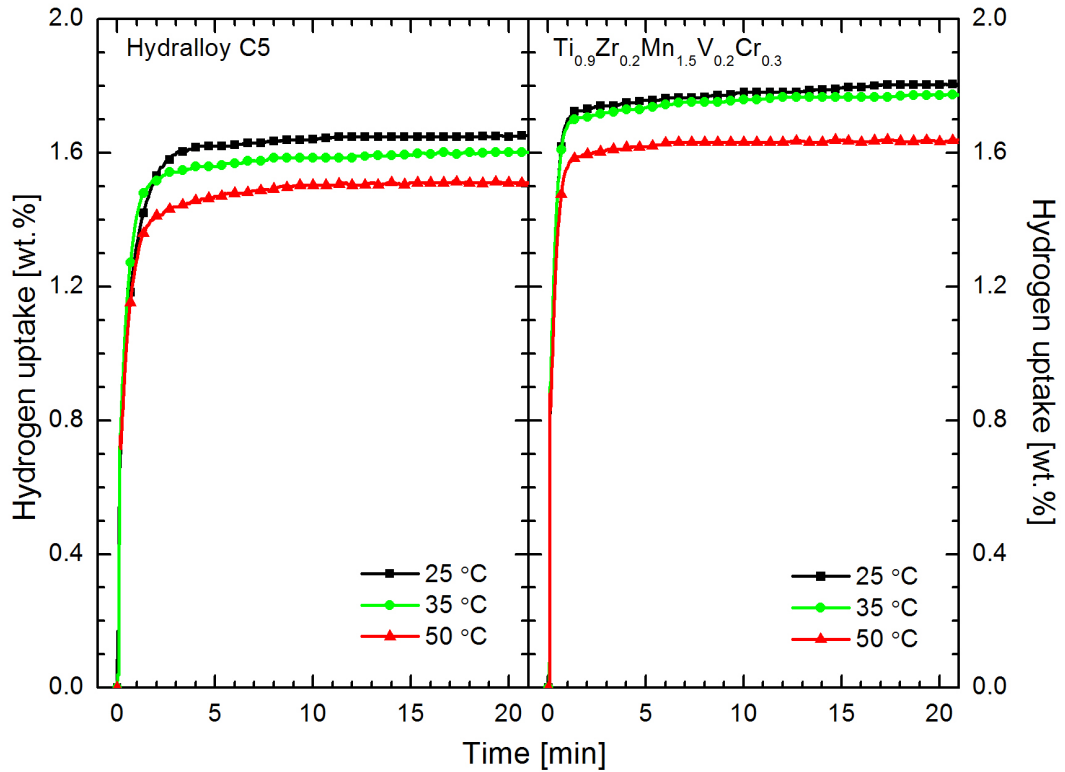


Figure 5.22: Hydrogenation kinetics of Hydralloy C5 and $\text{Ti}_{0.9}\text{Zr}_{0.2}\text{Mn}_{1.5}\text{V}_{0.2}\text{Cr}_{0.3}$ in the temperature range of 25-50 °C after 5 (de)hydrogenation cycles.

PCI characteristics

The hydrogenation and dehydrogenation pressure-composition-isotherms of Hydralloy C5 and $\text{Ti}_{0.9}\text{Zr}_{0.2}\text{Mn}_{1.5}\text{V}_{0.2}\text{Cr}_{0.3}$ are shown in Figures 5.23 and 5.24 respectively. The PCIs demonstrate the existence of the three regions - α , $\alpha+\beta$ and β phase. The plateau pressure (P_{plat}) of these alloys were measured at 0.85 wt.%. From these PCIs, it was observed that the dehydrogenation plateau pressure at 22 °C decreased from 7.6 bar for Hydralloy C5 to 2.0 bar for $\text{Ti}_{0.9}\text{Zr}_{0.2}\text{Mn}_{1.5}\text{V}_{0.2}\text{Cr}_{0.3}$. Furthermore, the in-house fabricated alloy was found to possess a maximum storage capacity of 1.82 wt.% after cycling, an increase of 0.09 wt.% compared to the commercial

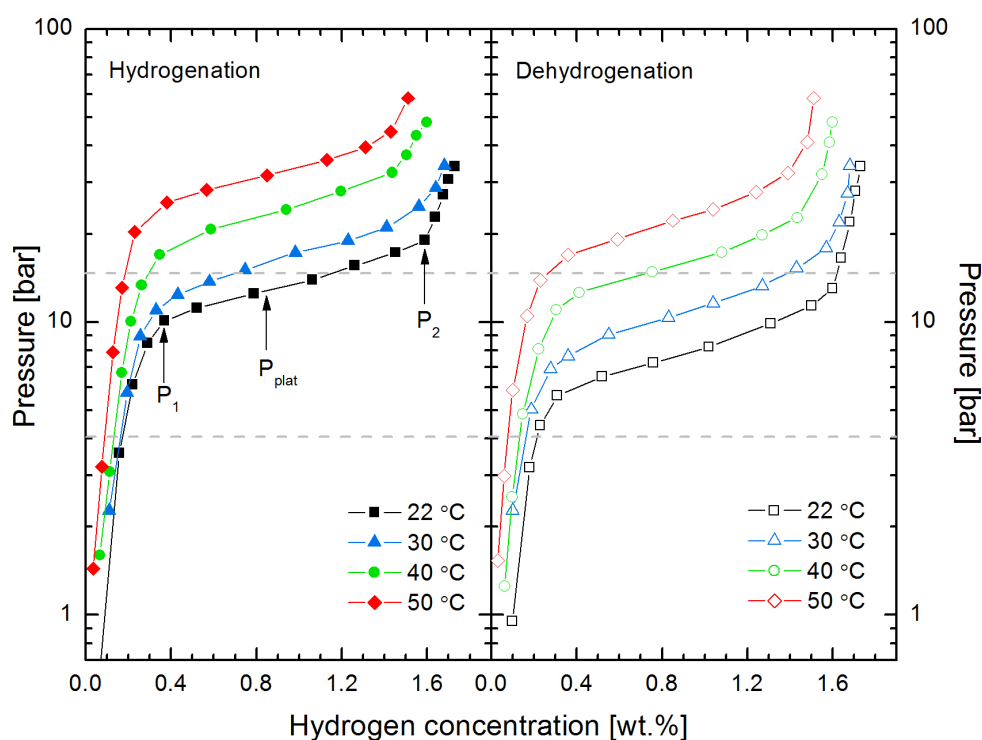


Figure 5.23: Pressure-composition hydrogenation and dehydrogenation isotherms of Hydralloy C5 in the temperature range 22-50 °C. Horizontal lines signify the working pressure region of 4-15 bar for the hydrogen store application.

Hydralloy C5.

For potential application in a hydrogen store, the commercial electrolyser is capable of producing hydrogen gas at a maximum pressure of 15 bar and the fuel cell can operate with a minimum inlet hydrogen gas pressure of 4 bar. Hence the working pressure limit is 4-15 bar for the hydrogenation and dehydrogenation process for this stationary application. The working capacity is the amount of useable reversible hydrogen storage capacity in the pressure range 4-15 bar. Based on this, the working capacity at 22 °C for Hydralloy C5 was seen to exceed $\text{Ti}_{0.9}\text{Zr}_{0.2}\text{Mn}_{1.5}\text{V}_{0.2}\text{Cr}_{0.3}$ by twelve times, at 0.96 wt.%. As the temperature increases however, the working capacity of Hydralloy C5 reduces whereas it increases for $\text{Ti}_{0.9}\text{Zr}_{0.2}\text{Mn}_{1.5}\text{V}_{0.2}\text{Cr}_{0.3}$

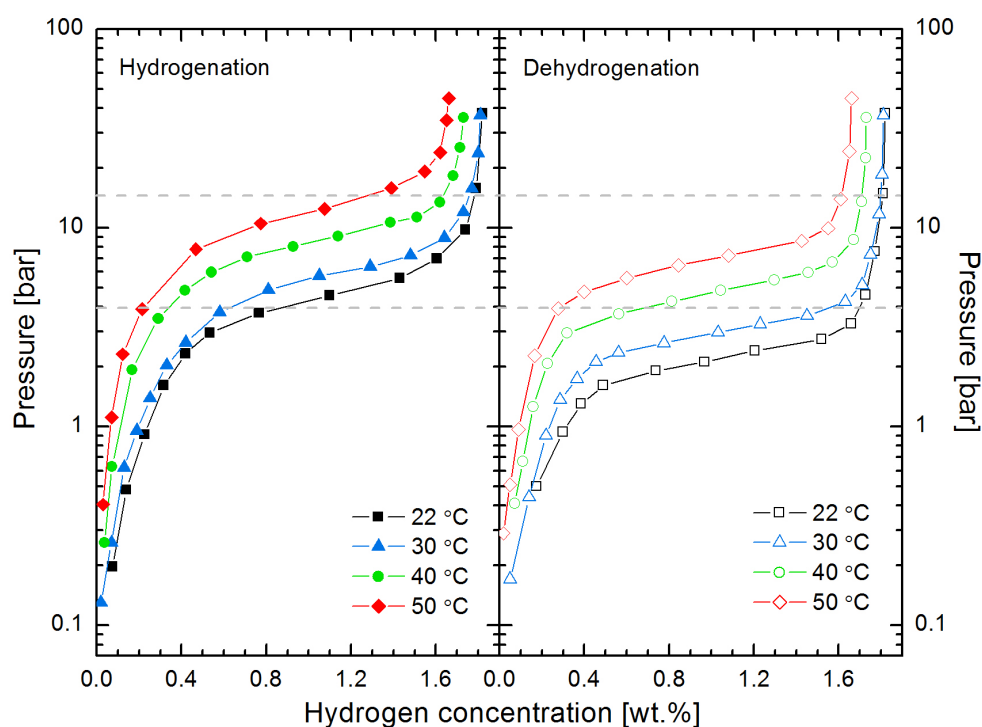


Figure 5.24: Pressure-composition hydrogenation and dehydrogenation isotherms of $\text{Ti}_{0.9}\text{Zr}_{0.2}\text{Mn}_{1.5}\text{V}_{0.2}\text{Cr}_{0.3}$ in the temperature range 22-50 °C. Horizontal lines signify the working pressure region of 4-15 bar for the hydrogen store application.

and by 50 °C its working capacity exceeds Hydralloy C5 by 0.91 wt.%.

The values of (de)hydrogenation plateau pressure at 22 °C, 30 °C, 40 °C and 50 °C, maximum hydrogen storage capacity, working capacity and charge time all at 22 °C for both alloys are listed in Table 5.10. The hydrogenation and dehydrogenation isotherms of these alloys exhibit the presence of hysteresis, which was 0.15 higher at 22 °C for $\text{Ti}_{0.9}\text{Zr}_{0.2}\text{Mn}_{1.5}\text{V}_{0.2}\text{Cr}_{0.3}$. The plateau slope factors of hydrogenation and dehydrogenation at 22 °C, calculated using $\ln(P_2/P_1)$, were found to be higher by 0.3 and 0.1 for $\text{Ti}_{0.9}\text{Zr}_{0.2}\text{Mn}_{1.5}\text{V}_{0.2}\text{Cr}_{0.3}$ compared to Hydralloy C5.

As described in Section 5.2.1 the van't Hoff equation was utilised to determine thermodynamic properties of the alloys. The ΔH and ΔS for the (de)hydrogenation

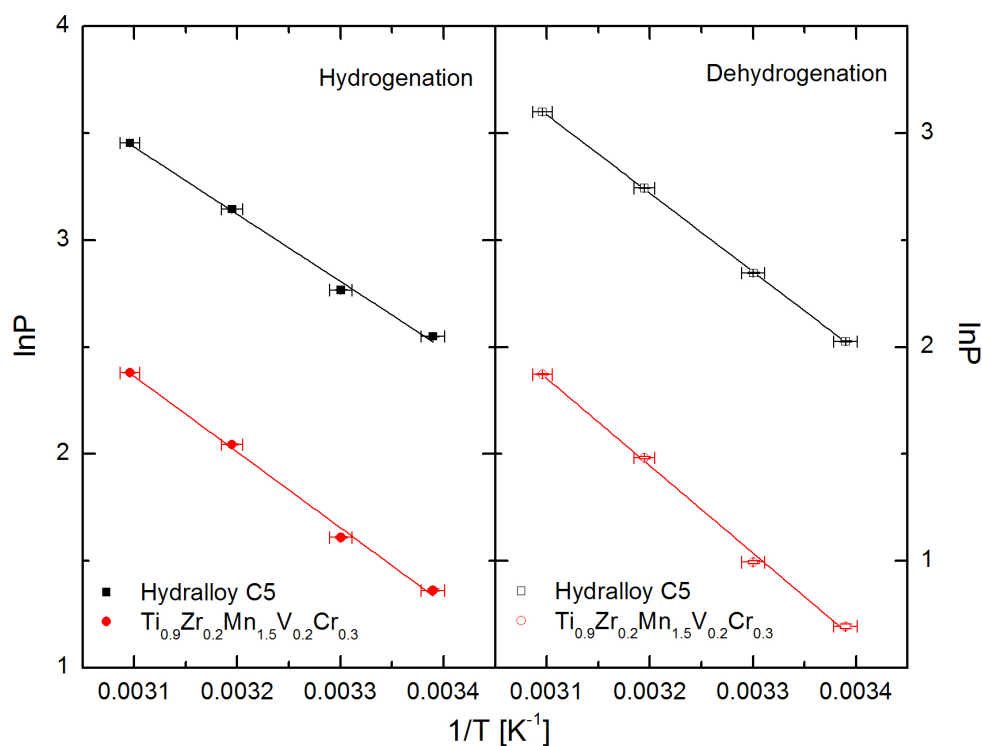


Figure 5.25: van't Hoff plot of $\ln P$ versus $1/T$ for the hydrogenation and dehydrogenation process of Hydralloy C5 and $\text{Ti}_{0.9}\text{Zr}_{0.2}\text{Mn}_{1.5}\text{V}_{0.2}\text{Cr}_{0.3}$. Errors in $\ln P$ contained in symbols.

processes of these alloys have been calculated from the slope and intercept of the van't Hoff plot respectively (Figure 5.25). The hydrogenation ΔH and ΔS for $\text{Ti}_{0.9}\text{Zr}_{0.2}\text{Mn}_{1.5}\text{V}_{0.2}\text{Cr}_{0.3}$ was $-29.5 \pm 1.4 \text{ kJ}\cdot\text{mol}^{-1} \text{ H}_2$ and $-111 \pm 5 \text{ J}\cdot\text{K}^{-1}\cdot\text{mol}^{-1} \text{ H}_2$ respectively. This was a rise of $3.4 \text{ kJ}\cdot\text{mol}^{-1} \text{ H}_2$ in enthalpy and a $1 \text{ J}\cdot\text{K}^{-1}\cdot\text{mol}^{-1} \text{ H}_2$ increase in entropy compared to the hydrogenation values of Hydralloy C5. A similar trend was seen for the corresponding dehydrogenation ΔH and ΔS values for the alloys, as detailed in Table 5.11.

| Alloy | Plateau Pressure [bar] | | | | Max. storage capacity [wt.%] at 22 °C | Working capacity [wt.%] (4-15 bar) | Charge time: 95% [min] |
|--|------------------------|-------------------|-------------------|-------------------|--|---------------------------------------|---------------------------|
| | 22 °C | 30 °C | 40 °C | 50 °C | | | |
| Hydralloy C5 | 12.8 | 15.9 | 23.2 | 31.7 | 1.73 | 1.40 | 2.7 |
| | 7.6 ^d | 10.5 ^d | 15.6 ^d | 22.2 ^d | | | |
| Ti _{0.9} Zr _{0.2} Mn _{1.5} V _{0.2} Cr _{0.3} | 3.9 | 5.0 | 7.7 | 10.8 | 1.82 | 0.13 | 0.9 |
| | 2.0 ^d | 2.7 ^d | 4.4 ^d | 6.5 ^d | | | |

d - dehydrogenation plateau pressure

Table 5.10: The values of plateau pressure in the temperature range 22-50 °C for (de)hydrogenation, maximum storage capacity, working capacity and charge time all at 22 °C for Hydralloy C5 and Ti_{0.9}Zr_{0.2}Mn_{1.5}V_{0.2}Cr_{0.3}.

| Alloy | Plateau slope factor ln(P ₂ /P ₁) at 22 °C | | Hysteresis ln(P _a /P _d) at 22 °C | ΔH [kJ.mol ⁻¹ H ₂] | | ΔS [J.K ⁻¹ mol ⁻¹ H ₂] | |
|--|--|-------|---|---|------------|--|---------|
| | Hyd | Dehyd | | Hyd | Dehyd | Hyd | Dehyd |
| | | | | | | | |
| Ti _{0.9} Zr _{0.2} Mn _{1.5} V _{0.2} Cr _{0.3} | 1.0 | 0.8 | 0.67 | -29.5 ± 1.4 | 34.0 ± 1.3 | -111 ± 5 | 121 ± 4 |

P₁ is $\alpha \rightleftharpoons \alpha + \beta$ phase transition pressure and pressure P₂ is $\alpha + \beta \rightleftharpoons \beta$ phase transition pressure, respectively Figure 5.23.

Table 5.11: The values of plateau slope factor and hysteresis at 22 °C, molar enthalpy (ΔH) and molar entropy (ΔS) for the (de)hydrogenation processes obtained from PCI measurements for Hydralloy C5 and Ti_{0.9}Zr_{0.2}Mn_{1.5}V_{0.2}Cr_{0.3}.

5.4.2 Structural Analysis

X-ray diffraction

X-ray diffraction patterns of Hydralloy C5 ($\text{Ti}_{0.95}\text{Zr}_{0.05}\text{Mn}_{1.5}\text{V}_{0.45}\text{Fe}_{0.01}\text{Cr}_{0.05}$) and $\text{Ti}_{0.9}\text{Zr}_{0.2}\text{Mn}_{1.5}\text{V}_{0.2}\text{Cr}_{0.3}$ reveal the single phase formation of these alloys, although trace amounts of Mn are detected (Figure 5.26). Both alloys crystallize in the C14 Laves phase hexagonal structure with the space group of $P6_3/mmc$. Comparison of X-ray diffraction patterns show the diffraction peaks shift towards a lower angle for the $\text{Ti}_{0.9}\text{Zr}_{0.2}\text{Mn}_{1.5}\text{V}_{0.2}\text{Cr}_{0.3}$ alloy. The lattice parameters of these alloys were determined from the X-ray diffraction peak positions. Both lattice parameters of

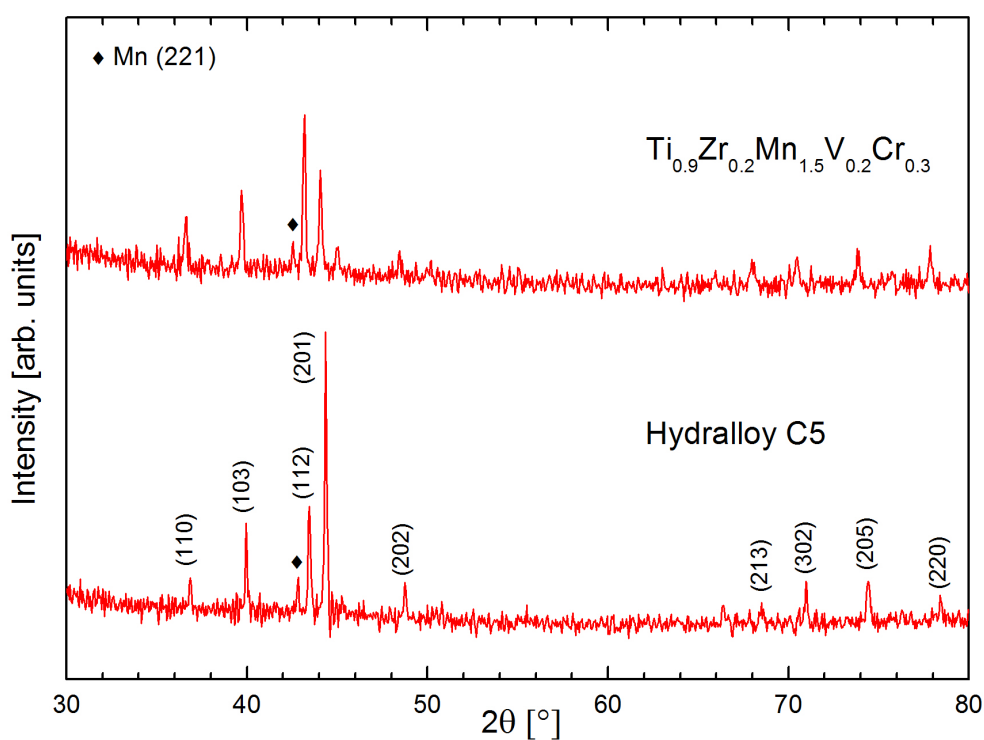


Figure 5.26: Powder X-ray diffraction patterns for Hydralloy C5 and $\text{Ti}_{0.9}\text{Zr}_{0.2}\text{Mn}_{1.5}\text{V}_{0.2}\text{Cr}_{0.3}$ using $\text{Cu K}\alpha$ radiation ($\lambda = 1.5418 \text{ \AA}$).

$\text{Ti}_{0.9}\text{Zr}_{0.2}\text{Mn}_{1.5}\text{V}_{0.2}\text{Cr}_{0.3}$ alloy were calculated to be larger than in Hydralloy C5, with a 0.028 Å increase in (a) and a 0.089 Å increase in (c). Correspondingly, this also resulted in a larger unit cell volume of 168.2(6) Å³ for $\text{Ti}_{0.9}\text{Zr}_{0.2}\text{Mn}_{1.5}\text{V}_{0.2}\text{Cr}_{0.3}$ compared to 164.5(3) Å³ for Hydralloy C5.

| Alloy | Lattice Parameters | | Unit cell volume (V) [Å ³] | Composition (EDX) |
|--|--------------------|----------|---|---|
| | (a) [Å] | (c) [Å] | | |
| Hydralloy C5 ($\text{Ti}_{0.95}\text{Zr}_{0.05}\text{Mn}_{1.5}\text{V}_{0.45}\text{Fe}_{0.01}\text{Cr}_{0.05}$) | 4.874(1) | 7.995(3) | 164.5(3) | $\text{Ti}_{1.02}\text{Zr}_{0.05}\text{Mn}_{1.43}\text{V}_{0.50}\text{Fe}_{0.09}\text{Cr}_{0.01}$ |
| $\text{Ti}_{0.9}\text{Zr}_{0.2}\text{Mn}_{1.5}\text{V}_{0.2}\text{Cr}_{0.3}$ | 4.902(2) | 8.084(5) | 168.2(6) | $\text{Ti}_{0.96}\text{Zr}_{0.21}\text{Mn}_{1.43}\text{V}_{0.22}\text{Cr}_{0.28}$ |

Table 5.12: The unit cell parameters, unit cell volume and the elemental composition of Hydralloy C5 and $\text{Ti}_{0.9}\text{Zr}_{0.2}\text{Mn}_{1.5}\text{V}_{0.2}\text{Cr}_{0.3}$.

Scanning electron microscopy

Comparison of SEM images (a) and (d) shown in Figure 5.27 reveal the as prepared forms of Hydralloy C5 and $\text{Ti}_{0.9}\text{Zr}_{0.2}\text{Mn}_{1.5}\text{V}_{0.2}\text{Cr}_{0.3}$ both consisted of a wide range of crushed pieces, varying in length from about 20 μm up to 150 μm. Both samples also possessed a high density of uneven rough surfaces generated via the crushing process. The evolution in microstructure of both samples following five cycles under hydrogen at room temperature are illustrated in images (b) and (e). At higher magnification (images (c & f)), the microstructure of both samples are still similar, with clear decrepitation of the crushed pieces in turn forming highly irregular shaped powders. The particulate size ranges about from 5 to 20 μm, although most were observed to have an approximate diameter of 15 μm. Furthermore, a high proportion of the larger particulates in both samples obtain cracks along the surfaces, which appears to demonstrate the initial stages of the decrepitation process.

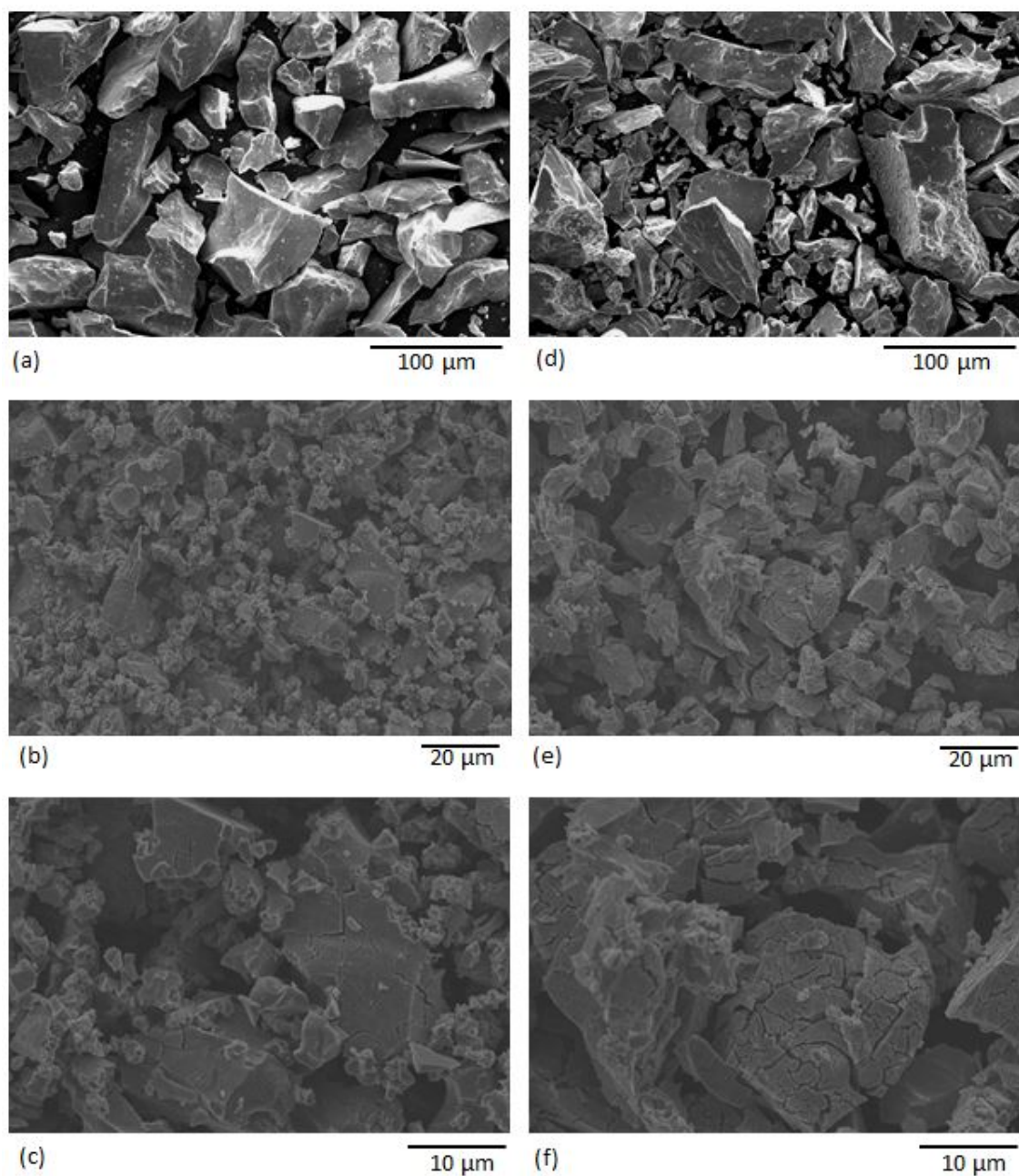


Figure 5.27: SEM images showing Hydralloy C5 and $\text{Ti}_{0.9}\text{Zr}_{0.2}\text{Mn}_{1.5}\text{V}_{0.2}\text{Cr}_{0.3}$ in as prepared forms in (a) and (d) respectively. Also following five cycles under hydrogen in (b & c) Hydralloy C5 and (e & f) $\text{Ti}_{0.9}\text{Zr}_{0.2}\text{Mn}_{1.5}\text{V}_{0.2}\text{Cr}_{0.3}$.

5.5 AB₂ Alloys Discussion

5.5.1 Properties of Alloys

The AB₂ alloy, Ti_{0.9}Zr_{0.2}Mn_{1.5}V_{0.2}Cr_{0.3}, was fabricated in house in an attempt to produce an alloy which was not only cost competitive but also obtained better hydrogen storage properties than the commercially available Hydralloy C5. SEM and EDX analysis revealed that both alloys were largely homogeneous in nature and the actual compositions were similar to the theoretical compositions (see Table 5.12). The trace presence of Mn phase in both alloys (Figure 5.26) is thought to have aided the fast initial hydrogenation observed in Figure 5.21 because Bououdina et al. (1998) suggested the existence of a secondary phase can promote activation.

From the PCI measurements post cycling, it was found that the hydrogen storage capacity of Ti_{0.9}Zr_{0.2}Mn_{1.5}V_{0.2}Cr_{0.3} exceeded Hydralloy C5 by 0.09 wt.% at 22 °C, which agrees with Oesterreicher and Bittner (1978); Li et al. (2005) who demonstrated increasing Zr content at the A site improves storage capacity. Ti_{0.9}Zr_{0.2}Mn_{1.5}V_{0.2}Cr_{0.3} was also observed to possess significantly lower plateau pressures compared to Hydralloy C5, as seen in Table 5.10. This is likely to be a result of a change in the chemical environment of the interstitial sites. The increased substitution of Zr and Cr into TiMn₂ based alloys are well documented to lower the plateau pressure and this has been attributed to the increase in size of the unit cell volume (Oesterreicher and Bittner, 1978; Bobet et al., 2000a). The 3.7 Å³ increase in unit cell volume of Ti_{0.9}Zr_{0.2}Mn_{1.5}V_{0.2}Cr_{0.3} compared to Hydralloy C5 (Table 5.12) further validates

this concept, suggesting the energy required to accommodate hydrogen atoms in the interstitial sites has decreased causing a reduction in the plateau pressure.

The dehydrogenation $\Delta H = 30.5 \pm 0.5 \text{ kJ.mol}^{-1} \text{ H}_2$ and $\Delta S = 120 \pm 2 \text{ J.K}^{-1}\text{mol}^{-1} \text{ H}_2$ for Hydralloy C5 calculated from the PCI measurements (Table 5.11) are comparable with those previously reported such as, $27.4 \text{ kJ.mol}^{-1} \text{ H}_2$ and $112 \text{ J.K}^{-1}\text{mol}^{-1} \text{ H}_2$ for $\text{Ti}_{0.98}\text{Zr}_{0.02}\text{Mn}_{1.5}\text{V}_{0.43}\text{Fe}_{0.09}\text{Cr}_{0.05}$ (Bernauer, 1989a), and $29.2 \text{ kJ.mol}^{-1} \text{ H}_2$ and $121.2 \text{ J.K}^{-1}\text{mol}^{-1} \text{ H}_2$ for $\text{Ti}_{0.98}\text{Zr}_{0.02}\text{Mn}_{1.46}\text{V}_{0.41}\text{Cr}_{0.05}\text{Fe}_{0.08}$ (Skripnyuk and Ron, 2003). Similarly, the hydrogenation $\Delta H = -29.5 \pm 1.4 \text{ kJ.mol}^{-1} \text{ H}_2$ and $\Delta S = -111 \pm 5 \text{ J.K}^{-1}\text{mol}^{-1} \text{ H}_2$ for $\text{Ti}_{0.9}\text{Zr}_{0.2}\text{Mn}_{1.5}\text{V}_{0.2}\text{Cr}_{0.3}$ calculated from the PCI measurements is comparable with that of $-26.7 \text{ kJ.mol}^{-1} \text{ H}_2$ and $-96.2 \text{ J.K}^{-1}\text{mol}^{-1} \text{ H}_2$ for $\text{Ti}_{0.9}\text{Zr}_{0.2}\text{Mn}_{1.4}\text{Cr}_{0.4}\text{V}_{0.2}$ (Xu et al., 2001). The values of ΔH and ΔS are different for hydrogenation and dehydrogenation, a common behaviour reported for these alloys (Hagstrom et al., 1995) also known as the hysteresis effect.

$\text{Ti}_{0.9}\text{Zr}_{0.2}\text{Mn}_{1.5}\text{V}_{0.2}\text{Cr}_{0.3}$ may have been expected to display a lower hysteresis than Hydralloy C5, seeing as increased Cr substitution was reported to reduce the hysteresis effect (Bobet et al., 2000a; Liu et al., 1996). While this was not the case, the 0.67 determined for $\text{Ti}_{0.9}\text{Zr}_{0.2}\text{Mn}_{1.5}\text{V}_{0.2}\text{Cr}_{0.3}$ remains in line with hysteresis values of similar alloys such as, 0.58 for $\text{Ti}_{0.9}\text{Zr}_{0.2}\text{Mn}_{1.4}\text{Cr}_{0.4}\text{V}_{0.2}$ and 1.06 for $\text{Ti}_{0.9}\text{Zr}_{0.15}\text{Mn}_{1.6}\text{Cr}_{0.2}\text{V}_{0.2}$ (Xu et al., 2001). The sloping plateau of these alloys is due to the multicomponent alloys obtaining various interstitial sites with different radii. The hydrogenation plateau slope factor of $\text{Ti}_{0.9}\text{Zr}_{0.2}\text{Mn}_{1.5}\text{V}_{0.2}\text{Cr}_{0.3}$ exceeded Hydralloy C5 by 0.3 and this has been attributed to the higher Zr content causing increased compositional

inhomogeneity (Liu et al., 1996).

5.5.2 Kinetic Reaction Mechanisms

A number of kinetic models have been developed to describe the mechanisms of the (de)hydrogenation process. When the models are fitted to experimental data they can reveal the rate-limiting mechanism because the faster mechanisms will not affect the actual kinetics of the sample. In the surface controlled model the rate-limiting step is the dissociation or re-combination of hydrogen molecules on the material's surface (Mintz and Zeiri, 1995). The Avrami-Erofeev model dictates that nucleation and growth occurs at random points in the bulk and on the surface of the material, where the rate-limiting step is the velocity of the moving interface between the metal and the hydride (Kelton, 1997). The contracting volume models is based upon nucleation starting at the surface of the sample and then moving towards the particle core through the bulk (Barkhordarian et al., 2006).

AB₂ alloys of similar composition to those investigated here were found to follow the Avrami-Erofeev model (Kandavel and Ramaprabhu, 2004; Manickam et al., 2015). Therefore, the hydrogenation reaction mechanisms of Hydralloy C5 and Ti_{0.9}Zr_{0.2}Mn_{1.5}V_{0.2}Cr_{0.3} were also analysed using the Avrami-Erofeev rate equation (Kelton, 1997):

$$F = 1 - \exp(-kt^n) \quad (5.1)$$

where, F is the fractional hydrogen concentration at a given time t and k is the

reaction rate constant. The exponent n provides information about the dimensionality of the transformation, with $n = 2$ and $n = 3$ representing two and three-dimensional growth of existing nuclei with constant interface velocity respectively (Mintz and Zeiri, 1995; Barkhordarian et al., 2006). To determine what reaction order best fitted the experimental hydrogenation kinetics of both alloys (Figure 5.22), the hydrogenation kinetics at 35 °C were fitted to the Avrami-Erofeev equation (5.1) with $n = 1, 2$ and 3 , as presented in Figure 5.28.

Each curve was found to fit two linear segments with a gradual change in slope and, by referring to the hydrogen concentration, this was observed to correspond to the transition region from the $\alpha+\beta$ phase (solid lines) to the β phase (dashed

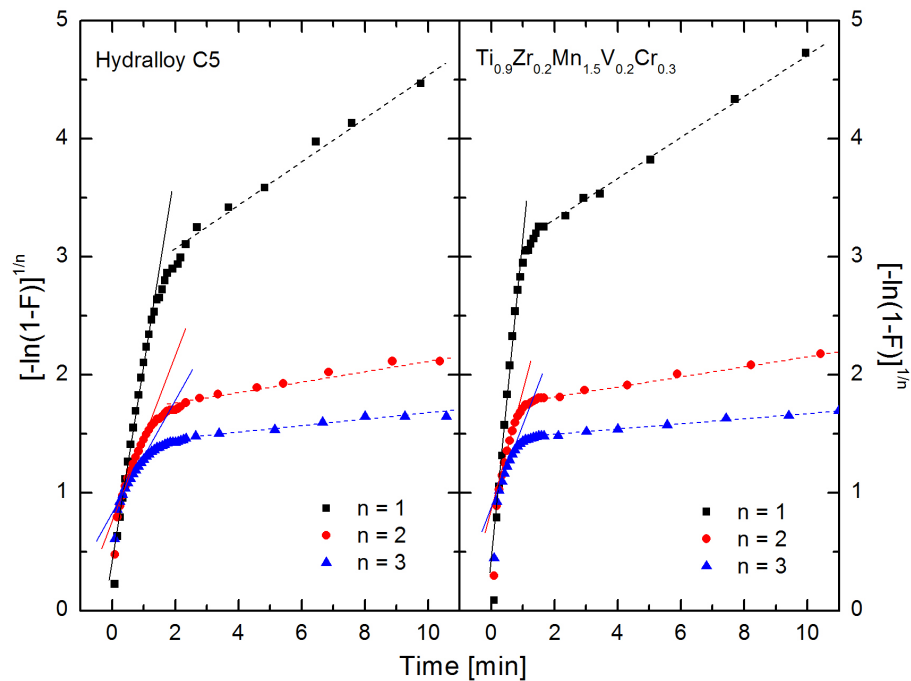


Figure 5.28: $[-\ln(1-F)]^{1/n}$ vs. time for Hydralloy C5 and $\text{Ti}_{0.9}\text{Zr}_{0.2}\text{Mn}_{1.5}\text{V}_{0.2}\text{Cr}_{0.3}$ at 35 °C. The solid fitted lines correspond to the reaction rate constant k during the $\alpha+\beta$ phase and the dashed fitted lines correspond to k during the β phase. The values for k and corresponding linear fit regression R^2 are shown in Table 5.13.

| Avrami-Erofeev $F = 1 - \exp(-kt^n)$ | Hydralloy C5 | | | | $Ti_{0.9}Zr_{0.2}Mn_{1.5}V_{0.2}Cr_{0.3}$ | | | |
|---|----------------|----------------|---------|----------------|---|----------------|---------|----------------|
| | $\alpha+\beta$ | | β | | $\alpha+\beta$ | | β | |
| | k | R ² | k | R ² | k | R ² | k | R ² |
| n = 1 | 1.69636 | 0.99793 | 0.18136 | 0.94759 | 2.84414 | 0.99407 | 0.17305 | 0.97645 |
| n = 2 | 0.69521 | 0.98338 | 0.04606 | 0.94559 | 1.06687 | 0.97858 | 0.04343 | 0.97352 |
| n = 3 | 0.43585 | 0.97508 | 0.02451 | 0.94466 | 0.64919 | 0.97049 | 0.02300 | 0.97273 |

Table 5.13: Gradient value (k) and the linear fit regression (R^2) of the Avrami-Erofeev kinetic model (with $n = 1, 2$ & 3) for the hydrogenation curves of Hydralloy C5 and $Ti_{0.9}Zr_{0.2}Mn_{1.5}V_{0.2}Cr_{0.3}$ at 35 °C.

lines). The α phase is not detectable as a result of the fast kinetics under these experiment conditions (Manickam et al., 2015). The rate constant k for the $\alpha+\beta$ phase and β phase were obtained from the slope of the two linear segments (Figure 5.28) respectively. From the linear fit regression R^2 values, both alloys were found to best follow a first order rate equation (5.2) in both the $\alpha+\beta$ and β phases (see Table 5.13):

$$-\ln(1 - F) = kt \quad (5.2)$$

The first order fittings of the kinetics data at different temperatures for both alloys and the corresponding rate constants k are presented in Figure 5.29 and Table 5.14 respectively. Interestingly, the temperature dependence of the rate constant in the $\alpha+\beta$ phase does not show an Arrhenius relationship (5.3) as would be expected (Kandavel and Ramaprabhu, 2004).

$$k = k_0 \exp\left(-\frac{E_a}{k_b T}\right) \quad (5.3)$$

This is likely to be associated with the fast hydrogenation kinetics of these two alloys and the experimental setup utilised. For investigation of isothermal kinetics the heat

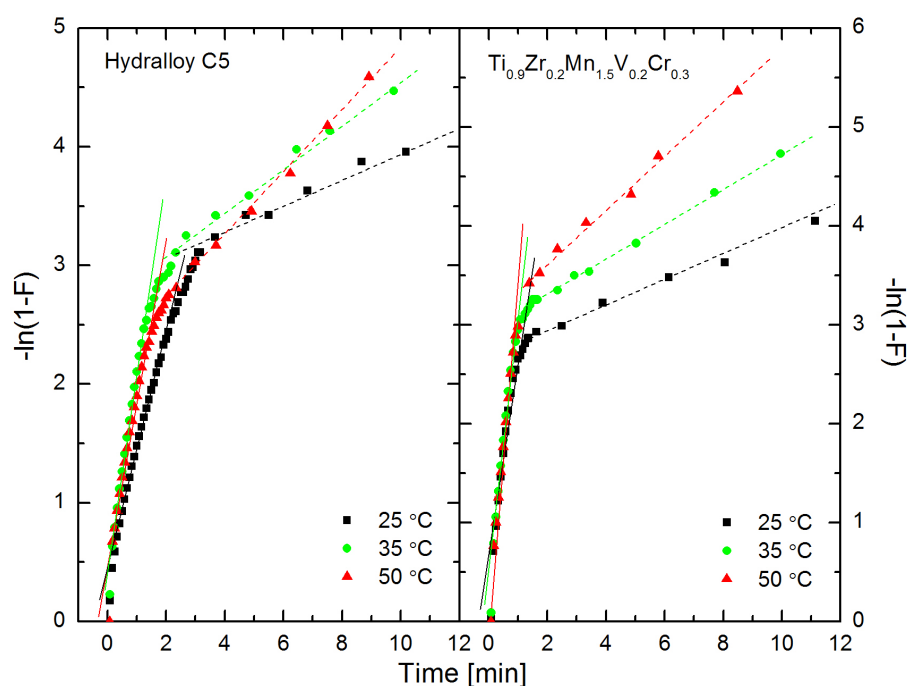


Figure 5.29: Kinetic data for the hydrogenation of Hydralloy C5 and $\text{Ti}_{0.9}\text{Zr}_{0.2}\text{Mn}_{1.5}\text{V}_{0.2}\text{Cr}_{0.3}$ in the temperature range 25-50 °C, fitted to a first order model. Solid fitted lines correspond to the reaction rate constant k in the $\alpha+\beta$ phase and the dashed fitted lines correspond to k in the β phase. The values for k and corresponding linear fit regression R^2 are shown in Table 5.14.

exchange of the experimental setup must be faster than the heat production due to hydriding enthalpy (Bernauer et al., 1989b). For both alloys, during the initial stages of the hydrogenation kinetic measurements, the temperature of the experimental set up was found to increase by up to 3 °C above the set temperature, implying there was a temperature gradient through the material despite only using a sample mass of ca. 0.6 g. As a result, a reliable activation energy value for the $\alpha+\beta$ phase was unobtainable because the k values were inaccurate of the true behaviour of each alloy during the initial stage of hydrogenation (see Table 5.14).

In the β phase region, the rate of hydrogenation was much slower (Figure 5.22)

| Temperature [°C] | Hydralloy C5 | | | | Ti _{0.9} Zr _{0.2} Mn _{1.5} V _{0.2} Cr _{0.3} | | | |
|---------------------|----------------|----------------|---------|----------------|--|----------------|---------|----------------|
| | $\alpha+\beta$ | | β | | $\alpha+\beta$ | | β | |
| | k | R ² | k | R ² | k | R ² | k | R ² |
| 25 | 1.01868 | 0.99408 | 0.11764 | 0.97744 | 2.53982 | 0.98887 | 0.12918 | 0.97435 |
| 35 | 1.69636 | 0.99793 | 0.18136 | 0.94759 | 2.84414 | 0.99407 | 0.17305 | 0.97645 |
| 50 | 1.45519 | 0.99658 | 0.26205 | 0.97305 | 2.92874 | 0.99876 | 0.27137 | 0.96156 |

Table 5.14: Gradient value (k) and the linear fit regression (R²) using the 1st order rate equation (n = 1) for the isothermal hydrogenation curves of Hydralloy C5 and Ti_{0.9}Zr_{0.2}Mn_{1.5}V_{0.2}Cr_{0.3}.

and by this point the heat due to hydriding enthalpy had dissipated, meaning the sample was again at the set temperature. During the β phase, diffusion of hydrogen atoms is the dominating and rate determining process. The rate constant k at different temperatures for the β phase of both alloys are shown in Table 5.14. The rate constant is directly related to the diffusion coefficient of hydrogen in the β phase (Lee et al., 1982) and the diffusion coefficient can be determined from:

$$D = \frac{k_D r^2}{\pi^2} \quad (5.4)$$

where r is the average particle radius. Microstructural analysis of Hydralloy C5 and Ti_{0.9}Zr_{0.2}Mn_{1.5}V_{0.2}Cr_{0.3} after 5 (de)hydrogenation cycles revealed most particles had an approximate size of 15 μm (Figure 5.27 (c & f)), therefore a value of 7.5 μm was used for r in the diffusion coefficient calculations. The calculated diffusion coefficients of hydrogen in the β phase in the temperature range of 25-50 °C was found to range from 6.7 x 10⁻⁹ to 1.5 x 10⁻⁸ cm².s⁻¹ for Hydralloy C5 and from 7.4 x 10⁻⁹ to 1.6 x 10⁻⁸ cm².s⁻¹ for Ti_{0.9}Zr_{0.2}Mn_{1.5}V_{0.2}Cr_{0.3}. The temperature dependence of diffusion coefficient shows an Arrhenius relation:

$$D = D_0 \exp\left(-\frac{E_a}{k_b T}\right) \quad (5.5)$$

The related activation energy E_a for each alloy has been calculated from the slope of the Arrhenius plot $\ln D$ versus $1/T$ (Figure 5.30). The activation energy value in the β phase obtained for Hydralloy C5 and $\text{Ti}_{0.9}\text{Zr}_{0.2}\text{Mn}_{1.5}\text{V}_{0.2}\text{Cr}_{0.3}$ was 25.8 ± 0.3 kJ.mol H_2 and 23.3 ± 0.4 kJ.mol H_2 respectively. These determined values are comparable to the activation energy and self-diffusion coefficient of $\text{Ti}_{0.8}\text{Zr}_{0.2}\text{MnCrH}_3$ measured by neutron scattering (21.2 ± 2.0 kJ.mol H_2 and 6×10^{-8} $\text{cm}^2.\text{s}^{-1}$ at 27°C) (Hempelmann et al., 1983) and $\text{Ti}_{0.98}\text{Zr}_{0.02}\text{V}_{0.43}\text{Fe}_{0.09}\text{Cr}_{0.05}\text{Mn}_{1.5}$ measured by neutron scattering (18.3 ± 3.0 kJ.mol H_2 and 1.2×10^{-7} $\text{cm}^2.\text{s}^{-1}$ at 20°C) (Bernauer et al., 1989b).

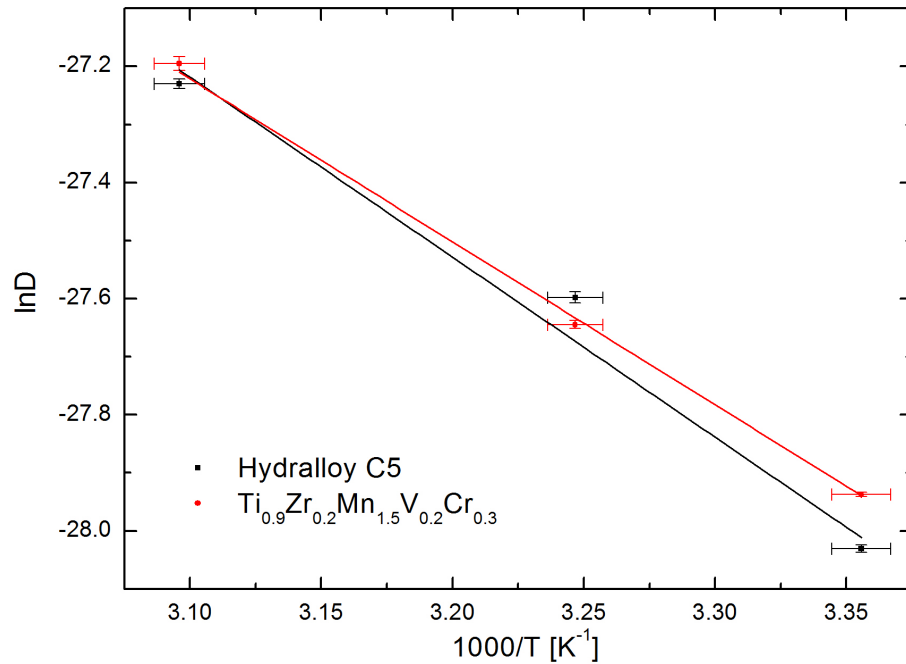


Figure 5.30: Arrhenius plot of $\ln D$ versus $1/T$ for the β phase for Hydralloy C5 and $\text{Ti}_{0.9}\text{Zr}_{0.2}\text{Mn}_{1.5}\text{V}_{0.2}\text{Cr}_{0.3}$.

5.5.3 Summary of AB₂ alloy comparison

An in house fabricated AB₂ alloy of composition Ti_{0.9}Zr_{0.2}Mn_{1.5}V_{0.2}Cr_{0.3} was successfully produced and obtained a higher maximum storage capacity (1.82 wt.%) than the commercially available Hydralloy C5. Hydralloy C5 remained the most promising alloy for the hydrogen store application with the highest working capacity, ca. 0.88 wt.% greater than Ti_{0.9}Zr_{0.2}Mn_{1.5}V_{0.2}Cr_{0.3} in the pressure range of 4-15 bar at 22 °C. However as shown in Figure 5.31, increasing temperature has a detrimental impact on the working capacity of Hydralloy C5, while the opposite is seen for Ti_{0.9}Zr_{0.2}Mn_{1.5}V_{0.2}Cr_{0.3}. For temperatures above 34 °C Ti_{0.9}Zr_{0.2}Mn_{1.5}V_{0.2}Cr_{0.3} is the best performing alloy under the given pressure conditions and therefore it is proposed Ti_{0.9}Zr_{0.2}Mn_{1.5}V_{0.2}Cr_{0.3} may be better suited for a hydrogen store in hotter climates such as Southeast Asia or the Middle East.

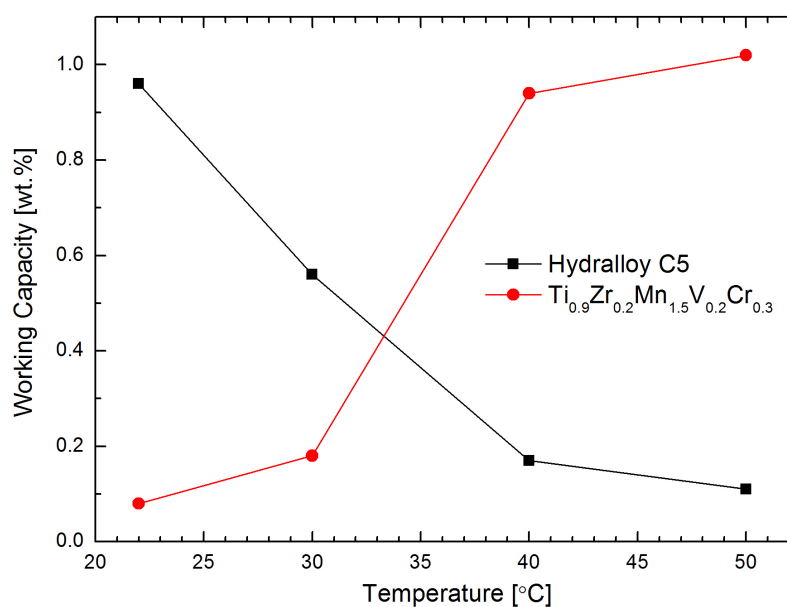


Figure 5.31: Comparison of working capacities in the temperature and pressure ranges (22-50 °C and 4-15 bar) for Hydralloy C5 and Ti_{0.9}Zr_{0.2}Mn_{1.5}V_{0.2}Cr_{0.3}.

The kinetics of hydrogenation for both alloys is so fast that for technical application only the heat transfer of the storage system is the rate limiting parameter for hydrogen exchange. Therefore, before commercialisation of an application containing either of these alloys is possible a study into improving the heat management of the system is also required.

The aim of producing an AB₂ alloy that is cost competitive with Hydralloy C5 has also been achieved. Analysis of metal commodities between June and November 2015 revealed average prices of £7 kg⁻¹ for Ti, £19 kg⁻¹ for Zr, £2 kg⁻¹ for Mn, £6 kg⁻¹ for Cr, £10 kg⁻¹ for Fe and £327 kg⁻¹ for V ([Metalpages, 2015](#); [Pureiron, 2015](#)). The rise in cost due to increasing Zr content from 0.05 to 0.2 is offset by the reduction in V content from 0.45 to 0.2. This leads to an approximate commodity price of £25 kg⁻¹ for Ti_{0.9}Zr_{0.2}Mn_{1.5}V_{0.2}Cr_{0.3} compared to £51 kg⁻¹ for Hydralloy C5.

Chapter 6

Conclusions

The aim of this thesis was to explore suitable materials for stationary applications, specifically a prototype hydrogen store, domestic thermal store operating between 25-100 °C and a moderate thermal store for a CSP plant operating at 400 °C. The approach incorporated a unique coating technique to deliver prototype hydrogen and thermal stores, where the coating could offer commercial advantages, for example, in the form of hydride activation and enhanced kinetics during successive cycling. The research was categorised into two key areas: the moderate temperature thermal store which explored the use of magnetron sputtered catalysts applied to the surfaces of commercial atomised magnesium powder, and the domestic thermal and hydrogen stores which included a selection of AB and AB₂ intermetallics that were enhanced through catalysis or thermodynamic modification.

Elevated temperature cycling studies were performed on commercial atomised Mg powder with magnetron sputtered catalysts (chromium, iron, vanadium and stainless

steel) applied to their surfaces; the aim of which was to fabricate hydrogen storage materials that possess (de)hydrogenation characteristics equal to or even bettering their nanocrystalline equivalents, yet in a potentially economic and scalable manner. Following 50 cycles at 400 °C, the coatings were found to have little to no positive impact on the behaviour of the atomised Mg powders and this was mainly attributed to the lack of multivalency in the catalysts. In addition, for both uncoated and coated samples the effects of an activation process at 400 °C (exposing the material to 40 bar H₂ until saturation) are matched by cycling the material 5 times from the outset, after which identical behaviour is observed during subsequent cycles.

At 350 °C, the benefit of catalyst coatings, in particular vanadium and chromium, on the hydrogen storage properties of atomised Mg powders are evident during activation and successive cycling up to 90 times. The material undergoes different microstructural evolution during cycling when in the presence of a surface catalyst, causing an enhancement of the ‘nucleation and growth’ stage of (de)hydrogenation. This was attributed to particle reorientation dominating particle sintering, whereas the opposite occurs for the uncoated material. Therefore, by combining these findings it proposed this increased density of nucleation sites causes a sufficient number of particles to transform into the metallic state and contract before adequate generation of sintered particle bridges is possible, which would otherwise act to restrict particle reorientation.

TiFe produced via powder atomisation obtained thermodynamic properties (dehydrogenation $\Delta H = 28.9 \pm 0.7 \text{ kJ.mol}^{-1} \text{ H}_2$ and $\Delta S = 105 \pm 2 \text{ J.K}^{-1}\text{mol}^{-1} \text{ H}_2$) in

line with published results. However, the maximum capacity achieved was ca. 0.4 wt.% lower than the theoretical value and this was attributed to several possible factors: the minor presence of an unhydriding TiFe_2 phase and the inability to remove internal stresses in the crystal structure despite undergoing an annealing stage post powder fabrication, which could be a key flaw in this powder atomisation route.

The minor substitution of Ni into $\text{TiFe}_{1-x}\text{Ni}_x$ resulted in different hydrogenation characteristics to TiFe. For example, $\text{TiFe}_{0.96}\text{Ni}_{0.04}$ possessed a dehydrogenation of $\Delta H = 29.9 \pm 0.9 \text{ kJ.mol}^{-1} \text{ H}_2$ and $\Delta S = 107 \pm 5 \text{ J.K}^{-1}\text{mol}^{-1} \text{ H}_2$ which was also demonstrated to follow the same linear enthalpy trend as those in $\text{TiFe}_{1-x}\text{Ni}_x$ alloys with greater Ni content ($x = 0.1, 0.15 \text{ \& } 0.2$) (Mintz et al., 1981). Like TiFe, $\text{TiFe}_{0.96}\text{Ni}_{0.04}$ was also observed to suffer a severe capacity reduction (0.5 wt.%) but this was mainly associated with minor carbon contamination. The introduction of carbon into the alloy was likely caused by the utilization a base Fe alloy with trace amounts of carbon and emphasises the importance of fabricating TiFe based alloys from pure elements.

The difficulties of activating atomised TiFe powder was demonstrated and the substitution of 0.04 Ni for Fe in $\text{TiFe}_{1-x}\text{Ni}_x$ was not found to produce the necessary activation requirements. Yet, with only a minor addition of Pd (1.17 wt.%) magnetron sputtered to the surface of $\text{TiFe}_{0.96}\text{Ni}_{0.04}$ successful room temperature hydrogenation is achieved with no activation treatment required. The reasonably large radial separation between Pd clusters (ca. 10-20 μm) and variation in cluster thickness (ca.

10-30 nm) demonstrate it is not necessary to have complete Pd coverage in the form of a uniform coating. In addition, it confirmed [Zaluski et al. \(1995\)](#) findings that the effectiveness of the Pd does not rely upon it alloying with the TiFe powder. Through XPS analysis, the activation of Pd-TiFe_{0.96}Ni_{0.04} is suggested to be linked to the reduction of PdO to Pd, which then adsorbs hydrogen molecules and dissociates it into atomic hydrogen. The hydrogen atoms are then likely to diffuse through the thin Pd layer, given its high hydrogen diffusibility, and directly into the alloy.

A comparison of the selected AB₂ alloys revealed that Ti_{0.9}Zr_{0.2}Mn_{1.5}V_{0.2}Cr_{0.3} obtained a higher maximum storage capacity (1.82 wt.%) but Hydralloy C5 remained the most promising alloy for the hydrogen store application with the higher working capacity (ca. 0.96 wt.%) in the pressure range of 4-15 bar at 22 °C. Nevertheless, Ti_{0.9}Zr_{0.2}Mn_{1.5}V_{0.2}Cr_{0.3} may be suitable for a hydrogen store in hotter climates as the working capacity rises with temperature in these pressure ranges, for example 0.18 wt.% at 30 °C compared to 0.94 wt.% at 40 °C. Analysis of the hydrogenation kinetics revealed both alloys best fitted the first order Avrami-Erofeev reaction rate model. Hydralloy C5 found to have an activation energy of 25.8 ± 0.3 kJ.mol H₂ and diffusion coefficients of hydrogen in the β phase ranging from 6.7×10^{-9} to 1.5×10^{-8} cm².s⁻¹ between 25-50 °C. The corresponding values for Ti_{0.9}Zr_{0.2}Mn_{1.5}V_{0.2}Cr_{0.3} were 23.3 ± 0.4 kJ.mol H₂ and 7.4×10^{-9} to 1.6×10^{-8} cm².s⁻¹. The kinetics of hydrogenation for both alloys is sufficiently fast that only the heat transfer of the storage system is the rate limiting parameter for hydrogen exchange for most technical applications.

Chapter 7

Future Work

A series of hydrogen storage studies were conducted which incorporated the magnetron sputtering of catalyst materials onto atomised powders via a Teer Coatings UDP450 system modified to a ‘tilted cup’ design. The potential application of this fairly rudimentary coating technique has been demonstrated through the improvement in the activation properties of TiFe-based intermetallics with Pd and the kinetic enhancement of catalysed atomised magnesium powders during successive cycling at 350 °C. A project desirable was to explore the scale up of the coating technique with atomised powders, given that the ‘tilted cup’ design was limited to batches of up to 50 g. It would be of interest to validate the next development in the coating technique which utilized a ‘barrel coater’ design, capable of handling powder batches ca. 200 g.

Further analysis through XPS depth profiling is necessary to quantify subsurface elemental quantities and oxidation states, as this will help to clarify whether the

mechanisms of TiFe activation involves the dissociation of hydrogen molecules on to TiFe or elemental Fe in the subsurface. Despite the failing of Mn coatings to enable room temperature activation of TiFe, it may be worthwhile to investigate magnetron sputtered vanadium on TiFe-based alloys, especially since [Oguro et al. \(1983\)](#) found only a minor addition of V in $\text{TiFe}_{0.8}\text{Ni}_{0.15}\text{V}_{0.05}$ can have a marked effect on activation.

Although Hydralloy C5 was demonstrated to be the more promising AB_2 alloy for the hydrogen store up to ca. 34 °C, new compositions based on $\text{Ti}_{0.9}\text{Zr}_{0.2}\text{Mn}_{1.5}\text{V}_{0.2}\text{Cr}_{0.3}$ could be formulated and tested. If the working capacity can be improved to match or better that of Hydralloy C5, the alloy may become commercially attractive given the lower vanadium content. In order to maximise the working capacity in the pressure range of 4-15 bar the plateau pressure needs to be increased and this may be achieved through minor substitution of Fe for either Mn or Cr ([Hong et al., 1994](#); [Komazaki et al., 1983](#)). Therefore, compositions of $\text{Ti}_{0.9}\text{Zr}_{0.2}\text{Mn}_{1.5-x}\text{V}_{0.2}\text{Cr}_{0.3}\text{Fe}_x$ and $\text{Ti}_{0.9}\text{Zr}_{0.2}\text{Mn}_{1.5}\text{V}_{0.2}\text{Cr}_{0.3-x}\text{Fe}_x$ where $x = 0.05$ and 0.1 are proposed for future testing.

Cycling stability is also of great importance and while [Bernauer et al. \(1989b\)](#) demonstrated that after 2000 cycles the capacity loss of $\text{Ti}_{0.98}\text{Zr}_{0.02}\text{Mn}_{1.5}\text{V}_{0.43}\text{Cr}_{0.05}\text{Fe}_{0.09}$ was less than 5%, this was only performed on a small laboratory sample. A 600 g prototype hydrogen store containing Hydralloy C5 was produced as part of the project. By connecting the store to a commercial electrolyser and an automated Sieverts apparatus both designed by ITM Power, cycling experiments were started however remained somewhat off the number of cycles required to replicate a commer-

cial application ($>10,000$ cycles). For this reason it is suggested the extended cycling experiments should be continued or another study with the new formulation should be undertaken.

To gain a better understanding of the porous structures generated from successive cycling of uncoated/coated magnesium powders at $350\text{ }^{\circ}\text{C}$, high resolution micro-CT and mercury porosimetry is suggested. This would enable quantification of the pore size distribution throughout the samples as opposed to the only the sample cross-section during SEM analysis. In addition, since the porous Mg structures produced by cycling at $350\text{ }^{\circ}\text{C}$ were too large to fit inside the standard ASAP 2020 N_2 adsorption sample cell, another possibility may be to conduct N_2 adsorption measurements at 77 K on the Sievert's apparatus immediately after the H_2 cycling experiments. This would provide an estimation of the surface area and therefore the porosity within the structures formed.

Lastly, it would be of interest to investigate the effects of transition metal oxide catalysts sputtered on to atomized Mg powders. The literature reports similar or even better hydrogen sorption kinetics when MgH_2 has been milled with transition metal oxides compared to transition metals (see Section 2.3.1). This was not achievable in this project because the sputter targets utilized by Teer-Miba Coating Group were also being used in other coating projects and reactive sputtering can lead to undesirable target poisoning.

Bibliography

Abbott, D. 2010. Keeping the Energy Debate Clean: How Do We Supply the World's Energy Needs? *Proceedings of the IEEE*, **98**(1):42–66.

Abedin, A.H. and Rosen, M.A. 2011. A Critical Reivew of Thermochemical Energy Storage Systems. *The Open Renewable Energy Journal*, **4**:42–46.

Ahluwalia, R.K., Hua, T.Q., and Peng, J.K. 2009. Automotive storage of hydrogen in alane. *International Journal of Hydrogen Energy*, **34**(18):7731–7740.

Akiba, E. and Okada, M. 2002. Metallic Hydrides III: Body-Centred-Cubic Solid Solution Alloys. *Materials Research Society*, **27**(9):699–703.

Akyildiz, H., Özenbas, M., and Öztürk, T. 2006. Hydrogen absorption in magnesium based crystalline thin films. *International Journal of Hydrogen Energy*, **31**(10): 1379–1383.

Amano, M., Sasaki, Y., Watanabe, R., and Shibata, M. 1983. Hydrogen storage properties of FeTi_{1+x} and $\text{FeTi}_{1+y}\text{O}_y$ flakes produced by splat cooling. *Journal of the Less Common Metals*, **89**(2):513–518.

- Amirkhiz, B.S., Zahiri, B., Kalisvaart, P., and Mitlin, D. 2011. Synergy of elemental Fe and Ti promoting low temperature hydrogen sorption cycling of magnesium. *International Journal of Hydrogen Energy*, **36**(11):6711–6722.
- Anderson, I.E. and Terpstra, R.L. 2002. Progress toward gas atomization processing with increased uniformity and control. *Material Science and Engineering A*, **326**(1):101–109.
- Andreasen, A. 2004. Predicting formation enthalpies of metal hydrides.
- Angstrom, J. 2015. Structural Basis for Hydrogen Interaction in Selected Metal Hydrides. *Uppsala Universitet*, pages 101–109.
- Antonov, V.E., Cornell, K., Fedotov, V.K., Kolesnikov, A.I., Ponyatovsky, E.G., Shiryayev, V.I., and Wipf, H. 1998. Neutron diffraction investigation of the dhcp and hcp iron hydrides and deuterides. *Journal of Alloys and Compounds*, **264**(1-2):214–222.
- Arboleda, N.B., Kasai, H., Nobuhara, K., Dino, W.A., and Nakanishi, H. 2004. Dissociation and sticking of H₂ on Mg(0001), Ti(0001) and La(0001) surfaces. *Journal of the Physical Society of Japan*, **73**(3):745–748.
- Asselli, A.A.C., Hébert, N.B., and Huot, J. 2014. The role of morphology and severe plastic deformation on the hydrogen storage properties of magnesium. *International Journal of Hydrogen Energy*, **39**(24):12778–12783.

- Baldi, A., Gremaud, R., Borsa, D.M., Balde, C.P., van-der Eeden, A.M.J., Kruijtzter, G.L., de Jongh, P.E., Dam, B., and Griessen, R. 2009. Nanoscale composition modulations in $\text{Mg}_y\text{Ti}_{1-y}\text{H}_x$ thin film alloys for hydrogen storage. *International Journal of Hydrogen Energy*, **34**(3):1450–1457.
- Barkhordarian, G., Klassen, T., and Bormann, R. 2003. Fast hydrogen sorption kinetics of nanocrystalline Mg using Nb_2O_5 as catalyst. *Scripta Materialia*, **49**(3): 213–217.
- Barkhordarian, G., Klassen, T., and Bormann, R. 2006. Kinetic investigation of the effect of milling time on the hydrogen sorption reaction of magnesium catalyzed with different Nb_2O_5 content. *Journal of Alloys and Compounds*, **407**(1-2):249–255.
- Barrett, C.S. 1973. Metallography, Structures and Phase Diagrams: Crystal Structures of Metals. *Metals Handbook*, **8**:233–250.
- Beck, R. and Mueller, W.M. 1962. *Investigation of Hydriding Characteristics of Intermetallic Compounds*. Denver Research Institute, Denver, CO.
- Beggs, C. 2009. *Energy: Management, Supply and Conservation*. Butterworth-Heinemann, Oxford, UK, 2nd edition.
- Belkbir, L., Joly, E., and Gerard, N. 1981. Comparative study of the formation-decomposition mechanisms and kinetics in LaNi_5 and magnesium reversible hydrides. *International Journal of Hydrogen Energy*, **6**(3):285–294.

- Bellemare, J. and Huot, J. 2012. Hydrogen storage properties of cold rolled magnesium hydrides with oxides catalysts. *Journal of Alloys and Compounds*, **512**(1):33–38.
- Bernauer, O. 1989a. Metal Hydride Storages. *Journal of Physical Chemistry*, **164**: 1381–1390.
- Bernauer, O. and Halene, C. 1987. Properties of metal hydrides for use in industrial applications. *Journal of the Less Common Metals*, **131**(1-2):213–224.
- Bernauer, O., Topler, J., Noreus, D., Hepplemann, R., and Richter, D. 1989b. Fundamentals and properites of some Ti/Mn based laves phase hydrides. *International Journal of Hydrogen Energy*, **14**(3):187–200.
- Bershadsky, E., Josephy, Y., and Ron, M. 1991. Investigations of kinetics and structural changes in $\text{TiFe}_{0.8}\text{Ni}_{0.2}$ after prolonged cycling. *Journal of the Less Common Metals*, **172-174**(3):1036–1043.
- Bérubé, V., Radtke, G., Dresselhaus, M., and Chen, G. 2007. Size effects on the hydrogen storage properties of nanostructured metal hydrides: A review. *International Journal of Energy Research*, **31**(6-7):636–663.
- Bevan, A., Züttel, A., Book, D., and Harris, I.R. 2011. Performance of a metal hydride store on the “Ross Barlow” hydrogen powered canal boat. *Faraday Discussions*, **151**:353–367.
- Blaine, R.L. and Kissinger, H.E. 2012. Homer Kissinger and the Kissinger equation. *Thermochemica Acta*, **540**:1–6.

- Bobet, J.L., Pechev, S., Chevalier, B., and Darriet, B. 1998. Structural and hydrogen sorption studies of $\text{NdNi}_{5-x}\text{Al}_x$ and $\text{GdNi}_{5-x}\text{Al}_x$. *Journal of Alloys and Compounds*, **267**(1-2):136–141.
- Bobet, J.L., Chevalier, B., and Darriet, B. 2000a. Crystallographic and hydrogen sorption properties of TiMn_2 based alloys. *Intermetallics*, **8**(4):359–363.
- Bobet, J.L., Akiba, E., Nakamura, Y., and Darriet, B. 2000b. Study of Mg-M (M = Co, Ni and Fe) mixture elaborated by reactive mechanical alloying - hydrogen sorption properties. *International Journal of Hydrogen Energy*, **25**(10):987–996.
- Bobet, J.L., Chevalier, B., Song, M.Y., Darriet, B., and Etourneau, J. 2002. Reactive mechanical grinding of magnesium in hydrogen and the effect of additives. *Materials and Manufacturing Processes*, **17**(3):351–361.
- Bogdanovic, B. and Schwickardi, M. 1997. Ti-doped alkali metal aluminium hydrides as potential novel reversible hydrogen storage materials. *Journal of Alloys and Compounds*, **253-254**:1–9.
- Bogdanovic, B., Bohmhammel, K., Christ, B., Schlichte, A., Vehlen, R., and Wolf, U. 1999. Thermodynamic investigation of the magnesium-hydrogen system. *Journal of Alloys and Compounds*, **282**(1):84–92.
- Bohmhammel, K., Christ, B., and Wolf, G. 1998. Kinetic investigations on the basis of isothermal DSC measurements of hydrogenation and dehydrogenation of magnesium hydride. *Thermochemica Acta*, **310**(1-2):167–171.

- Bououdina, M., Enoki, H., and Akiba, E. 1998. The investigation of the $Zr_{1-y}Ti_y(Cr_{1-x}Ni_x)_2-H_2$ system $0.0 \leq y \leq 1.0$ and $0.0 \leq x \leq 1.0$ phase compositional analysis and thermodynamic properties. *Journal of Alloys and Compounds*, **281**(2):290–300.
- Bououdina, M., Fruchart, D., Jacquet, S., Pontonnier, L., and Soubeyroux, J.L. 1999. Effect of nickel alloying by using ball milling on the hydrogen absorption properties of TiFe. *International Journal of Hydrogen Energy*, **24**(9):885–890.
- Bowman, R.C. and Tadlock, W.E. 1979. Hydrogen diffusion in β -phase titanium iron hydride. *Solid State Communications*, **32**(4):313–318.
- BP. 2015. Energy outlook 2035. pages 1–98.
- Broom, D.P. 2011. *Hydrogen Storage Materials: The Characterisation of Their Storage Properties*. Springer, London, UK, 1st edition.
- Bystrzycki, J., Czujko, T., and Varin, R.A. 2005. Processing by controlled mechanical milling of nanocomposite powders Mg + X (X = Co, Cr, Mo, V, Y, Zr) and their hydrogenation properties. *Journal of Alloys and Compounds*, **404-406**:507–510.
- Callear, S.K., Ramirez-Cuesta, A.J., Kamazawa, K., Towata, S., Noritake, T., Parker, S.F., Jones, M.O., Sugiyama, J., Ishikiriyama, M., and David, W.I. 2014. Understanding composition-property relationships in Ti-Cr-V-Mo alloys for optimisation of hydrogen storage in pressurised tanks. *Royal Society of Chemistry*, **16**:16563–16572.

- Cemak, J. and Kral, L. 2008. Hydrogen diffusion in Mg-H and Mg-Ni-H alloys. *Acta Materialia*, **56**(12):2677–2686.
- Chang, I. and Zhao, Y. 2013. *Advances in powder metallurgy - Properties, processing and applications*. Woodhead, Cambridge, UK, 1st edition.
- Chen, C.P., Liu, B.H., Li, Z.P., Wu, J., and Wang, Q.D. 1993. The activation mechanism of Mg-based hydrogen storage alloys. *Journal of Physical Chemistry*, **181**(1-2):259–267.
- Chung, H.S. and Lee, J.Y. 1986. Effect of partial substitution of Mn and Ni for Fe in FeTi on hydriding kinetics. *International Journal of Hydrogen Energy*, **11**(5): 335–339.
- Croston, D.L., Grant, D.M., and Walker, G.S. 2010. The catalytic effect of titanium oxide based additives on the dehydrogenation and hydrogenation of milled MgH₂. *Journal of Alloys and Compounds*, **492**(1-2):251–258.
- Danaie, M., Mauer, C., Mitlin, D., and Huot, J. 2011. Hydrogen storage in bulk Mg-Ti and Mg-stainless steel multilayer composites synthesized via accumulative roll-bonding (ARB). *International Journal of Hydrogen Energy*, **36**(4):3022–3036.
- Dauids, M.W., Lototsky, M., Nechaev, A., Naidoo, Q., Williams, M., and Klochko, Y. 2011. Surface modification of TiFe hydrogen storage alloy by metal-organic chemical vapour deposition of palladium. *International Journal of Hydrogen Energy*, **36**:9743–9750.

DECC, UK. 2015. 2013 UK greenhouse gas emissions, final figures. pages 1–43.

Dehouche, Z., Djaozandry, R., Huot, J., Boily, S., Goyette, J., Bose, T.K., and Schulz, R. 2000. Influence of cycling on the thermodynamic and structure properties of nanocrystalline magnesium based hydride. *Journal of Alloys and Compounds*, **305** (1-2):264–271.

Dehouche, Z., Klassen, T., Oelerich, W., Goyette, J., Bose, T.K., and Schulz, R. 2002. Cycling and thermal stability of nanostructured $\text{MgH}_2\text{-Cr}_2\text{O}_3$ composite for hydrogen storage. *Journal of Alloys and Compounds*, **347**(1-2):319–323.

Delhomme, B., de Rango, P., Marty, P., Bacia, M., Zawilski, B., Raufast, C., Miraglia, S., and Fruchart, D. 2012. Large scale magnesium hydride tank coupled with an external heat source. *International Journal of Hydrogen Energy*, **37**(11):9103–9111.

Devanathan, M.A. and Stachurski, Z. 1962. The Adsorption and Diffusion of Electrolytic Hydrogen in Palladium. *Proceedings of the Royal Society A*, **270** (1340):90–102.

DOE. 2009. Technical System Targets: Onboard Hydrogen Storage for Light-Duty Fuel Cell Vehicles.

DOE. 2013a. SunShot - Concentrating Solar Power Program Review.

DOE. 2013b. Hydride Storage Material Database: Hydride Information Center.

DOE. 2014. Hydrogen and Fuel Cells Program, Annual Progress Report.

- Dornheim, M. 2011. *Thermodynamics of Metal Hydrides: Tailoring Reaction Enthalpies of Hydrogen Storage Materials*. INTECH, 1st edition.
- Dornheim, M., Eigen, N., Barkhordarian, G., Klassen, T., and Bormann, R. 2006. Tailoring hydrogen storage materials towards application. *Advanced Engineering Materials*, **8**(5):377–385.
- Eberle, U., Felderhoff, M., and Schüth, F. 2009. Chemical and Physical Solutions for Hydrogen Storage. *Angew. Chem. Int. Ed.*, **48**(36):6608–6630.
- Edalati, K., Matsuda, J., Yanagida, A., Akiba, E., and Horita, Z. 2014. Activation of TiFe for hydrogen storage by plastic deformation using groove rolling and high pressure torsion: Similarities and differences. *International Journal of Hydrogen Energy*, **39**(28):15589–15594.
- EIA. 2015. Primary Energy Consumption by Source and Sector, 2012.
- Eigen, N., Keller, C., Dornheim, M., Klassen, T., and Bormann, R. 2007. Industrial production of light metal hydrides for hydrogen storage. *Scripta Materialia*, **56**(10):847–851.
- Ensinger, W. and Muller, H.R. 2003. Surface treatment of aluminum oxide and tungsten carbide powders by ion beam sputter deposition. *Surface and Coatings Technology*, **163-164**:281–285.
- FCHEA. 2015. Enhancing the Role of Fuel Cells for Northeast Grid Resiliency. pages 1–18.

- Fernandes, C.M., Ferreira, V.M., Senos, A.M., and Viera, M.T. 2003. Stainless steel coatings sputter-deposited on tungsten carbide powder particles. *Surface and Coatings Technology*, **176**(1):103–108.
- Ferrer, R.D., Sridharan, M.G., Garcia, G., Pi, F., and Viejo, J.R. 2007. Hydrogenation properties of pure magnesium and magnesium-aluminium thin films. *Journal of Power Sources*, **169**(1):117–122.
- Fischer, P., Schefer, J., Yvon, K., Schlapbach, L., and Riesterer, T. 1987. Orthorhombic structure of γ -TiFeD₂. *Journal of the Less Common Metals*, **129**: 39–45.
- Flanagan, T.B. and Clewley, J.D. 1982. Hysteresis in metal hydrides. *Journal of the Less Common Metals*, **83**(1):127–141.
- Freedonia. 2014. Industry Study 3165 - World Hydrogen.
- Freidrichs, O., Klassen, T., Sánchez-López, J.C., Bormann, R., and Fernández, A. 2006. Hydrogen sorption improvement of nanocrystalline MgH₂ by Nb₂O₅ nanoparticles. *Scripta Materialia*, **54**(7):1293–1297.
- Friedlmeier, G. and Bolcich, J. 1988. Production and characterization of Mg-10 wt% Ni alloys for hydrogen storage. *International Journal of Hydrogen Energy*, **13**(8): 467–474.
- Friedlmeier, G., Manthey, A., Wanner, M., and Groll, M. 1995. Cyclic stability of

- various application-relevant metal hydrides. *Journal of Alloys and Compounds*, **231**(1-2):880–887.
- Fry, C.M.P., Grant, D.M., and Walker, G.S. 2014. Catalysis and evolution on cycling of nano-structured magnesium multilayer thin films. *International Journal of Hydrogen Energy*, **39**(2):1173–1184.
- Fukai, Y. 2005. *The Metal-Hydrogen System - Basic Bulk Properties*. Springer, Berlin, Germany, 2nd edition.
- Furukawa, H., Ko, N., Go, Y.B., Aratani, N., Choi, S.B., Choi, E., Yazaydin, A.O., Snurr, R.Q., O’Keeffe, M., Kim, J., and Yaghi, O.M. 2010. Ultrahigh Porosity in Metal-Organic Frameworks. *Science*, **329**(5990):424–428.
- Gamo, T., Moriwaki, Y., Yanagihara, N., Yamshita, T., and Iwaki, T. 1985. Formation and properties of titanium-manganese alloy hydrides. *International Journal of Hydrogen Energy*, **10**(1):39–47.
- Garrier, S., Chaise, A., de Rango, P., Marty, P., Delhomme, B., Fruchart, D., and Miraglia, S. 2011. MgH₂ intermediate scale tank tests under various experimental conditions. *International Journal of Hydrogen Energy*, **36**(16):9719–9726.
- Gock, E. and Kurrer, K.E. 1999. Eccentric vibratory mills - theory and practice. *Powder Technology*, **105**(1-3):302–310.
- Gorodetskii, V.V. and Matveev, A.V. 2001. Hydrogen spillover in H₂ oxidation on Pd-Ti³⁺/TiO₂. *Studies in Surface Science and Catalysis*, **138**:85–92.

- Gray, J.E. and Luan, B. 2002. Protective coatings on magnesium and its alloys - a critical review. *Journal of Alloys and Compounds*, **336**(1-2):88–113.
- Grochala, W. and Edwards, P.P. 2004. Thermal decomposition of the non-interstitial hydrides for the storage and production of hydrogen. *Chemical Reviews*, **104**(3): 1283–1316.
- Guo, X. and Wu, E. 2008. Thermodynamics of hydrogenation for $Ti_{1-x}Zr_xMnCr$ Laves phase alloys. *Journal of Alloys and Compounds*, **455**(1-2):191–196.
- Gupta, M. Faisal A., Shervani, S., Balani, K., and Subramaniam, A. 2015. Enhanced hydrogen storage in accumulative roll bonded Mg-based hybrid. *International Journal of Hydrogen Energy*, **40**(35):11498–11505.
- Güvendirren, M., Baybörü, E., and Öztürk, T. 2004. Effects of additives on mechanical milling and hydrogenation of magnesium powders. *International Journal of Hydrogen Energy*, **29**(5):491–496.
- Hagstrom, M.T., Lund, P.D., and Vanhanen, J.P. 1995. Metal hydride hydrogen storage for near ambient temperature and atmospheric pressure applications. *International Journal of Hydrogen Energy*, **20**(11):897–909.
- Hajdu, J.B., Yarkosky, E.F., Cacciatore, P.A., and Suplicki, M.H. 1990. Electroless nickel processes for memory disks. *Symposium on Magnetic Materials, Processes and Devices*, **90**:685.

- Hall, H.W. 1949. X-ray line broadening in metals. *Proceedings of the Physical Society. Section A*, **62**(11):741–743.
- Hanada, N., Ichikawa, T., and Fujii, H. 2005. Catalytic effect of nanoparticle 3d-transition metals on hydrogen storage properties in magnesium hydride MgH_2 prepared by mechanical milling. *Journal of Physical Chemistry B*, **109**(15):7188–7194.
- Harries, D.N., Paskevicius, M., Sheppard, D.A., Price, T.E.C., and Buckley, C.E. 2012. Concentrating Solar Thermal Heat Storage Using Metal Hydrides. *Proceedings of the IEEE*, **100**(2):539–549.
- Harsha, K.S. Sree. 2006. *Principles of Physical Vapor Deposition of Thin Films*. Elsevier, The Boulevard, Langford Lane Kidlington, Oxford OX5 1GB UK, 1st edition.
- He, Y., Fan, J., and Zhao, Y. 2010. The role of differently distributed vanadium nanocatalyst in the hydrogen storage of magnesium nanostructures. *International Journal of Hydrogen Energy*, **35**(9):4162–4170.
- Heller, E.M.B., Vredenberg, A.M., and Boerma, D.O. 2006. Hydrogen uptake kinetics of Pd coated FeTi films. *Applied Surface Science*, **253**(2):771–777.
- Hempelmann, R., Richter, D., Pugliesi, R., and Vinhas, L.A. 1983. Hydrogen diffusion in the storage compound $\text{Ti}_{0.8}\text{Zr}_{0.2}\text{CrMnH}_3$. *Journal of Physics F: Metal Physics*, **13**(1):59–68.

- Hiebl, K., Tuscher, E., and Bittner, H. 1979. Investigations of hydrides in the field of η -phase $\text{Ti}_4\text{Fe}_2\text{O}$. *Chemical Monthly*, **110**(1):9–19.
- Higuchi, K., Yamamoto, K., Kajioka, H., Toiyama, K., Honda, M., Orimo, S., and Fujii, H. 2002. Remarkable hydrogen storage properties in three-layered Pd/Mg/Pd thin films. *Journal of Alloys and Compounds*, **330-332**:526–530.
- Hirscher, M. 2010. *Handbook of Hydrogen Storage: New materials for Future Energy Storage*. Wiley VCH, Darmstadt, Germany, 1st edition.
- Hoffman, K.C., Winsche, W.E., Wiswall, R.N., Reilly, J.J., Sheehan, T.V., and Waide, C.H. 1969. Metal Hydrides as a Source of Fuel for Vehicular Propulsion. *Society of Automotive Engineers*, (690232).
- Hong, C., Zhang, Y., and Han, D. 1994. Hydrogen absorption properties of pseudo-binary alloys $\text{Ti}_{0.8}\text{Zr}_{0.2}\text{Mn}_{1.5}\text{M}_{0.5}$. *Journal of Physical Chemistry*, **183**(1-2): 169–174.
- Hordeski, M.F. 2009. *Hydrogen & Fuel Cells: Advances in Transportation and Power*. Fairmont Press, USA, 1st edition.
- Horvath, H. 2009. Gustav Mie and the scattering and absorption of light by particles: Historic developments and basics. *Journal of Quantitative Spectroscopy & Radiative Transfer*, **110**(11):787–799.
- Huhn, P.A., Dornheim, M., Klassen, T., and Bormann, R. 2005. Thermal stability of

- nanocrystalline magnesium for hydrogen storage. *Journal of Alloys and Compounds*, **404-406**:499–502.
- Huot, J. 2012. Nanocrystalline metal hydrides obtained by severe plastic deformations. *Metals*, **2**(1):22–40.
- Huot, J., Liang, G., Boily, S., Van-Neste, A., and Schulz, R. 1999. Structural study and hydrogen sorption kinetics of ball-milled magnesium hydride. *Journal of Alloys and Compounds*, **293-295**:495–500.
- Huot, J., Pelletier, J.F., Lurio, L.B., Sutton, M., and Schulz, R. 2003. Investigation of dehydrogenation mechanism of MgH₂-Nb nanocomposites. *Journal of Alloys and Compounds*, **348**(1-2):319–324.
- Huston, E.L. and Sandrock, G.D. 1980. Engineering properties of metal hydrides. *Journal of the Less Common Metals*, **74**(2):435–443.
- IEA. 2014a. World energy outlook 2014 executive summary. pages 1–7.
- IEA. 2014b. World energy outlook 2014 fact sheet. pages 1–5.
- IEA. 2014c. CO₂ Emissions from Fuel Combustion. pages 1–544.
- IEA. 2014d. Technology Roadmaps for Solar Electricity. pages 1–18.
- Infomine. 2015a. Vanadium Prices and Vanadium Price Charts.
- Infomine. 2015b. Magnesium Prices and Magnesium Price Charts.

- Ingason, A.S. and Olafsson, S. 2006. Influence of MgO nano-crystals on the thermodynamics, hydrogen uptake and kinetics in Mg films. *Thin Solid Films*, **515**(2):708–711.
- IPHE. 2011. Renewable hydrogen report March 2011. pages 1–22.
- Jaccard, M. 2005. *Sustainable Fossil Fuels: The Unusual Suspect in the Quest for Clean and Enduring Energy*. Cambridge University Press, Cambridge, UK, 1st edition.
- Jain, I.P., Vijay, Y.K., Malhotra, L.K., and Uppadhyay, K.S. 1988. Hydrogen storage in thin film metal hydride - a review. *International Journal of Hydrogen Energy*, **13**(1):15–23.
- Jain, I.P., Jain, P., and Jain, A. 2010. Novel hydrogen storage materials: A review of lightweight complex hydrides. *Journal of Alloys and Compounds*, **503**(2):303–339.
- Johnson, J.R. 1980. Reaction of hydrogen with the high temperature (C14) form of TiCr_2 . *Journal of the Less Common Metals*, **73**(2):345–354.
- Jolibois, P. 1912. Study of pure magnesium and magnesium hydrides. *Compt. Rend. Acad. Sci. Paris*, **155**:353–355.
- Kabiri, Y., Kermanpur, A., and Foroozmehr, A. 2012. Comparative study on microstructure and homogeneity of NiTi shape memory alloy produced by copper boat induction melting and conventional vacuum arc melting. *Vacuum*, **86**(8): 1073–1077.

- Kalisvaart, W.O., Kubis, A., Danaie, M., Amirkhiz, B.S., and Mitlin, D. 2011. Microstructural evolution during hydrogen sorption cycling of Mg-FeTi nanolayered composites. *Acta Materialia*, **59**(5):2083–2095.
- Kalkarni, N.S., Warmack, R.J.B., Radhakrishnan, B., Hunter, J.L., Sohn, Y., Coffey, K.R., Murch, G.E., and Belova, I.V. 2014. Overview of SIMS-Based Experimental Studies of Tracer Diffusion in Solids and Application to Mg Self-Diffusion. *Journal of Phase Equilibria and Diffusion*, **35**(6):762–778.
- Kandavel, M. and Ramaprabhu, S. 2004. Hydriding properties of Ti-substituted non-stoichiometric AB₂ alloys. *Journal of Alloys and Compounds*, **381**(1-2):140–150.
- Kelly, P.J. and Arnell, R.D. 2000. Magnetron sputtering: a review of recent developments and applications. *Vacuum*, **56**(3):159–172.
- Kelton, K.F. 1997. Analysis of crystallization kinetics. *Materials Science and Engineering A*, **226**:142–150.
- Kim, H.C. and Lee, J.Y. 1985. The effect of surface conditions on the activation of FeTi. *Journal of the Less Common Metals*, **105**(2):247–253.
- Klose, W. and Stuke, V. 1995. Investigations of the thermodynamic equilibrium in the hydrogen-magnesium-magnesium hydride system. *International Journal of Hydrogen Energy*, **20**(4):309–316.
- Klyamkin, S.N., Verbetsky, V.N., and Demidov, V.A. 1994. Thermodynamics of

- hydride formation and decomposition for TiMn₂-H₂ system at pressure up to 2000 atm. *Journal of Alloys and Compounds*, **205**(1-2):L1–L2.
- Komazaki, Y., Uchida, M., and Suda, S. 1983. Equilibrium properities of Ti-Zr-Fe-Mn hydrides. *Journal of the Less Common Metals*, **89**(1):269–274.
- Kramer, R. and Andre, M. 1979. Adsorption of atomic hydrogen on alumina by hydrogen spillover. *Journal of Catalysis*, **58**(2):287–295.
- Krozer, A. and Kasemo, B. 1989. Equilibrium hydrogen uptake and associated kinetics for the Mg-H₂ system at low pressures. *Journal of Physics: Condensed Matter*, **1**(8):1533–1538.
- Kuravi, S., Trahan, J., Goswami, D.Y., Rahman, M.M., and Stefanakos, E.K. 2013. Thermal energy storage technologies and systems for concentrating solar power plants. *Progress in Energy and Combustion Science*, **39**(4):285–319.
- Kurrer, K.E. and Gock, E. 1986. Influence of operating conditions on the motion and shock collision in tube vibrating mills. *Mineral Processing*, **10**:546–554.
- Kusadome, Y., Ikeda, K., Nakamori, Y., Orimo, S., and Horita, Z. 2007. Hydrogen storage capabilities of Mg₂Ni processed by high pressure torsion. *Scripta Materialia*, **57**(8):751–753.
- Lang, J., Asselli, A.A.C., Hérbert, N.B., and Huot, J. 2011. The influence of morphology on the hydrogen storage properties of magnesium based materials processed by cold rolling. *Advanced Materials Research*, **922**:400–405.

- Laversenne, L., Andrieux, J., Plante, D., Lyard, L., and Miraglia, S. 2013. In operando study of TiVCr additive in MgH₂ composites. *International Journal of Hydrogen Energy*, **38**(27):11937–11945.
- Law, H.H., Vyas, B., Zahurak, S.M., and Kammlott, G.W. 1996. A novel plating process for microencapsulating metal hydrides. *Journal of the Electrochemical Society*, **143**(18):2596–2600.
- Lee, J.Y., Byun, S.M., Park, C.N., and Park, J.K. 1982. A study of the hydriding kinetics of tife and its alloys. *Journal of Less Common Metals*, **87**:149–164.
- Lee, S.M. and Perng, T.P. 1999. Correlation of the substitutional solid solution with hydrogenation properties of TiFe_{1-x}M_x (M = Ni, Co, Al) alloys. *Journal of Alloys and Compounds*, **291**(1-2):254–261.
- Lee, S.M. and Perng, T.P. 2000. Effects of boron and carbon on the hydrogenation properites of TiFe and Ti_{1.1}Fe. *International Journal of Hydrogen Energy*, **25**: 831–836.
- Léon, A., Knystautas, E., Huot, J., and Schulz, R. 2002. Hydrogenation characteristics of air-exposed magnesium films. *Journal of Alloys and Compounds*, **345**(1):158–166.
- Li, G., Nishimiya, N., Satoh, H., and Kamegashira, N. 2005. Crystal structure and hydrogen absorption of Ti_xZr_{1-x}Mn₂. *Journal of Alloys and Compounds*, **393**(1-2): 231–238.

- Liang, G., Huot, J., Van-Neste, S. Boily A., and Schulz, R. 1999a. Catalytic effect of transition metals on hydrogen sorption in nanocrystalline ball milled MgH_2 -Tm (Tm = Ti, V, Mn, Fe and Ni) systems. *Journal of Alloys and Compounds*, **292**(1-2):247–252.
- Liang, G., Huot, J., Van-Neste, S. Boily A., and Schulz, R. 1999b. Hydrogen storage properties of the mechanically milled MgH_2 -V nanocomposite. *Journal of Alloys and Compounds*, **291**(1-2):295–299.
- Libowitz, G.G., Hayes, H.F., and Gibb, T.R.P. 1958. The system zirconium-nickel and hydrogen. *Journal of Physical Chemistry*, **62**(1):76–79.
- Liu, B.H., Kim, D.M., Lee, K.Y., and Lee, J.Y. 1996. Hydrogen storage properties of TiMn_2 -based alloys. *Journal of Alloys and Compounds*, **240**(1-2):214–218.
- Liu, J. and Huston, E.L. 1983. RNi_5 hydrogen storage compounds (R = rare earth). *Journal of the Less Common Metals*, **90**(1):11–20.
- Liu, W. and Kondo-Francois, A.Z. 2014a. Size effects and hydrogen storage properties of Mg nanoparticles synthesised by an electroless plating method. *Journal of Materials Chemistry A*, **2**(25):9718–9726.
- Liu, W., Setijadi, E.J., and Kondo-Francois, A.Z. 2014b. Tuning the Thermodynamic Properties of MgH_2 at the Nanoscale via a Catalyst or Destabilizing Element Coating Strategy. *Journal of Materials Chemistry C*, **118**(48):27781–27792.

- Lykhach, Y., Staudt, T., Vorokhta, M., Skala, T., Johaneck, V., Prince, K.C., Matolin, V., and Libuda, J. 2012. Hydrogen spillover monitored by resonant photoemission spectroscopy. *Journal of Catalysis*, **285**(1):6–9.
- Maeland, A.J. 1964. Investigation of the Vanadium-Hydrogen System by X-Ray Diffraction Techniques^{1,2}. *Journal of Physical Chemistry*, **68**(8):2197–2200.
- Manickam, K., Grant, D.M., and Walker, G.S. 2015. Optimization of AB₂ type alloy composition with superior hydrogen storage properties for stationary applications. *International Journal of Hydrogen Energy*, **40**(46):16288–16296.
- Matsumoto, T. and Amano, M. 1981. The hydriding of FeTi during an activation treatment by in-situ X-Ray diffraction. *Scripta Metallurgica*, **15**(8):879–883.
- May, M.M., Lewerenz, H.J., Lackner, D., Dimroth, F., and Hannappel, T. 2015. Efficient direct solar-to-hydrogen conversion by in situ interface transformation of a tandem structure. *Nature*, **6**(8286):1–7.
- Metalpages. 2015. Titanium, Manganese, Zirconium, Chromium and Vanadium Price Charts.
- Mintz, M.H. and Zeiri, Y. 1995. Hydriding Kinetics of powders. *Journal of Alloys and Compounds*, **216**(2):159–175.
- Mintz, M.H., Vaknin, S., Biderman, S., and Hadari, Z. 1981. Hydrides of ternary TiFe_xM_{1-x} (M= Cr, Mn, Co, Ni) intermetallic. *Journal of Applied Physics*, **52**(463):463–467.

- Mitchell, P.C., Ramirez-Costa, A.J., Parker, S.F., Tomkinson, J., and Thompsett, D. 2003. Hydrogen spillover on carbon-supported metal catalysts studied by inelastic neutron scattering. Surface vibrational states and hydrogen riding modes. *Journal of Physical Chemistry B*, **107**(28):6838–6845.
- Mitrokhin, S.V., Bezuglaya, T.N., and Verbetsky, V.N. 2002. Structure and hydrogen sorption properties of (Ti,Zr)-Mn-V alloys. *Journal of Alloys and Compounds*, **330-332**:146–151.
- Mizuno, T. and Morozumi, T. 1982. Titanium concentration in FeTi_x ($1 \leq x \leq 2$) alloys and its effect on hydrogen storage properties. *Journal of the Less Common Metals*, **84**(1):237–244.
- Montone, A., Aurora, A., Gattia, D.M., and Antisari, M.V. 2010. On the barriers limiting the reaction kinetics between catalysed Mg and hydrogen. *Scripta Materialia*, **63**(4):456–459.
- Montone, A., Aurora, A., and Gattia, D.M. 2013. Effect of the temperature and of the catalyst on the hollow particle formation in the Mg composites. *International Journal of Hydrogen Energy*, **38**(27):12146–12151.
- Moretto, P., Zlotea, C., Dolci, F., Amieiro, A., Bobet, J.L., Borgschulte, A., Chandra, D., Enoki, H., Rango, P. De, Fruchart, D., Jepsen, J., Latroche, M., Jansa, I. Llamas, Moser, D., Sartori, S., Wang, S.M., and Zan, J.A. 2013. A Round Robin

- Test exercise on hydrogen absorption/desorption properties of a magnesium hydride based material. *International Journal of Hydrogen Energy*, **38**(16):6704–6717.
- Murray, J.L. 1981. The Mn-Ti (Manganese-Titanium) system. *Bulletin of Alloy Phase Diagrams*, **2**(3):334–343.
- Mushinikov, N.V., Ermakov, A.E., Uimin, M.A., Gaviko, V.S., Terent'ev, P.B., Skripov, A.V., Tankeev, A.P., Soloninin, A.V., and Buzlukov, A.L. 2006. Kinetics of interaction of Mg-based mechanically activated alloys with hydrogen. *The Physics of Metals and Metallography*, **102**(4):421–431.
- Nagai, H., Kitagaki, K., and Shoji, K. 1987. Microstructure and hydriding characteristics of FeTi alloys containing manganese. *Journal of the Less Common Metals*, **134**(2):275–286.
- Nakano, H., Wakao, S., and Shimizu, T. 1997. Correlation between crystal structure and electrochemical properties of C14 Laves-phase alloys. *Journal of Alloys and Compounds*, **253-254**:609–612.
- Nemirovskaya, I.E., Alekseev, A.M., and Lunin, V.V. 1991. Thermodynamics of processes of hydrogen sorption by hydrides of intermetallic compounds of CrB structural type. *Journal of Alloys and Compounds*, **177**(1):1–15.
- Neto, M.B., Patzschke, C., Lange, M., Möllmer, J., Möllmer, A., Fichtner, S., Schrage, C., Lässig, D., Lincke, J., Staudt, R., Krautscheid, H., and Gläser, R.

2012. Assessment of hydrogen storage by physisorption in porous materials. *Energy & Environmental Science*, **5**:8294–8303.
- Nijkamp, M.G., Raaymakers, J.E.M.J., van Dillen, A.J., and de Jong, K.P. 2001. Hydrogen storage using physisorption - materials demands. *Applied Physics A*, **72** (5):619–623.
- NIST. 2009. Database of the Thermophysical Properties of Gases Used in the Semiconductor Industry.
- Noritake, T., Aoki, M., Towata, S., Seno, Y., Hirose, Y., Nishibori, E., Takata, M., and Sakata, M. 2002. Chemical bonding of hydrogen in MgH₂. *Applied Physics Letters*, **81**(11):2008–2010.
- Norskov, J.K., Houmoller, A., Johansson, P.K., and Lundqvist, B.I. 1981. Adsorption and dissociation of H₂. *Physical Review Letters*, **46**(4):257–260.
- Oelerich, W., Klassen, T., and Bormann, R. 2001a. Comparison of the catalytic effects of V, V₂O₅, VN and VC on the hydrogen sorption of nanocrystalline Mg. *Journal of Alloys and Compounds*, **322**(1-2):L5–L9.
- Oelerich, W., Klassen, T., and Bormann, R. 2001b. Metal oxides as catalysts for improved hydrogen sorption in nanocrystalline Mg-based materials. *Journal of Alloys and Compounds*, **315**(1-2):237–242.
- Oesterreicher, H. and Bittner, H. 1978. Studies of hydride formation in Ti_{1-x}Zr_xMn₂. *Materials Research Bulletin*, **13**(1):83–88.

- Oguro, K., Osumi, Y., Suzuki, H., and Kato, A. 1983. Hydrogen storage properties of $\text{TiFe}_{1-x}\text{Ni}_y\text{M}_z$ alloys. *Journal of the Less Common Metals*, **89**(1):275–279.
- Orimo, S., Nakamori, Y., Eliseo, J.R., Züttel, A., and Jensen, C.M. 2007. Complex Hydrides for Hydrogen Storage. *Chem. Rev*, **107**(10):4111–4132.
- Oriňáková, R. and Oriňák, A. 2011. Recent applications of carbon nanotubes in hydrogen production and storage. *Fuel*, **90**(11):3123–3140.
- Ouyang, L.Z., Ye, S.Y., Dong, H.W., and Zhu, M. 2007. Effect of interfacial free energy on hydriding reaction of Mg-Ni thin films. *Applied Physics Letter*, **90**(2): 021917.
- Pan, Y. *Formation of Superhexagonal Chromium Hydride by Exposure of Chromium Thin Film to High Temperature, High Pressure Hydrogen in a Ballistic Compressor*. PhD thesis, Portland State University, 1991.
- Pande, C.S., Pick, M.A., and Sabatini, R.L. 1980. The “activation” of FeTi for hydrogen absorption; an electron microscopy study. *Scripta Metallurgica*, **14**(8): 899–903.
- Panzas, P.K., Dornheim, M., Bellmann, D., Aguey-Zinsou, K.F., Klassen, T., and Schreyer, A. 2006. SANS/USANS investigations of nanocrystalline MgH_2 for reversible storage of hydrogen. *Physica B*, **385-386**(1):630–632.
- Park, C.N. 1992. A simple method of electroless copper plating for the preparation of metal hydride electrodes. *Journal of Alloys and Compounds*, **182**(2):321–330.

- Paskevicius, M., Sheppard, D.A., and Buckley, C.E. 2010. Thermodynamic changes in mechanochemically synthesized magnesium hydride nanoparticles. *Journal of the American Chemical Society*, **132**(14):5077–5083.
- Pasquini, L., Montone, A., Callini, E., Antisari, M.V., and Bonetti, E. 2011. Formation of hollow structures through diffusive phase transition across a membrane. *Applied Physics Letters*, **99**(2):021911.
- Patah, A., Takasaki, A., and Szmyd, J.S. 2009. Influence of multiple oxide ($\text{Cr}_2\text{O}_3/\text{Nb}_2\text{O}_5$) addition on the sorption kinetics of MgH_2 . *International Journal of Hydrogen Energy*, **34**(7):3032–3037.
- Pebler, A. and Gulbransen, E.A. 1967. Equilibrium studies on the systems $\text{ZrCr}_2\text{-H}_2$, $\text{ZrV}_2\text{-H}_2$ and $\text{ZrMo}_2\text{-H}_2$ between 0° and 900°C . *Transactions of the Metallurgical Society of AIME*, **239**(10):1593–1600.
- Pedersen, A.S., Kjølner, J., Larsen, B., and Vigeholm, B. 1983. Magnesium for hydrogen storage. *International Journal of Hydrogen Energy*, **8**(3):205–211.
- Pedersen, A.S., Kjølner, J., Larsen, B., Vigeholm, B., and Jensen, J.A. 1984. Long-term cycling of the magnesium hydrogen system. *International Journal of Hydrogen Energy*, **9**(9):799–802.
- Pighin, S.A., Capurso, G., Russo, S.L., and Peretti, H.A. 2012. Hydrogen sorption kinetics of magnesium hydride enhanced by the addition of $\text{Zr}_8\text{Ni}_{21}$ alloy. *Journal of Alloys and Compounds*, **530**:111–115.

- Pinaud, B.A., Benck, J.D., Seitz, L.C., Forman, A.J., Chen, Z., Deutsch, T.G., James, B.D., Baum, K.N., Baum, G.N., Ardo, S., Wang, H., Miller, E., and Jaramillo, T.F. 2013. Technical and economic feasibility of centralized facilities for solar hydrogen production via photocatalysis and photoelectrochemistry. *Energy and Environmental Science*, **6**(7):1983–2002.
- Pitt, M.P., Paskevicius, M., Webb, C.J., Sheppard, D.A., Buckley, C.E., and Gray, E.M. 2012. The synthesis of nanoscopic Ti based alloys and their effects on the MgH₂ system compared with the MgH₂ + 0.01Nb₂O₅ benchmark. *International Journal of Hydrogen Energy*, **37**(5):4227–4237.
- Prins, R. 2012. Hydrogen Spillover. Facts and Fiction. *Chemical Reviews*, **112**(5): 27142738.
- Pureiron. 2015. Iron Price Chart.
- Qu, J., Sun, B., Yang, R., Zhao, W., Wang, Y., and Li, X. 2010. Hydrogen absorption kinetics of Mg thin films under mild conditions. *Scripta Materialia*, **62**(5):317–320.
- Ramzan, M., Hussain, T., and Ahuja, R. 2009. Hydrogen diffusion in bulk and nanoclusters of MgH₂ and the role of catalysts on the basis of ab initio molecular dynamics. *Applied Physics Letters*, **94**(22):221910.
- Reichelstein, S. and Yorston, M. 2013. The prospect for cost competitive solar PV power. *Energy Policy*, **55**:117–127.

- Reilly, J.J. 1978. Applications of metal hydrides. *Hydrides for Energy Storage*, pages 527–550.
- Reilly, J.J. 1979. Metal Hydride Technology. *Brookhaven National Laboratory*.
- Reilly, J.J. and Wiswall, R.H. 1968. The Reaction of Hydrogen with Alloys of Magnesium and Nickel and the Formation of Mg_2NiH_4 . *Inorganic Chemistry*, **7**(11):2254–2256.
- Reilly, J.J. and Wiswall, R.H. 1970. The Higher Hydrides of Vanadium and Niobium. *Inorganic Chemistry*, **9**(7):1678–1682.
- Reilly, J.J. and Wiswall, R.H. 1972. Hydrogen Storage and Purification Systems II. *Brookhaven National Laboratory*.
- Reilly, J.J. and Wiswall, R.H. 1974. Formation and Properties of Iron Titanium Hydride. *Inorganic Chemistry*, **13**(1):218–222.
- Reilly, J.J., Johnson, J.R., and Reidinger, F. 1980. Lattice Expansion as a Measure of Surface Segregation and Solubility of Hydrogen in $\alpha\text{-FeTiH}_x$. *Brookhaven National Laboratory*.
- Renner, J. and Grabke, H.G. 1978. Determination of diffusion coefficients in the hydriding of alloys. *Journal of Physical Metallurgy*, **69**(10):639–642.
- Rosnagel, S.M. 1995. Sputter Deposition. *Advanced and Surface Engineering*, Technomic Publishing.

- Rupp, B. 1984. On the change in physical properties of $\text{Ti}_{4-x}\text{Fe}_{2+x}\text{O}_y$ during hydrogenation I: Activation behaviour of ternary oxides $\text{Ti}_{4-x}\text{Fe}_{2+x}\text{O}_y$ and $\beta\text{-Ti}$. *Journal of the Less Common Metals*, **104**(1):51–63.
- RWE Solar Millennium. 2009. The parabolic trough power plants Andasol 1 to 3. pages 1–26.
- Sabitu, S.T. and Goudy, A.J. 2012. Dehydrogenation Kinetics and Modeling Studies of MgH_2 Enhanced by Transition Metal Oxide Catalysts Using Constant Pressure Thermodynamic Driving Forces. *Metals*, **2**(3):219–228.
- Sakai, T., Miyamura, H., Kuriyama, N., Kato, A., Oguro, K., and Ishikawa, H. 1990. Metal Hydride Anodes for Nickel-Hydrogen Secondary Battery. *Journal of the Electrochemical Society*, **137**(3):795–799.
- Sakintuna, B., Lamari-Darkrim, F., and Hirscher, M. 2007. Metal hydride materials for solid hydrogen storage: A review. *International Journal of Hydrogen Energy*, **32**(9):1121–1140.
- San-Martin, A. and Manchester, F.D. 1987. The H-Mg (Hydrogen-Magnesium) system. *Journal of phase equilibria*, **8**(5):431–437.
- Sandrock, G. 1997. State-of-the-art review of hydrogen storage in reversible metal hydrides for military fuel cell application. pages 1–169.
- Sandrock, G. 1999. A panoramic overview of hydrogen storage alloys from a gas reaction point of view. *Journal of Alloys and Compounds*, **293-295**:877–888.

- Sandrock, G. and Goodell, P.D. 1984. Cyclic life of metal hydrides with impure hydrogen: Overview and engineering considerations. *Journal of Less Common Metals*, **104**:159–173.
- Sandrock, G., Murray, J.J., Post, M.L., and Taylor, J.B. 1982. Hydrides and deuterides of CaNi_5 . *Materials Research Bulletin*, **17**(7):887–894.
- Schlapbach, L. and Riesterer, T. 1983. The Activation of FeTi for Hydrogen Absorption. *Applied Physics A*, **32**(4):169–182.
- Schlapbach, L. and Züttel, A. 2001. Hydrogen-storage materials for mobile applications. *Nature*, **414**(6861):353–358.
- Schlapbach, L., Seiler, A., Stuck, F., and Siegmann, H.C. 1980. Surface effects and the formation of metal hydrides. *Journal of the Less Common Metals*, **73**(1):145–160.
- Schmid, G., Eisenmenger-Sittner, C., Hell, J., Horkel, M., Keding, M., and Mahr, H. 2010. Optimization of a container design for depositing uniform metal coatings on glass microspheres by magnetron sputtering. *Surface and Coatings Technology*, **205**(7):1929–1936.
- Schober, T. 1979. The iron titanium - hydrogen system: A transmission electron microscopy (TEM) study. *Scripta Metallurgica*, **13**(2):107–112.
- Schober, T. and Westlake, D.G. 1981. The activation of FeTi for hydrogen storage: A different view. *Scripta Metallurgica*, **15**(8):913–918.

- Schüth, F., Bogdanovic, B., and Felderhoff, M. 2004. Light metal hydrides and complex hydrides for hydrogen storage. *Chemical Communications*, (20):2249–2258.
- Sevlam, P., Viswanathan, B., Swamy, C.S., and Srinivasan, V. 1987. X-Ray photoelectron spectroscopic investigations of the activation of FeTi for hydrogen uptake. *International Journal of Hydrogen Energy*, **2**(4):245–250.
- Shao, H., Wang, Y., Xu, H., and Li, X. 2004. Hydrogen storage properties of magnesium ultrafine particles prepared by hydrogen plasma-metal reaction. *Materials Science and Engineering: B*, **110**(2):221–226.
- Shenzhong, Y., Rong, Y., Tiesheng, H., Shilong, Z., and Bingzhao, C. 1988. A study of the activation of FeTi and Fe_{0.9}TiMn_{0.1}. *International Journal of Hydrogen Energy*, **13**(7):433–437.
- Sholl, D.S. 2007. Using density functional theory to study hydrogen diffusion in metals: A brief overview. *Journal of Alloys and Compounds*, **446-447**:462–468.
- Skripnyuk, V. and Ron, M. 2003. Hydrogen desorption kinetics in intermetallic compounds C2, C5₁ and C5₂ with Laves phases structure. *International Journal of Hydrogen Energy*, **28**(3):303–309.
- Skripnyuk, V., Buchman, E., Rabkin, E., Estrin, Y., Popov, M., and Jorgensen, S. 2007. The effect of equal channel angular pressing on hydrogen storage properties of a eutectic Mg-Ni alloy. *Journal of Alloys and Compounds*, **436**(1):99–106.

- Stackelberg, M. Von and Ludwig, P. 1964. For diffusion behaviour of hydrogen in palladium hydrogen. *Journal for Nature Research A*, **19**(1):93–99.
- Stampfer, J.F., Holley, C.E., and Suttle, J.F. 1960. The Magnesium-Hydrogen System. *Journal of the American Chemical Society*, **82**(14):3504–3508.
- Stolten, D. 2010. *Hydrogen and Fuel Cells - Fundamentals, Technologies and Applications*. Wiley VCH, Morlenbach, Germany, 1st edition.
- Suib, S.L. 2013. *New and Future Developments in Catalysis: Batteries, Hydrogen Storage and Fuel Cells*. Elsevier, Oxford, UK, 1st edition.
- Suryanarayana, C. and Grant-Norton, M. 2013. *X-Ray Diffraction: A Practical Approach*. Springer, New York, 2nd edition.
- Tamme, R. 2003. Concrete Storage: Update on the German concrete TES program. *Institute of Technical Thermodynamics*, pages 1–25.
- Tan, X., Harrower, C.T., Amirkhiz, B.S., and Mitlin, D. 2009. Nano-scale bi-layer Pd/Ta, Pd/Nb, Pd/Ti and Pd/Fe catalysts for hydrogen sorption in magnesium thin films. *International Journal of Hydrogen Energy*, **34**(18):7741–7748.
- Tanniru, M., Tien, H.Y., and Ebrahimi, F. 2010. Study of the dehydrogenation behavior of magnesium hydride. *Scripta Materialia*, **63**(1):58–60.
- Thomas, K.M. 2009. Adsorption and desorption of hydrogen on metal-organic

- framework materials for storage applications: comparison with other nanoporous materials. *Dalton Transactions*, (9):1487–1505.
- Thompson, P., Reilly, J.J., Reidinger, F., Hastings, J.M., and Corliss, L.M. 1979. Neutron diffraction study of γ iron titanium deuteride. *Journal of Physics F: Metal Physics*, **9**(4):61–66.
- Thompson, P., Reilly, J.J., and Hastings, J.M. 1989. The application of the Reitveld method to a highly strained material with microtwins: $\text{TiFeD}_{1.9}$. *Journal of Applied Crystallography*, **22**(3):256–260.
- Tian, Y. and Zhao, C.Y. 2013. A review of solar collectors and thermal energy storage in solar thermal applications. *Applied Energy*, **104**:538–553.
- Ulmer, U., Asano, K., Patyk, A., Enoki, H., Nakamura, Y., Pohl, A., Dittmeyer, R., and Fichtner, M. 2015. Cost reduction possibilities of vanadium-based solid solutions - Microstructural, thermodynamic, cyclic and environmental effects of ferrovandium substitution. *Journal of Alloys and Compounds*, **648**:1024–1030.
- Van-Essen, R.M. and Buschow, K.H.J. 1979. Hydrogen absorption in various zirconium- and hafnium-based intermetallic compounds. *Journal of Less Common Metals*, **64**(2):277–284.
- Varin, R.A., Czujko, T., and Wronski, Z. 2006. Particle size, grain size and γ - MgH_2 effects on the desorption properties of nanocrystalline commercial magnesium

- hydride processed by controlled mechanical milling. *Nanotechnology*, **17**(15): 3856–3865.
- Verga, M., Armanasco, F., Guardamagna, C., Valli, C., Bianchin, A., Agresti, F., Russo, S.L., Maddalena, A., and Principi, G. 2009. Scaling up of Mg hydride in a temperature and pressure-controlled hydrogen storage device. *International Journal of Hydrogen Energy*, **34**(10):4602–4610.
- Vigeholm, B., Kjølner, J., Larsen, B., and Pedersen, A.S. 1983. Formation and decomposition of magnesium hydride. *Journal of the Less Common Metals*, **89**(1): 135–144.
- Vigeholm, B., Jensen, K., Larsen, B., and Pedersen, A.S. 1987. Elements of hydride formation mechanisms in nearly spherical magnesium powder particles. *Journal of the Less Common Metals*, **131**(1-2):133–141.
- Vijay, R., Sundaresan, R., Maiya, M.P., Murthy, S.S., Fu, Y., Klein, H.P., and Groll, M. 2004. Characterisation of Mg-x wt% FeTi ($x = 5-30$) and Mg-40 wt% FeTiMn hydrogen absorbing materials prepared by mechanical alloying. *Journal of Alloys and Compounds*, **384**(1-2):283–295.
- Villeroy, B., Cuevas, F., Bettembourg, J., Olier, P., and Latroche, M. 2006. Influence of Ti/Zr ratio and the synthesis route on hydrogen absorbing properties of $(\text{Ti}_{1-x}\text{Zr}_x)\text{Mn}_{1.5}\text{V}_{0.5}$ alloys. *Journal of Physics and Chemistry of Solids*, **67**(5-6): 1281–1285.

- Vincent, S.D., Lang, J., and Huot, J. 2012. Addition of catalysts to magnesium hydride by means of cold rolling. *Journal of Alloys and Compounds*, **512**(1): 290–295.
- Walker, G. 2008. *Solid-state hydrogen storage: materials and chemistry*. Woodhead Publishing, Cambridge, UK, 1st edition.
- Wang, B., Ji, Z., Zimone, F.T., Janowski, G.M., and Rigsbee, J.M. 1997. A technique for sputter coating of ceramic reinforcement particles. *Surface and Coatings Technology*, **91**(1-2):64–68.
- Ward, P.A., Corgnale, C., Teprovich, J.A., Motyka, T., Hardy, B., Peters, B., and Zidan, R. 2015. High performance metal hydride based thermal energy storage systems for concentrating solar power applications. *Journal of Alloys and Compounds*, Available Online:1–5.
- Wengenmayr, R. and Bürke, T. 2013. *Renewable Energy: Sustainable Energy Concepts for the Energy Change*. Wileys VCH, Weinheim, Germany, 2nd edition.
- Wernick, J.H. 1967. “*Topologically Close-Packed Structures*” in *Intermetallic Compounds*. John Wiley, New York.
- Williams, M., Lototsky, M.V., Davids, M.W., Linkov, V., Yartys, V.A., and Solberg, J.K. 2011. Chemical surface modification for the improvement of the hydrogenation kinetics and poisoning resistance of TiFe. *Journal of Alloys and Compounds*, **509S**: 770–774.

- Xu, G., Zhu, Y., Ma, J., Yan, H., and Xie, Y. 1997. TPR of Pd/MnO₂ and Pd/Fe₂O₃ systems - effects of hydrogen spillover. *Studies in Surface Science and Catalysis*, **112**:333–338.
- Xu, Y.H., Chen, C.P., Geng, W.X., and Wang, Q.D. 2001. The hydrogen storage properties of Ti-Mn based C14 Laves phases intermetallics as hydrogen resource for PEMFC. *International Journal of Hydrogen Energy*, **26**(6):593–596.
- Yamanaka, K., Saito, H., and Someno, M. 1975. Hydride formation of intermetallic compounds of titanium-iron, titanium-cobalt, titanium-nickel and titanium-copper. *The Chemical Society of Japan*, **8**:1267–1272.
- Yan, T., Wang, R.Z., Li, T.X., Wang, L.W., and Fred, I.T. 2015. A review of promising candidate reactions for chemical heat storage. *Renewable and Sustainable Energy Reviews*, **43**:13–31.
- Yang, J., Sudik, A., Wolverton, C., and Siegel, D.J. 2010. High capacity hydrogen storage materials: attributes for automotive applications and techniques for materials discovery. *Chemical Society Reviews*, **39**(2):656–675.
- Yang, S.J., Jung, H., Kim, T., and Park, C.R. 2012. Recent advancements in hydrogen storage technologies based on nanoporous carbon materials. *Progress in Natural Science: Materials International*, **22**(6):631–638.
- Young, K., Fetchenko, M.A., Li, F., and Ouchi, T. 2008. Structural, thermodynamic

- and electrochemical properties of $\text{Ti}_x\text{Zr}_{1-x}(\text{VNiCrMnCoAl})_2$ C14 Laves phase alloys. *Journal of Alloys and Compounds*, **464**(1-2):238–247.
- Young, K., Ouchi, T., Koch, J., and Fetchenko, M.A. 2009. The role of Mn in C14 Laves phase multi-component alloys for NiMH battery application. *Journal of Alloys and Compounds*, **477**(1-2):749–758.
- Yu, X.B., Wu, Z., Xia, B.J., and Xu, N.X. 2004. Enhancement of hydrogen storage capacity of Ti-V-Cr-Mn BCC phase alloys. *Journal of Alloys and Compounds*, **372**(1-2):272–277.
- Yu, X.B., Wu, Z., Chen, Q.R., Dou, T., Chen, J.Z., Xia, B.J., and Xu, N.X. 2007. Effect of V addition on activation performances of $\text{TiMn}_{1.25}\text{Cr}_{0.25}$ hydrogen storage alloy. *Journal of Materials Processing Technology*, **182**(1-3):549–554.
- Yvon, K. 1998. Complex Transition-Metal Hydrides. *Chimia*, **52**:613–619.
- Zaluska, A., Zaluski, L., and Ström-Olsen, J.O. 1999. Nanocrystalline magnesium for hydrogen storage. *Journal of Alloys and Compounds*, **288**(1-2):217–225.
- Zaluska, A., Zaluski, L., and Ström-Olsen, J.O. 2001. Structure, catalysis and atomic reactions on the nano-scale: a systematic approach to metal hydrides for hydrogen storage. *Applied Physics A*, **72**(2):157–165.
- Zaluski, L., Tessier, P., Ryan, D.H., Doner, C.B., Zaluska, A., Ström-Olsen, J.O., Trudeau, M.L., and Schulz, R. 1993. Amorphous and nanocrystalline Fe-Ti prepared by ball milling. *Journal of Materials Research*, **8**(12):3059–3068.

- Zaluski, L., Hosatte, S., Tessier, P., Ryan, D.H., and Ström-Olsen, J.O. 1994. Hydrogen Absorption in Amorphous and Nano-crystalline FeTi. *Journal of Physical Chemistry*, **183**(1-2):45–49.
- Zaluski, L., Zaluska, A., Tessier, P., Ström-Olsen, J.O., and Schulz, R. 1995. Catalytic effect of Pd on hydrogen absorption in mechanically alloyed Mg₂Ni, LaNi₅ and FeTi. *Journal of Alloys and Compounds*, **217**(2):295–300.
- Zaluski, L., Zaluska, A., and Ström-Olsen, J.O. 1997. Nanocrystalline metal hydrides. *Journal of Alloys and Compounds*, **253-254**:70–79.
- Zlota, C., Oumellal, Y., Hwang, S.J., Ghimbeu, C.M., de Jongh, P.E., and Latroche, M. 2015. Ultrasmall MgH₂ Nanoparticles Embedded in an Ordered Microporous Carbon Exhibiting Rapid Hydrogen Sorption Kinetics. *Journal of Physical Chemistry C*, **119**(32):18091–18098.
- Züttel, A. 2003. Materials for hydrogen storage. *Materials today*, **6**(9):24–33.
- Züttel, A., Sudan, P., Mauron, P., and Wenger, P. 2004. Model for the hydrogen adsorption on carbon nanostructures. *Applied Physics A*, **78**:941–946.
- Züttel, A., Remhof, A., Borgschulte, A., and Friedrichs, O. 2010. Hydrogen: the future energy carrier. *Philosophical Transactions of the Royal Society A*, **368** (1923):3329–3342.